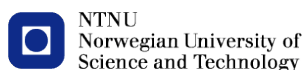


# Unravelling the Sandy Shorelines Dynamics Derived from Satellite Images

Nan Wang





ERASMUS +: ERASMUS MUNDUS MOBILITY PROGRAMME

Master of Science in

COASTAL AND MARINE ENGINEERING AND  
MANAGEMENT

CoMEM

**UNRAVELLING THE SANDY SHORELINE DYNAMICS  
DERIVED FROM SATELLITE IMAGES**

Delft University of Technology  
10 July 2018

Nan Wang

The Erasmus+: Erasmus Mundus MSc in Coastal and Marine Engineering and Management is an integrated programme including mobility organized by five European partner institutions, coordinated by Norwegian University of Science and Technology (NTNU).

The joint study programme of 120 ECTS credits (two years full-time) has been obtained at two or three of the five CoMEM partner institutions:

- Norges Teknisk- Naturvitenskapelige Universitet (NTNU) Trondheim, Norway
- Technische Universiteit (TU) Delft, The Netherlands
- Universitat Politècnica de Catalunya (UPC). BarcelonaTech. Barcelona, Spain
- University of Southampton, Southampton, Great Britain
- City University London, London, Great Britain

During the first three semesters of the programme, students study at two or three different universities depending on their track of study. In the fourth and final semester an MSc project and thesis has to be completed. The two-year CoMEM programme leads to a multiple set of officially recognized MSc diploma certificates. These will be issued by the universities that have been attended by the student. The transcripts issued with the MSc Diploma Certificate of each university include grades/marks and credits for each subject.

Information regarding the CoMEM programme can be obtained from the programme coordinator:

Øivind A. Arntsen, Dr.ing.  
Associate professor in Marine Civil Engineering  
Department of Civil and Environmental Engineering  
NTNU Norway  
Mob.: +4792650455 Fax: + 4773597021  
Email: oivind.arntsen@ntnu.no

CoMEM URL: <https://www.ntnu.edu/studies/mscomem>

Disclaimer:

*"The European Commission support for the production of this publication does not constitute an endorsement of the contents which reflects the views only of the authors, and the Commission cannot be held responsible for any use which may be made of the information contained therein."*

## CoMEM Thesis

This thesis was completed by:

*Nan Wang*

Under supervision of:

*Prof.dr.ir. S.G.J. Aarninkhof, TU Delft*

*Prof. R.J. Nicholls, University of Southampton*

*Ir. A.P. Luijendijk, TU Delft/ Deltares*

*Dr.ir. S. de Vries, TU Delft*

*Dr. F.Baart, Deltares*

As a requirement to attend the degree of

*Erasmus+: Erasmus Mundus Master in Coastal and Marine Engineering and Management  
(CoMEM)*

Taught at the following educational institutions:

*Norges Teknisk- Naturvitenskapelige Universitet (NTNU)  
Trondheim, Norway*

*Technische Universiteit (TU) Delft  
Delft, The Netherlands*

*University of Southampton,  
Southampton, Great Britain*

At which the student has studied from August 2016 to July 2018.



# Preface

This master thesis is submitted as part of the requirement for obtaining the Master of Science in Coastal and Marine Engineering and Management (CoMEM), in the track of Coastal Engineering, at the Technical University of Delft.

This work would only be possible with the support and guidance I could count on, to which I would like to express my gratitude. First of all, I would like to appreciate Arjen for creating this fascinating topic and offering the project to me. I am really grateful for your helps on providing the original data (SDS), making guidance and discussions throughout all the steps and aspects of this thesis. Thank you Sierd and Baart for the regular meetings and always inspiring me with useful comments. I am particularly grateful to Professor Nicholls for his helps to clear my idea at the beginning of the project, and you have saved me much time by pointing out the aim and potential research questions. Thank you Professor Aaninkhof for the insightful remarks and suggestion on how to present in a more scientific and logical way, which will be really helpful during the rest of my career. Thank you Hagenars for inspiring me of the essence of extracting shoreline from satellite images.

I would like to appreciate the helps from my friends, both from CoMEM and from back home. Your supports and inspirations make the thesis time more comforting. I am really appreciated my parents, Wang Zhilin and Xu Lijie, and I do not think that it possible to receive more love and supports than what you have provided me. Finally, thank you the Erasmus+ for waiving the tuition and providing living fees throughout this master study.

Thanks to everyone.

Nan Wang

Delft, July 2018



# Summary

Coastal zones all over the world have become heavily populated and developed due to the aesthetic value and diverse ecosystem services that they provide (Luijendijk et al. 2018). In recent years, however, climate change and anthropogenic pressures have exacerbated unprecedented coastal recession, threatening billions of dollars' worth of coastal developments and infrastructure (Ranasinghe et al. 2012). In order to counteract the erosion trend and protect shoreline positions, it is necessary to carry out reliable assessments of shoreline dynamics to monitor the erosion process. Therefore, this thesis attempts to explain different spatial and temporal patterns of sandy shoreline evolution.

The strict definition of shoreline is the physical land-water boundary (Boak & Turner 2005). However, considering the dynamic nature of water levels and the cross-shore and longshore sediment transport in the littoral zone, many coastal state indicators have been used as proxies to represent the 'true' shoreline position for practical purposes (Boak & Turner 2005). The satellite derived shorelines (SDS), considered as a new type of coastal state indicator, provide a global shoreline dataset from 1984 to present. Hagenaaers et al. (2017) stated that for long-time scales, similarities can be found between coastline dynamics based on the SDS positions and traditional indicators based on topographic measurements. Thus, for any coastal sandy stretch, time series of the SDS can be analyzed to get a first understanding of the coastline evolution in the period of 1984 – present.

Three knowledge gaps are identified regarding using the SDS on unravelling shoreline dynamics:

**Does the time series of the SDS contain signatures of expected shoreline behaviour?**

**To what extent is the limitation of the SDS important for unravelling shoreline dynamics?**

**What is the application range of using the SDS for unravelling shoreline dynamics?**

The above knowledge gaps were addressed through the following steps. (1) We narrowed down the forcing types that would be focused on, including extreme storms, seasonal forcing, climate variability, land subsidence, sea level rise (SLR) and anthropogenic processes. (2) The shoreline changes at the eleven knowledge-intensive sites were focused on, each of which was selected based on the available documentation to verify if the influence of a specific forcing type could be unravelled through the SDS. The sites of interests include Narrabeen, Moruya and Pedro, Perranporth, Ocean Shores (CRLC), the Nile Delta, Perth, Ocean Beach, Fire Island, Gatseau sandspit and Cap Ferret sandspit (SW France), the Gulf of Valencia and Wrightsville Beach. (3) We decomposed the time series of the SDS with a range of data analysis methods, in order to extract spatiotemporal patterns of shoreline variation and correlate the variation patterns to forcing types at the eleven sites. (4) Three indices were calculated to classify rotational/non-rotational and seasonal/non-seasonal beaches based on the analysis results of the SDS. (5) The knowledge gaps were addressed through comparing the shoreline behaviour patterns derived from the SDS to the analysis within the related literature.

We found that the spatiotemporal patterns of shoreline variation on the seasonal scale (due to seasonal forcing), inter-annual scale (due to climate variability) and decadal scale (due to land subsidence) extracted through the SDS are largely in line with the conclusions listed in the related literature, in which the dataset such as field measurements or video monitoring were used. Moreover, the influence of groins and beach nourishment projects on shoreline changes can also be clearly unravelled using the SDS. However, the SDS cannot be considered as the best solution to study shoreline variation governed by storms, considering the low frequency of satellite image acquisition and the influence of the image composite technique. Moreover, only using the SDS to assess the shoreline responses to SLR may not provide promising results, since the limited length of the record (over 30 years) make it hard to capture

the influence of SLR on open coasts on long-term scales.

To sum up, the SDS could be used as an ideal tool for unravelling coastline dynamics on seasonal, inter-annual and decadal scales governed by the seasonal forcing, climate variability and land subsidence, respectively. The shoreline changes caused by beach nourishment projects can also be clearly unravelled with the SDS. The introduction of new satellite missions can be expected in the near future, which helps to obtain an increasing temporal, spatial and spectral resolution of satellite images ([Hagenaars et al. 2018](#)). Therefore, it is highly possible that the SDS will become a more powerful tool for studying shoreline changes governed by extreme storms as time goes by. Furthermore, when the longer-recorded SDS are achieved in the future, it can be expected that the capabilities of using the SDS for studying the long-term shoreline variation governed by SLR will be improved.

# Contents

<b>Preface</b>	<b>iii</b>
<b>Summary</b>	<b>v</b>
<b>1 Introduction</b>	<b>1</b>
1.1 Project overview . . . . .	1
1.2 Motivation . . . . .	1
1.2.1 Background . . . . .	1
1.2.2 Research questions . . . . .	4
1.3 Methodology . . . . .	4
1.4 Report outline . . . . .	5
<b>2 Background Information</b>	<b>7</b>
2.1 Remote sensing . . . . .	7
2.1.1 Google Earth Engine . . . . .	7
2.1.2 Satellite derived shorelines . . . . .	8
2.2 Forcing types . . . . .	13
2.2.1 Storms . . . . .	13
2.2.2 Seasonal forcing . . . . .	13
2.2.3 Climate variability . . . . .	13
2.2.4 Sea level rise . . . . .	17
2.2.5 Land subsidence . . . . .	18
2.2.6 Other types of forces . . . . .	18
<b>3 Methodology</b>	<b>21</b>
3.1 Specify the sites of interests . . . . .	21
3.2 Spatiotemporal subsets of the global dataset . . . . .	27
3.2.1 Time series decomposition . . . . .	27
3.2.2 STL decomposition . . . . .	28
3.2.3 Principal component analysis . . . . .	29
3.3 Extract behavioural patterns of shoreline variation . . . . .	32
3.3.1 Spectral analysis . . . . .	32
3.3.2 Regression analysis . . . . .	35
3.4 Beach classifications . . . . .	37
3.4.1 Rotational/non-rotational beach . . . . .	37
3.4.2 Seasonal/non-seasonal beaches . . . . .	38
3.5 A Framework of time series analysis . . . . .	40
3.6 Narrabeen Beach (Example 1) . . . . .	41
3.6.1 Principal component analysis . . . . .	42
3.6.2 The STL decomposition . . . . .	42
3.6.3 Fast Fourier transform . . . . .	43
3.6.4 Wavelet analysis . . . . .	44
3.6.5 Shoreline variation and the SOI . . . . .	45
3.6.6 Regression analysis . . . . .	45
3.6.7 Summary . . . . .	47
3.7 Moruya and Pedro (Example 2) . . . . .	48
3.7.1 Principal component analysis . . . . .	48
3.7.2 The STL decomposition . . . . .	49
3.7.3 Fast Fourier transform . . . . .	49
3.7.4 Trend component analysis . . . . .	50
3.7.5 Summary . . . . .	51

<b>4</b>	<b>Results</b>	<b>53</b>
4.1	Storm	53
4.1.1	Fire Island	53
4.1.2	The Gulf of Valencia	56
4.1.3	Other sites	58
4.1.4	Discussion and conclusion	58
4.2	Seasonal forcing	59
4.2.1	CRLC (Ocean Shores)	59
4.2.2	Perth	61
4.2.3	Other sites	64
4.2.4	Discussion and conclusion	64
4.3	Climate variability	65
4.3.1	Ocean Beach	65
4.3.2	CRLC (Ocean Shores)	67
4.3.3	Other sites	69
4.3.4	Discussion and conclusion	69
4.4	Land subsidence	70
4.4.1	Nile Delta (Rosetta mouth)	70
4.4.2	Other sites	71
4.4.3	Discussion and conclusion	71
4.5	Sea level rise	72
4.5.1	Gatseau sandspit and Cap Ferret sandspit (SW France)	72
4.5.2	Other sites	74
4.5.3	Discussion and conclusion	74
4.6	Anthropogenic processes	75
4.6.1	Wrightsville Beach	75
4.6.2	Discussion and conclusion	76
<b>5</b>	<b>Discussion</b>	<b>77</b>
5.1	Sensitivity analysis	77
5.2	Summary of analysis results	78
<b>6</b>	<b>Conclusions and recommendations</b>	<b>81</b>
6.1	Conclusions	81
6.2	Recommendations	84
	<b>Bibliography</b>	<b>85</b>
	<b>List of Figures</b>	<b>93</b>
	<b>List of Tables</b>	<b>97</b>
<b>A</b>	<b>Maps of the sites of interests</b>	<b>99</b>
<b>B</b>	<b>Figures of sensitivity analysis</b>	<b>111</b>
<b>C</b>	<b>Result plots of data analysis</b>	<b>117</b>
<b>D</b>	<b>Other data process techniques</b>	<b>133</b>
D.1	Narrabeen Beach	133
D.2	Moruya and Pedro	135
D.3	Perranporth	135

# 1

## Introduction

### 1.1. Project overview

Coastal zones all over the world have become heavily populated and developed due to the aesthetic value and diverse ecosystem services that they provide (Luijendijk et al. 2018). However, serious concerns have been raised in recent years, since coastal squeeze is exacerbated by climate change and a high percentage of sandy shorelines in nature-protected areas worldwide are eroding (Luijendijk et al. 2018). According to Ranasinghe et al. (2012), the accelerating sea level rise in the twenty-first century will result in unprecedented coastal recession, and wave and water level anomalies induced by a suite of climate variability will also exacerbate. Combined with the extreme events (e.g. hurricanes) and anthropogenic pressures (e.g. land subsidence caused by groundwater extraction), these forcing types may threaten billions of dollars' worth of coastal developments and infrastructure (Ranasinghe et al. 2012). For counteracting the erosion trend and protecting shoreline positions, it is necessary to carry out reliable assessments of shoreline variation to monitor the erosion process so that the sandy shoreline dynamics could be understood well. Thus, **the aim of this thesis is to explain different spatial and temporal patterns of sandy shoreline evolution.**

This thesis addresses the required research on unravelling the sandy shoreline dynamics with satellite images. The satellite derived shorelines (SDS), considered as a new type of coastal state indicator (Hagenaars et al. 2017), provide a global shoreline dataset from 1984 to present. The time series of the SDS are decomposed with a series of data analysis methods to study the dynamic behaviours of sandy shorelines on different spatiotemporal scales. A range of **forcing types**, including extreme storms, seasonal forcing, climate variability, land subsidence and sea level rise, are correlated with shoreline variation, in order to analyze what mechanism governs the shoreline evolution (Figure 1.1). Through comparing the extracted spatiotemporal patterns of shoreline variation based on the SDS with those concluded in the related literature, the application range of using the SDS for studying shoreline dynamics is tested.

### 1.2. Motivation

The demand for the research to be completed in the present study is specified in this section. This is addressed in the following two subsections: a review of the field of study (background) and the analysis of the limitations in the current knowledge (research questions).

#### 1.2.1. Background

Analysis of shoreline changes is fundamental to a broad range of investigations undertaken by coastal scientists, coastal engineers, and coastal managers (Boak & Turner 2005). An idealized definition of shoreline is that it coincides with the physical interface of land and water (Dolan et al. 1980). In reality, however, this definition is a challenge to be applied considering the cross-shore and longshore

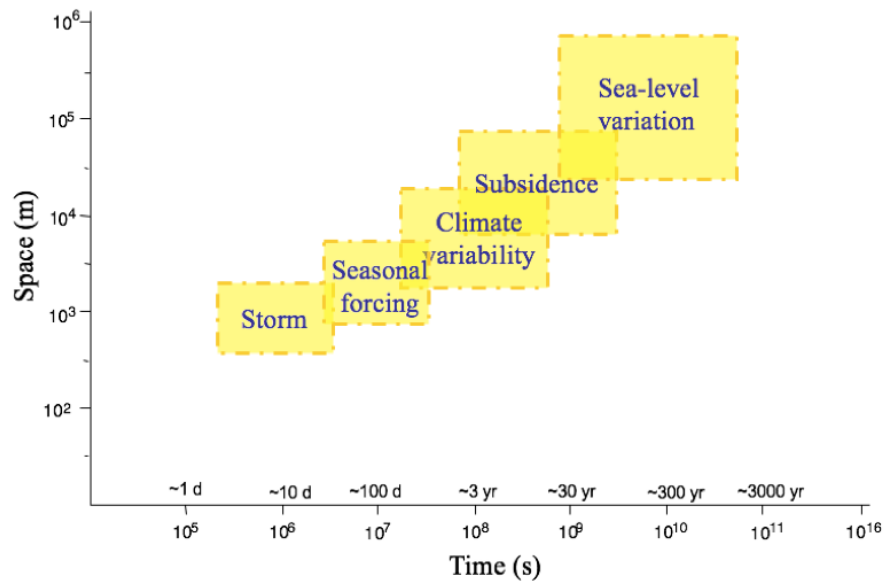


Figure 1.1: Temporal and spatial scales in coastal morphodynamics.

sediment transport in the littoral zone and the dynamic nature of water levels at the coastal boundary. Thus, series of coastal state indicators have been used as proxies to represent the 'true' shoreline position for practical purposes (Boak & Turner 2005).

Traditionally, there are two types of proxies, including the feature that is visibly discernible in coastal imagery (e.g. high-water line or the wet/dry boundary, Figure 1.2) and the intersection of a tidal datum with the coastal profile (e.g. mean high water or mean sea level, Figure 1.3) (Boak & Turner 2005). For the shoreline detection techniques through the visibly discernible shoreline features, they highly rely on the individual skills of the interpreters and photogrammetrist, so these methods are by definition subjective (Boak & Turner 2005). A more objective shoreline detection method could be obtained through tidal datum shoreline indicators. It can be determined from a digital terrain model created by techniques such as softcopy photogrammetry and the LiDAR topographic data (Stockdon et al. 2002). However, this objective shoreline detection is limited to analyze the historical trend because of lack of good-quality stereo pairs and the accurate ground control points in old days (Boak & Turner 2005).

The third type of coastal state indicator has been developed recently based on the application of image-processing techniques (Boak & Turner 2005). It extracts proxy shoreline features from digital coastal images that are not necessarily visible to the human eye (Boak & Turner 2005). Unlike the other two types of proxies which are largely dependent on subjective interpretation and opportunistic data collection, digital images can develop more objective, repeatable, and robust detection techniques (Aarninkhof et al. 2001).

Satellite images, which provide a unique source of data given its spatial and temporal coverage, could be used to generate the third type of indicator. Since 1984, satellite imagery provides data on a global scale with a frequent revisit time (every 5-16 days) and a moderate spatial resolution (approx. 10-30 m) (Gorelick et al. 2017). The development of image processing techniques makes it possible to distinct pixels containing different landscapes. However, this process used to be laborious and time-consuming, limiting the capability of satellite imaging (Hagenaars et al. 2018). In these days, Google Earth Engine (GEE) platform launched by Google helps to remove traditional computational limitations in image processing. Combined with Google's computational infrastructure and archive of available imagery, GEE provides the opportunity to study all available images (Gorelick et al. 2017).

A detection algorithm has been developed and tested to automatically determine the satellite derived



Figure 1.2: An example of a range of visibly discernible shoreline indicator features, Duranbah Beach, New South Wales, Australia (E: Seaward dune vegetation line, G: Storm/debris line, H: An old high tide water level, I: Previous high tide high water level, K: Wet/dry line or runup maxima, L: Groundwater exit point, M: Instantaneous water line, N: shorebreak maximum intensity). Figure from [Boak & Turner \(2005\)](#).

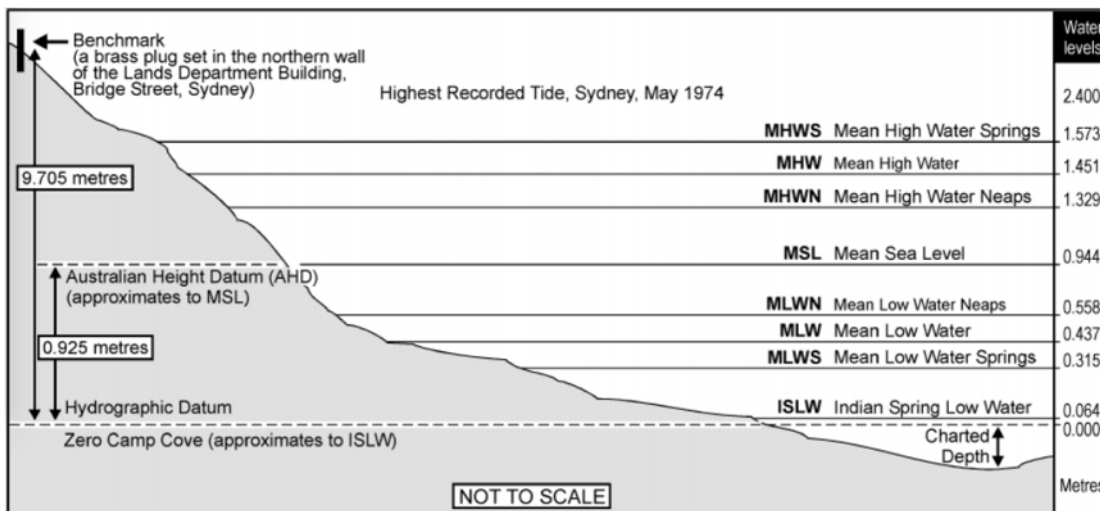


Figure 1.3: Tidal datums used along the New South Wales coastline, Australia. Figure from [Boak & Turner \(2005\)](#).

shorelines (SDS) using GEE by [Hagenaars et al. \(2017\)](#). [Hagenaars et al. \(2018\)](#) found the accuracy of the SDS derived from moving average composite images to be of subpixel precision (approx. half a pixel size, i.e., 15 m for Landsat and 5 m for Sentinel-2). Similarities can be found between coastline dynamics based on the SDS positions and traditional indicators based on topographic measurements, hence the SDS may serve as a coastal state indicator ([Hagenaars et al. 2017](#)). Thus, time series of the SDS can be used to get a first understanding of coastline evolution. This method has been applied to all historic and cloud free satellite images of shoreline, resulting in a 34-year time series of coastline positions and a construction of global dataset ([Luijendijk et al. 2018](#)). The map shown in Figure 1.4 illustrates the global hot spots of beach erosion and accretion over the last three decades ([Luijendijk](#)

et al. 2018).

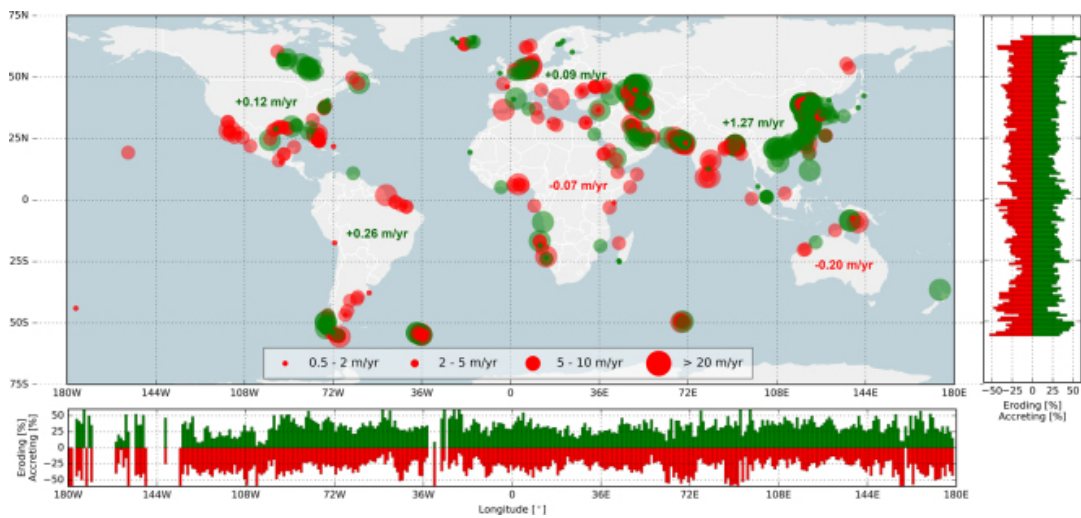


Figure 1.4: Global hot spots of beach erosion and accretion; the red (green) circles indicate erosion (accretion) for the four relevant shoreline dynamic classifications (see legend). The bar plots to the right and at the bottom present the relative occurrence of eroding (accreting) sandy shorelines per degree latitude and longitude, respectively. The numbers presented in the main plot represent the average change rate for all sandy shorelines per continent. Figure from [Luijendijk et al. \(2018\)](#).

### 1.2.2. Research questions

The SDS as a type of coastal state indicator have some known advantages. According to [Hagenaars et al. \(2017\)](#), the time series of the SDS can be employed to get a first understanding of the coastline evolution on long-time scale in the period of 1984 to present. Moreover, the SDS are less expensive and constrained in time and/or space compared with the visibly discernible shoreline indicators and the tidal datum shoreline indicators, and the detection algorithm for deriving the SDS has become less laborious and time-consuming thanks to the GEE platform. However, the application range of using the SDS to extract behavioural patterns of sandy shoreline variation is still unknown. Based on the background information specified in Section 1.2.1, the main research question can be identified:

#### What is the application range of using the SDS for unravelling shoreline dynamics?

The two sub-questions are:

- Does the time series of the SDS contain signatures of expected shoreline behaviour?
- To what extent is the limitation of the SDS important for unravelling shoreline dynamics?

## 1.3. Methodology

The present thesis aims to identify different spatial and temporal patterns of sandy beach evolution. The methodology can be summarized as Figure 1.5 and details will be specified in Chapter 3.



Figure 1.5: Methodology to test the application range of using the SDS for unravelling sandy shoreline dynamics.

### Step 1: specify the sites of interests

The shoreline changes at around ten sandy beaches will be the main research objects for the present

study, each of which will be selected based on the available documentation to verify if the influence of a specific forcing type could be unravelled through the SDS. In the present study, the forcing types including storms, seasonal forcing, climate variability, land subsidence, SLR and anthropogenic processes will be focused on. Considering the spatial resolution of satellite images (30m), the sandy beaches with 'obvious' shoreline movement (e.g. larger than 100m) are more appropriate to be selected. For each site of interest, transects will be generated perpendicular to the latest available SDS. The number and location of the transects will depend on the extent of sandy shoreline and the specific coastal features on site, so that the transects are sufficient and representative to study the spatial patterns of sandy shoreline variation (e.g. identify the hot spots of erosion).

### **Step 2: generate spatiotemporal subsets of the global dataset**

Various data analysis methods will be used to create spatiotemporal subsets. For instance, dominant modes of shoreline movement will be extracted via principal component analysis (PCA) by isolating the temporal and spatial dependence of the data; the time series of shoreline change will be decomposed to a range of signals (i.e. trend, cyclic and residual components) by a seasonal-trend decomposition procedure based on Loess (STL decomposition).

### **Step 3: extract behavioural patterns of shoreline variation from spatiotemporal subsets**

A range of data analysis techniques will be used to identify spatial and temporal patterns of sandy shoreline variation. The spectral analysis methods can transform the time series of shoreline positions to the frequency space, such as the fast Fourier transform (FFT) and wavelet analysis. For unravelling the drivers of sandy shoreline evolution and interpreting the specific signals, different forcing types will be correlated to shoreline movement. The analysis results will then be used to classify seasonal/non-seasonal and rotational/non-rotational beaches. Finally, the behavioural patterns of shoreline variation derived from the SDS will be compared with the conclusions listed in the related literature, and thus the application range of using the SDS for unravelling coastline dynamics could be tested.

## **1.4. Report outline**

The relevant literature to contextualize the present work is presented in Chapter 2. Chapter 3 contains the methodology used to study the sandy shoreline dynamics, an overall description of sites of interests and examples for introducing the whole processes on unravelling shoreline dynamics with the SDS. Chapter 4 shows the analysis results of spatiotemporal patterns of sandy shoreline variation at different sites based on the SDS data. The discussion and conclusions of the research work are presented in Chapter 5 and Chapter 6, respectively.



# 2

## Background Information

This chapter presents a summary of the existing knowledge on the topics considered in this research. In the first part of this chapter, an introduction of remote sensing and the SDS is specified. The second part describes different forcing types, including extreme storms, seasonal forcing, climate variability, land subsidence, sea level rise, etc.

### 2.1. Remote sensing

A formal definition of remote sensing is 'the measurement or acquisition of information of some property of an object or phenomenon, by a recording device that is not in physical or intimate contact with the object or phenomenon under study' (Jensen 2009). Since the 1960s, remote sensing has been used to describe a new field of information collection, which includes aircraft and satellite platforms carrying cameras to electro-optical and antenna sensor systems (Jensen 2009). Compared to field-base studies, it has many advantages in terms of quantitatively measuring and forecasting land-cover changes, considering practical data acquisition, application of spatiotemporal data and effective cost (Lu et al. 2004). In order to extract useful information from the images, image processing techniques are employed to enhance the image for visual interpretation, and to correct or restore the image if the image has been subjected to geometric distortion, blurring or degradation by other factors (Lu et al. 2004). In many cases, image segmentation and classification algorithms are used to delineate different areas in an image into thematic classes. The resulting product is a thematic map of the study area, which can be combined with other databases of the test area for further analysis and utilization (Liew 2001).

#### 2.1.1. Google Earth Engine

Satellite imagery is gaining popularity due to its global scale and spatiotemporal resolution. However, many problems exist when using satellite imagery in a traditional way. For instance, this process used to be laborious and time-consuming; the specialist knowledge of correcting and adjusting techniques was needed; and the specific software skills and computing power of processing were required (Gorelick et al. 2017). These all limit the capabilities of satellite imaging to be used for studying a variety of high-impact societal issues.

Google Earth Engine (GEE) launched by Google seems to provide promising solutions to these problems (Fragkopoulos 2016). GEE is a cloud-based platform for the analysis of geospatial data with the Google's computational infrastructure and archive of available imagery combined. Unlike the traditional desktop software model, GEE allows the user to focus on the analysis but not on acquiring data, since the data has been precomputed by Google on the platform (Fragkopoulos 2016). It empowers not only traditional remote sensing scientists, but also a much wider audience who lacks the technical capacity needed to utilize traditional supercomputers or large-scale commodity cloud computing resources

(Gorelick et al. 2017).

The major advantages of using GEE include (i) the Earth Engine public data catalog contains the entire Landsat archive as well as complete archives of data from Sentinel-1 and Sentinel-2 (Table 2.1). It also includes climate forecasts, land cover data and many other environmental, geophysical and socio-economic datasets, making the process of collecting data easier (ii) the combination of cloud storage and parallel cloud computing on the server side of the platform considerably reduces the image processing time from hours to minutes (Gorelick et al. 2017).

Table 2.1: Frequently used datasets in the earth engine data catalog

Dataset	Nominal resolution	Temporal granularity	Temporal coverage	Spatial coverage
Landsat 8 OLI/TIRS	30 m	16 day	2013-Now	Global
Landsat 7 ETM+	30 m	16 day	2000-Now	Global
Landsat 5 TM	30m	16 day	1984-2012	Global
Landsat 4-8 surface reflectance	30m	16 day	1984-Now	Global
Sentinel 1 A/B ground range detected	10 m	6 day	2014-Now	Global
Sentinel 2A MSI	10/30 m	10 day	2015-Now	Global

### 2.1.2. Satellite derived shorelines

The strict definition of shoreline is the physical land-water boundary (Dolan et al. 1980). However, due to the dynamic nature of this boundary and its dependence on the temporal and spatial scale at which it is being considered, a range of coastal state indicators are used as proxies to represent the ‘true’ shoreline position for practical purposes (Boak & Turner 2005). Traditionally, there are two types of these proxies (Section 1.2.1). According to Boak & Turner (2005), a third category of shoreline indicator has begun to be reported in the literature recently, which is based on the application of image-processing techniques to extract proxy shoreline features from digital coastal images that are not necessarily visible to the human eye. Compared with the two traditional types of proxies, it is more objective, repeatable and robust (Section 1.2.1).

The SDS may serve as a third type of coastal state indicator, as for long-term scales, similarities can be found between coastline dynamics based on the SDS positions and traditional indicators based on topographic measurements (Hagenaars et al. 2017). A continuous dataset with subpixel precision (10-30 m, depending on the satellite mission) has been constructed, implying that structural trends can be detected for coastlines that have changed with at least a pixel resolution within the considered timespan (Hagenaars et al. 2018). A global-scale assessment of the occurrence of sandy beaches and the rate of shoreline erosion/accretion along the sandy coasts of the world have been presented by Luijendijk et al. (2018). Thus, for any coastal sandy stretch, time series of the SDS can be analyzed to get a first understanding of the coastline evolution in the period of 1984 – present (Hagenaars et al. 2017).

Figure 2.1 shows the workflow containing the methodology to derive the SDS as a coastal state indicator. The related processing techniques are outlined as following.

#### Image processing

The detection algorithm to determine the SDS was developed and tested by Hagenaars et al. (2017). They extracted the coastline with an automatic, unsupervised thresholding algorithm. The Normalized Difference Water Index (NDWI) value per pixel was calculated using:

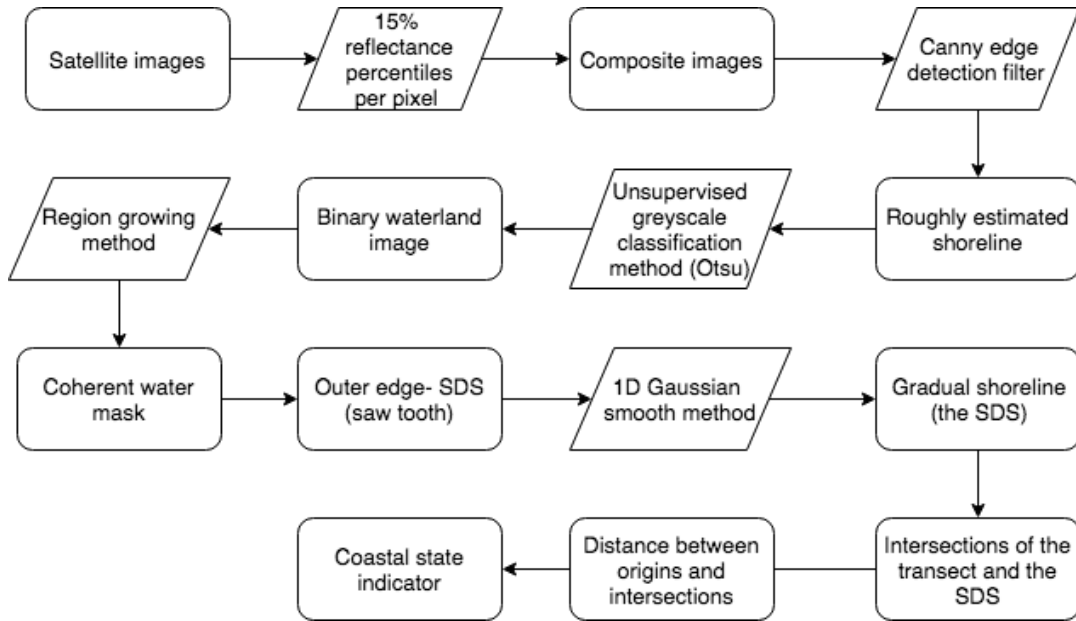


Figure 2.1: The workflow of the methodology for deriving the SDS as a coastal state indicator. Summarized based on Hagenaars et al. (2018) and Luijendijk et al. (2018).

$$NDWI = \frac{\lambda_{NIR} - \lambda_{GREEN}}{\lambda_{NIR} + \lambda_{GREEN}} \quad (2.1)$$

where  $\lambda_{NIR}$  is the TOA radiance value in the near infrared (NIR) and  $\lambda_{GREEN}$  is the TOA radiance value in green band per pixel (Liu et al. 2017). Calculating the NDWI value per pixel results in a greyscale image with NDWI values ranging from -1 to 1 (Hagenaars et al. 2018). The **Canny edge detection filter** is then used to roughly estimate the position of the water-land transition. The **Otsu thresholding method** is then employed on a buffer polygon around the roughly estimated water-land transition to classify the grey-scale image into a binary water-land image (Luijendijk et al. 2018). The optimal threshold value which determines shoreline position depends on the statistical properties of the NDWI histogram, and an example of such a NDWI histogram and the optimal threshold is shown in Figure 2.2. In the most optimal manner of this example, a threshold value of -0.01 is chosen to separate the NDWI values into two distinct regions. All NDWI values greater than the threshold value are classified as land and all NDWI values smaller than the value are classified as water. A **region growing algorithm** is then used to obtain a coherent water mask (Kamdi & Krishna 2012), and the **outer edge** of the obtained water mask is defined as the location of the SDS. This vector has a saw tooth pattern since it is defined at the image pixel edges, which could be smoothed to obtain a gradual shoreline using the **1D Gaussian smoothing operation** (Hagenaars et al. 2018). The method may result in several shoreline vectors since also lakes and small channels can be detected; if so, only the most seaward SDS position is analyzed (Luijendijk et al. 2018).

Hagenaars et al. (2018) found the accuracy of the SDS is within subpixel precision (approx. half a pixel size, i.e., 15 m for Landsat and 5 m for Sentinel-2). In their case study at Sand Engine, an average offset of 1.3 m, 8.5 m and 1 m was found for the Sentinel 2, Landsat 8 and Landsat 5 benchmarks, respectively (the benchmark accuracy provides information on the best possible accuracy for the satellite sensors, the in-situ data and the applied offset calculation methodology). This indicates subpixel precision and the absence of large offset values in case of Sentinel 2 and Landsat 5. However, the benchmark accuracy cannot be obtained for most times due to the presence of drivers of inaccuracy. According to Hagenaars et al. (2018), six drivers can cause the SDS position to deviate from the actual shoreline. Drivers related to the environmental conditions on the image include: (i) cloud cover, (ii) waves (surface roughness and foam) and (iii) soil moisture and grain size ( $D_{50}$ ). Drivers related to the satellite instrument include: (i) sensor corrections, (ii) georeferencing and (iii) image pixel resolution.

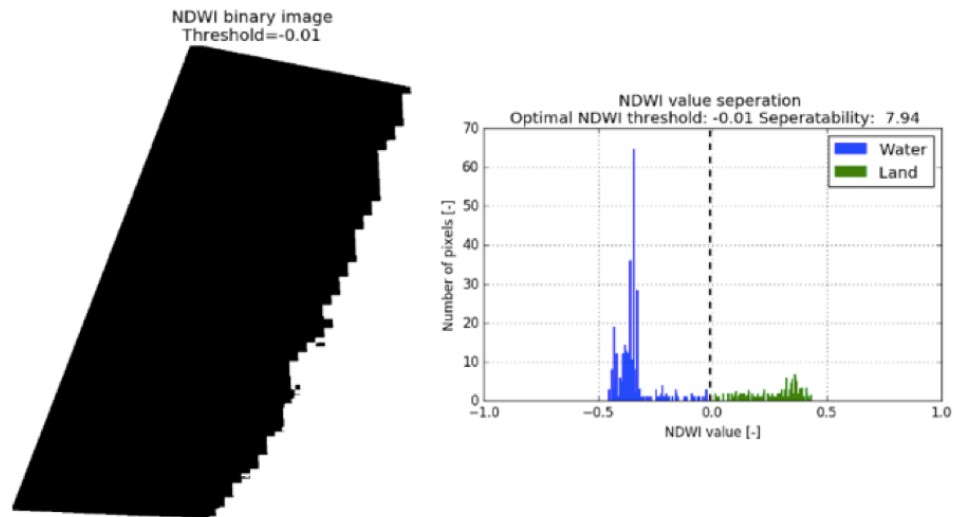


Figure 2.2: NDWI resulting binary image (left) and NDWI histogram (right) for Sentinel 2 image acquire on 1984-05-03 10:38:32. An optimal threshold value of -0.01 classifies the NDWI values into water (blue) and land (green) pixels. Figure from [Hagenaars et al. \(2018\)](#).

Clouds have NDWI values in the range of land, and foam caused by breaking waves has identical NDWI values as land, which both result in a seaward offset of the SDS in case cloud or foam is present close to the shoreline. For other drivers of inaccuracy, they all introduce a seaward shift of the SDS. To reduce the inaccuracy caused by the drivers, [Donchyts et al. \(2016\)](#) used an image composite processing technique, which is discussed in the next subsection.

### The composite images

The principle of image composite processing technique is to use a sequence of satellite images to generate a single composite image ([Hagenaars et al. 2018](#)). According to [Luijendijk et al. \(2018\)](#), the construction of their global sandy shoreline dataset applied this technique, and each pixel in the composite image was obtained from the 15th percentile value of the TOA green and NIR reflectance values of the concurrent pixels within a sequence of individual images (Figure 2.3). The reason for choosing 15th percentile value is that clouds cause high reflection values, and choose the 15th percentile value can result in clear pixels ([Hagenaars et al. 2018](#)).

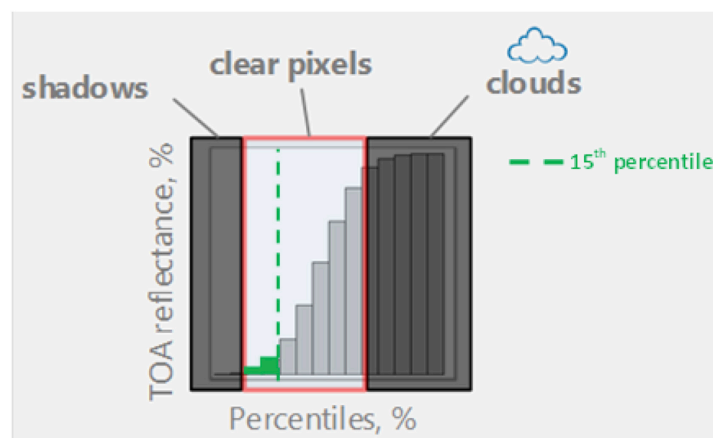


Figure 2.3: The principle of the image composite technique based on the distribution of all TOA reflectance values within the image composite time window per pixel. Figure from [Hagenaars et al. \(2018\)](#).

Although longer averaging windows have the tendency towards generating a higher accuracy of SDS (lower average offset values), the downside is that the information on shoreline variability within the time sequence is lost to some extent (Hagenaars et al. 2018). Thus, the longer windows are less suitable for the detection of intra-annual variation, and a balance between the positional accuracy and the temporal variability should be obtained. Luijendijk et al. (2018) applied an averaging period of 192 days (i.e. the first integer that is found when dividing the global revisiting time of the satellite sensor (16 days) by a semidiurnal tidal period (approx. 12 hrs)), since this averaging period can also significantly decrease the influence of tidal ranges on detecting the SDS. Thus, all satellite images in this averaging interval are cloud-free with the average water level corresponds to mean sea level.

### Coastline trends

Time series of the SDS can help to study the coastline evolution. According to the study of Hagenaars et al. (2017), firstly, they obtained a time series of the points of intersection between the transect and the subsequent SDS positions. The distance between the transect origin, which was fixed in time and located at the landward side of the transect, and the point of intersection was then stored for all the SDS positions and all transects. This distance is proposed to serve as a coastal indicator, and changes in this distance over time reveal information on the dynamics at the shoreline.

To quantify shoreline variation trend, Hagenaars et al. (2018) made a fit through the data with the method of Ordinary Least Squares (OLS) of the linear equation (fitting a line-of-best fit):

$$y(t) = a \times t + b \quad (2.2)$$

where  $y(t)$  [m] is the distance between the transect origin and the SDS intersection at time instance  $t$ , and  $a$  [m/yr] is an indicator for the structural rate of change. The suitability of the technique to identify structural trends in the shoreline position was assessed by Hagenaars et al. (2018). They compared the trends obtained from the SDS (erosive rate of 54.2 m/yr) and from the topographic surveys (erosive rate of 52.0 m/yr) of shoreline movement at transect 54 on Sand Engine, showing that the similar trends can be extracted from both data sources with a small deviation of 2.2 m/yr (Figure 2.4).

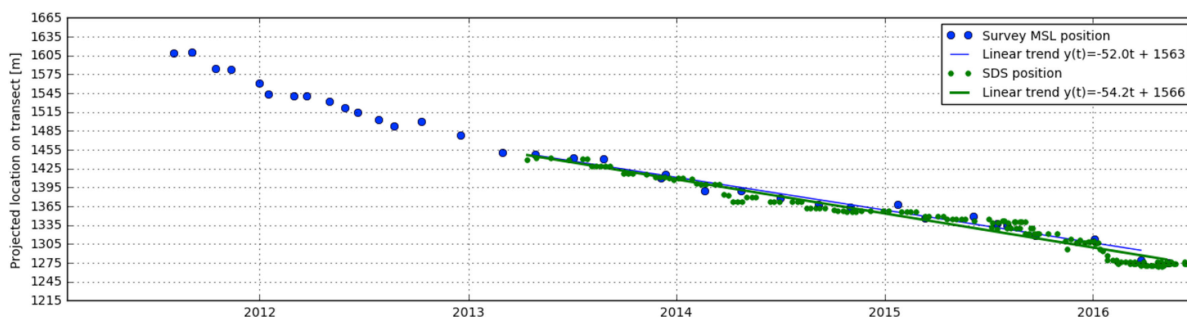


Figure 2.4: Time series of the SDS positions and the MSL contour lines obtained from the survey projected along transect 54 on Sand Engine. An OLS fit is made based on the information between 01 and 04-2013 and 01-07-2016. Figure from Hagenaars et al. (2017).

### Global sandy shoreline dataset

Luijendijk et al. (2018) presented the first global-scale assessment of the occurrence of sandy beaches and rate of shoreline erosion/accretion along the sandy coasts (Figure 2.5), using freely available optical satellite images captured since 1984 and sophisticated image processing methods. They applied linear regression to capture trends of shoreline changes, which showed good performance after being verified for several sites. They also stated that other data analysis methods may be more appropriate to be used when it comes to episodic events or human-induced interventions.

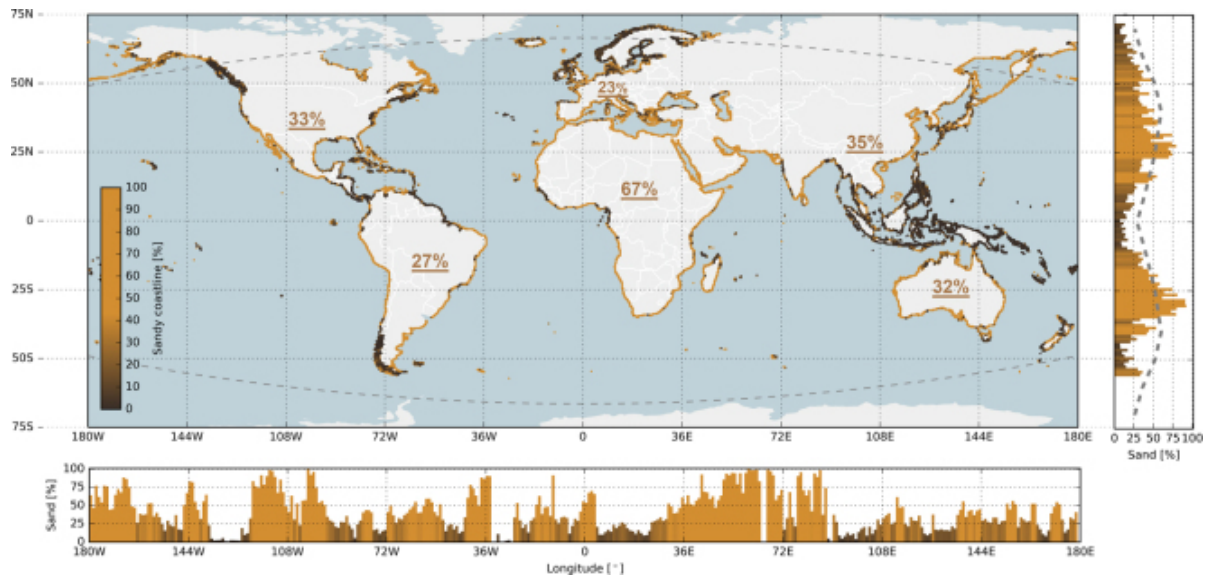


Figure 2.5: Global distribution of sandy shorelines; the coloured dots along the world's shoreline represent the local percentage of sandy shorelines (yellow is sand, dark brown is non-sand). Figure from [Luijendijk et al. \(2018\)](#).

The construction of the global-scale sandy shoreline dataset provides the opportunity to make local scale analysis of shoreline changes. It can help to identify erosive/accretive impacts of known natural and human drivers on shoreline evolution. Therefore, **the present study is based on the hypothesis that the global database could reveal shoreline variations locally, which can be correlated to different forcing types on various time scales.**

## 2.2. Forcing types

Over the last decade, people have paid substantial attention to the morphological change governed by various forcing types on the timescales from days to years, thanks to the increasingly building observational datasets. The variation of incoming wave energy controls shoreline changes on the short-term scale (Davidson et al. 2013, Yates et al. 2009). Climate variability and land subsidence result in coastline variation on the medium-term scale. The large-scale coastal sediment budget, such as sea level rise and the variation of river sediment supply, governs the chronic patterns of shoreline changes on the long-term scale (Rosati 2005). Additional factors controlling shoreline movement include the anthropogenic coastal works, such as constructions of groins, beach nourishment projects and artificial sand bypassing (Bouvier et al. 2017).

In this section, the background information of different forcing types and corresponding coastline responses is specified, including both natural and human-induced factors, from rapid storm-driven erosion (Masselink et al. 2016) to large-scale shoreline variation by SLR (Regnaud et al. 1996).

### 2.2.1. Storms

Storms are associated with periods of strong often damaging winds, flood-producing rainfall, heavy snowfall or blizzard conditions (NIWA 2016). The revolving storms which start in the tropics are called tropical cyclones. In the North Atlantic and eastern Pacific, the storms of this type are called hurricanes, while in South East Asia and China they are called typhoons (NIWA 2016).

Storms can induce various morphodynamic responses on beaches and greatly change the coastal landscape over short periods of time (Jiménez et al. 2012). According to Morton (2002), the primary factors affecting morphological responses of beaches and barrier islands include differences in locations between the wave run-up and adjacent land surface, differences in hydrostatic head between the ocean and adjacent lagoon, and differences in the duration of back beach flooding. Morton (2002) found that coastal responses include: beach erosion, berm migration, dune erosion, washover terrace construction, perched fan deposition, sheetwash, washover channel incision, washout formation, and forced and unforced ebb flow (listed in the order from high frequency beach erosion to low frequency barrier inundation). Some anthropogenic processes can also be related to the impact of particularly aggressive storms, such as beach nourishment and dredge/fill activities (Bender & Dean 2003, Rosati & Ebersole 1997).

### 2.2.2. Seasonal forcing

Shoreline variability on the seasonal scale is one of the shortest-term types of variability relevant to coastal management. It concerns periodic fluctuations in the dynamic behaviour of a beach on the time scales of seasons (Stive et al. 2002). For instance, the high-energetic wave conditions can cause a gentle slope 'storm profile' during the winter, while the mild incoming wave would generate a steep 'swell' profile during the summer (Komar 1998). The seasonal variation of the littoral drift direction can also influence the shoreline positions on the seasonal time scale (Masselink & Pattiaratchi 2001).

### 2.2.3. Climate variability

In order to understand climate variability, a comparison among key concepts of weather, climate variability and climate change is outlined here. The different time scales on which weather, climate variability and climate change operate is shown in Figure 2.6. Weather refers to the atmospheric conditions experienced or expected in a particular location during periods of hours or days, such as rainfall, temperature, and wind speed (Rob 2017). Climate is the average pattern of weather for a particular place over much longer periods—decades to millennia. Climate change can be induced by natural processes, such as volcanic activity, solar variability, or shifts in the Earth's orbit. Moreover, the changes can also be caused by human activities, such as increased greenhouse gas emissions (Rob 2017).

Although the climate tends to change quite slowly, shorter-term fluctuations on seasonal or multi-

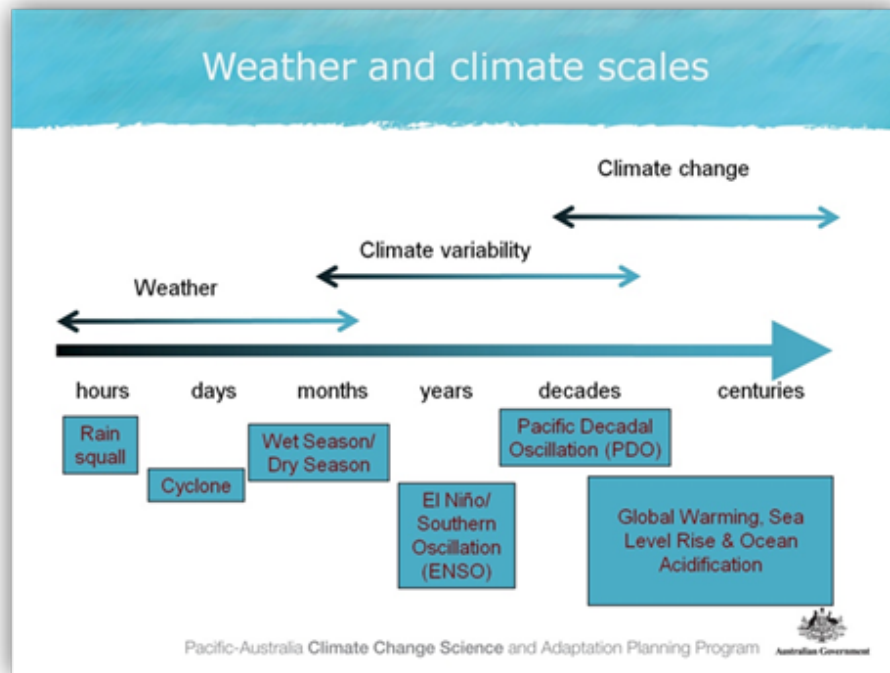


Figure 2.6: A guide to the timescale applicable to weather, climate variability and climate change. Figure from Hoegh-Guldberg O (2017).

seasonal time scales also exist. For example, some types of forcing can cause temperature variation around the average without leading to the change of long-term average itself (Rob 2017). This phenomenon is climate variability, which has a time scale from months to 30 years. Generally, climate variability is referred to the natural processes which can affect atmosphere (Rob 2017). For example, the North Atlantic Oscillation (NAO) refers to anomalous changes in atmospheric pressure at sea level that occur near Iceland and the Azores High; El Niño/Southern Oscillation (ENSO) refers to fluctuations of sea surface temperatures near the equatorial Pacific Ocean, which alternates every few years between a warming phase (El Niño) and cooling phase (La Niña) with a neutral phase in between (Hoegh-Guldberg O 2017).

Climate variability can be characterized by a series of indices, such as MEI and SOI. Barnard et al. (2015) established a link between climate variability and coastal change via key indices, and they found that observed coastal erosion across the Pacific varies most closely with ENSO. An introduction of ENSO, NAO and several climate indices is specified in the following subsections.

### El Niño/Southern Oscillation

El Niño/Southern Oscillation, also known as ENSO, is a periodic fluctuation (i.e., every 2–7 years) in sea surface temperature (El Niño) and the air pressure of the overlying atmosphere (Southern Oscillation) across the equatorial Pacific Ocean (Hoegh-Guldberg O 2017). The warming phase of the sea temperature is known as El Niño and the cooling phase as La Niña. El Niño is accompanied with high, and La Niña with low air surface pressure in the tropical western Pacific. The two periods last several months each (typically occurring every few years) and their effects vary in intensity (Steve 2018). Three phases exist in ENSO (Figure 2.7):

#### Normal conditions

In the normal conditions (neither El Niño nor La Niña) a buildup of warm surface water (orange-red areas) in the West Pacific is caused by the trade winds (white arrows) blow to the west. The air is heated by the warm water below it causing the rising moist air and forming clouds. Then the warmer air moves east to where the air is cooler, and the cooler air sinks towards the surface and moves west,

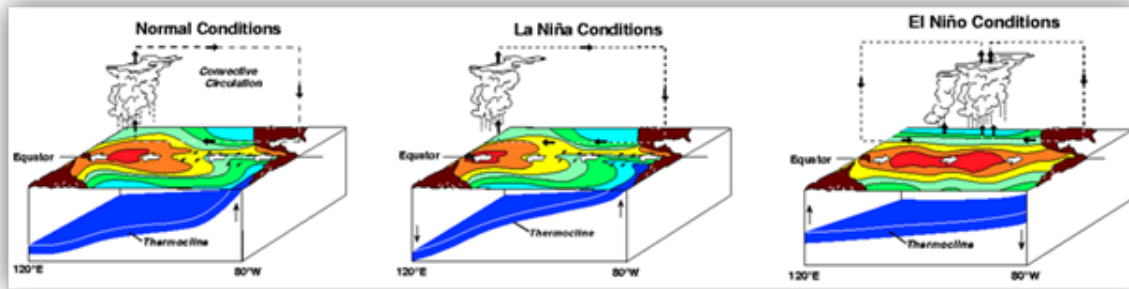


Figure 2.7: Three-dimensional depiction of three important phases of the El Niño/Southern Oscillation (ENSO): Normal (left), La Niña (centre) and El Niño (right). Figure from Hoegh-Guldberg O (2017).

generating the Walker Circulation (Steve 2018).

### La Niña conditions

During La Niña conditions, the Walker Circulation intensifies with greater convection over the western Pacific and stronger trade winds, and ocean temperatures across the central and eastern tropical Pacific Ocean are cooler than normal (blue and green areas). La Niña usually brings wetter than normal conditions to countries such as Australia and Tonga, because rainfall moves farther to the south-west than under normal conditions (Steve 2018).

### El Niño conditions

During an El Niño event, trade winds weaken or may even reverse, allowing the area of warmer than normal water to move into the central and eastern tropical Pacific Ocean. Generally, El Niño conditions in the northern hemisphere winter result in the western Pacific experiencing dry conditions and the central Pacific around the equator experiencing wetter conditions (Steve 2018).

Barnard et al. (2015) found that during El Niño events, the combined effects of elevated wave energy, water levels and wave directional shifts caused severe coastal erosion along the North American west coast in boreal winter (e.g. in 1997/98 and 2009/10 events). In contrast, during La Niña phases, increased cyclonic activity, wave heights and sea-surface elevations lead to higher rates of coastal erosion along the southeastern coastline of Australia (Bryant 1983, Phinn & Hastings 1992). The phase shifts of ENSO can also induce rotational shifts in embayed beach orientation along the southeast coast of Australia (Barnard et al. 2015).

### El Niño Modoki

El Niño Modoki (CP-El Niño) is another coupled ocean-atmosphere phenomenon in the tropical Pacific, which is different from conventional El Niño (EP-El Niño). It is characterized by strong anomalous warming in the central tropical Pacific and cooling in the eastern and western tropical Pacific, opposed to the eastern Pacific during a classic El Niño (Figure 2.8). Such zonal sea surface temperature (SST) gradients result in anomalous two-cell Walker Circulation over the tropical Pacific, with a wet region in the central Pacific JAMSTEC-APL (2009).

According to Barnard et al. (2011), the El Niño Modoki of 2009/10 was the strongest of this newly identified climate event on record. They stated that the event was characterized by a distinct south-north gradient of decreasing anomalies for wave energy and water levels in U.S. West Coast beaches, providing evidence for a latitudinal dependence on oceanographic forcing.

### North Atlantic Oscillation

North Atlantic Oscillation (NAO) is one of the major modes of variability of the Northern Hemisphere atmosphere (Hurrell 1995). Unlike the ENSO in the Pacific Ocean, the NAO is a largely atmospheric mode. It is a weather phenomenon in the North Atlantic Ocean of fluctuations in the difference of atmospheric

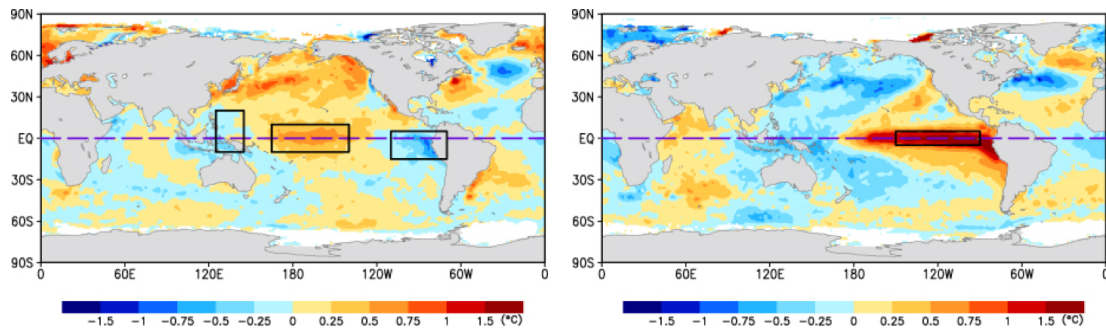
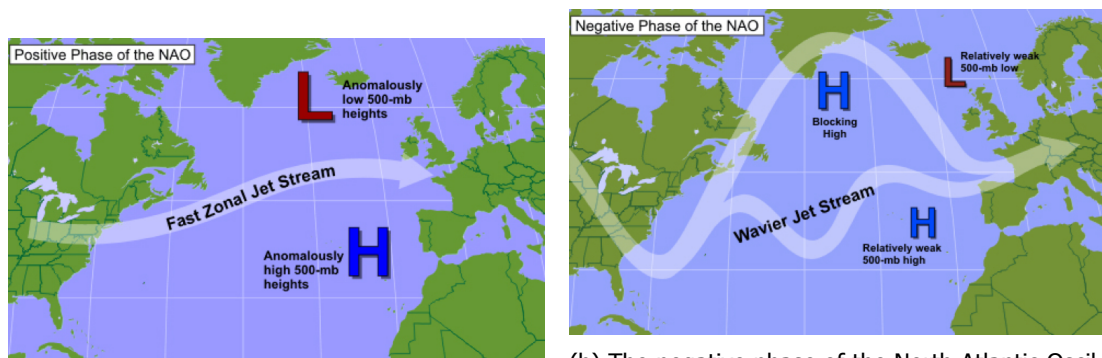


Figure 2.8: Anomalous SST during El Niño Modoki (left) and conventional El Niño (right). Figure from [JAMSTEC-APL \(2009\)](#).

pressure at sea level (SLP) between the Icelandic low and the Azores high ([Osborn 2011](#)). It controls the strength and direction of westerly winds and location of storm tracks across the North Atlantic, through fluctuations in the strength of the Azores high and the Icelandic low. The NAO is particularly important in winter ([Osborn 2011](#)), which exhibits strong inter-decadal variability ([Osborn 2004](#)).

The positive phase of the NAO reflects below-normal heights and pressure across the high latitudes of the North Atlantic and above-normal heights and pressure over the central North Atlantic, the eastern United States and western Europe (Figure 2.9a, [Else \(2017\)](#)). During the positive phase, there is above-average precipitation over northern Europe and Scandinavia in winter, and below-average precipitation over southern and central Europe ([Team 2012](#)). In contrast, there is an opposite pattern of height, pressure anomalies, temperature and precipitation over these regions during the negative phase (Figure 2.9b, [Else \(2017\)](#), [Team \(2012\)](#)).



(a) The positive phase of the North Atlantic Oscillation is marked by low 500-mb heights near Iceland and high 500-mb heights near the Azores Islands.

(b) The negative phase of the North Atlantic Oscillation is marked by high 500-mb heights near Iceland, a pattern that typically develops with a blocking ridge or blocking high.

Figure 2.9: Positive and negative phase of NAO. Figure from [Grenci \(2018\)](#).

### Climate index

Climate index is a calculated value that can be employed to describe the state and changes in the climate system. Typically, selected stations, grid points and regional average data can be used to derive assorted indices, such as Nino 3.4 and Southern Oscillation Index ([Staff 2015](#)). For generating a defining equation of the climate index, climate elements are normally used. Climate elements are measurable parameters that influence the properties of the climate system, including atmospheric ones such as air pressure, air temperature and precipitation, and also non-atmospheric ones such as sea surface temperature and ice cover ([Stockhause & Höck 2010](#)).

**The Southern Oscillation Index (SOI)** is a measure of the strength of the Southern Oscillation,

which also indicates the intensity of the Walker Circulation (ENSO event). There are a few different methods to calculate the SOI, and normally it is calculated based on the pressure differences between Tahiti and Darwin. The method used by the Australian Bureau of Meteorology is the Troup SOI: sustained positive SOI values above about +7 indicate a La Niña event, while sustained negative values below about -7 indicate an El Niño (Bureau of 2018).

**Multivariate ENSO Index (MEI)** can be used to characterize the intensity of ENSO event. It is regarded as the most comprehensive index for monitoring ENSO, since it combines analysis of multiple meteorological and oceanographic components (Mazzarella et al. 2013). MEI is determined as the first principal component of six different parameters: sea level pressure, zonal and meridional components of the surface wind, sea surface temperature, surface air temperature and cloudiness using data from the International Comprehensive Ocean-Atmosphere Data Set (ICOADS) (Wolter 2000). Large positive MEI values indicate the occurrence of El Niño conditions, while large negative MEI values indicate the occurrence of La Niña conditions (Wolter 2000).

#### 2.2.4. Sea level rise

Global sea levels have risen through the 20th century. Due to global warming, these rises will almost certainly accelerate through the 21st century and beyond, but their magnitude remains uncertain (Figure 2.10, Nicholls & Cazenave (2010)). Sea level rise (SLR) has long been assumed as the primary cause for the observed chronic shoreline erosion (Vellinga & Leatherman 1989). Furthermore, some anthropogenic processes often amplify local vulnerability associated with climate-related SLR, such as reduced sediment supply to deltas due to dam building and land subsidence caused by oil and groundwater extraction (Nicholls & Cazenave 2010).

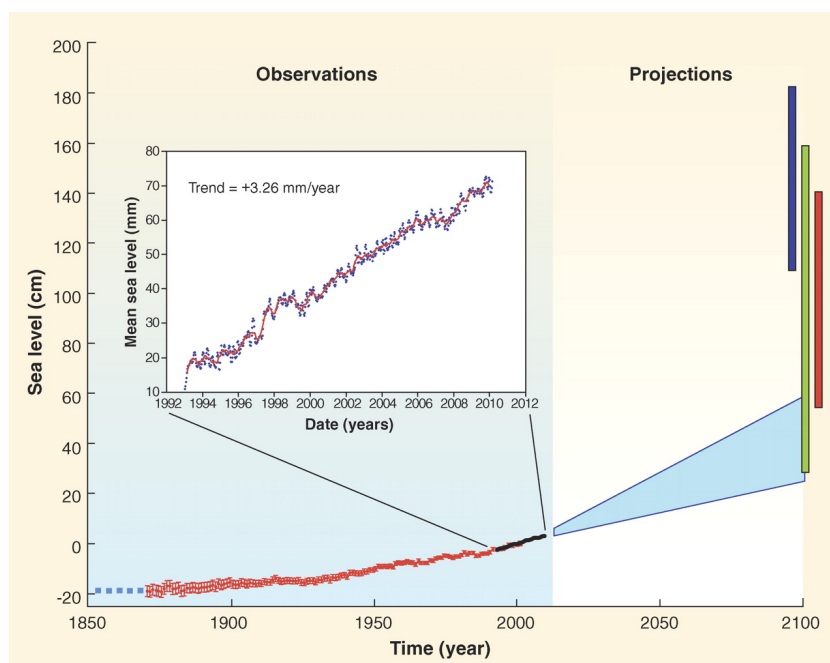


Figure 2.10: Global mean sea level evolution over the 20th and 21st centuries. Figure from Nicholls & Cazenave (2010).

The Bruun rule and its variants can be used to estimate the shoreline erosion driven by SLR (Bruun 1962, Weggel 1979). However, the Bruun rule showed poor agreement with observation in many locations worldwide due to the omission of forcing factors discussed above (it may provide a fair indication of the isolated impact of SLR). Additionally, the sea-level-rise driven shoreline variation adjacent to the tidal inlets is not only influenced by the Bruun effect, but also mostly by sea-level-rise driven basin infilling and other factors such as climate-change driven variations in rainfall (Ranasinghe et al. 2013).

Le Cozannet et al. (2016) showed that the influence of SLR on open coasts can only be captured on long timescales (greater than 50 years). Since the SDS is only available after 1984, the impact of SLR on open coasts will not be analyzed in the present study, while the influence of the sea-level-rise driven basin infilling will be analyzed.

### 2.2.5. Land subsidence

Except for sea level rise, land subsidence is another major process that influences the stability of the coastline. Land subsidence is a global problem due to the loss of surface elevation via removal of subsurface support (of the Interior 2017). It can happen over very large areas like whole states or provinces, or small areas like the corner of a yard. Subsidence can be caused by natural events such as soil compaction, sinkhole formation, earthquakes, glacial isostatic adjustment and loess deposits (NOAA 2017). Anthropogenic influence, however, is the main driver for land subsidence, such as withdrawal of fluids (groundwater, petroleum and geothermal) and subterranean mining (of the Interior 2017).

Land subsidence can cause a range of problems. Many low lands, especially deltaic areas, are experiencing a continuous erosion under the influence of subsidence. Even modest subsidence may change flooding conditions over large areas, resulting in increases in the depth and duration of annual flooding (Erban et al. 2014). Moreover, the problems of incursion of saline groundwater and reduction in wetland area are also exacerbated.

### 2.2.6. Other types of forces

#### Nodal tidal cycle

The 18.6-year nodal tidal cycle is a decadal-scale variation of ocean forcing. It is presented across the globe with a varying phase and a median amplitude of 2.2 cm (Baart et al. 2011). Gratiot et al. (2008) focused on the coast of French Guiana and found that the dominant control of ocean forcing was the 18.6-year nodal tidal cycle, which caused the redistribution of sediment and migration of the mud banks along the 1,500 km coast. Additionally, they stated that the nodal tidal cycle modulates the tidal amplitude by about 3%, so the regions experiencing macro-tidal regimes are particularly concerned. According to Gratiot et al. (2008), many coastal areas in Canada, China, Australia, England and France will experience SLR of several tens of centimeters due to the 18.6-year tidal cycle over the next decade (Figure 2.11).

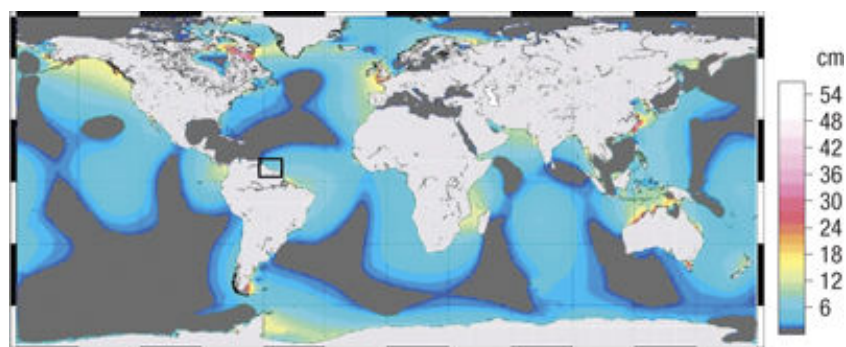


Figure 2.11: Predicted shifting of the MHWL under the 18.6-year nodal tidal cycle for the next decade. Figure from (Gratiot et al. 2008).

#### Beach nourishment

Beach nourishment is a soft engineering method for coastal protection. It addresses the sediment deficit which is the underlying cause of erosion by providing large quantities of material to the coastal sediment budget from external sediment source (Linham & Nicholls 2010). It also increases wave energy attenuation by turning an eroding, reflective beach into a wider, dissipative beach (French 2002).

However, it cannot halt the erosion, but provide a sacrificial barrier against coastal erosion.

The success of the project is a major question regarding beach nourishment. Monitoring beach nourishment projects would help to understand the behaviour of the beach fill area in response to various coastal processes. Determining the success of nourishment projects can also establish justification for future projects ([Gares et al. 2006](#)).



# 3

## Methodology

This chapter introduces the methods used to unravel the sandy shoreline dynamics through the SDS. Firstly, the way to select the sites of interests is introduced, and an overall description of the selected beaches is specified. Secondly, the techniques used to generate spatiotemporal subsets of the global dataset are reviewed, and the background information on how to extract all patterns of shoreline variation is outlined. Then the beach classification methods and the workflow for data processing are specified. Finally, the SDS along the three beaches in southeast Australia are analyzed as an example to illustrate how to study shoreline dynamics through the SDS using the workflow.

### 3.1. Specify the sites of interests

The shoreline changes at around ten sandy beaches are the main research objects for the present study, each of which is selected based on the available documentation to verify if the influence of a specific forcing type could be unravelled through the SDS. In the present study, the forcing types including storms, seasonal forcing, climate variability, land subsidence, SLR and anthropogenic processes are focused on. Considering the spatial resolution of satellite images (30m), the sandy beaches with 'obvious' shoreline movement (e.g. larger than 100m) are more appropriate to be selected. Availability of the external forces data, such as climate indices and wave climate, should also be concerned for choosing the sites, so that the correlation of the external forces data and the shoreline change can explain what mechanism causes the specific shoreline behaviour.

For each site of interest, transects are generated perpendicular to the latest available SDS. The number and location of the transects depend on the extent of sandy shoreline and the specific coastal features on site, so that the transects are sufficient and representative to study the spatial patterns of sandy shoreline variation (e.g. identify the hot spots of shoreline erosion).

The background information of the selected sites of interests is outlined in the following subsections, including Narrabeen, Moruya and Pedro, Perranporth, Ocean Shores, the Nile Delta, Perth, Ocean Beach, Fire Island, Gatseau sandspit and Cap Ferret sandspit (SW France), the Gulf of Valencia and Wrightsville Beach. A global map showing all the considered sites is presented in Figure 3.1.

#### Narrabeen Beach

Narrabeen is a 3.6-km long embayed beach located on the northern Sydney coast (Turner et al. 2016). It is bounded to the north by Narrabeen Head and to the south by Collaroy and Long Reef points (Figure A.1). The morphodynamic variability has been regularly and extensively monitored during the last few decades, with beach profiles being surveyed at 5 locations (Figure A.1) along the beach by the Coastal Studies Unit, University of Sydney (Short et al. 2001).



Figure 3.1: The global map of all the considered sites.

The deepwater wave climate for Narrabeen Beach is of moderate to high wave energy (mean  $H_s = 1.6$  m and  $T_p = 10$  s) and dominated by persistent long period swell waves from the SSE direction (Turner et al. 2016). Mortlock & Goodwin (2016) showed that the directional wave climate can be encapsulated in three primary modes of variability (Figure A.2a). The summer tropical cyclones in the southern Coral Sea produce moderate northeast to easterly swells (sub-tropical easterly mode, Mode 1) which arrive at Sydney an average of 16.5 days a year. The east coast cyclones in the northern Tasman Sea generate larger easterly seas and swells (south-easterly mode, Mode 2) 38 days a year. The mid latitudes cyclone tracking across the southern Tasman Sea produces low to moderate southerly swells (extra-tropical southerly mode, Mode 3) over 200 days a year (Short & Trenaman 1992). On inter-annual time scales, the wave climate is influenced by the ENSO. Thus, wave climate at Narrabeen varies in considerable different size and direction with daily, monthly, and seasonal scales (Short & Trembanis 2004, Short & Trenaman 1992).

Narrabeen Beach has been observed to rotate clockwise during El Niño events and anti-clockwise during La Niña events (Ranasinghe et al. 2004a). This phenomenon is attributed to a predominant southerly wave climate during El Niño (a dominant southerly Mode 3 with sub-dominant easterly Mode 1, Figure A.2), and a predominant south-east to east wave climate during La Niña (enhanced Modes 1 and 2, Figure A.2) (Mortlock & Goodwin 2016). El Niño events usually only last the length of one summer, while La Niña can be longer, impacting successive winter and summer wave and beach conditions (Mortlock & Goodwin 2016). Thus, the reversal of wave angle, variability of wave climate and the sheltering of headland are the causes of the beach rotation phenomenon on the inter-annual time scale at Narrabeen.

### Moruya and Pedro

Moruya and Pedro are two embayed beaches located 270 km south of Narrabeen in southeast Australia (Figure A.3). Moruya is 2.4 km long and partly sheltered by a submerged rock reef, with breaker wave height averaging 1.2 m in the north, decreasing to less than 1 m in the south and maintaining a transverse bar and rip/low tide terrace to reflective (TBR/LTT to R) beach state (Short et al. 2014). Adjoining Pedro Beach is 2.5 km long, which maintains a rhythmic bar and beach to transverse bar and rip (RBB to TBR) beach state with wave heights averaging 1.4 m. Together with Narrabeen Beach, they all have similar lengths around 3 km, easterly orientation and medium to fine sand, and they are exposed to a similar deepwater wave climate ( $H_s = 1.5$  m,  $T = 10$  s) and identical tides (spring range 1.6 m) (Short et al. 2014).

Short et al. (2014) analyzed the three beaches based on surveys between November 2007 and October 2013. They stated that the three beaches have synchronous oscillation and rotation, though at different magnitudes. They showed that local factors contribute to shoreline dynamics on each of the beaches, and the lower energy beach has a more dynamic shoreline behaviour. However, as the shoreline data they used for the analysis only lasted for 6 years, longer-term trends of shoreline variation cannot be detected. Therefore, the SDS of the three coasts over three decades will be analyzed to test if the SDS can unravel the shoreline changes on a longer-term scale.

### Perranporth

Perranporth is a 3.5-km long sandy beach along the north Cornish coast (UK) (Figure A.4). It is a double-barred beach of low-tide bar/rip type with MSR = 4.5 m (Masselink et al. 2016). The intertidal beach is relatively flat ( $\tan\beta = 0.015\text{--}0.025$ ) and composed of medium quartz sand ( $D_{50} = 0.28\text{--}0.34$  mm). The beach has an annual average significant wave height and peak period of  $H_s = 1.5$  m and  $T_p = 10.6$  s, respectively (Scott et al. 2015).

The 2013/14 winter for the Atlantic coast of Europe was unusual in terms of wave conditions and coastal impacts. It was the most energetic winter along most of the Atlantic coast of Europe since at least 1948, and the extreme storms experienced during this winter had very considerable impacts on the Atlantic European beaches (Scott et al. 2015). According to Scott et al. (2015), during an 8-week period from December 2013 to February 2014, there were 15–20 individual storms with offshore significant wave heights ( $H_s$ ) > 5.9 m (1% exceedence wave height), resulting in a mean  $H_s$  > 4 m for the period.

Due to Perranporth faces west-northwest and is predominantly exposed to Atlantic storm and swell waves, it experienced a uniform lowering of approximately 0.5 m across the entire intertidal profile during the 2013/14 winter (Masselink et al. 2016). It lost more than  $200\text{ m}^3\text{m}^{-1}$  sediment from the intertidal beach and dune system, which was a typical situation for most exposed beaches along the coasts of SW England and France during that winter (Castelle et al. 2015). The sediment loss was transported offshore, contributing to the subtidal bar systems (Scott et al. 2015). The beach recovery occurred during the subsequent 1.5 years at Perranporth (Castelle et al. 2015).

### Columbia River Littoral Cell (Ocean Shores)

The Columbia River Littoral Cell (CRLC) extends approximately 165 km between Washington, Point Grenville, Oregon, and Tillamook Head, consisting of four concave-shaped barrier plain subcells separated by estuary entrances of the Grays Harbor, Willapa Bay, and Columbia River (Ruggiero et al. 2005) (Figure A.6). It is characterized by a seasonally variable high-energy wave climate (average winter  $H_s = 3$  m,  $T = 12$  s) (Gelfenbaum & Kaminsky 2010), a mixed semi-diurnal tide with a range of 2–4 m, and a preponderance of easily transported fine sand ( $D_{50} = 0.2\text{mm}$ ) (Ruggiero et al. 2005).

Ocean Shores is a coastal community adjacent to Grays Harbor, where many homes and urban infrastructure had recently been built on accreted lands that have now started to erode (Gelfenbaum & Kaminsky 2010). Initially, the adjacent shoreline prograded over a few kilometers caused by the construction of jetties, since sand from the flanks of the nearby ebb-tidal deltas was driven landward by waves and welded onto the shore (Gelfenbaum & Kaminsky 2010). Then the modified shoreline orientation changed the longshore transport away from the inlets, which resulted in sand to effectively diffuse away. Eventually, the sand deficits along the shoreline due to the loss of local sand supply (ebb-tidal deltas were deflated) resulting in the local shoreline retreat adjacent to the inlets (Gelfenbaum & Kaminsky 2010).

### Nile Delta

The Nile Delta is situated in northern Egypt, where the river Nile reaches the Mediterranean Sea (Figure A.7). It has been in an overall construction phase over the past 7000 years, but it converted to a destruction phase as a result of subsidence, water regulation and erosive effects of coastal processes

during the last 150 years (Stanley & Warne 1998). Nowadays, it is only about 1 m above mean sea level at the Mediterranean coast, and subject to a high rate of submergence (Stanley & Clemente 2017). The destruction phases have caused a range of problems, such as the increasing rate of coastal erosion, incursion of saline groundwater and reduction in wetland area (Stanley & Warne 1998). According to Ali & El-Magd (2016), the two maximum erosion hot spots are located at the mouth of the Rosetta and Damietta branches, where the erosion rates of which are around 24 m/year and 36 m/year, respectively. Based on the IPCC scenarios, there will be around 59 cm SLR by the end of this century, leading to one fifth of the Nile Delta seriously vulnerable to inundation (Ali & El-Magd 2016).

A range of factors induce the fast shoreline retreat, such as the accelerating subsidence of the northern delta and the increasing rate of eustatic SLR in Mediterranean (Stanley & Clemente 2017). The High Aswan Dam constructed in 1965 has greatly reduced the total amount of water flowing below the Dam and to the delta. As a result, a large fraction of Nile sediment that once accounted for around 100 million tons deposited below Aswan is now trapped in the southern part of the reservoir (Stanley & Clemente 2017), largely reducing the sediment supply to the delta area. Furthermore, the extraction of hydrocarbon and ground water (Figure A.7) have caused the delta surface artificially lowered to around 1 m or more (Stanley & Clemente 2017). The eustatic SLR, however, only represents about 26% to 45% of total relative SLR measured in this area (Stanley & Clemente 2017).

### Perth

The shoreline of Perth located in Western Australia exhibits a distinct seasonality in beach morphology (Figure A.8). The coastline is characterized by sandy beaches punctuated by short stretches of rocky outcrops, and is subject to mixed, mainly diurnal, microtidal conditions with a maximum spring tide range of 0.6 m (Masselink & Pattiaratchi 2001). The coast is exposed to one of the most energetic sea breeze systems in the world. In contrast to the 'classic' sea breeze system characterized by sea breezes blowing in the onshore direction, the sea breeze in Perth blows in a predominantly alongshore direction (Masselink & Pattiaratchi 2001).

Masselink & Pattiaratchi (2001) studied five Perth beaches at weekly or bi-weekly intervals from November 1995 to October 1997 using standard surveying techniques. They showed that beaches located south of coastal structures or natural headlands/outcrops become wider when northward sediment transport prevails due to sea breeze activity in summer, while these beaches subsequently erode in winter during storms when the littoral drift changes direction. In contrast, beaches located north of obstacles experience shoreline retreat during summer and accrete during winter. Thus, the disparate behaviour of the Perth beaches was caused by the seasonal variation in littoral drift direction (Masselink & Pattiaratchi 2001).

### Ocean Beach

Ocean Beach is a 7-km long north-south trending sandy coastline, which stretches south from a rocky headland near the San Francisco Bay entrance (Point Lobos) to the bluffs at Fort Funston (Figure A.10). The wave climate in the region is dominated by an abundance of low frequency energy (greater than 20 s period) and prevailing northwest incident wave angles (Eshleman et al. 2007). In the southern portion wave energy is greater, and the erosion hotspot there has resulted in damage to local infrastructure and is the cause of continued concern (Eshleman et al. 2007). The beach is exposed to very strong tidal flows, and current magnitudes are greater in the northern portion of the beach than south.

According to Barnard et al. (2007), the sub-aerial beach volume fluctuates seasonally up to  $400,000m^3$  for the 7-km stretch. The beach also shows a strong pattern of counterclockwise rotation, manifested in accretion of the north end of the beach and erosion of the south (Hansen & Barnard 2010). According to Dallas & Barnard (2011), the rotation feature can be linked to the multi-decadal contraction of the ebb-tidal delta.

According to Barnard et al. (2011), 2009/10 was the only winter since 1997/98 in which the wave-energy flux throughout California was approx. 20% above the mean. The increase in extreme waves

was coupled with elevated water levels and a more southerly wave approach than the long-term mean, resulting in greater shoreline retreat than during the 1997/98 winter (the last significant El Niño). They stated that El Niño Modoki phenomena is considered to be principally linked to the great shoreline retreat observed during the 2009/10 winter. The climate variability resulted in the responses that the warm sea surface temperature (SST) anomaly was focused in the central equatorial Pacific (as opposed to the eastern Pacific during a classic El Niño), featuring a more temporally persistent SST anomaly that caused longer periods of elevated wave energy but lower coastal water levels in the region (Barnard et al. 2011).

### Fire Island

Fire Island is a 50 km-long barrier island system centrally located along the southern shore of Long Island (Figure A.11). Most part of Fire Island is relatively low-lying and less than 1 km wide, and is subject to a microtidal conditions with a mean tidal range of 1.3 m (Brenner et al. 2018). The barrier island is a wave-dominated system, and the mean significant wave height and the dominant mean period is 1.3 m and 7.3 s, respectively (Wilson et al. 2015). A westerly net alongshore sediment transport is driven by the predominant southeast wave and storms (Brenner et al. 2018).

Fire Island has an extensive storm history (Lentz et al. 2013). Hurricane Sandy of 2012 was the deadliest and most destructive one, which had the diameter nearly 2,000 km, leading to an extensive area of the east coast of the United States impacted. It largely affected the morphology of Fire Island and resulted in an extremely low elevation and low relief configuration that left the barrier island vulnerable to future storms (Hapke et al. 2013).

Beach nourishment projects have been undertaken intermittently since the 1960s to help stabilized the position of dunes and beaches (Lentz et al. 2013, Psuty et al. 2005). A history of beach replenishment and estimates of volumes emplaced on dunes and beaches is shown in Figure A.12. In the winter and spring of 2009, a beach renourishment project was carried out on Fire Island, and it was credited with saving the island from the full effects of Hurricane Sandy in 2012 (Lentz et al. 2013).

### Gatseau sandspit and Cap Ferret sandspit (SW France)

Gatseau and Cap Ferret are two sandspits located closed to the Maumusson and Arcachon tidal inlets, respectively, SW France (Figure A.13). The beaches are primarily composed of fine to medium quartz sand, and the highest astronomical tidal range is approximately 6.5 m (Castelle et al. 2018). The most frequent and strongest wind events are from the NNW and WSW, and during extreme storms the offshore significant wave height can reach up to 8 m (Baumann et al. 2017). The wave climate has a strong seasonal variability and is energetic with a dominant W to NW incidence, which drives a net southerly longshore drift approximately  $100 \times 10^3 m^3/year$  (Butel et al. 2002, Idir et al. 2013). According to Baumann et al. (2017), the incoming winter waves show a strong inter-annual variability caused by climate variability, primarily the West Europe Pressure Anomaly (Castelle et al. 2017) and to a lesser extent the North Atlantic Oscillation (Dodet et al. 2010).

Castelle et al. (2018) observed the large shoreline evolution over the two coasts and found that the erosion and accretion alternated over time on the timescale of decades. Based on the dataset of 15 geo-referenced orthomosaic photos, they showed that the two inlet-sandspit systems of Arcachon and Maumusson exhibited a quasi-synchronous behaviour, and the two updrift coasts accreted until the 1970s and subsequently eroded since then.

### The Gulf of Valencia

Saler Beach and Cullera Beach are two sandy coasts located in the central part of the Gulf of Valencia, Spain (Figure A.16) with the length of 4 km and 3 km respectively. Both coasts are in microtidal condition with the average astronomical tidal range less than 20 cm, but the water level position can change more than 70 cm when affected by meteorological factors (Pardo-Pascual et al. 2014). The wave regime is characterized by low waves and short period (the mean  $H_s$  was 0.78 m and the average

$T_p$  was 5.97 s from 1986 to 2005) (Pardo-Pascual et al. 2014). During storms, general westerlies can generate low-pressure areas centered on the Gulf of Lyon, producing large waves in Gulf of Valencia (Pascual & i Verger 1991). The annual net direction of the littoral drift in the Gulf of Valencia is from north to south, and thus the coasts oriented to the north-east or north (e.g. Cullera Beach) are subject to more effective sediment transport than those oriented to the north-west (e.g. Saler Beach) (Pardo-Pascual et al. 2014).

Cullera Beach is backed by developed areas, and the submerged profiles made by the Valencia coastal authority show that gentle slopes (approx.  $3.8^\circ$ ) appear in the region (Pardo-Pascual et al. 2014). For Saler Beach, however, foredunes are back to the coast and the beach slopes are steeper (approx.  $6.2^\circ$ ). According to Pardo-Pascual et al. (2014), between November 2001 and May 2002 there were six storms: two of them in November 2001, one in December 2001, one in January 2002, one in March 2002, and one in May 2002. The storm starting on 10 and 11 November was the largest one with the highest wave registered at 8 m and the storm surge of 0.32 m. The five successive storms exhibited lower wave heights and sea level elevations.

### Wrightsville Beach

Wrightsville Beach is an 8-km barrier island system located on the southern North Carolina coast, 14 km east of Wilmington (Figure A.17). It lies south of Figure Eight Island, separated by Mason's Inlet, and north of Masonboro Island, separated by Masonboro Inlet. Wrightsville Beach is subject to microtidal conditions with a mean tidal range of about 1 m (Thieler et al. 1999). The average significant wave height is 0.948 m and the average dominant wave period is 7.892 s (data from Station 41110 - Masonboro Inlet, ILM2, NC). The dominant direction of wave approach is from the northeast during the winter months and from the southeast during the summer (Thieler et al. 1999).

Wrightsville Beach has a very high development density (on the order of 15 houses/ha), which has caused filling in of marshes and the truncation of the foredune (Gares et al. 2006), and it is one of the most-nourished beaches on the U.S. East Coast (Thieler et al. 1999). Major nourishments have been carried out at approx. four-year intervals since 1965 (Figure A.18), which involved the placement of sediment in the middle section of the barrier island, to offset the losses of sediment and reduce the threat to the Shell Island Resort (an upscale condominium community) (Thieler et al. 1999). Dunes are also maintained along the length of the Wrightsville Beach with a consistent elevation, bulldozed into place after replenishment projects, and stabilized with grass planting and fencing (Gares et al. 2006).

## 3.2. Spatiotemporal subsets of the global dataset

In this section, the methods used for generating spatiotemporal subset of shoreline variation are outlined. The SDS employed in the present study were extracted with the same methods used by [Luijendijk et al. \(2018\)](#), and the image composite technique was employed to reduce the inaccuracy caused by different drivers (Section 2.1.2). Here we firstly introduce the time series decomposition methods, including the classical method, the X-11 decomposition method, and the seasonal and trend decomposition using Loess (STL). Then the principal component analysis (PCA) method is reviewed, which could extract dominant modes of variability contained in a dataset.

### 3.2.1. Time series decomposition

The decomposition of time series of shoreline variation can help to achieve invaluable insights on the occurrence of both accretional and erosional changes of various temporal and spatial scales within the coastal system ([Hyndman & Athanasopoulos 2014](#)). Generally, there are two types of decomposition models: the additive decomposition and multiplicative decomposition. For the additive decomposition, there is

$$y_t = S_t + T_t + R_t \quad (3.1)$$

where  $y_t$  is the data,  $S_t$  is the seasonal component,  $T_t$  is the trend component, and  $R_t$  is the remainder component, all at period  $t$ . For the multiplicative decomposition, there is

$$y_t = S_t \times T_t \times R_t \quad (3.2)$$

If the magnitude of the seasonal patterns does not vary with the level of the time series, the additive decomposition is more appropriate. On the other hand, when the variation in the seasonal variation is proportional to the level of the time series, the multiplicative decomposition is more appropriate ([Hyndman & Athanasopoulos 2014](#)).

#### Classical decomposition

The classical decomposition method originated in the 1920s, which forms the starting point for most other methods of time series decomposition. While classical decomposition is still widely used, it is not recommended. The classical decomposition has two main problems ([Hyndman & Athanasopoulos 2014](#)):

- The trend component estimate tends to over-smooth rapid rises and falls in the data, and the estimate of the trend component is unavailable for the first few and last few observations.
- It assumes that the seasonal component repeats from year to year. For some longer series, however, it is not a reasonable assumption. For example, the shoreline erosion patterns from decades ago was most severe during winter, while the current seasonal patterns probably have maximum erosion during summer due to climate variability. The classical decomposition methods are unable to capture the seasonal changes over time.

#### X-11 decomposition

X-11 decomposition is a popular method for decomposing quarterly and monthly data, which can overcome the drawbacks of classical decomposition mentioned above ([Hyndman & Athanasopoulos 2014](#)). The trend component estimates are available for all observations including the end points, and the seasonal component is allowed to vary slowly over time. The process is entirely automatic and tends to be highly robust to outliers and level shifts in the time series (The details of the X-11 decomposition method can be achieved in [Dagum & Bianconcini \(2016\)](#)).

### 3.2.2. STL decomposition

Seasonal and trend decomposition using Loess (STL) is a method developed by Cleveland et al. (1990), which is more versatile and robust for decomposing time series (Hyndman & Athanasopoulos 2014). Compared to the classical and X-11 decomposition methods, STL decomposition has a range of advantages. According to Hyndman & Athanasopoulos (2014), except for quarterly and monthly data, STL can also handle other types of seasonality. Additionally, the user can better control the patterns of decomposition results with STL method. For example, the rate of change of the seasonal component can be controlled, and the smoothness of the trend component can also be adjusted by the user. Moreover, a robust decomposition can be specified so that the estimates of the trend and seasonal components will not be affected by the occasional unusual observations. On the other hand, STL also has some disadvantages. For example, it cannot make the multiplicative decomposition (Hyndman & Athanasopoulos 2014), and this method is more computationally expensive (Wikipedia 2012).

In this subsection, we provide a brief introduction of the STL method and the explanation for parameter selections. The following information of STL decomposition is mostly adjusted based on Cleveland et al. (1990).

#### Loess

Loess is a locally weighted regression method. One of the main advantages of Loess is that the data analyst is not required to specify a global function to fit a model to the data, only to fit segments of the data. On the other hand, this method is more computationally expensive (Wikipedia 2012).

Suppose  $x_i$  and  $y_i$  for  $i = 1$  to  $n$  are measurements of an independent (time) and dependent (shoreline position) variable, respectively. For loess smoother, a regression curve is computed with a selection of positive integer  $q$ , which means  $q$  values of the  $x_i$  that are closest to  $x$  are selected and each is given a neighborhood weight based on its distance from  $x$ . The weights decrease as  $x_i$  increase in distance from  $x$  and become zero at the  $q$ th farthest point. Then a polynomial of degree 1 or 2 is fit to the data with the weight at that point. Basically, as  $q$  increases the regression curve becomes smoother. When  $q$  tends to infinity, the weight tends to one and the curve tends to an ordinary least-squares polynomial fit (Cleveland et al. 1990).

#### Inner and outer loops for the STL operations

Two recursive procedures are consisted in STL: an inner loop nested inside an outer loop. Each complete run of the inner loop consists of  $n_i$  passes, and in each of the passes the seasonal and trend components are updated once. Each pass of the outer loop consists of the inner loop followed by a computation of robustness weights, which are used in the next run of the inner loop to reduce the influence of aberrant behaviour on the trend and seasonal components (Cleveland et al. 1990).

For the inner loop, a seasonal smoothing that updates the seasonal component is followed by a trend smoothing that updates the trend component. The updates are computed with six steps. Steps 2, 3, and 4 are for the seasonal-smoothing partition of the inner loop, and the step 6 is for the trend-smoothing portion (Cleveland et al. 1990):

**Step 1:** Detrending. A detrended series is computed.

**Step 2:** Cycle-subseries smoothing. Each cycle-subseries of the detrended series is smoothed by loess with  $q = n_s$ . The collection of smoothed values for all of the cycle-subseries is a *temporary seasonal series*.

**Step 3:** Low-Pass filtering of smoothed cycle-subseries. A low-pass filter is applied to the *temporary seasonal series* generated from the step 2. The filter consists of a moving average of length  $n_p$ , followed by another moving average of length  $n_p$ , followed by a moving average of length 3, followed by a loess smoothing with  $q = n_t$ . A *low-pass filtering trend* is then generated.

**Step 4:** Detrending of smoothed cycle-subseries. The seasonal component is calculated by subtracting the *low-pass filtering trend* (generated by Step 3) from the *temporary seasonal series* (generated by Step 2).

**Step 5:** Deseasonalizing. The *seasonal component* is subtracted from the original data and generate the *deseasonalized series*.

**Step 6:** Trend smoothing. The *deseasonalized series* (generated from step 5) is smoothed by loess with  $q = n_t$ .

For the outer loop, the *robustness weights* are calculated for reflecting how extreme the remainder is. The remainder is the value calculated by subtracting seasonal and trend components from the original data. An outlier in the data that results in a very large residual will have a small or zero weight. In each outer loop, the inner loop is repeated, and in the smoothings of Steps 2 and 6 the neighborhood weight is multiplied by the *robustness weights* (Cleveland et al. 1990).

#### Parameter selection for the STL decomposition

According to Cleveland et al. (1990), six parameters are required to complete the procedure of inner and outer loops for STL decomposition:

$n_p$  is the number of observations in each cycle of the seasonal component. If yearly periodicity exists,  $n_p = 12$  for the monthly data and  $n_p = 365$  for the daily data.

$n_i$  is the number of passes through the inner loop and  $n_o$  is the number of robustness iteration of the outer loop. In order to ensure that the updating of the trend and seasonal components converges,  $n_i$  should be large enough. In many cases, however,  $n_i = 1$  or 2 is sufficient. For ensuring the trend and seasonal components converge,  $n_o$  should also be large enough, and it is found that  $n_o = 5$  is already a very safe value.

$n_l$  is the smoothing parameter of the low-pass filter. For preventing the trend and seasonal components from competing for the same variation in the data,  $n_l$  should be equal to the least odd integer greater than or equal to  $n_p$  (e.g.  $n_l = 365$  for the daily data and  $n_l = 13$  for the monthly data).

$n_s$  is the seasonal smoothing parameter. The choice of  $n_s$  determines the extent to which seasonal component varies from year to year. A large value will result in similar components for all years, whereas a small value will allow more rapid changes and thus introduce difficulties in separating seasonal component from observation (Ming et al. 2016). According to Cleveland et al. (1990), the value for  $n_s$  should be odd and at least 7. The choice depends critically on the characteristics of the series, and a diagnostic graphical method can help in the choice of  $n_s$  (seasonal-diagnostic plot). This parameter is the only one which do not have a default value in R language.

$n_t$  is the trend smoothing parameter. The trend component extracts less variation and becomes smoother as  $n_t$  becomes larger. For ensuring that the smoother does not miss the persistent and long-term variation,  $n_t$  should be small. On the other hand, it cannot be too small, causing the trend and seasonal components to compete for variation in the data. Based on Cleveland et al. (1990),  $n_t$  ranges from about  $1.5n_p$  to  $2n_p$  (e.g.  $n_t = 573$  for the daily data and  $n_t = 21$  for the monthly data).

### 3.2.3. Principal component analysis

Principal component analysis (PCA), also referred as empirical orthogonal function (EOF) analysis, provides a simple and efficient way to extract the dominant modes of variability contained in a dataset. It was first developed in the early 1900's and has been widely used in a range of fields including meteorology, psychology and more recently coastal science (Miller & Dean 2007). The early applications of PCA mainly focused on the analysis of cross-shore variability, such as using PCA to describe variation in barrier island geology (Vincent et al. 1976). Then Miller & Dean (2007) started to use PCA to identify the dominant modes of shoreline variability at Duck, the Columbia River Littoral Cell and the Gold

Coast, and they found that nearly 95% of the total shoreline variability can be described by the first four eigenfunctions.

The following introduction of PCA on shoreline variation is adjusted according to [Winant et al. \(1975\)](#). PCA can separate the temporal and spatial dependence of the data, permitting shoreline changes to be described objectively by a linear combination of corresponding time and space function. In the present study, time series of shoreline changes are used to generate sets of empirical eigenfunctions. One seeks to represent the data, in our case the shoreline position  $y_t$ , as a linear combination of functions of longshore position  $x$  and functions of time  $t$ .  $x$  is an index ranging between 1 and  $n_x$  (the total number of transects along the beach where data are take), and  $t$  varies between 1 and  $n_t$  (the total number of times at which shoreline positions were recorded). For example, if the shoreline changes at both ends and central part of the beach are analyzed and the monthly data is used over 2 years, then  $n_x$  equals 3 and  $n_t$  equals 24. According to [Winant et al. \(1975\)](#),  $y(x, t)$  can be represented in terms of a normal mode expansion of the form

$$y_{xt} = \sum_n c_{nt} e_{nx} \quad (3.3)$$

where  $e_{nx}$  is the spatial eigenfunctions, and  $c_{nt}$  is the temporal coefficients. The spatial eigenfunctions have to satisfy

$$\sum_x e_{nx} e_{mx} = \delta_{nm} \quad (3.4)$$

where  $\delta_{nm}$  is the Kronecker delta, ensuring the resultant eigenfunctions form a set of uncorrelated vectors (statistically independent) and are normalized to unity.

Different from other series decomposition method (e.g. FFT), PCA does not specify the form of eigenfunctions a priori, but rather it selects a set of empirical eigenfunctions which best fit the data in the least square sense using the data itself ([Winant et al. 1975](#)). A symmetric correlation matrix  $A$  is formed for generating these functions with elements

$$a_{ij} = \frac{1}{n_x n_t} \sum_{t=1}^{n_t} h_{it} h_{jt} \quad (3.5)$$

The diagonal elements of this matrix are

$$a_{xx} = \frac{1}{n_x n_t} \sum_t h_{xt}^2 \quad (3.6)$$

which also represent the mean square value of the data in time divided by  $n_x$ . The sum of the diagonal elements is defined as the trace of  $A$ :

$$TrA = \sum_x a_{xx} = \frac{1}{n_x n_t} \sum_x \sum_t h_{xt}^2 \quad (3.7)$$

Thus,  $TrA$  represents the mean square value of all the data. Like any square matrix, matrix  $A$  possesses a set of eigenvalues run and a set of corresponding eigenfunctions  $e_{nx}$  which are defined as

$$Ae_n = \lambda_n e_n \quad (3.8)$$

Since the sum of all the eigenvalues is equal to the trace of the matrix (mean square value of all the data), **each eigenvalue can be representative of a certain percentage of the mean square value of the data.** As a result of the orthonormal property, the coefficient  $c_{nt}$  are evaluated as

$$c_{nt} = \sum_{x=1}^{n_x} h_{xt} e_{nx} \quad (3.9)$$

The first eigenfunction represents most of the variability of the overall data, and each subsequent eigenfunction accounts for the bulk of the remaining variability. Therefore, the first a few eigenfunctions can be used to describe the majority of the variation (Miller & Dean 2007).

Although the eigenfunctions do not have any inherent physical meaning, corroborating evidence can provide a physical interpretation of the results. Since the time series of shoreline positions is the original data of this study, **the derived eigenfunctions  $e_{nx}$  represent modes of longshore shoreline variability.** Miller & Dean (2007) showed that the primary mode of longshore variability had a strong resemblance to the statistical mean when the data sets were not demeaned before the PCA. Additionally, extrema in the spatial eigenfunctions represents areas with maximum variability, while nodal points identify stability and shoreline change are out of phase across a node. The presence of nodal point in spatial eigenfunctions indicates the importance of longshore processes, while the absence of nodal point represents that the shoreline response to cross-shore processes where the entire coastline advances or retreats in phase (Miller & Dean 2007).

### 3.3. Extract behavioural patterns of shoreline variation

In this section, the methods to identify spatiotemporal patterns of sandy beach evolution are outlined. The spectral analysis methods are specified first, including the fast Fourier transform and wavelet analysis, and then the linear regression model is introduced.

#### 3.3.1. Spectral analysis

The methods for analyzing the time-frequency of a signal are presented in this section. The important theme in analysis is the representation of a function (time series or signal)  $x(t)$  by special known functions (Blatter 2003). In the discrete case, the time series  $x(t)$  can be represented as

$$x(t) = \sum_{\alpha \in I} c_{\alpha} e_{\alpha}(t) \quad (3.10)$$

where  $e_{\alpha}$  is the basis function, and the  $c_{\alpha}$  is the coefficient belonging to the basis function  $e_{\alpha}$ . A range of different families can be used as basis functions, such as the complex exponentials in Fourier analysis and wavelets in wavelet analysis (de Rooij 2017). A brief introduction of these methods is presented in the following subsections.

##### Fourier transform

The Fourier transform (FT) is a common and much-used transformation to convert a signal from its original domain to frequency components and vice versa (Chac & Wriggers 2002). These components are single sinusoidal oscillations at distinct frequencies each with their own amplitude and phase. The example shown in Figure C.4 illustrates three distinct dominant frequencies contained over the time series.

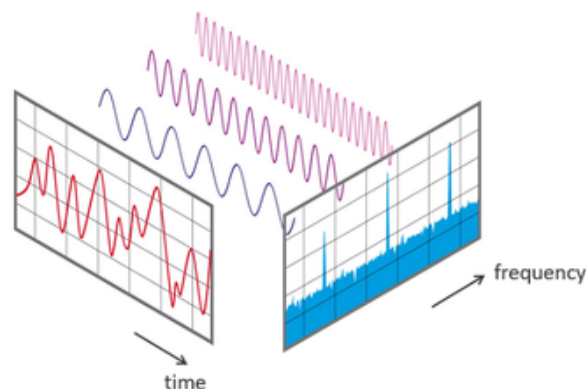


Figure 3.2: View of a signal in the time and frequency domain. Figure from Chac & Wriggers (2002).

The following introduction of Fourier transform is mostly adjusted based on (Chac & Wriggers 2002). In the formal Fourier analysis, the basis functions as described in Equation 3.10 are from the family of complex exponentials:

$$t \mapsto e^{ikt} = \cos(kt) + i\sin(kt), \quad k \in \mathbb{Z} \quad (3.11)$$

This results in the Fourier series representation of  $x(t)$ :

$$x(t) := \sum_{k=-\infty}^{\infty} c_k e^{ikt} \quad (3.12)$$

Most signals are discrete in the field of coastal engineering, and time series of SDS are also discrete. The sum of delta functions can represent the discrete signals, which can be described as

$$x_{sampled}(t) = \sum_{k=-\infty}^{\infty} x(t)\delta(t - k\Delta t) = \sum_{k=-\infty}^{\infty} x(k\Delta t)\delta(t - k\Delta t) \quad (3.13)$$

assuming that the signal is sampled with the sampling frequency  $f_s = \Delta t^{-1}$  Hz. The discrete Fourier transform (DFT) can be used for transforming these discrete time series ( $x_{sampled}(t)$ ). For a signal of length  $N$ , the discrete time Fourier transform can be described as

$$X(\omega) = \sum_{k=0}^{N-1} x(k\Delta t)e^{-i\omega k\Delta t} \quad (3.14)$$

The following set of orthogonal basis function is often used in DFT:

$$\left\{ e_n[k] = \exp \frac{i2\pi nk}{N} \right\}_{0 \leq n \leq N} \quad (3.15)$$

so for a discrete time signal  $x[k]$ , with  $k = N$  and a duration of time  $T$ , the DFT becomes:

$$F \{x[k]\} [n] := X[n] = \sum_{k=0}^{k=N-1} x[k] \exp^{-i2\pi nk/N}, \quad \text{where } n = 0, 1, 2, \dots, N-1 \quad (3.16)$$

The fast Fourier transform (FFT) is a faster implementation of the DFT algorithm transforms, which is widely used for many applications in engineering, science, and mathematics (Chac & Wriggers 2002). The Fourier coefficients generated by the DFT and FFT are the same. The direct computation of the DFT is of  $O(N^2)$  arithmetic operations (Bria 1999), while the FFT algorithm brings this number down to  $O(N \log N)$  operations by breaking the large convolution into shorter convolutions, lowering the number of operations (de Rooij 2017). In 1994, Gilbert Strang described the FFT as 'the most important numerical algorithm of our lifetime' (Chac & Wriggers 2002).

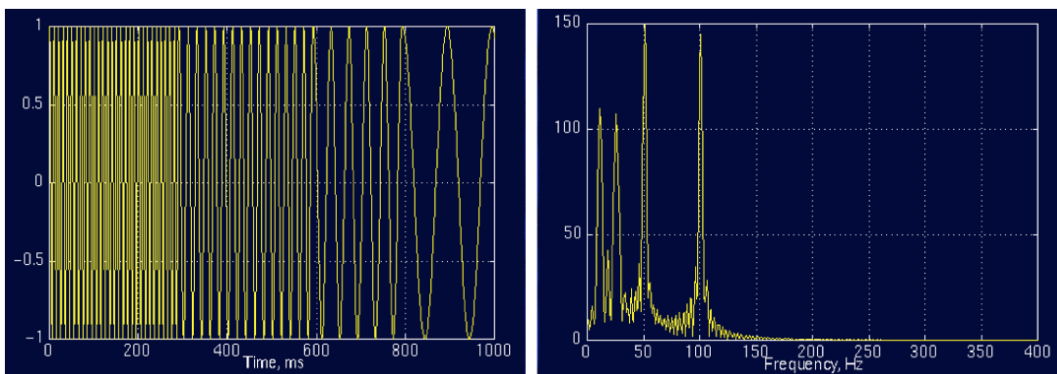


Figure 3.3: Time series and its Fourier transform. Figure from Polikar (1996).

Although the Fourier transform can provide the frequency information of the signal, it does not show when in time these frequency components exist (Polikar 1996). For instance, the left panel of Figure 3.3 shows a non-stationary signal with four frequency components at four different time intervals, and

the right panel is the Fourier transform of it. The FT has four peaks, corresponding to four frequencies with reasonable amplitudes, but it does not show when these frequency components occur (Polikar 1996).

In order to know the time interval when the frequency occurs, the Gabor transform was developed in the early twentieth century, in which the combination of a window function and the Fourier transform was used to derive a coupling of the temporal and frequency domain (de Rooij 2017). Later this work was placed in the framework of the short-term Fourier transform (STFT). A disadvantage of this method is the relatively large loss of both temporal and frequency information (Polikar 1996). A visual representation of these domains is shown in Figure 3.4(c). A visual representation of the time and frequency domain of the signal is shown in Figure 3.4(a-b).

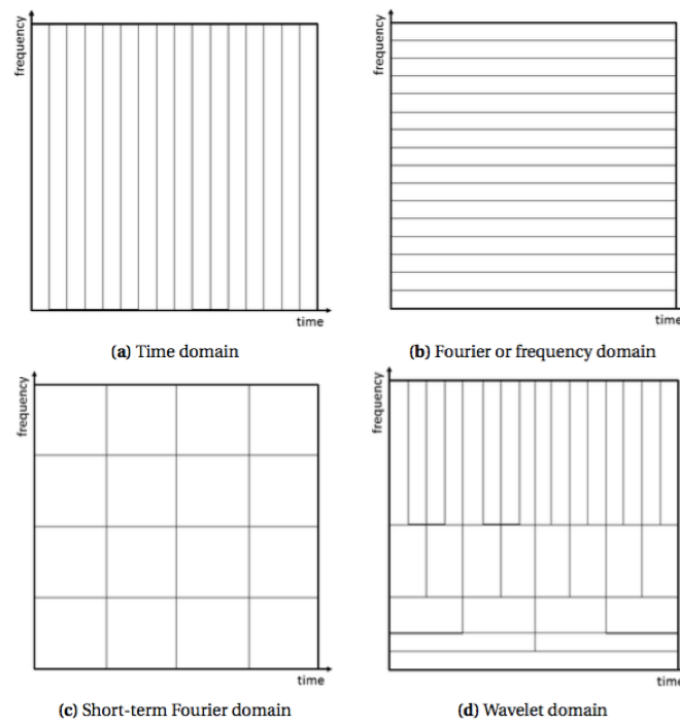


Figure 3.4: Schematic representation of the four different analyses of a signal. Figure from de Rooij (2017).

### Wavelet analysis

Wavelet analysis (WT) is a spectral analysis method capable of providing the time and frequency information simultaneously. It is a tool that cuts the function  $x(t)$  up into different frequency components, studying each component with a resolution matching its scale (Graps 1995). There are other transforms which provide time information too, such as the short time Fourier transform (STFT) mentioned above, but wavelet analysis is more optimized. Unlike the STFT which has a constant resolution at all times and frequencies (Figure 3.4c), the WT has a good time and poor frequency resolution at high frequencies, and good frequency and poor time resolution at low frequencies (Figure 3.4d) (Graps 1995).

An example of wavelet transform is illustrated in Figure 3.5, with a non-stationary signal shown on left and the continuous wavelet transform (CWT) of it on right. The axes of Figure 3.5b are translation and scale, strictly related to time and actually inverse of frequency, respectively (smaller scales correspond to higher frequencies) (Polikar 1996). Based on the result of WT, it is clear to know the time intervals when the frequency components at 30 Hz, 20 Hz, 10 Hz and 5 Hz exist.

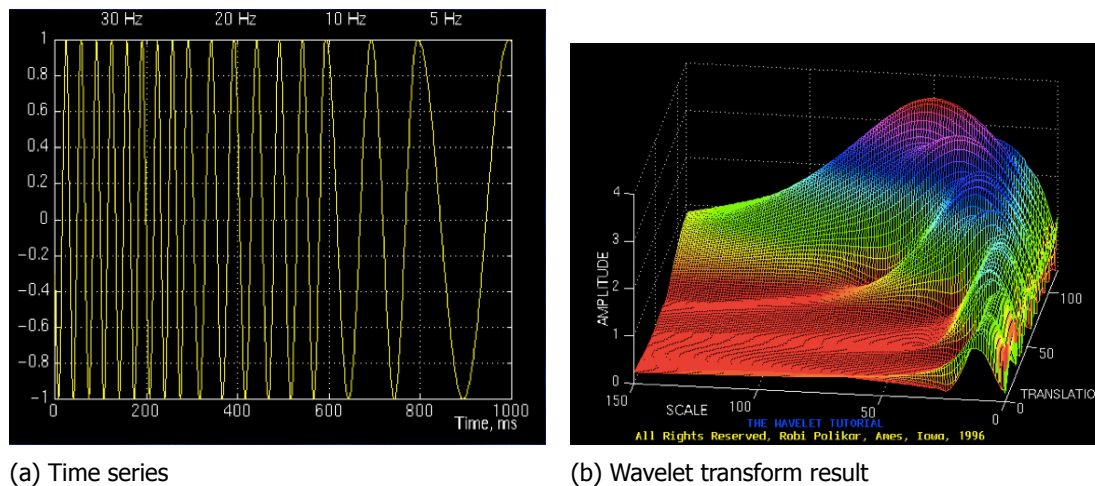


Figure 3.5: Time series and wavelet transform of the time series. Figure from Polikar (1996).

### 3.3.2. Regression analysis

Regression analysis is a set of statistical processes for analyzing the relationship between a dependent variable and one or more independent variables. It helps to understand how the value of the dependent variable changes when any one of the independent variables is varied, while the other independent variables are held fixed (of Mathematics 2012). The ordinary least squares (OLS) or linear least squares is one of the developed techniques for regression analysis. It chooses the parameters of a linear function of a set of explanatory variables by minimizing the sum of the squares of the differences between the observed dependent variable (values of the variable being predicted) in the given dataset and those predicted by the linear function (Rao et al. 1973).

#### Multiple regression analysis

Multiple regression analysis can be used to find if there is a statistically significant relationship between sets of variables. It is quite similar to the simple linear regression (with a single independent variable), and the only difference is that the number of independent variables is higher (Library 2007). In the present study, the multiple regression analysis is used to produce an equation that predicts the dependent variable (shoreline position) with several independent variables (e.g. climate indices, wave height or wave angle). The equation has the form

$$Y = b_1X_1 + b_2X_2 + \dots + A \quad (3.17)$$

where  $Y$  is the dependent variable;  $X_1$ ,  $X_2$  and so on are the independent variables;  $b_1$ ,  $b_2$  and so on are the coefficients that describe the size of the effect the independent variables are having on the dependent variable  $Y$ ;  $A$  is the value  $Y$  is predicted to have when all the independent variables are equal to zero (Library 2007).

#### R-squared, the standard error of a coefficient, T-value and P-value

The **R-squared** of the regression is the fraction of variation in the dependent variable that is predicted by the independent variables. For example, 0.1 R-square means that the model explains 10% of variation within the data (Wilhelm 2015). However, since not all of the relevant predictors are included to explain the dependent variable, a low R-square does not necessarily mean a bad fit result.

The **standard error** of a coefficient tells us how much sampling variation there is if we were to re-sample and re-estimate the coefficient. It is an indication of how reliable the sample estimates are, and it is vitally important in determine whether there is a true relationship between the dependent and independent variables (Library 2007).

The ratio of the coefficient ( $b_i$ ) to the standard error is the **T-value**, which indicates how many standard errors is the coefficient away from zero. For example, if the coefficient of wave period and beach width is 1 and the standard error of it is 0.2, then the coefficient is 5 standard errors away from zero, indicating that coefficient = 1 is pretty far away from zero. This is an evidence that there is a true relationship between wave period and beach width. On the other hand, if the T-value is near zero, it is likely to be no relationship between beach width and wave period. The greater the magnitude of T, the greater the evidence against the null hypothesis that there is no significant difference. The closer T is to 0, the more likely there is no significant difference ([Library 2007](#)).

**P-value** and T-value are inextricably linked. The larger the absolute value of the T-value, the smaller the P-value, and the greater the evidence against the null hypothesis. Normally, if the P-value is less than the significance level (usually 0.05), then the model is statistically significant and fits the data well ([Library 2007](#)).

### 3.4. Beach classifications

Different kinds of classification models have been applied to coast, which provide conceptual frameworks for studying and understanding beach and surf zone environments. Figure 3.6 shows an example of the traditional beach classification model, which was extended using the Australian beach model by Masselink & Short (1993), parameterized by the dimensionless fall velocity  $\Omega$  and the relative tide range RTR. Moreover, Shepard (1963) group beaches into primary and secondary coasts based on terrestrial processes and marine processes, respectively. Some other models classify the beaches based on sediments (rock, reef and cliff coasts; gravel/shingle coasts; sand coasts; mud coasts), tectonics (trailing margins, leading margins), and inundation (emergent coasts, submergent coasts). According to Finkl (2004), however, some of the general classification systems are broad in scope but lack specificity, while the specialized systems can be narrowly focused but not applicable to all coastal types.

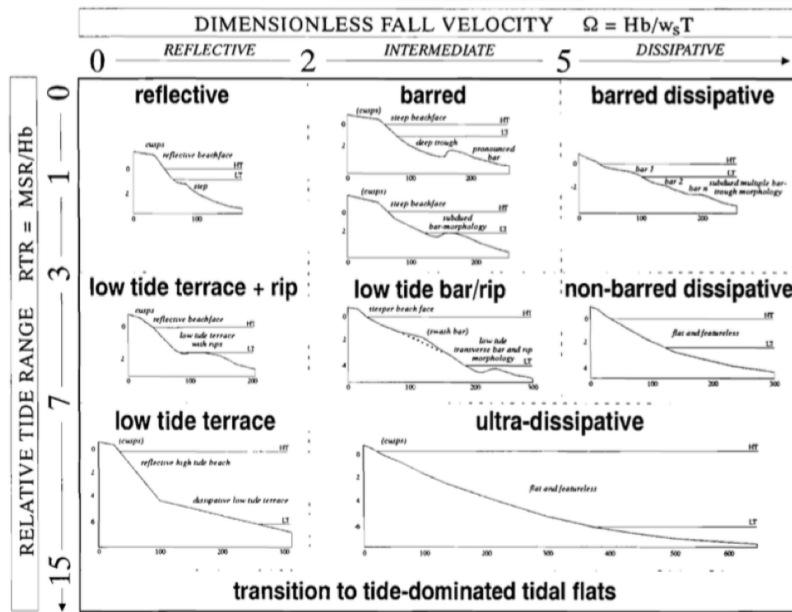


Figure 3.6: Classification model of beach state of Masselink & Short (1993).

In the present study, new indices are defined for classifying seasonal/non-seasonal and rotational/non-rotational beaches using the SDS. The new indices can be applied to almost all sandy beaches worldwide and indicate patterns of shoreline variation temporally and spatially.

#### 3.4.1. Rotational/non-rotational beach

The rotational pattern of shoreline variation can be observed from the result plot of PCA. For example, Figure 3.7 shows the PCA of shoreline changes at two ends and central part of Moruya Beach. The primary mode represents the rotational pattern, indicating that 79.5% of the overall shoreline variation can be explained by the beach rotation (Section 3.2.3) (the eigenfunction at two ends shows opposite signs and the value approaches zero at central part of the beach, representing that the shoreline varies out of phase at the ends while the shoreline at the center behaves as a hinge).

The index  $\beta$  is derived to determine if the rotational pattern is obvious.  $\beta$  is defined to be equal to the eigenvalue corresponding to the rotational mode ( $\beta$  may not exist for every beach), which also represents what percentage of overall shoreline change can be explained by the rotational mode (Section 3.2.3). Based on the literature of different coasts combined with the trial and error process, the beach can be classified as rotational beach if

$$\beta \text{ exists and } \beta \geq 15\% \quad (3.18)$$

when averaging window for image composite equals 180 days (Section 5.1 and Section 2.1.2).

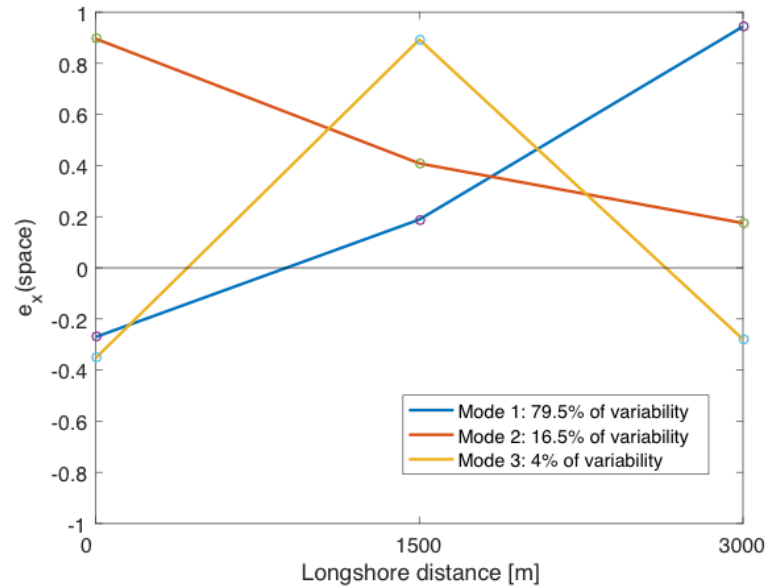


Figure 3.7: PCA result of shoreline variation at Moruya.

### 3.4.2. Seasonal/non-seasonal beaches

The indices representing the relative importance of seasonal variation within overall shoreline changes are determined based on the results of the STL decomposition and FFT analysis.  $R_{st}$  is derived through the STL decomposition:

$$R_{st} = \frac{R_s}{R_t} \quad (3.19)$$

where  $R_s$  is the range of seasonal component and  $R_t$  is the range of trend component (Figure 3.8).  $R_{st}$  indicates the relative importance of the seasonal component compared with the trend component within the overall shoreline change. The larger value of  $R_{st}$  indicates a higher possibility that the shoreline exhibits a distinct variation on the seasonal scale.

$\alpha$  is another index indicating the importance of seasonal variation, which is calculated based on the FFT analysis:

$$\alpha = \frac{E_s}{E_{max}} \quad (3.20)$$

where  $E_s$  is the energy of seasonal variation in frequency space and  $E_{max}$  is the maximum energy of all the generated frequencies (Figure 3.9).  $\alpha$  represents the amount of seasonal variation energy relative to the maximum energy in frequency space. Similarly, the possibility of the shoreline greatly varying on the seasonal scale tends to be higher when  $\alpha$  becomes larger.

Based on the related literature of different beaches combined with the trial and error process, the seasonal beach can be classified if one of the following criteria is satisfied (when the SDS is generated with the averaging window for image composite set to 180 days):

$$R_{st} \geq 0.3 \quad (3.21)$$

$$\alpha \geq 0.5 \tag{3.22}$$

The values of  $R_{st}$  and  $\alpha$  at different transect positions of the same beach can be slightly different considering the disparity of local topography. It is defined that as long as shoreline changes satisfy one of the above criteria at any one of the transects, the beach can be classified as a seasonal one.

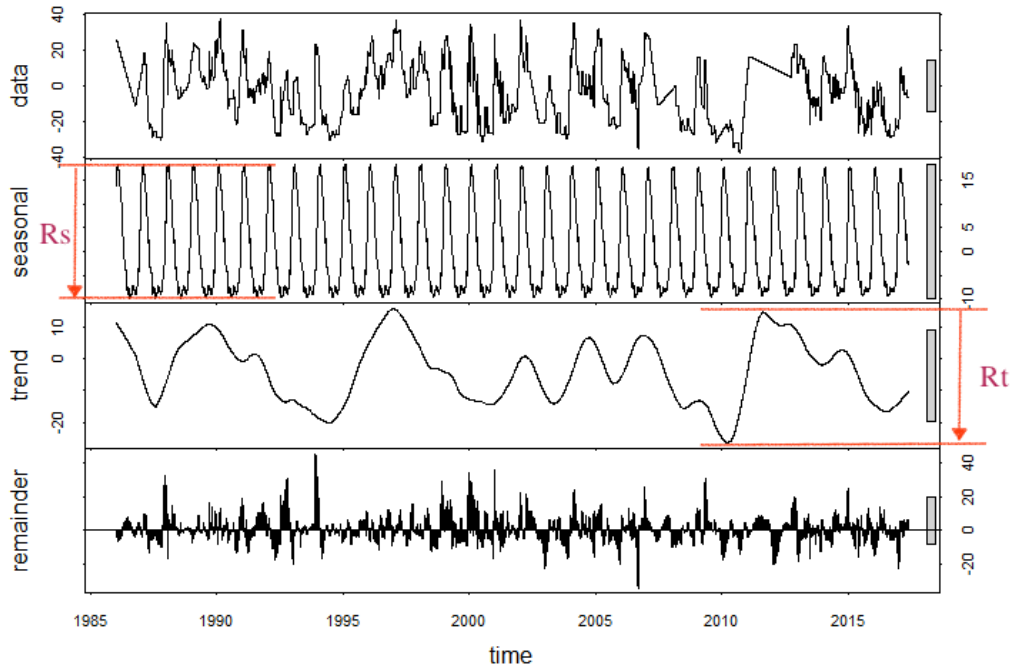


Figure 3.8: The STL decomposition result of shoreline variation at Perth. The filtering parameters are listed in Section 4.2.2

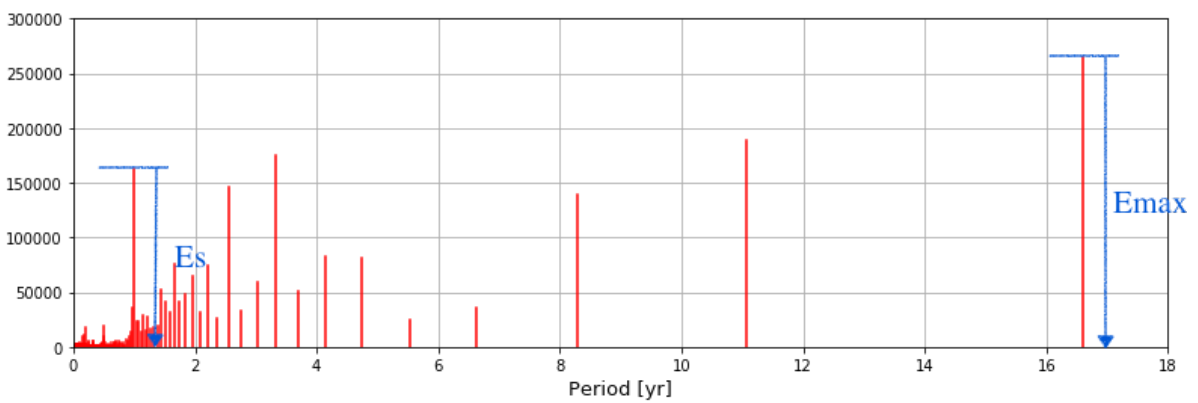


Figure 3.9: The result plot of FFT of shoreline variation at Ocean Shores (CRLC) (Section 4.2.1).

### 3.5. A Framework of time series analysis

In the present study, the time series analysis of shoreline positions at different beaches mainly follows the framework shown in Figure 3.10:

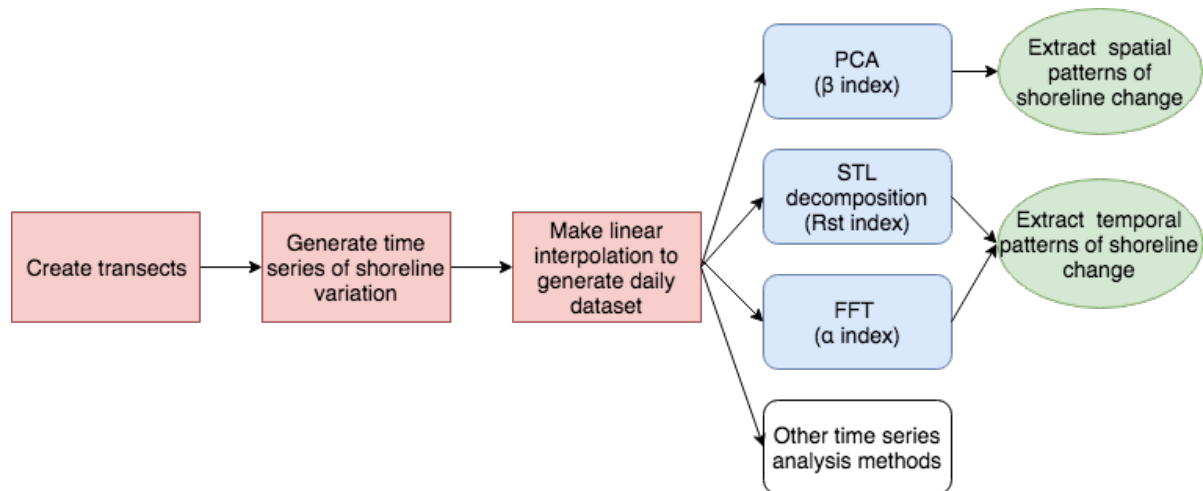


Figure 3.10: The framework for time series analysis of shoreline variation derived from the SDS.

1. Transects are generated perpendicular to the latest available SDS. The number and location of transects are based on the extent and features of the beach, so that the transects are sufficient and representative to study the patterns of sandy shoreline variation (e.g. identify hot spots of shoreline erosion). Normally, the longshore resolution of transects is 100 m, 250 m or 500 m.
2. Intersections between the SDS and transects are generated over time. The distance between the transect origin, which is fixed in time and located at the landward side of the transect, and the point of intersection is stored for all SDS positions and all transects. This distance is proposed to serve as a coastal indicator, and changes of this distance over time provide information on shoreline dynamics.
3. Time series of the shoreline change is linear interpolated to get a daily dataset at each transect, as some of the analysis methods used later, such as FFT, require a constant time interval of the dataset.
4. The PCA is used to spatially unravel shoreline variation at selected transect positions, determining whether the shoreline changes in a more oscillation mode (shoreline at each transects move in phase) or rotational mode (shoreline changes out of phase at the two ends). The  $\beta$  index is calculated at this step to classify if the beach is a rotational beach (Section 3.4.1).
5. The STL decomposition is used to extract trend, seasonal and residual components from the overall shoreline variation. Absolute range of seasonal change can be observed from the result plot, and  $R_{st}$  index is derived with the seasonal and trend components in this step (Section 3.4.2).
6. The FFT is employed to transform the time series of shoreline positions to frequency space, and the index  $\alpha$  is calculated based on the result of FFT. Combined with  $R_{st}$ , these two indices can classify if the beach is a seasonal beach (Section 3.4.2).
7. Other types of time series analysis methods are used for correlating shoreline movement to different forcing types, such as linear regression analysis and cross correlation function.
8. The application range of using the SDS for unravelling shoreline dynamics is tested by comparing the analysis results derived from the SDS to the conclusions listed in the related literatures.

### 3.6. Narrabeen Beach (Example 1)

In the following sections, the SDS along the three beaches in southeast Australia are analyzed as an example to illustrate how to study shoreline dynamics using the workflow (Figure 3.10).

**Background:** Narrabeen is a 3.6-km long embayed beach located on the northern Sydney coast (Turner et al. 2016). Short & Trembanis (2004) analyzed shoreline variation based on the 26 years of monthly measured beach profiles. They found that the rotation phenomenon can be confirmed by the 2nd PCA component, and the decadal scale patterns of shoreline response can be identified with wavelet analysis. Ranasinghe et al. (2004a) used the same measured dataset to establish links between the SOI, wave climate and beach rotation. They stated that the embayed beach rotated clockwise during El Nino phases, while rotated anti-clockwise during La Ninar phases.

In this section, the SDS at Narrabeen are analyzed to test the capabilities of using the SDS on unraveling shoreline dynamics governed by climate variability. Based on the SDS extracted from the satellite image on 2017-04-30, 42 transects were generated with the spatial resolution of 100 m along the coastline (Figure 3.11). The SDS were obtained from Landset 5, Landset 7 and Landset 8 dataset. The intersections between the SDS and transects were created to achieve shoreline changes over time. Five main transects were selected as shown in Figure 3.11, and the following signal processing techniques mainly focused on the shoreline variation at these five transects.



Figure 3.11: Transect locations at Narrabeen Beach.

No obvious seasonal variation can be observed from the original SDS data at transect 9 and 29 (Figure C.6), which can be supported by the following analysis with the STL and FFT methods. The linear interpolation method was then used to generate daily data for shoreline changes over the entire time series. The primary advantage of working with an interpolated data set is that the resulting time series (with constant  $\Delta t$ ) can be subjected to spectral analysis later, such as the FFT analysis. The time series of shoreline positions were not averaged alongshore, otherwise some of the variance containing information will be filtered out.

### 3.6.1. Principal component analysis

The PCA was carried out on shoreline changes at transect 9, 21 and 29 (Figure 3.12). The primary mode (64%) represents shoreline oscillation, indicating a uniform shoreline advancement or recession with the north end (N9) experiencing a bit more dramatic changes. Mode 2 is the rotational mode (29%), and based on the criteria in Section 3.4.1,  $\beta$  equals 29% > 15%, showing that Narrabeen is a **rotational** beach.

Trend component analysis of shoreline movement at the five main transects was then carried out (Appendix D.1). The cross-correlation analysis (Table D.2) shows that the shoreline change at transect 9 is positive correlated (+0.879) with the change at transect 2, while it is negative correlated (-0.44) with the change at transect 29. Thus, the conclusion that Narrabeen exhibits a rotational feature can be corroborated with the results of trend component analysis.

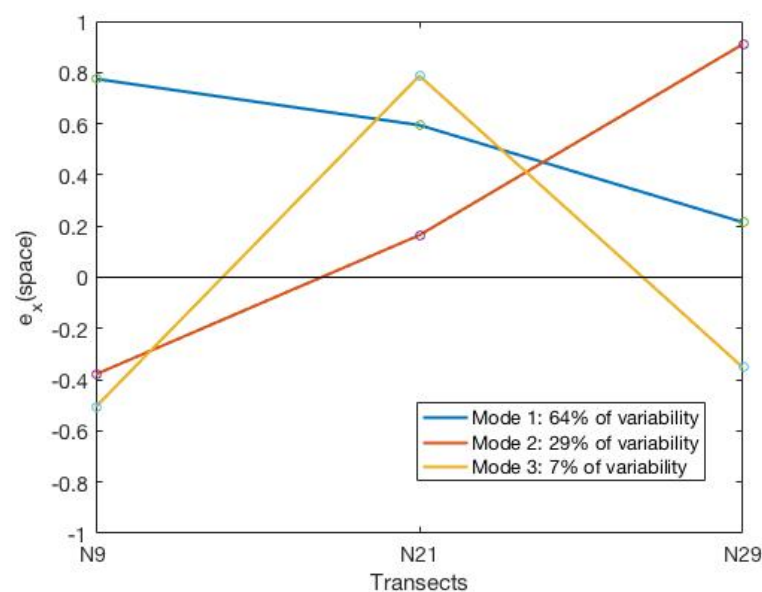


Figure 3.12: The result plot of PCA of shoreline movement at Narrabeen Beach.

### 3.6.2. The STL decomposition

A filtering procedure, seasonal-trend decomposition procedure based on Loess (STL), was applied to decompose the time series of shoreline changes at Narrabeen into trend, seasonal, and remainder components on the basis of locally weighted regression (Loess) (Ming et al. 2016). The description of loess smoother and the STL operations can be found in Cleveland et al. (1990), and the method and the explanation for parameter selections are introduced in Section 3.2.2.

The smoothing parameters used in the STL decomposition are listed in Table 3.1. The seasonal smoothing parameter  $n_s$  and trend smoothing parameter  $n_t$  were chosen in order to visually elucidate trends. The seasonal-diagnostic plot shown in Figure C.3a approves that  $n_s = 45$  is a reasonable choice, since each line is approximately straight. Thus, for the inner loop portion, the annual seasonal component was firstly smoothed by the locally weighted regression (loess) with  $p = n_s = 45$  on the original time series, and then smoothed by several moving averages of length  $n_p = n_l = 365$ . The trend component was then created by applying a moving average with the length  $n_t = 573$  (around 1.5 years) on the deseasonalized series. The number of passes through the inner loop is  $n_i = 1$ , and the number of robustness iteration for the outer loop portion is  $n_o = 5$ .

Table 3.1: Parameters for STL decomposition of coastline movement at Narrabeen Beach.

Parameter	$n_p$	$n_s$	$n_t$	$n_l$	$n_o$	$n_i$
Values	365	45	573	365	5	1

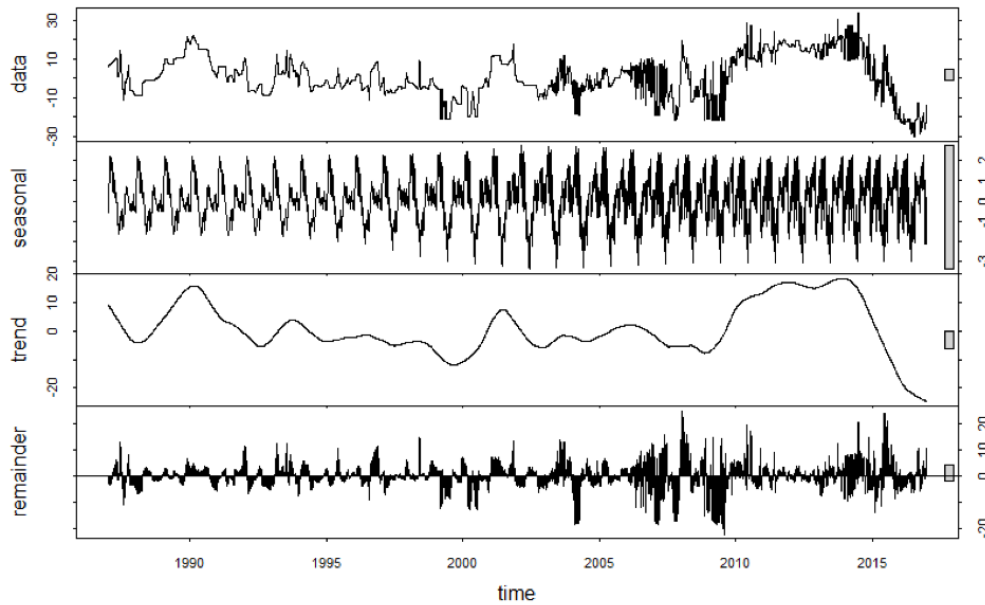


Figure 3.13: Result plot of STL decomposition of shoreline change at transect 29 on Narrabeen Beach. The annually averaged seasonal component and the long-term trend component are shown in the second and third panel, respectively. The original shoreline change and remainder component are shown at the top and bottom panels, respectively.

The result plot of the STL decomposition of shoreline changes at transect 29 is shown in Figure 3.13, which was implemented in R 3.3.3. The seasonal component changes slowly over time, so that any two consecutive years have very similar patterns, but years far apart may have different seasonal patterns. It can be observed that the seasonal component pattern during the first decade and the rest of time are different, which can be explained by the fact that fewer number of satellite images was available during the first decade. The relative scales of the components are shown with the grey bars to the right of each panel. Each grey bar represents the same length but since the plots are on different scales, the bars vary in size. The large grey bar in the seasonal panel indicates that the variation on the seasonal scale is much less compared to that in trend, and the index  $R_{st}$  equals  $5/48 = 0.104 < 0.3$  (Section 3.4.2).

### 3.6.3. Fast Fourier transform

The time series of shoreline positions contain more information than just the amplitude at a given time. The fast Fourier transform was used here to convert the signals from the original domain to frequency space. As mentioned in Section 3.3.1, the Fourier transform is not that appropriate to analyze the non-stationary time series, since the time information cannot be obtained. However, it is worthwhile using the FFT to get a first understanding of the frequency component of the shoreline variation.

The shoreline variation at transect 9 was used as an example for FFT analysis, from which several peaks can be distinguished (Figure 3.14). The shoreline shows a high variability on the decadal scale, which can probably be explained by the nodal tidal cycle with the periodicity of 18.6 years (Gratiot et al. 2008) and Pacific Decadal Oscillation (PDO) with a periodicity of a decade (Short & Trembanis

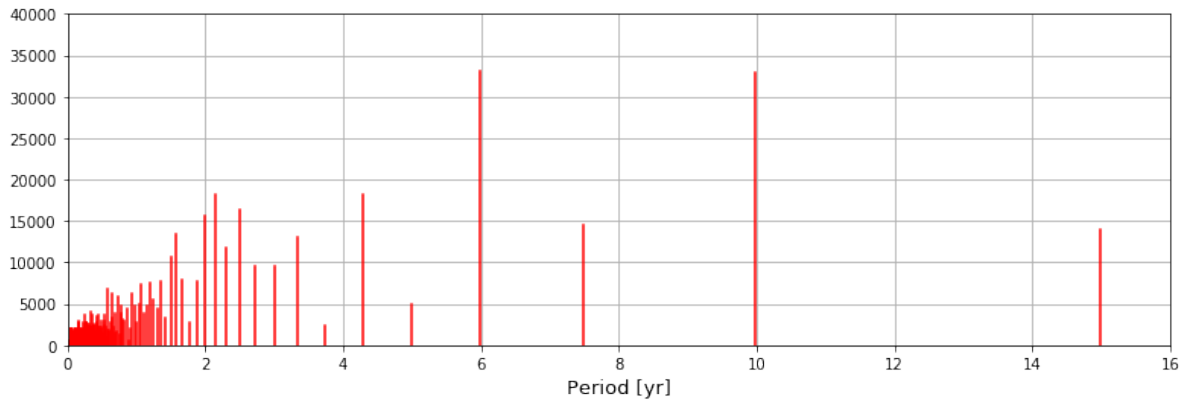


Figure 3.14: The result plot of FFT of the shoreline variation at Narrabeen Beach from 1987 to 2017.

2004). However, the limited length of the record (over 30 years) requires the signals in the extreme low frequency range to be interpreted cautiously as they are frequently spurious. Furthermore, several high peaks exist in the time interval of 2-8 years. These variabilities are probably caused by the El Niño/Southern Oscillation (ENSO) with the periodicity of 2-7 years (Hanley et al. 2003), and the verification will be specified in Section 3.6.5 and 3.6.6. The shoreline variation on the seasonal scale is relatively trivial here, corroborating the results of the STL decomposition (the index  $\alpha$  equals  $0.15 < 0.5$ ). Since both indices are lower than the threshold, Narrabeen can be classified as a **non-seasonal** beach.

Figure C.5a shows the time series of shoreline positions at transect 9 reconstructed selecting only the components with the frequency larger than 2 years. It can be observed that the reconstructed time series largely follows the original shoreline variation, suggesting the seasonal component only accounts for a small part of variability in the overall shoreline movement.

### 3.6.4. Wavelet analysis

The FFT can indicate the overall strength of the signal at prescribed frequencies (Section 3.3.1), but the information of the time intervals a spectral component occurs is required in some cases. For example, it is interesting to know in which years the inter-annual patterns occur due to ENSO. Thus, wavelet analysis was used here to quantify the way in which a spectral signal behaves on various scales with respect to time.

In the present study, the Continuous Wavelet Transform (CWT) was employed to transform time series into frequency space with the 'DOG 2' (2nd derivative Gaussian curve) mother wavelet (Torrence & Compo 1998). Analysis was conducted with a suite of software written and freely distributed by Torrence and Compo for the Matlab environment. The result is a matrix of  $M \times N$  wavelet coefficients, where  $M=12$  is the dyadic scale level and  $N=10936$  days (around 30 years) is time (Figure 3.15).  $M$  is plotted along the ordinate while  $N$  is plotted along the abscissa.

It can be observed that most of the variability is expressed on the scale range between 2 to 10 years (Figure 3.15). The episodes with a 5-year scale periodicity existed during 1990-1997 and 2012-2016, and the decadal scale periodicity exists during 1990-2011. The scattered sporadic bright patches indicate that no consistently cyclic pattern exists on any scale level. Thus, the time series of shoreline positions of Narrabeen Beach is non-stationary, because the periodicity and the magnitude of the variation in shoreline position are variable in time. Additionally, it is promising to see that the result plot of wavelet analysis based on the SDS is quite similar to that created by Short & Trembanis (2004), in which they used the measured beach width provided by the Narrabeen survey program. It indicates that the SDS can be used as a coastal state indicator for unravelling shoreline dynamics at Narrabeen to some extent.

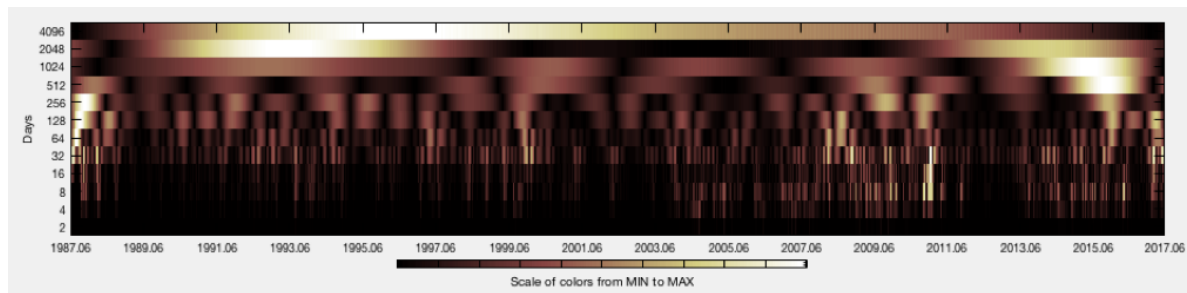


Figure 3.15: The result plot of wavelet analysis of shoreline variation at Narrabeen Beach.

### 3.6.5. Shoreline variation and the SOI

The relationship between shoreline changes derived from the SDS and SOI data (Section 2.2.3) is analyzed in this section. The very strong El Niño in 1997/98 was selected for analysis, during which time the running 3-month mean sea surface temperature (SST) anomaly was greater than  $2.0^{\circ}$  (Null 2011). The time series of monthly averaged Troup Southern Oscillation index (SOI) from 1997-1998 is shown in Figure 3.16 (obtained from the Australian Bureau of Meteorology). Sustained positive SOI values above about +7 indicate a La Niña event, while sustained negative values below about  $-7$  indicate an El Niño event (Bureau of 2018).

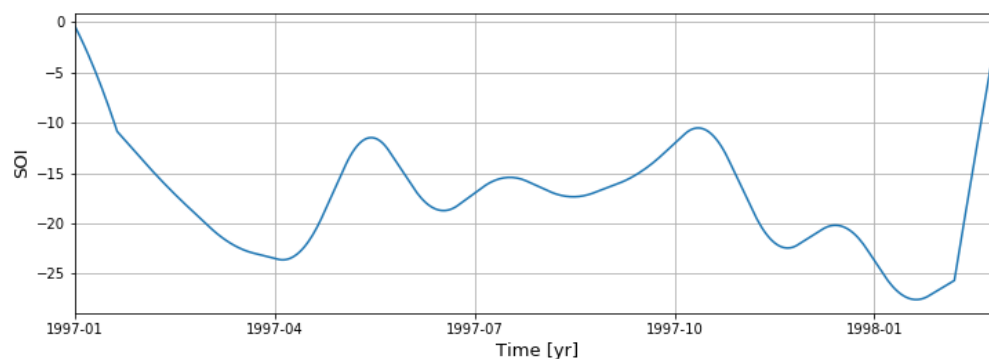


Figure 3.16: The time series of monthly averaged Troup Southern Oscillation index (SOI) from 1997-1998 (3-month filtered time series). Data from Australia Government Bureau of Meteorology.

Short et al. (1995) and Ranasinghe et al. (2004b) found that there is lag between the beach response to the change of the SOI at Narrabeen. Thus, here we calculated the lagged cross-correlation between shoreline positions and the SOI (Figure 3.17) to test if the SDS could be used to unravel the same pattern. The negative correlation between the SOI and the shoreline movement at transect 9 (Figure 3.17a) indicates that decreasing SOI (El Niño phase) is accompanied by accretion at the northern part of the beach. In contrast, the positive correlation between the SOI and the beach width at transect 29 (Figure 3.17b) shows that decreasing SOI is associated with erosion at the southern part of the beach. Therefore, shoreline rotates clockwise during El Niño and anti-clockwise during La Niña, corroborated with Mortlock & Goodwin (2016) (Figure A.2). The lags associated with the peak values indicate that the shoreline variation at transect 9 lagged the SOI by around 90 days, while that at transect 29 lagged the SOI by around 110 days.

### 3.6.6. Regression analysis

In order to assess the relative influence of different variables on shoreline movement at Narrabeen, the regression analysis of shoreline changes at transect 9 with the ordinary least squares model was carried out (Figure 3.18). The beach width at transect 9 was set as the dependent variable, and the independent variables included significant wave height, SOI and wave angle. The inshore wave climate data

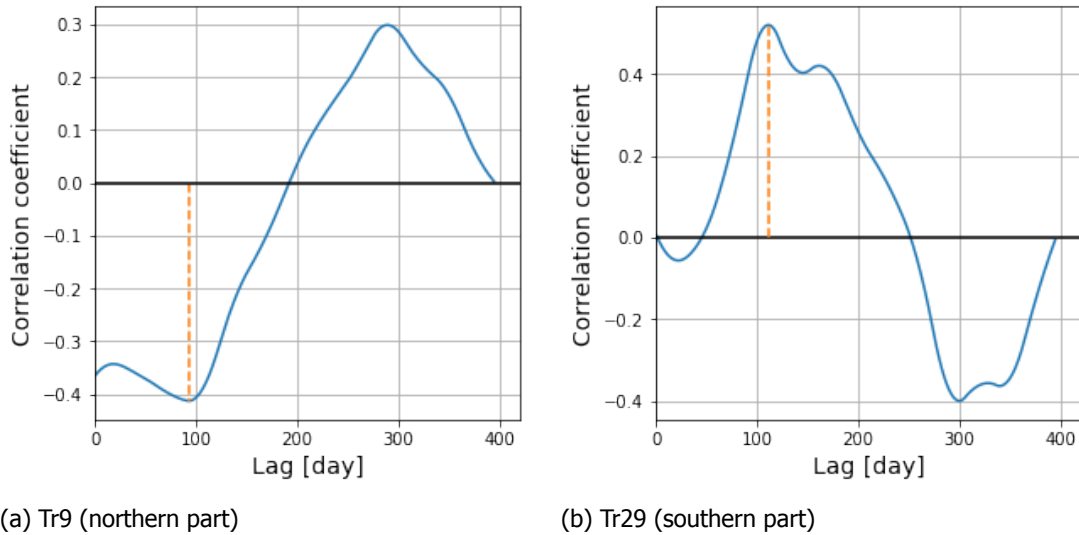


Figure 3.17: Lagged cross-correlations between the SOI and shoreline variation at (a) Tr9 (northern part), and (b) Tr29 (southern part) on Narrabeen Beach.

from 1988-01-01 to 2013-01-01 was obtained from Narrabeen-Collaroy Beach Survey Program (9133 daily observations). A rolling window of 7 days was applied to preprocess the time series of independent variables, considering the lagged beach response to the external forces. Normalized value for each independent variable was calculated in order to analyze the relative importance of independent variables on shoreline variation.

OLS Regression Results						
Dep. Variable:	Tr9	R-squared:	0.187			
Model:	OLS	Adj. R-squared:	0.187			
Method:	Least Squares	F-statistic:	525.1			
Date:	Tue, 03 Apr 2018	Prob (F-statistic):	0.00			
Time:	22:21:12	Log-Likelihood:	-12013.			
No. Observations:	9133	AIC:	2.403e+04			
Df Residuals:	9129	BIC:	2.406e+04			
Df Model:	4					
Covariance Type:	nonrobust					
	coef	std err	t	P> t	[0.025	0.975]
Hs	-0.4661	0.029	-16.252	0.000	-0.522	-0.410
SOI	-0.3804	0.010	-38.194	0.000	-0.400	-0.361
sin(alpha)	0.8543	0.095	8.962	0.000	0.667	1.041
cos(alpha)	-0.9799	0.099	-9.886	0.000	-1.174	-0.786

Figure 3.18: The fit result for shoreline variation at transect 9 with the ordinary least squares model. The explanation of parameters listed in the figure can be achieved in Section 3.3.2.

The negative coefficient in the term of  $H_s$  indicates that higher wave height corresponding to the coastline erosion at transect 9. Similarly, the negative coefficient in the term of the SOI shows that lower value of the SOI (i.e. during El Niño event) correlated to the shoreline accretion at transect 9 (north), in line with Figure 3.17 and Figure A.2. The correlation with the wave angle shows that when southerly wave climate dominates (e.g. during El Niño event, Figure A.2), accretion dominates at transect 9 (north). The magnitude of T-value indicates the extent of correlation between the independent variable with shoreline movement (Section 3.3.2). Thus, shoreline variation at Narrabeen Beach correlated best with the SOI, followed by the inshore wave height and then the wave angle. The small P-value indicates that the coefficients on individual variables are significant.

### 3.6.7. Summary

The PCA was carried out to study the spatial pattern of shoreline variation at Narrabeen. The rotation feature is described by the mode 2 (29%), and thus  $\beta$  equals 29% indicating that Narrabeen is a **rotational** beach. This conclusion can be corroborated by the trend component analysis (Table D.2).

The trend, seasonal and residual components of shoreline variation were generated by the STL decomposition (Figure 3.13). Compared with trend component, the seasonal signal is trivial, and  $R_{st}$  equals  $0.104 < 0.3$ . As the index  $\alpha$  equals  $0.15 < 0.5$  based on the result of FFT (Figure 3.14), Narrabeen can be classified as a **non-seasonal** beach.

The FFT transferred the time series of shoreline movement to the frequency space, indicating that the variation in 2-8 years and decadal scales account more than the seasonal scale in the overall variation (Figure 3.14). The variation scale of 2-8 years is probably caused by ENSO (approved in Section 3.6.5 and 3.6.6), and the decadal-scale variation may be induced by the nodal tidal cycle and the PDO. However, with the limited data for 30 years, it is impossible to prove the repeatability of the ultra low frequency oscillations.

The wavelet analysis shows that most of the variability can be expressed in the scale range between 2 to 10 years (Figure 3.15). The scattered sporadic bright patches do not show consistently cyclic pattern on any scale level, indicating that shoreline change at Narrabeen Beach is non-stationary. Additionally, it is promising to know that the result plot of wavelet analysis is quite similar as that created by Short & Trembanis (2004), suggesting that the SDS can be used as a coastal state indicator for unravelling shoreline dynamics at Narrabeen.

The cross correlation between the SOI and shoreline movement during the strong El Niño event in 1997/98 was calculated (Figure 3.17), showing that the shoreline rotates clockwise during El Niño events. Moreover, it can be observed that the shoreline movement at transect 9 lagged the SOI by around 90 days, while that at transect 29 lagged the SOI by around 110 days. Finally, the regression analysis was carried out on shoreline variation with the ordinary least squares model (Figure 3.18). The results indicate that the SOI correlated best with shoreline variation at Narrabeen Beach, followed by the inshore wave height and then the wave angle.

### 3.7. Moruya and Pedro (Example 2)

**Background:** Moruya and Pedro are two embayed beaches located 270 km south of Narrabeen in southeast Australia. Short et al. (2014) analyzed the three beaches based on surveys between November 2007 and October 2013 and found that the beaches showed the synchronous oscillation and rotation, though at different magnitudes. They stated that local factors contributed to shoreline dynamics on each of the beaches with the lower energy beach having a more dynamic shoreline. However, longer-term shoreline variation cannot be detected in their study, as the shoreline position data for Moruya and Pedro is only available for 5 years. Therefore, the SDS of the three coasts will be analyzed to test if they can unravel the patterns of beach responses on a longer-term scale.

Based on the latest available satellite image on 2017-12-18, 12 (9) transects were created perpendicular to the SDS with spatial resolution of 250 m along the shoreline at Moruya (Pedro) (Figure 3.19). The SDS were obtained from Landset 5 dataset. The intersections between the SDS and transects were created to represent shoreline variation at Moruya and Pedro over 30 years. The SDS at Narrabeen were created with the parameters set as in Section 3.6.



Figure 3.19: Transect locations at Moruya and Pedro.

#### 3.7.1. Principal component analysis

The PCA was performed on shoreline movement at Moruya and Pedro (Figure 3.20). The primary mode (67%) shows that shoreline changes on opposite sides of each beach are out of phase. Additionally, the primary mode clearly demonstrates two more aspects of the rotation: the directional coherence at M1 and P1 (M3 and P3) and the hinge role of the central profile M2 (P2). Thus, coastline changes at the two beaches show a synchronized rotation scenario, consistent with the observation of Short & Trembanis (2004). Since  $\beta$  equals 67% (>15%), Moruya and Pedro can be classified as **rotational** beaches.

The correlation analysis of shoreline variation at Moruya, Pedro and Narrabeen indicates that the three beaches show the synchronized rotational (Table D.4, Section D.2). Thus, it is possible that the data of shoreline variation of a single beach can be representative of general trends over large section of similar coasts.

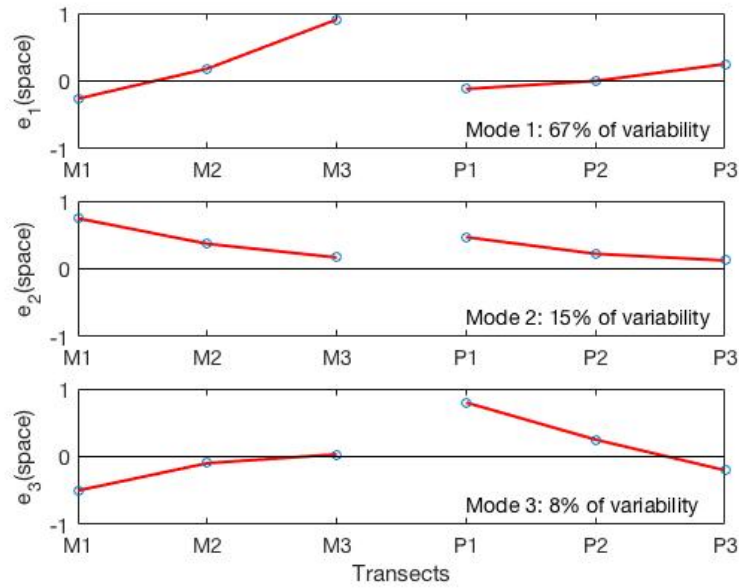


Figure 3.20: The result plots of PCA of shoreline variation at Moruya (M1-M3) and Pedro (P4-P6) (Figure 3.19). The meaning of axes can be found in Section 3.2.3.

### 3.7.2. The STL decomposition

The smoothing parameters used for the STL decomposition of shoreline variation at Moruya and Pedro are listed in Table 3.2. The seasonal smoothing parameter  $n_s$  and trend smoothing parameter  $n_t$  are chosen in order to visually elucidate trends. The seasonal-diagnostic plots approve that  $n_s = 35$  is a reasonable choice (Figure C.3b and C.3c), since each line is approximately straight. Thus, for the inner loop portion, the annual seasonal component was firstly smoothed by the locally weighted regression (loess) with  $p = n_s = 35$  (Section 3.2.2) on the original time series, and then smoothed by several moving averages of length  $n_p = n_l = 365$ . The trend component was then created by applying a moving average with the length  $n_t = 573$  (around 1.5 years) on the deseasonalized series. All the other parameters are set as the same as those for Narrabeen Beach (Section 3.6.2).

Table 3.2: Parameters for STL decomposition of shoreline variation at Moruya and Pedro.

Parameter	$n_p$	$n_s$	$n_t$	$n_l$	$n_o$	$n_i$
Values	365	35	573	365	5	1

The result plots of the STL decomposition of shoreline changes at M1 and P1 are shown in Figure 3.21 and Figure 3.22, respectively. Similarly, the seasonal components of shoreline variation at both beaches have small contribution to the overall shoreline variation. The index  $R_{st}$  equals  $8/65 = 0.12$  and  $11/85 = 0.13$  for Moruya Beach and Pedro Beach, respectively.

### 3.7.3. Fast Fourier transform

It is interesting to see that the overall patterns of FFT results resemble at Narrabeen, Moruya and Pedro (Figure 3.23 and Figure 3.14), and the values of index  $\alpha$  are also similar ( $\alpha = 0.142 < 0.5$  for Moruya,  $\alpha = 0.139 < 0.5$  for Pedro and  $\alpha = 0.15 < 0.5$  for Narrabeen). These comparable patterns might be caused by the fact that the three beaches are exposed to a similar deepwater wave climate, identical tides and have similar lengths, easterly orientation and medium to fine sand (Short et al. 2014). As the values of index  $\alpha$  and  $R_{st}$  are both below the thresholds, Moruya and Pedro are classified as **non-seasonal** beaches.

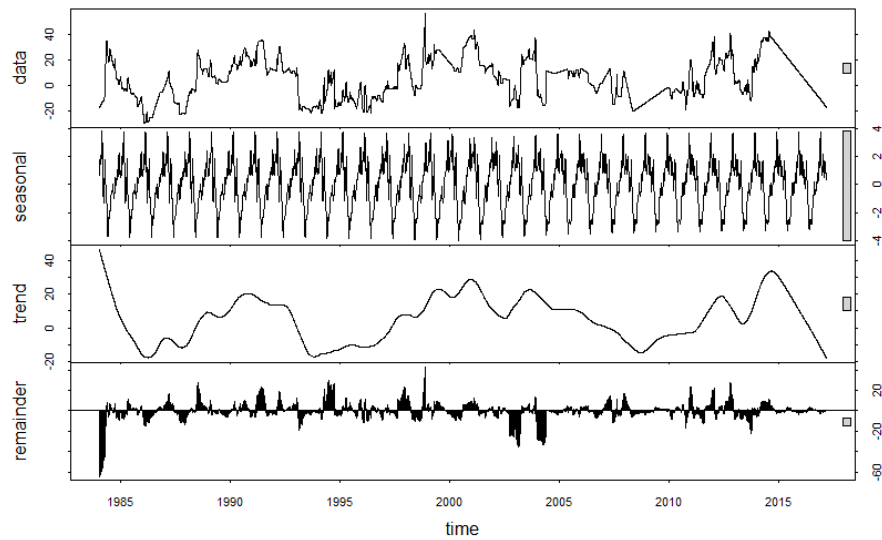


Figure 3.21: The result plot of the STL decomposition of shoreline movement at M1, Moruya.

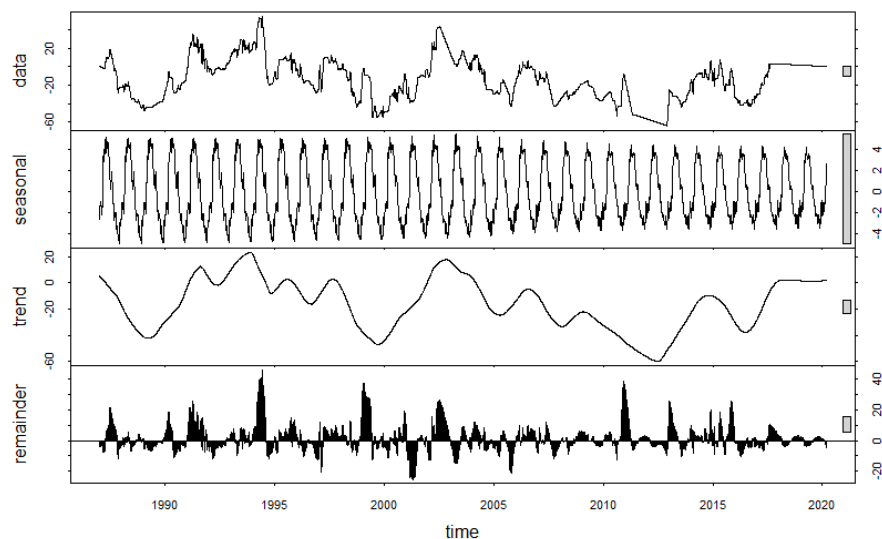


Figure 3.22: The result plot of the STL decomposition of shoreline movement at P1, Pedro.

The time series of shoreline positions at M1 and P1 were reconstructed selecting only the components with a frequency of larger than 2 years (Figure C.5b and Figure C.5c). It can be observed that the reconstructed time series largely follow the original shoreline variation pattern, and thus shoreline movement on the seasonal scale is relatively trivial at both sites.

#### 3.7.4. Trend component analysis

In this section, the trend components of shoreline variation are analyzed at the nine main transects (Figure 3.11 and 3.19) of the three embayed beaches from 1998-01 to 2017-01. The range and standard deviation of trend component of shoreline movement at the three beaches are shown in Table 3.3. It is interesting to observe that Moruya undergoes a more dynamic shoreline variation compared to the adjoining beach Pedro, in line with the analysis of Short et al. (2014), even though Moruya is the

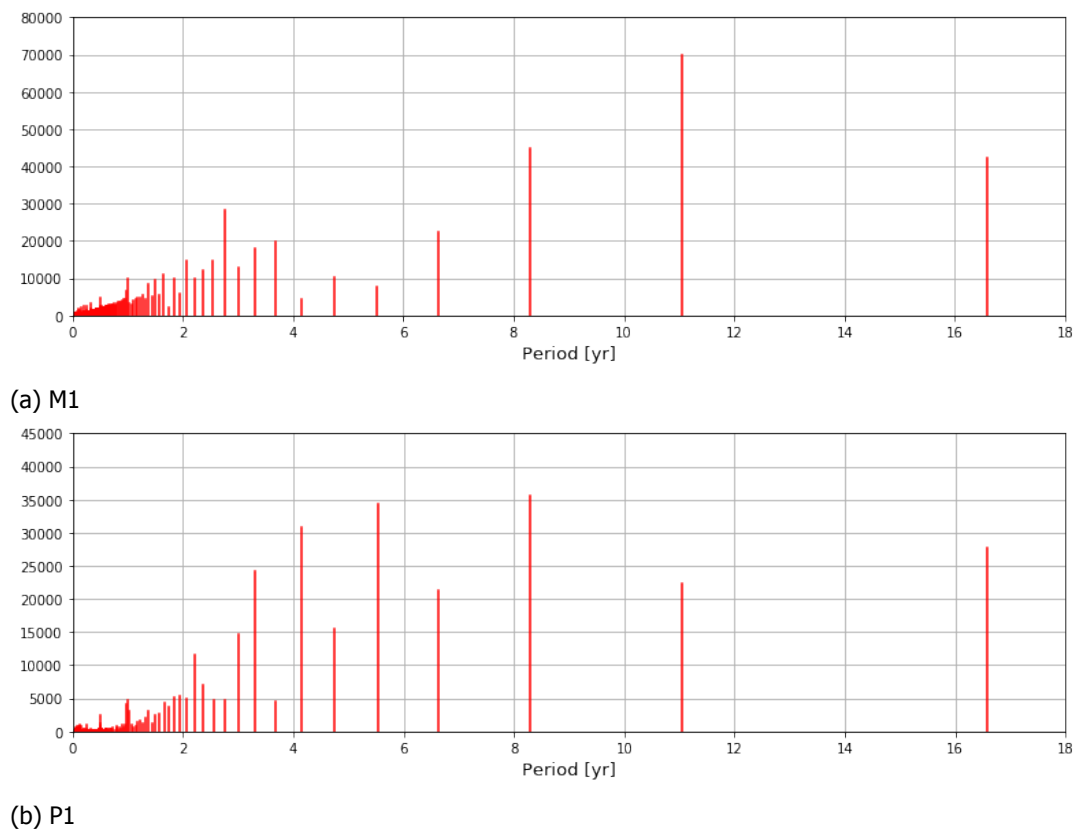


Figure 3.23: Result plots of FFT of shoreline changes at Moruya and Pedro from 1984 to 2017.

lower energy beach. A probable explanation is that the lower energy Moruya beach switches between an LTT and R state, causing substantial sediment transport across the shoreline during the full recovery between the erosion events (Short et al. 2014). In contrast, the higher energy Pedro beach is partially sheltered by the bar and will not widen substantially until the bar attaches and migrates onshore (Short et al. 2014). Therefore, the rapid transfer of sand between the R-LTT state compared to those with a detached bar results in greater shoreline variation at the lower energy beach.

The patterns of shoreline variation derived from the SDS and the analysis shown by Short et al. (2014) were then compared. For Moruya Beach, the SDS show that the greatest variation occurs on the southern profiles (M3) (Table 3.3). For Narrabeen Beach, the shoreline exhibits the greatest oscillation at the northern profile (N9) and least at the sheltered southern profile (N29). It is good to know that the above observations are in line with the analysis of Short et al. (2014). For Pedro beach, however, the SDS show that the shoreline at the northern end (P1) exhibits a higher variability than at the southern end (P3), opposite to the analysis of Short et al. (2014). An explanation may lie in the limited shoreline position data Short et al. (2014) used, which only lasted from 2007-11 to 2013-10. Thus, the longer-recorded shoreline positions may increase the capability of the SDS to unravel the full range of beach .

### 3.7.5. Summary

Moruya, Pedro and Narrabeen are three embayed beaches located in southeast Australia. They are exposed to a similar deepwater wave climate, identical tides and have similar lengths, easterly orientation and medium to fine sand (Short et al. 2014).

The result of PCA shows that the rotational mode (Mode 1) and oscillation mode (Mode 2) explain 67% and 15% of the overall shoreline variance, respectively (Figure 3.20). The index  $\beta$  equals 67% ( $> 15\%$ ), suggesting that Moruya and Pedro can be classified as **rotational** beaches. The correlation analysis of shoreline variation at Moruya, Pedro and Narrabeen in Section D.2 indicates that the three

Table 3.3: Variability and trends of shoreline positions at the three beaches over 1998-2017.

Transect	Linear trend (m/yr)	Range (m)	Standard deviation (m)
N9	-0.4	51.8	13.2
N21	-0.2	21.2	3.96
N29	-0.1	25.5	5.02
M1	0.4	48.5	11.4
M2	0.5	32.8	7.34
M3	0.7	108.4	25.9
P1	-0.8	77.9	19.1
P2	-0.3	17.1	4.32
P3	0.1	40.3	10.4

beaches have the synchronized rotational (Table D.4). Thus, it is possible that the data of shoreline variation of a single beach can be representative of general trends over large section of similar coasts.

The trend, seasonal and residual components of shoreline variation at Moruya and Pedro were generated by the STL method. The seasonal components of shoreline changes at both beaches have a small contribution to the overall shoreline variation (Figure 3.21 and 3.22), and index  $R_{st}$  equals 0.12 and 0.13 ( $< 0.3$ ). Based on the results of FFT (Figure 3.23), the index  $\alpha$  equals 0.142 and 0.139 ( $< 0.5$ ). Thus, Moruya and Pedro can be classified as **non-seasonal** beaches.

Local factors also contribute to shoreline dynamics at the three beaches, resulting in significant variation on the scale of these trends ranging from 17m to 108 m (Table 3.3). The patterns of shoreline variation derived from the SDS and the ones concluded by Short et al. (2014) were then compared, and the analysis results based on the SDS are in line with Short et al. (2014) at Narrabeen and Moruya. For shoreline changes at Pedro, the longer-recorded shoreline positions possessed by the SDS may provide a higher accuracy to be used for studying shoreline dynamics at Pedro.

# 4

## Results

In this chapter, the capabilities of using the SDS on studying shoreline variation governed by different forcing types are tested, including the influence of storms, seasonal forcing, climate variability, land subsidence, SLR and anthropogenic processes. The sites of interests are shown in Figure 3.1, each of which was selected based on the available documentation to verify if the influence of a specific forcing type could be unravelled through the SDS. The verification was achieved by comparing the behaviour patterns of shoreline variation extracted through the SDS to the ones concluded in the related literature.

### 4.1. Storm

Storms are associated with periods of strong often damaging winds, flood-producing rainfall, heavy snowfall or blizzard conditions. Various morphodynamic responses on beaches and greatly changes of the coastal landscape can be induced by storms over short periods of time (Jiménez et al. 2012), such as beach erosion, berm migration, dune erosion, washover construction, etc (Morton 2002). In this section, the capabilities of using the SDS for unravelling shoreline dynamics on the short-term scale governed by storms are tested.

#### 4.1.1. Fire Island

**Background:** Fire Island is a 50 km-long barrier island system centrally located along the southern shore of Long Island (Figure A.11). Brenner et al. (2018) defined a new contour-based morphologic change metric, the Beach Change Envelope (BCE), based on the time series of beach profile data at Fire Island. They used the BCE to capture beach responses to storms and human modification between 2005-2012, and found that the BCE can capture distinctive upper beach morphologic change characteristic of different beach building and erosional events.

Based on the latest available satellite image (2018-04-21), 18 transects were generated perpendicular to the SDS with spatial resolution of 500 m along the west and east Fire Island (Figure 4.1). The SDS were obtained from Sentinel 2 dataset with the composite averaging window set as 180 days. The intersections between the SDS and transects were generated to create time series of shoreline variation over 34 years.

#### Time series analysis

Fire Island has an extensive storm history (Brenner et al. 2018). To help mitigate erosion threatening oceanfront homes and infrastructure, beach replenishment projects have been carried out since the 1960s (Lentz et al. 2013). Here we focused on the influence of four storm events (2005-2012) on shoreline dynamics (Table 4.1), and the large-scale replenishment project completed in the spring of 2009 was also investigated.



Figure 4.1: Transect locations at west (left) and east (right) Fire Island.

Table 4.1: Name, date and general impacts of storms within the recent historic storm record at Fire Island, NY used in the present study (adjusted according to Brenner et al. (2018)).

Storm History			
Name	Date	Peak wave height (m)	Impact
Halloween Storm	22-26 Oct 2005	6	The large offshore wave height and extended storm duration (5 days) caused the widespread erosion along the island (Lentz & Hapke 2011).
Nor'Ida	12-14 Nov 2009	6	The extratropical storm led to substantial beach erosion and dune scarping along most beaches, many of which had recently been renourished (Lentz et al. 2013).
Hurricane Irene	27-28 Aug 2011	5	The modest offshore wave heights, the long period swell throughout the storm and the steady onshore southwest winds resulted in an accretional event, since sediment were moved from the lower portion of the shoreface to the near-dune and upper beach regions (Brenner et al. 2018, Release 2011).
Hurricane Sandy	24-27 Oct 2012	10	Morphologic impacts included frontal dune erosion, scarping, extensive dune overwashing, flattening of the primary dune, and/or complete island breaching (Hapke et al. 2013).

The coastline changes were analyzed based on the ensemble averaged shoreline movement at the nine transects on the west Fire Island (Figure 4.2). The analysis results based on the SDS and the ones from literature are compared as following.

- Lentz & Hapke (2011) used the LiDAR and real-time kinematic GPS surveys to study the beach responses to storms on Fire Island, and they found that Halloween Storm induced widespread erosion in the region. The interpolated shoreline variation derived from the SDS, however, shows an accreting pattern. Considering the low availability of satellite images when the storm struck (no images were taken in October 2005), the SDS are not that optimum to be used for investigating the influence of Halloween Storm at the west Fire Island.
- A large-scale replenishment project was undertaken at Fire Island in the winter and spring of 2009, with about 1,400,000  $m^3$  of sediment added in front of the participating communities (Lentz et al. 2013) (Figure A.12). The SDS show that shoreline accreted greatly in the region, in line with the analysis of Lentz et al. (2013).
- Nor'Ida is an extratropical storm that formed from the remnants of Hurricane Ida in 2009. According to Lentz et al. (2013), the storm caused a large beach erosion by removing substantial amounts of sand that had been placed along the western reach of Fire Island during the large

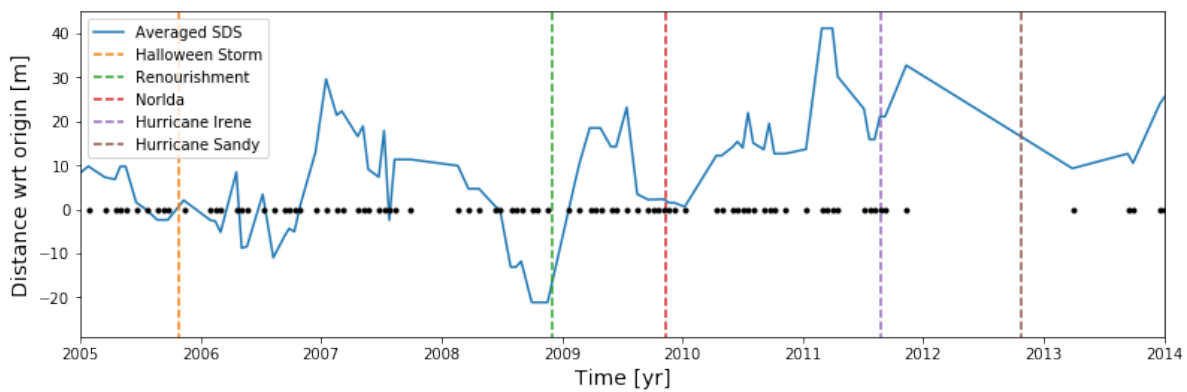


Figure 4.2: Time series of ensemble averaged shoreline positions at the west Fire Island in 2005-2013. The black dots represent the time when the satellite images were taken.

replenishment project completed in April 2009. It can be observed that the availability of satellite images is ideal during Nor'Ida, and the SDS show a slight retreat pattern during the storm.

- According to [Release \(2011\)](#) and [Brenner et al. \(2018\)](#), an accretion of sand was noted on the majority of Fire Island during Hurricane Irene, since the sediment was moved from the lower portion of the shoreface to the near-dune and upper beach regions under southwest winds. The SDS show that the shoreline accreted during the storm, in line with the analysis of [Brenner et al. \(2018\)](#). It should be noted that, however, the limited availability of satellite images requires the interpolated time series of shoreline changes to be interpreted cautiously as they are frequently spurious.
- According to [Brenner et al. \(2018\)](#), shifted material from the upper beach to the lower beach caused a positive signal for shoreline variation at Fire Island during Hurricane Sandy. However, no clear information is provided through the SDS, as no image was taken during the whole year of 2012. On the other hand, the SDS did capture the breach on the east side of Fire Island, which formed near Old Inlet after October 29, 2012, and water has flowed freely between the ocean and the bay since then ([Release 2015](#)). Figure 4.3 shows the time series of shoreline positions derived from the SDS at transect 1 on the east Fire island (Figure 4.1 shows where the breach exists), and the breach near Old Inlet can be depicted by the fact that the SDS do not exist after Hurricane Sandy.

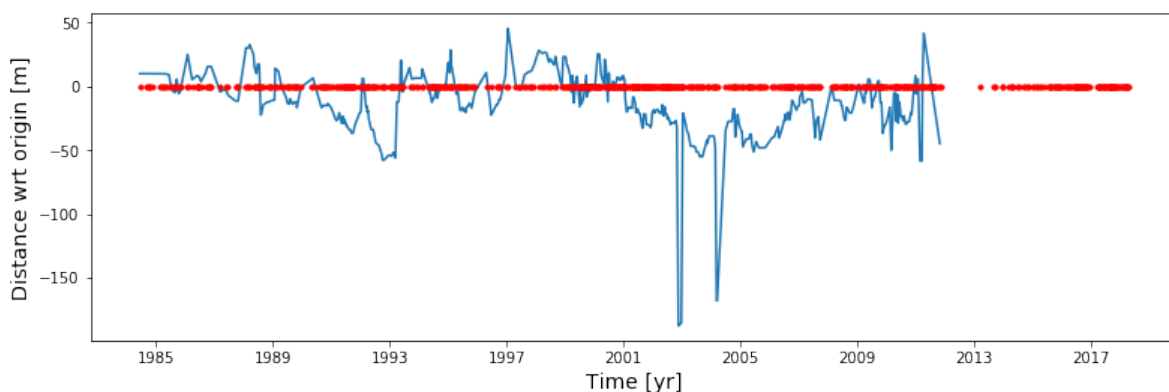


Figure 4.3: Shoreline variation at transect 1 on the east Fire Island. Red dots represent the time when satellite images were taken.

#### 4.1.2. The Gulf of Valencia

**Background:** The Gulf of Valencia is an inlet of the western Mediterranean Sea on the eastern coast of Spain (Figure A.15). Pardo-Pascual et al. (2014) focused on the impacts of the six storms on a 100-km segment of the coastline from 2001-11 to 2002-05 with data obtained from Landsat 5 TM and Landsat 7 ETM+ imagery. They found that coastlines showed a high level of spatial variability: beaches with steeper slopes experienced fewer changes; well-developed foredunes minimized the reduction in the beach width after the storms; and the coastal orientation also influence storm impacts and the recovery processes.

Saler Beach and Cullera Beach are two sandy coasts located in the central part of the Gulf of Valencia (Figure A.16). According to Pardo-Pascual et al. (2014), the shoreline changes exhibited different behaviours at the two sites during the six storms. Based on the latest available satellite image (2018-04-28), 11 transects were generated perpendicular to the SDS with the spatial resolution of 500 m and 250 m along the Saler Beach and Cullera Beach, respectively (Figure 4.4). The SDS were obtained from Sentinel 2 dataset. In order to largely extract shoreline movement induced by storms, the averaging window for image composite is set to **30 days** to capture more variation on the short-term scale (Section 5.1). The intersections between the SDS and transects were generated to create time series of shoreline variation over 34 years.

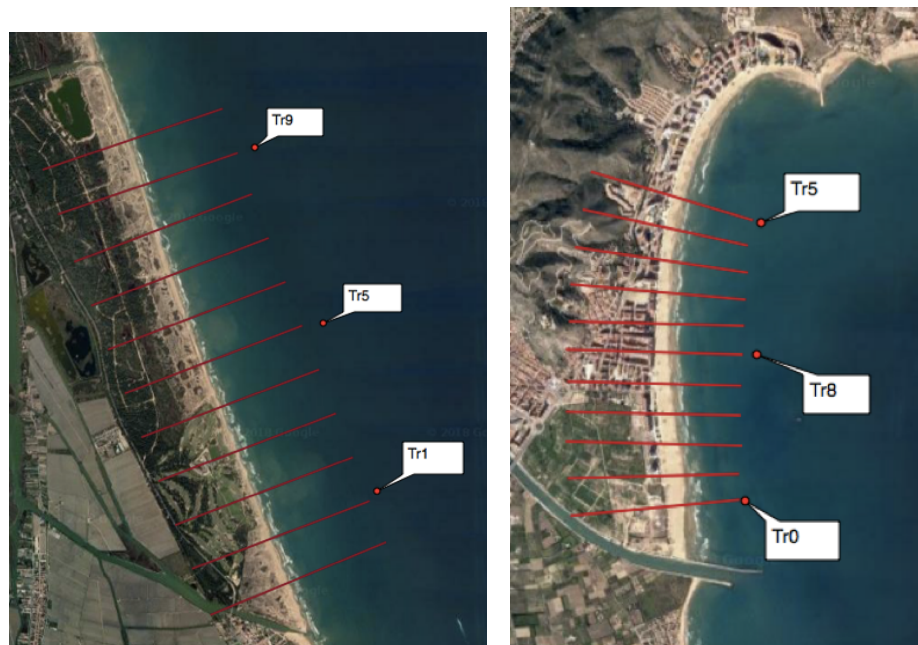


Figure 4.4: Transect positions at Saler Beach (left) and Cullera Beach (right).

#### Time series analysis

In this section, the shoreline changes derived from the SDS are analyzed to investigate storm impacts on Saler Beach and Cullera Beach from 2001-11 to 2002-05. The information of the six storms happened in the region during the study time is shown in Table 4.2, which is adjusted according to Pardo-Pascual et al. (2014). The shoreline responses to the storms at the two beaches are compared in Figure 4.5.

The shoreline responses to the biggest storms which happened in 2001-11 were very different on the two beaches. The coastline retreated slightly at Saler Beach and showed a rapid accretion afterwards, even recovering to seaward of the pre-storm position at the beginning of December. In contrast, the shoreline eroded greatly at Cullera Beach due to the storms in 2001-11, and no beach recovery was observed in November. It is good to know that the above observations are largely in line with the analysis of Pardo-Pascual et al. (2014). It is interesting to see that Saler Beach was less affected by

Table 4.2: Information related to the storms from 2001-11 to 2002-05. Adjusted based on [Pardo-Pascual et al. \(2014\)](#)

Date	Duration (h)	$H_s$ (m)	$T_p$ (s)	Tidal level (m)
11/10/01	49	4.3	11.6	0.22
11/14/01	42	3.5	11.6	0.32
12/14/02	33	3.2	11.1	0.03
3/28/02	39	3.4	8.1	0.08
4/2/02	17	2.8	8	0.08
5/6/02	41	3	8.1	0.16

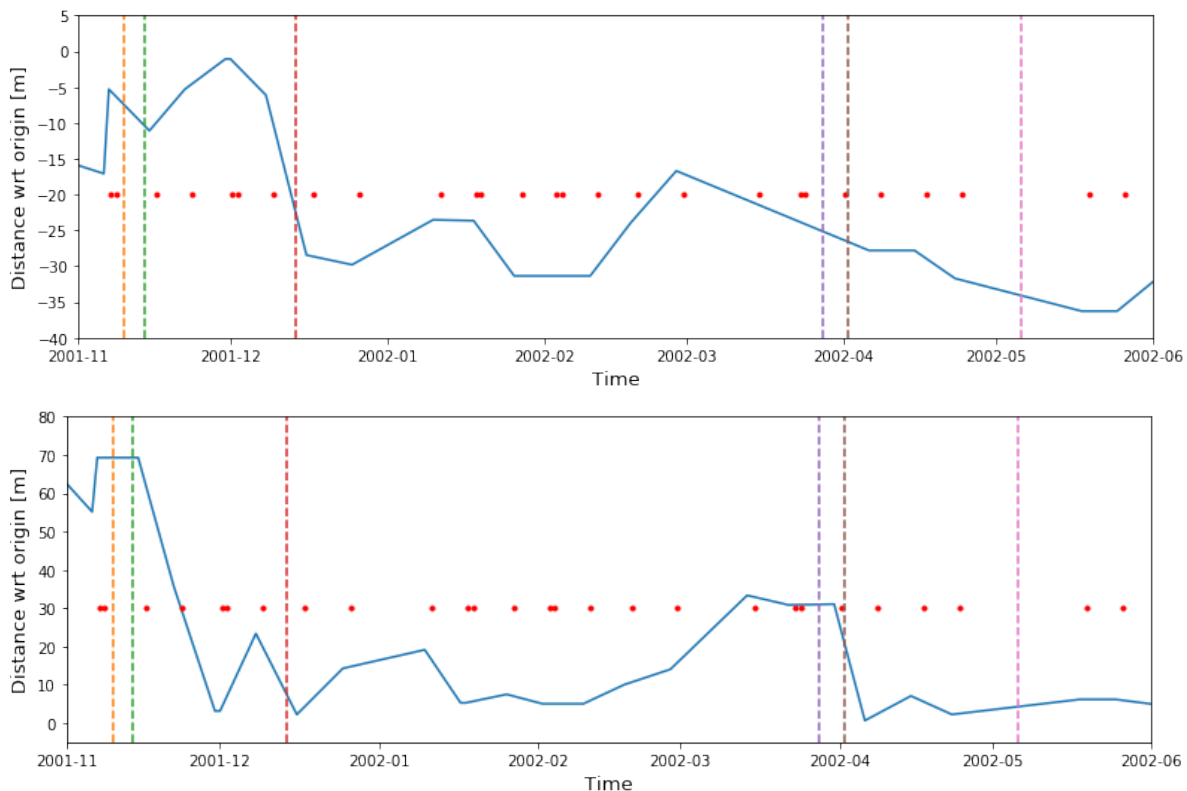


Figure 4.5: Shoreline responses to the storms on Saler Beach (upper panel) and Cullera Beach (lower panel). The start date of each storm is shown with dotted lines (11/10/01, 11/14/01, 12/14/01, 3/28/02, 4/2/02, 5/6/02) and detailed information is shown in Table 4.2. The red dots represent the time when the satellite images were taken.

the storms, even though the distance from the center of the storms to Saler Beach was shorter than to Cullera Beach during the storms in 2001-11 ([Pardo-Pascual et al. 2014](#)). The larger erosion on Cullera Beach could be explained by its N-S orientation, which increased the longitudinal transport efficiency in coasts ([Sanjaume & Pardo-Pascual 2005](#)) (Saler Beach oriented to the NW-SE). The severer erosion at Cullera Beach may also be explained by its shallower beach slope (approx.  $3.8^\circ$ ). For Saler Beach, the less erosion was probably caused by the well-developed foredunes backwards, so during the storms the eroded sediment from the dune act to widen the beach and reduce the level of wave action at the dune toe ([Davidson-Arnott 2010](#)).

For the successive storms after 2001-11, they generally produced a retreat in the position of the shorelines, but still different impacts and recovery processes happened on the two coasts. For Cullera Beach, it can be observed that the shoreline variation was less significantly until June compared to the first storms in 2001-11. According to [Del Río et al. \(2012\)](#), this phenomenon can be explained by the fact that beaches eroded and flattened by a storm tend to dissipate incident wave energy, which cause less vulnerability of the beach to the impact of subsequent storms. On the contrary, the successive

storms resulted in a progressive coastline retreat at Saler Beach, which achieved a maximum erosion in 2002-05, showing accumulative impacts on shoreline changes. [Pardo-Pascual et al. \(2014\)](#) explained this situation as flattened profiles allow the water level to reach areas further inland than in steeper beaches. It is good to know that these observations based on the SDS can be corroborated with the analysis of [Pardo-Pascual et al. \(2014\)](#).

#### 4.1.3. Other sites

Another site used for testing the ability of the SDS on unravelling shoreline variation governed by storms is the coastline at Perranporth (Section [D.3](#)). The influence of large wave height on shoreline changes during the winters of 1989/90, 1993/94, 1994/95, 2006/07 and 2013/14 was focused on. However, the availability of the SDS is not optimistic from 1991 to 1997, during which time almost no satellite images could be used for shoreline detection at Perranporth (Figure [D.5](#), dt =7-13). Thus, the trend and residual components of shoreline changes were mainly analyzed from 2006 to 2017 (Figure [D.9](#)), during which time the availability of the SDS is higher.

#### 4.1.4. Discussion and conclusion

The shoreline responses to extreme storms were analyzed with the SDS in this section, and the coastline changes at Fire Island, the Gulf of Valencia (Saler Beach and Cullera Beach) and Perranporth were focused on. For the storm impacts at Fire Island and Perranporth, the SDS are not ideal to be employed for studying the shoreline dynamics on the short-term scale, because no clear information is provided due to the shortage of satellite images and the long image composite window (180 days) used for generating the SDS (Section [2.1.2](#)). On the other hand, the breaching event happened on the east Fire Island caused by Hurricane Sandy and the beach recovery processes at Perranporth (Section [D.3](#)) were clearly captured through the SDS. For Saler and Cullera Beach, shoreline changes on the short-term scale were better extracted through the SDS generated with the shorter composite window (30 days). As a result, the coastline responses derived from the SDS at these two beaches are better correlated to the analysis of related documentation. However, the accuracy of the SDS reduces correspondingly when the composite window gets shorter (Section [2.1.2](#), [Hagenaars et al. \(2018\)](#)), so the SDS may not be considered as the best solution when the purpose is to evaluate the real impact of a particular storm on shoreline changes.

[Masselink et al. \(2016\)](#) stated that beach responses to storms are difficult to be observed when the survey occurs a long time after the event, particularly if the beach recovery is rapid. Sometimes the first image after a storm is taken so long afterwards that the shoreline variation due to storms is not recorded (e.g. Hurricane Sandy on Fire Island), and sometimes several events may happen between two consecutive available images. On the other hand, the introduction of new satellite missions can be expected in the near future, which helps to obtain an increasing temporal, spatial and spectral resolution of satellite images ([Hagenaars et al. 2018](#)). Therefore, it is possible that the SDS are appropriated to be used for studying shoreline changes governed by storms in the future.

To sum up, the SDS may not be considered as an ideal tool for studying shoreline dynamics governed by extreme storms for now. When an increasing temporal, spatial and spectral resolution of satellite images is obtainable as time goes by, the capabilities of using the SDS for studying shoreline changes governed by storms might be improved.

## 4.2. Seasonal forcing

Shoreline variation on the seasonal scale is one of the shortest-term types of variability relevant to coastal management (Stive et al. 2002). Generally, the high-energetic wave conditions can cause a gentle slope 'storm profile' during the winter, while the mild incoming wave would generate a steep 'swell' profile during the summer (Komar 1998). In this section, the capabilities of using the SDS on studying shoreline dynamics on the seasonal scale are tested.

### 4.2.1. CRLC (Ocean Shores)

**Background:** The Columbia River Littoral Cell (CRLC) extends approximately 165 km, consisting of four concave-shaped barrier plain subcells separated by estuary entrances of the Grays Harbor, Willapa Bay and Columbia River (Ruggiero et al. 2005) (Figure A.6). Ocean Shores is a coastal community adjacent to Grays Harbor, where many homes and urban infrastructure had recently been built on accreted lands that have now started to erode. Based on the morphology monitoring program at Ocean Shores, Gelfenbaum & Kaminsky (2010) found that elevated sea level and large waves during winter storms force the offshore and northerly sediment transport, inducing a horizontal shoreline retreat of 10–40 m. In contrast, the southerly sediment transport and beach recovery happen during summer months (fair-weather conditions) with swell and waves approaching from a more northerly direction.

Based on the SDS extracted from the satellite image on 2017-08-22, 8 transects were generated with a spatial resolution of 500 m along the shoreline of Ocean Shores (Figure 4.6). The SDS were obtained from Landsat 5 dataset with the composite averaging window of 180 days. The intersections between the SDS and transects were created to represent shoreline variation at Ocean Shores over 33 years.



Figure 4.6: Transect locations at Ocean Shores.

### The STL decomposition and FFT analysis

The smoothing parameters used for the STL decomposition of shoreline variation at Ocean Shores are listed in Table 4.3. The seasonal-diagnostic plot shown in Figure C.3d approves that  $n_s = 65$  is a reasonable choice, since each line is approximately straight. The result plot of the STL decomposition of shoreline changes at transect 6 is shown in Figure 4.7. It can be observed that the seasonal component accounts much more for the shoreline variation at Ocean Shores than that at Narrabeen (Figure 3.13) (the relative scales of the components are shown with the grey bars to the right of each panel), and the index  $R_{st}$  equals  $60/250 = 0.24 < 0.3$ . The seasonal components of shoreline variation at transect 0 and 6 from 2000 to 2004 are shown in Figure 4.8, which illustrates that shoreline retreated up to 60 m during winter months (November to April) while recovered during summer months (May to October). This observation can be corroborated by the analysis of Ruggiero et al. (2005) that a sub-

stantial seasonal exchange of sediment exists between the beaches and offshore bars at Ocean Shores.

Table 4.3: Parameters for STL decomposition of shoreline movement at Ocean Shores.

Parameter	$n_p$	$n_s$	$n_t$	$n_l$	$n_o$	$n_i$
Values	365	65	573	365	5	1

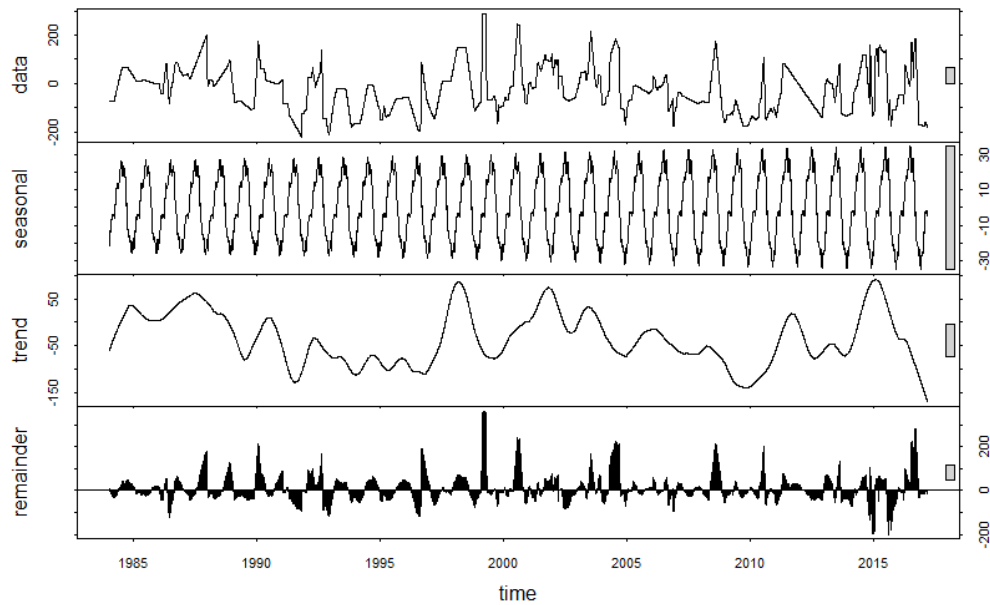


Figure 4.7: The result plot of the STL decomposition of shoreline variation at transect 6, Ocean Shores.

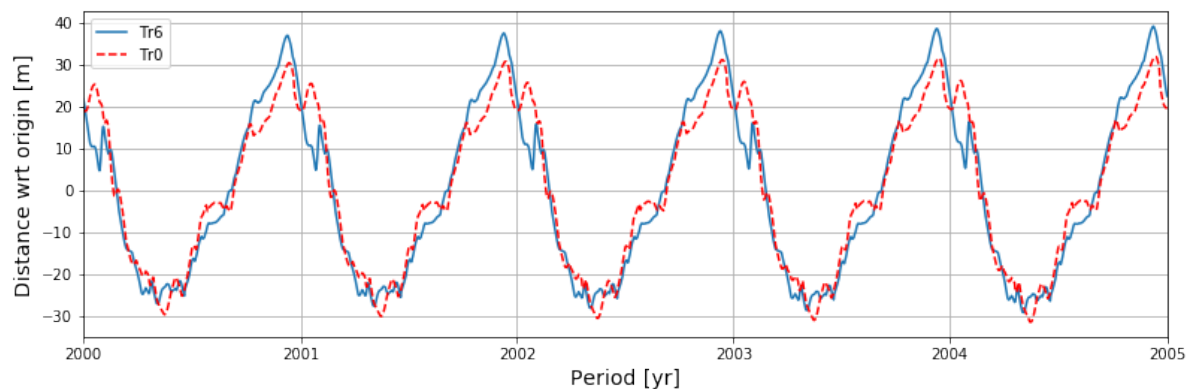


Figure 4.8: The seasonal component of shoreline variation at transect 0 and 6 from 2000 to 2004.

The result plot of the FFT of shoreline changes at transect 6 is shown in Figure 4.9 (the residual component was omitted for removing the influence of storms on frequency analysis). The shoreline variation on the seasonal scale is remarkable, and the index  $\alpha$  equals 0.63 ( $> 0.5$ ), indicating that the Ocean shores can be classified as a **seasonal** beach (Section 3.4.2). Additionally, the shoreline shows a high variability on the decadal scale, and this can probably be explained by the nodal tidal cycle with the periodicity of 18.6 years (Gratiot et al. 2008) and Pacific Decadal Oscillation (PDO) with the periodicity

of a decade (Short & Trembanis 2004). However, as stated in Section 3.6.3, with the limited data available (around 30 years), it is impossible to prove the repeatability of these ultra low frequency oscillations. Several peaks exist on the scale of 2-8 years, which is probably caused by the ENSO effect (periodicity of 2-7 years), and this though will be specified in the later Section 4.3.2.

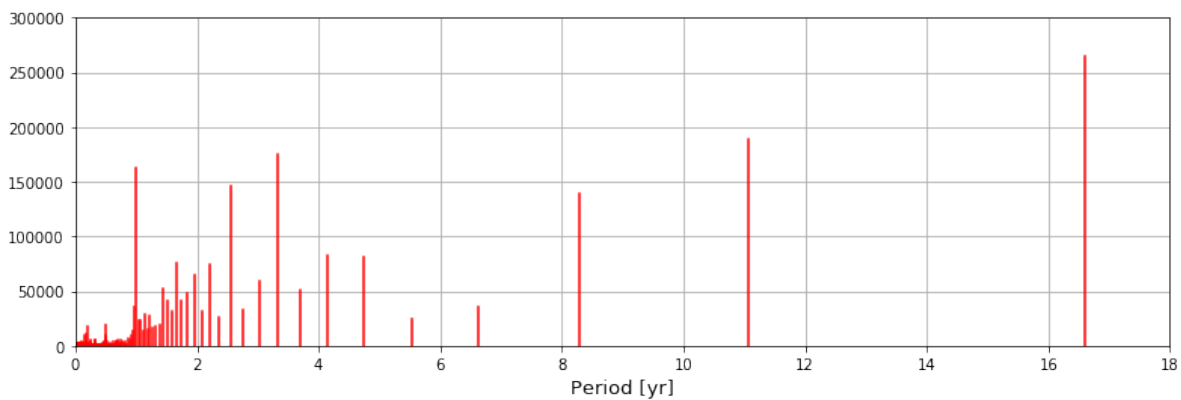


Figure 4.9: The result plot of FFT of shoreline change at transect 6 on Ocean Shores.

The time series of shoreline positions at transect 6 were reconstructed selecting only the components with a frequency of larger than 2 years (Figure C.5d). It can be observed that, however, the reconstructed coastline variation largely deviate from the original extracted SDS, suggesting that the seasonal change greatly accounts for the overall shoreline variation.

#### 4.2.2. Perth

**Background:** Perth is located in Western Australia (Figure A.8). Masselink & Pattiaratchi (2001) measured Perth coastline at weekly or bi-weekly intervals from November 1995 to October 1997 using standard surveying techniques, and found that the shoreline exhibits a distinct seasonality in beach morphology. They stated that the beaches located south of coastal structures or natural headlands/outcrops become wider when northward sediment transport prevails due to sea breeze activity in summer, while these beaches subsequently erode in winter during storms when the littoral drift changes direction. In contrast, beaches located north of obstacles experience shoreline retreat during summer and accretion during winter.

Here we analyzed the SDS at Floreat beach and the north City beach (Figure A.8 and Figure A.9) to test the capabilities of using the SDS on studying the disparate behaviours of shoreline variation on the seasonal scale. Based on the newest available satellite image (2017-12-28), 13 transects were generated perpendicular to the SDS with a spatial resolution of 250 m along the Floreat Beach and the north City Beach (Figure 4.10). The positions of the two groins are illustrated with orange lines. The SDS were obtained from Landsat 5 dataset with the composite averaging window of 180 days. The intersections between the SDS and transects were generated to create time series of shoreline positions over 32 years.

#### The STL decomposition and FFT analysis

The smoothing parameters used for the STL decomposition of shoreline variation at Perth are listed in Table 4.4. The seasonal-diagnostic plot shown in Figure C.3e approves that  $n_s = 45$  is a reasonable choice, since each line is approximately straight. The result plot of the STL decomposition of shoreline variation at transect 3 is shown in Figure 4.11. It can be observed that the range of the seasonal component is similar to that of the trend component ( $R_{st} = 29/46 = 0.63 > 0.3$ ). Thus, the Floreat Beach and the north City Beach can be classified as **seasonal** beaches.



Figure 4.10: Transect locations at the Perth (red) and the positions of groins (orange).

Table 4.4: Parameters for STL decomposition of shoreline variation at Perth.

Parameter	$n_p$	$n_s$	$n_t$	$n_l$	$n_o$	$n_i$
Values	365	45	573	365	5	1

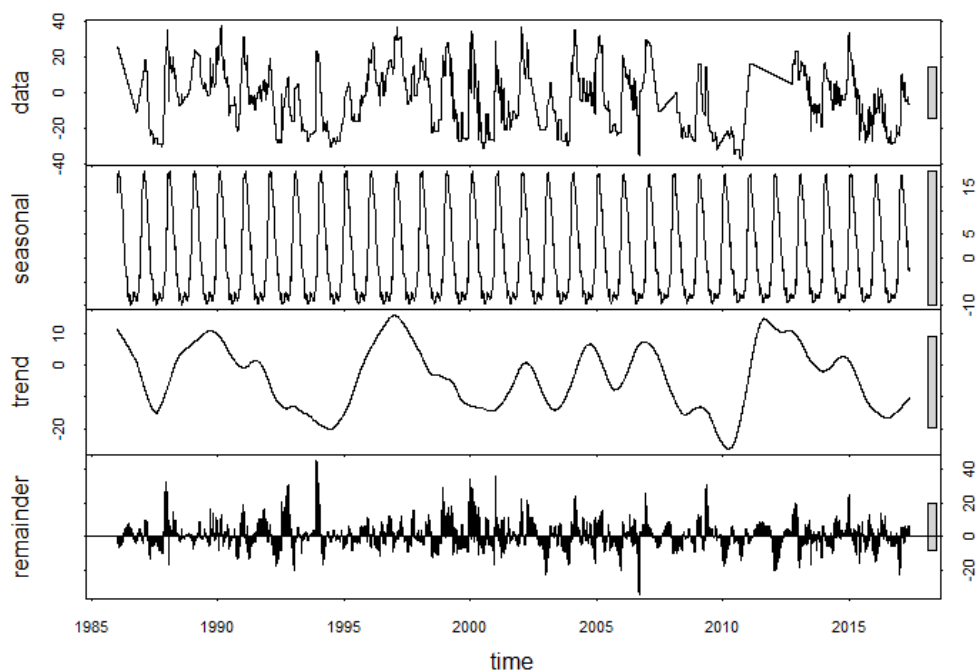


Figure 4.11: The result plot of the STL decomposition at transect 3 on the coast of Perth.

The result plot of the FFT of shoreline variation at the two beaches is shown in Figure 4.12. The noticeable spike at the annual scale suggests that the seasonal variation greatly occupies the overall shoreline changes in the region ( $\alpha = 1$ ), supporting the conclusion that both sites can be classified as

seasonal beaches.

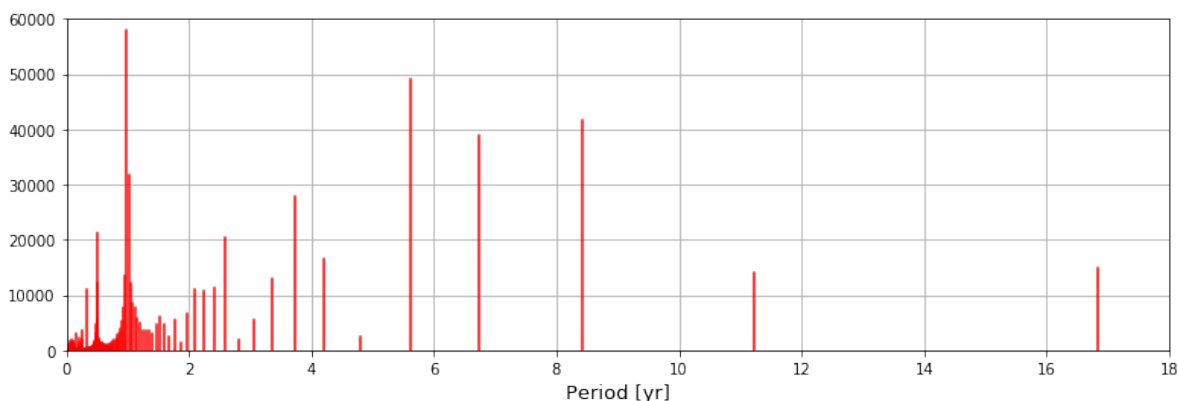


Figure 4.12: The result plot of FFT analysis of shoreline positions at transect 3 on the Floreat beach and the north City beach.

### Seasonal component analysis

The seasonal component of shoreline movement extracted through STL decomposition at transect 3 and 12 from 2005 to 2010 is shown in Figure 4.13. It can be observed that during summer times the beach located south of the groins (transect 12) becomes wider, while the one located north of the groins (transect 3) becomes narrower. The patterns reverse during winter times, which are in line with the analysis of [Masselink & Pattiaratchi \(2001\)](#). The shoreline variation on the seasonal scale can be explained as following: during summer times, the prevalence of northward sediment transport due to sea breeze activity leads to the accumulation of sediment south of the groins, and the shortage of sediment input results in beach erosion north of the groins; during winter times, the southward sediment transport due to storms results in the shoreline accretion north of the groins, and deficit of sediment leads to shoreline retreat south of the groins [Masselink & Pattiaratchi \(2001\)](#). The larger seasonal variation at transect 3 than that at transect 12 is caused by the shorter distance of transect 3 to the groins.

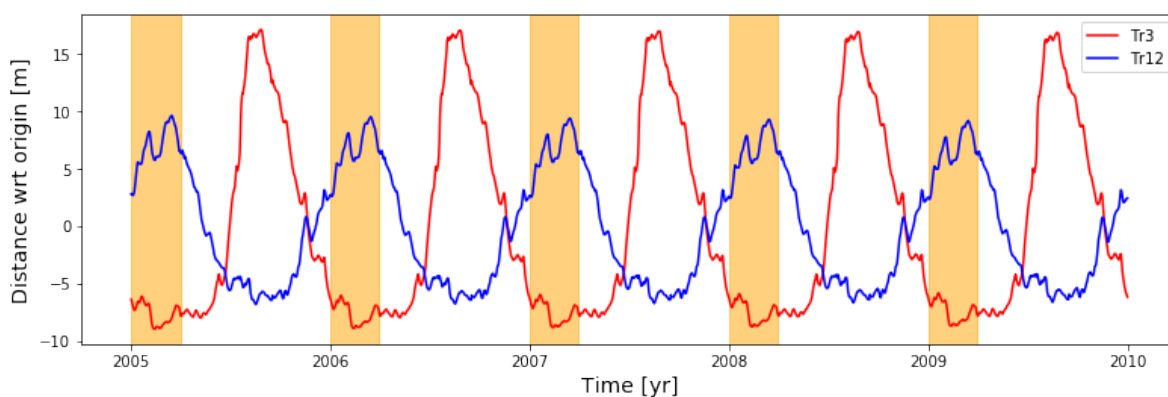


Figure 4.13: The seasonal components of shoreline changes at transect 3 and 12. The orange panels show the time period of January to March (summer in Australia).

The results of PCA of shoreline variation (Section D.3) corroborate the analysis of seasonal component. Figure D.14 illustrates that shoreline changes at transect 7 and 3 exhibit synchronized movement, while the coastline variation at transect 12 is out of phase with respect to transect 7 and transect 3.

#### 4.2.3. Other sites

The STL decomposition and FFT were carried out to the time series of shoreline positions at each site of interest. It turns out that, except for the beaches at Ocean Shores and Perth, shoreline movement at Ocean Beach also shows a high variability on the seasonal scale. The distinct seasonal variability at Ocean Beach derived from the SDS can be supported by the analysis of [Barnard et al. \(2007\)](#), which stated that the sub-aerial beach volume fluctuates seasonally up to 400,000 m<sup>3</sup> in the region. For all the other sites, the seasonal variability of shoreline dynamics is relatively trivial.

#### 4.2.4. Discussion and conclusion

The STL decomposition and FFT analysis were used as main tools for unravelling shoreline dynamics on the seasonal scale. It turns out that the shorelines at Ocean Shores, Perth and Ocean Beach exhibit a distinct seasonal variability, in line with the analysis shown in the related literature. Thus, the SDS is a powerful tool to be employed for studying shoreline variation on the seasonal scale.

### 4.3. Climate variability

Generally, climate variability represents the natural processes which can affect atmosphere (Rob 2017). For example, El Niño/Southern Oscillation (ENSO) near the equatorial Pacific Ocean refers to fluctuations of sea surface temperatures, which alternates every few years between a warming phase (El Niño) and cooling phase (La Niña) with a neutral phase in between (Hoegh-Guldberg O 2017); the North Atlantic Oscillation (NAO) represents anomalous changes in atmospheric pressure at sea level that occur near Iceland and the Azores High (Section 2.2.3). In this section, the capabilities of using the SDS on unravelling shoreline variation on the inter-annual scale governed by climate variability are tested.

#### 4.3.1. Ocean Beach

**Background:** Ocean Beach is a 7-km long north-south trending sandy coastline which stretches south from a rocky headland near the San Francisco Bay entrance (Point Lobos) to the bluffs at Fort Funston (Figure A.10). According to Barnard et al. (2011), 2009/10 was the only winter since 1997/98 in which the wave-energy flux throughout California was approx. 20% above the mean. The increase in extreme waves was coupled with elevated water levels and a more southerly wave approach than the long-term mean, resulting in a greater shoreline retreat than during the 1997/98 winter (the last significant El Niño). El Niño Modoki phenomena (Section 2.2.3) is considered to be principally linked to the great shoreline retreat observed during the 2009/10 winter (Barnard et al. 2011), which resulted in the warm sea surface temperature (SST) anomaly focusing in the central equatorial Pacific.

Based on the newest available satellite image (2017-12-26), 13 transects were generated perpendicular to the SDS with the spatial resolution of 250 m along the coastline of Ocean Beach (Figure 4.14). The SDS were obtained from Sentinel 2 dataset with the composite averaging window set as 180 days. The intersections between the SDS and transects were generated to create time series of shoreline changes over 33 years.



Figure 4.14: Transect locations at Ocean Beach.

#### Shoreline changes, $H_s$ , and MEI

In this section, the relationship between shoreline changes derived from the SDS, the Multivariate ENSO Index (MEI) (Section 2.2.3) and the significant wave height is analyzed at Ocean Beach. The shoreline variation (residual component removed) at Ocean Beach from 1997 to 2016 is shown in Figure 4.15. The ratios of the winter shoreline changes each year to the mean of all winters are listed in Table 4.5, from which the shoreline retreats in the winters of 1997/98, 2009/10 and 2015/16 stand

out. It can be observed that the shoreline retreat was 41%, 69% and 88% greater than the mean value during the 1997/98, 2009/10 and 2015/16 winters, respectively. Moreover, Figure 4.15 illustrates that beach recovery was poor through the fall of 1998, 2002, 2005, 2010 and 2015 with the shoreline located well landward of pre-winter positions. According to Barnard et al. (2011), the poor recovery may cause the beach and adjacent infrastructure highly exposed to subsequent winter storms.

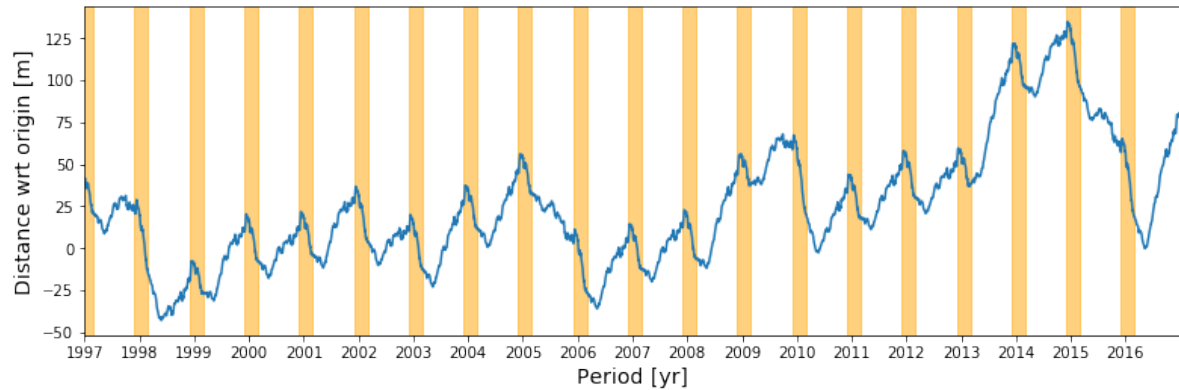


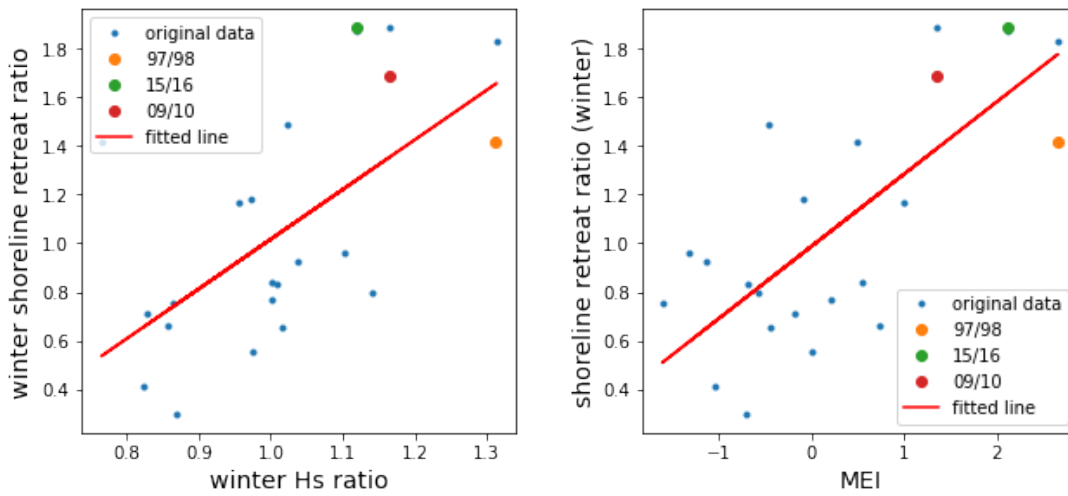
Figure 4.15: Shoreline variation derived from SDS at Ocean Beach (1997-2016, residual component removed). Orange panels represent winter months (December to February).

Table 4.5: Shoreline positions before and after winters (1997- 2016).

Winter	Before winter position (m)	After winter position (m)	Shoreline change (m)	Ratio
96/97	25.35	4.96	20.40	0.90
97/98	8.13	-23.90	32.03	1.41
98/99	-24.26	-38.73	14.47	0.64
99/00	-9.53	-32.54	23.02	1.02
00/01	-15.60	-29.87	14.27	0.63
01/02	15.31	-9.42	24.73	1.09
02/03	-0.06	-24.23	24.17	1.07
03/04	12.40	-5.74	18.14	0.80
04/05	43.63	25.05	18.58	0.82
05/06	-17.69	-47.90	30.20	1.33
06/07	-15.33	-32.99	17.66	0.78
07/08	4.28	-17.97	22.25	0.98
08/09	11.43	-0.79	12.21	0.54
09/10	23.00	-15.18	38.18	1.69
10/11	12.52	-2.35	14.87	0.66
11/12	26.04	6.97	19.07	0.84
12/13	35.90	18.27	17.63	0.78
13/14	63.36	36.67	26.69	1.18
14/15	78.79	57.18	21.61	0.95
15/16	39.99	-2.68	42.67	1.88

The correlation analysis shows that the winter shoreline retreat is significantly correlated to the winter  $H_s$  (Figure 4.16a,  $n = 20$ ,  $R^2 = 0.336$ ,  $p = 0.007$ ) (data of  $H_s$  was obtained from Station 46026 in National Data Buoy Center). Figure 4.17 shows the time series of the MEI and winter  $H_s$  ratio from 1997 to 2016, and the MEI (Section 2.2.3) was obtained from NOAA (<https://www.esrl.noaa.gov/psd/enso/mei/table.html>). The correlation analysis indicates that winter shoreline retreat is highly linked to the MEI (Figure 4.16b,  $n = 20$ ,  $R^2 = 0.488$ ,  $p = 0.000$ ). Therefore, the shoreline variation at Ocean Beach is highly correlated

with the variability of wave energy and El Niño events.



(a) Winter shoreline retreat ratio - winter Hs ratio      (b) Shoreline retreat ratio - MEI

Figure 4.16: (a) Winter shoreline retreat normalized by the mean value versus winter Hs normalized by the mean (the trend line  $y = 2.04x - 1.03$ ). (b) Winter shoreline retreat normalized by the winter mean versus MEI (the trend line  $y = 0.297x + 0.986$ ).

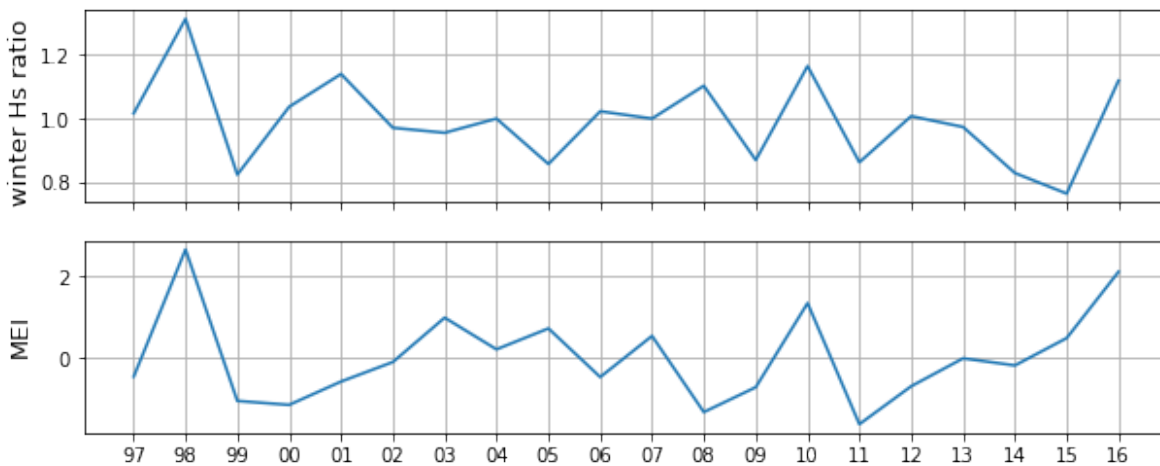


Figure 4.17: Time series of winter  $H_s$  normalized by winter mean (upper panel) and the MEI index (lower panel).

### 4.3.2. CRLC (Ocean Shores)

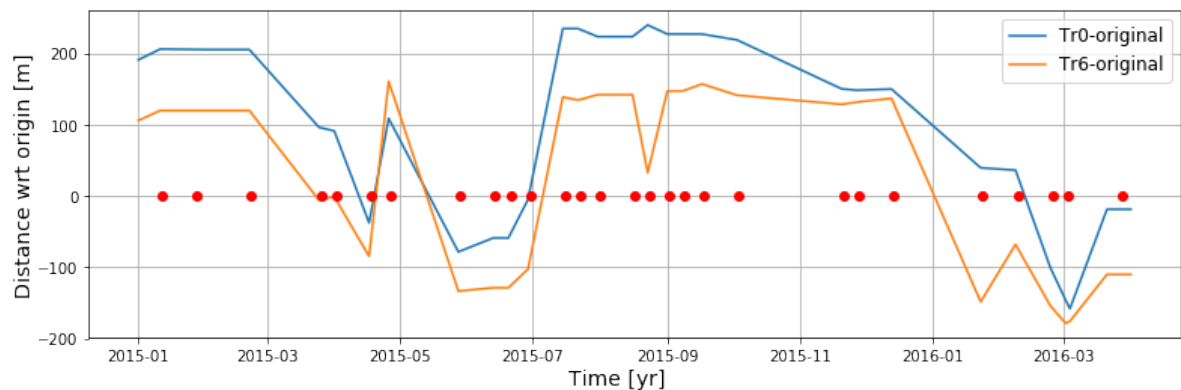
**Background:** Ruggiero et al. (2005) used the measured bathymetric and topographic profiles to capture the beach response at Ocean Shores during the major El Niño of 1997/98. They showed that the coast responded by transporting more sediment to the northern ends of sub-cells, as waves approached from a slightly more southerly direction.

In this section, the SDS at Ocean Shores are analyzed to test the capabilities of using the SDS on studying shoreline responses under the influence of El Niño events. The SDS were extracted with the same parameters set in Section 4.3.1, and the transect positions are shown in Figure 4.14.

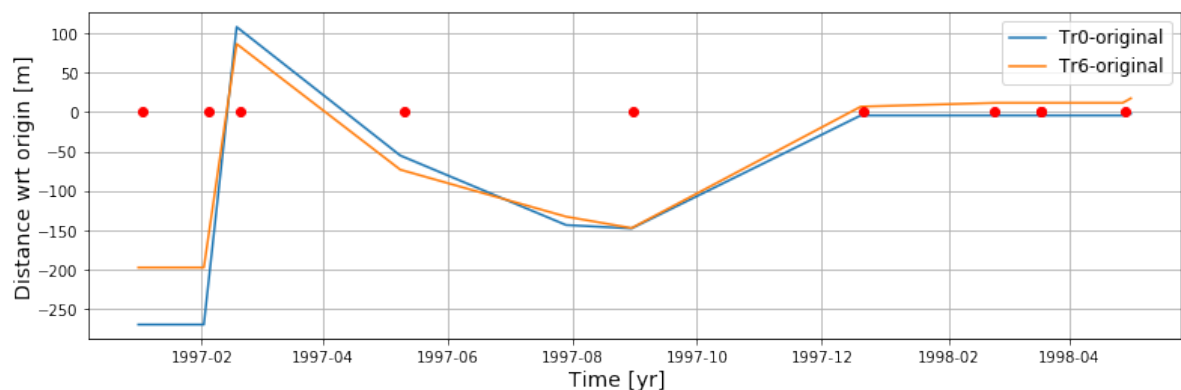
### Time series analysis

The influence of major El Niño events during 2015/16 and 1997/98 on shoreline changes at Ocean Shores is the main focus of this section. The time series of shoreline positions at transect 0 and transect 6 (Figure 4.6) in 2015/16 and 1997/98 is shown in Figure 4.18, and the red dots represent the time when the satellite images were taken. According to the analysis of Gelfenbaum & Kaminsky (2010), the erosion rate at the southern end was higher than that at the northern end during the El Niño event. The same pattern can be observed through the SDS (Figure 4.18a) during the strong El Niño in 2015/16, showing that the rate of shoreline retreat was faster at transect 6 than that at transect 0. Moreover, it can be observed that the shoreline retreated at transect 6 while accreted at transect 0 from 2015-08 to 2015-09, indicating that the eroded sediment from southern part may be transported to the northern part of the Ocean Shores. Thus, the SDS are capable of capturing the pattern that shoreline erosion rate was higher at southern end than at northern end of Ocean Shores during the El Niño event in 2015/16.

However, the similar pattern cannot be observed during the strong El Niño in 1997/98 through the SDS (Figure 4.18b). The erosion rates were almost the same at the southern and northern transects. This might be caused by the fact that the number of available satellite images from 1997 to 1998 is limited, and the shortage of satellite images impairs the ability of the SDS to unravel the feature of shoreline movement. Therefore, although the SDS can capture the shoreline variation under the impact of El Niño in 1997/98, it failed to extract the response that shoreline eroded at a higher rate along the southern end.



(a) During the 2015/16 El Niño.



(b) During the 1997/98 El Niño.

Figure 4.18: Time series of shoreline positions at transect 0 (north) and transect 6 (south) at Ocean Shores from 2015 to 2016 (17 months) and from 1997 to 1998 (17 months). The red dots illustrate the time when the satellite images were taken.

#### 4.3.3. Other sites

FFT analysis was conducted on shoreline variation at each site of interests. It turns out that the shoreline changes at Narrabeen, Moruya and Pedro also show a high variability on the inter-annual scale (Figure 3.14, Figure 3.23a and Figure 3.23b). The correlation analysis of shoreline movement and the climate index (e.g. SOI and MEI) shows that the coastline dynamics at these three beaches are highly correlated to the ENSO events (Figure 3.17 and Figure 3.18). The shoreline changes at all the other sites do not exhibit a high variability on the inter-annual scale caused by climate variability.

#### 4.3.4. Discussion and conclusion

The FFT analysis and correlation analysis (regression analysis) were used as main tools for unravelling inter-annual shoreline dynamics with the SDS. The results show that the shoreline changes at Narrabeen, Moruya, Pedro, Ocean Beach and Ocean Shores show a high variability on the inter-annual scale governed by the ENSO events. Moreover, almost all the analysis results above can be corroborated by the relative literature, as long as the number of satellite images is sufficient. Therefore, the SDS could be use as a powerful tool to study shoreline variation on the inter-annual scale governed by climate variability.

## 4.4. Land subsidence

Land subsidence is one of the major processes that influence the stability of the coastline. It is a global problem due to the loss of surface elevation via removal of subsurface support (of the Interior 2017), which can result in the increasing rate of coastal erosion, incursion of saline groundwater and reduction in wetland area (Stanley & Warne 1998). Anthropogenic influence is the main driver for land subsidence, such as withdrawal of fluids (groundwater, petroleum, geothermal) and subterranean mining (of the Interior 2017). In this section, the capabilities of using the SDS on unravelling shoreline variation on the decadal scale caused by land subsidence are tested.

### 4.4.1. Nile Delta (Rosetta mouth)

**Background:** The Nile delta is situated in northern Egypt (Figure A.7), where the river Nile reaches the Mediterranean Sea. Ali & El-Magd (2016) identified the dominant land use/cover classes with satellite images from 1990 to 2014 and used GIS techniques to spatially analyze and quantify the rate of changes along the Nile delta coast. They concluded that the general trend of the Nile Delta showed smoothing of the coastline, as the west-east current moves eroded sediments to be accreted in other places. Furthermore, they found that the highest rate of coastal shoreline retreat was at the mouth of the Rosetta and Damietta branches, with a high average annual retreat rate at both sites of 25 m/year and 36 m/year, respectively.

In this section, the SDS at the coast of Rosetta mouth in the Nile Delta (Figure A.7) are analyzed to test the capabilities of using the SDS on studying shoreline changes governed by the land subsidence. Based on the newest available satellite image (2017-12-28), 7 transects were created perpendicular to the SDS with the spatial resolution of 500 m along the coast of Rosetta mouth (Figure 4.19). The SDS were obtained from Landsat 5 dataset with the composite averaging window set as 180 days. The intersections between the SDS and transects were generated to create time series of shoreline variation over 33 years.



Figure 4.19: Transect locations at the Rosetta mouth.

### Trend component analysis

The trend component of the ensemble averaged shoreline variation extracted through STL decomposition is shown in Figure 4.20. Linear regression was carried out on three segments of the trend. It can be observed that the shoreline was relatively stable from 1984 to 2000. The erosional process started around 2000 with the rate of 11.5 m/yr, and then accelerated greatly up to 34.1 m/yr after 2014. Over the three decades, the average annual rate of shoreline retreat was 6.25 m/yr, which is less significant

than the rate analyzed by Ali & El-Magd (2016) (25m/yr).

The main factors inducing the large rate of shoreline retreat at the Rosetta mouth include the land subsidence and the shortage of sediment supply from the river (Ali & El-Magd 2016). The extraction of hydrocarbon and ground water has caused the delta surface artificially lowered to around 1 m or more (Stanley & Clemente 2017). The High Aswan Dam constructed in 1965 has greatly reduced the total amount of water flowing below the Dam and to the delta. As a result, a large fraction of Nile sediment that once accounted for around 100 million tons deposited below Aswan is now trapped in the southern part of the reservoir, largely reducing the sediment supply to the delta area (Stanley & Clemente 2017). Thus, this case shows that the SDS can reveal fingerprints of human interventions on the coastal dynamics on the decadal scale.

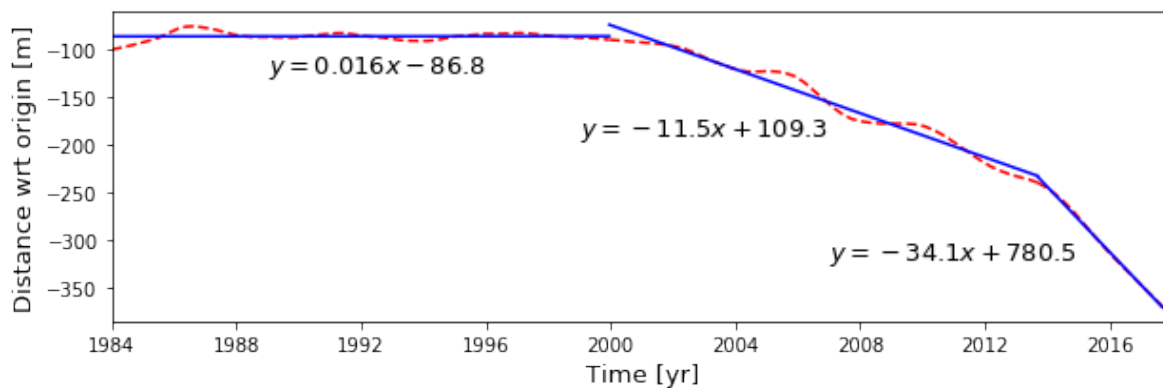


Figure 4.20: The trend component of shoreline change at Rosetta mouth (the red dot line) with the lines of linear fit (blue segments).

#### 4.4.2. Other sites

The trend component analysis was conducted on shoreline variation at all the other sites of interests. However, there are no more sites showing a large rate of shoreline retreat induced by land subsidence.

#### 4.4.3. Discussion and conclusion

The trend component analysis suggests that the shoreline erosion at the mouth of Rosetta, the Nile Delta started in around 2000 (Figure 4.20). During the years of 2000-2014, the average rate of shoreline retreat was around 11.5 m/yr, and the rate increased to 34.1 m/yr after 2014. According to Ali & El-Magd (2016), the spatial modeling of the shoreline from 1990 to 2014 with GIS techniques showed that the rate of the shoreline erosion was around 25 m/yr at the mouth of Rossetta branch, which is more significant than the retreat rate derived from the SDS (6.25 m/yr) during the same period of time. The disparate rates are probably caused by the different selections of study sites: Ali & El-Magd (2016) analyzed a larger area including both sides of the Rosetta mouth, while we only focused on the west part of the mouth. Thus, this case shows that the SDS can clearly reveal the influence of land subsidence and shortage of sediment input on the coastline dynamics on the decadal scale.

## 4.5. Sea level rise

Sea level rise (SLR) has long been assumed as the primary cause for the observed chronic shoreline erosion (Vellinga & Leatherman 1989). According to Nicholls & Cazenave (2010), SLR will almost certainly accelerate through the 21st century and beyond due to global warming. In this section, the capabilities of using the SDS for unravelling the shoreline variation induced by SLR are tested. Since the influence of SLR on open coasts can only be captured on long timescales (greater than 50 years) (Le Cozannet et al. 2016), the influence of the sea-level-rise driven basin infilling will be analyzed instead, considering the limited availability of the SDS (i.e. 34 years for now).

### 4.5.1. Gatseau sandspit and Cap Ferret sandspit (SW France)

**Background:** Gatseau and Cap Ferret are two sandspits located in SW France closed to the Maumusson and Arcachon tidal inlets, respectively (Figure A.13). Castelle et al. (2018) used 15 series of aerial photographs from 1950 to 2014 to study the long-term shoreline changes along approximately 270 km of high-energy sandy coast in SW France. They found that Gatseau sandspit and Cap Ferret sandspit show a quasi-synchronous behaviour that a slow accretion from the 1950s to the mid-1970s (approx. +4 m/year) reversed to a dramatic erosion trend on the order of 10 m/year in the recent decades. They stated that other than SLR, drivers such as sediment deficit mainly control the chronic erosion in the region.

In this section, the SDS at Gatseau sandspit and Cap Ferret sandspit are analyzed to test the capabilities of using the SDS on studying shoreline variation on the long-term scale governed by SLR. Based on the latest available satellite image (2017-12-19), 7 and 10 transects were generated perpendicular to the SDS with the spatial resolution of 500 m along the Gatseau sandspit and Cap Ferret sandspit, respectively (Figure 4.21). The SDS for Gatseau sandspit and Cap Ferret sandspit were obtained from Landsat 5 and Sentinel 2 dataset, respectively, with the composite averaging window of 180 days. The intersections between the SDS and transects were generated to create time series of shoreline changes over 33 years.

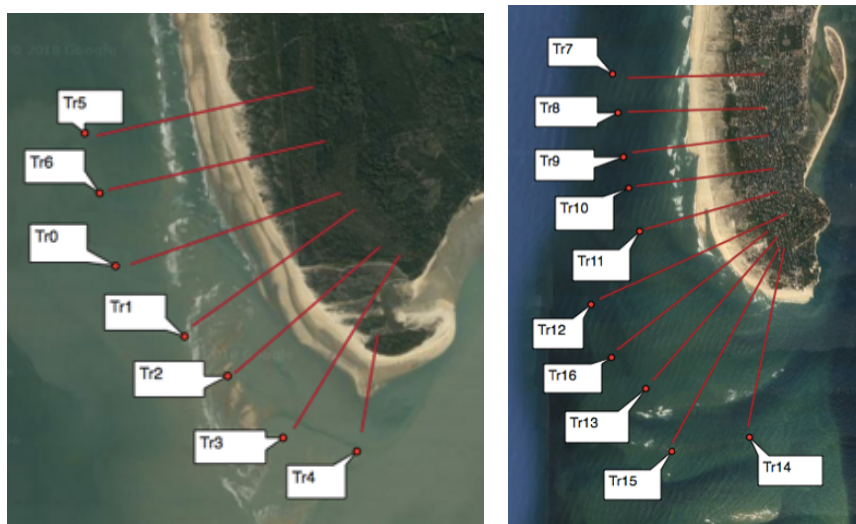


Figure 4.21: Transect locations at Gatseau sandspit (left) and Cap Ferret sandspit (right).

### Trend component analysis and SLR

The trend components of shoreline variation decomposed through STL method at Gatseau sandspit and Cap Ferret sandspit are analyzed in this section. Large and widespread erosion can be observed at both sites (Figure 4.22). The shoreline change at Cap Ferret sandspit exhibited a larger spatial variability compared with that at Gatseau sandspit (Figure 4.22 and Figure C.10). For Gatseau sandspit, the most erosive sector is located in the south of the study area (approx. 1km north of the tip) with a

high erosion rate exceeding 23 m/yr over the last three decades. For Cap Ferret sandspit, the hot spot of erosion is located near the tip of the sandspit with a retreat rate around 17 m/yr, and the erosion rates dramatically decrease to the north part of the coast (the shoreline located 4.5 km away of the tip exhibited a relatively stable pattern over the last three decades).

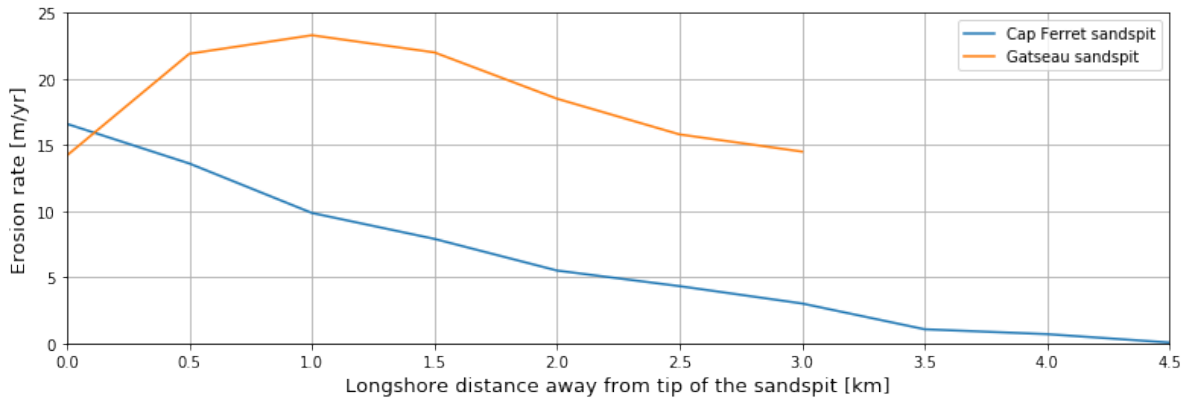


Figure 4.22: The average coastline erosion rates at two sandspits over the last 3 decades.

The trend components of ensemble averaged shoreline changes at the two sites are shown in Figure 4.23. It can be observed that the shoreline retreat rates at the tips were similar (i.e. 18.6 and 15.1 m/yr) over the three decades, in line with the analysis of [Castelle et al. \(2018\)](#).

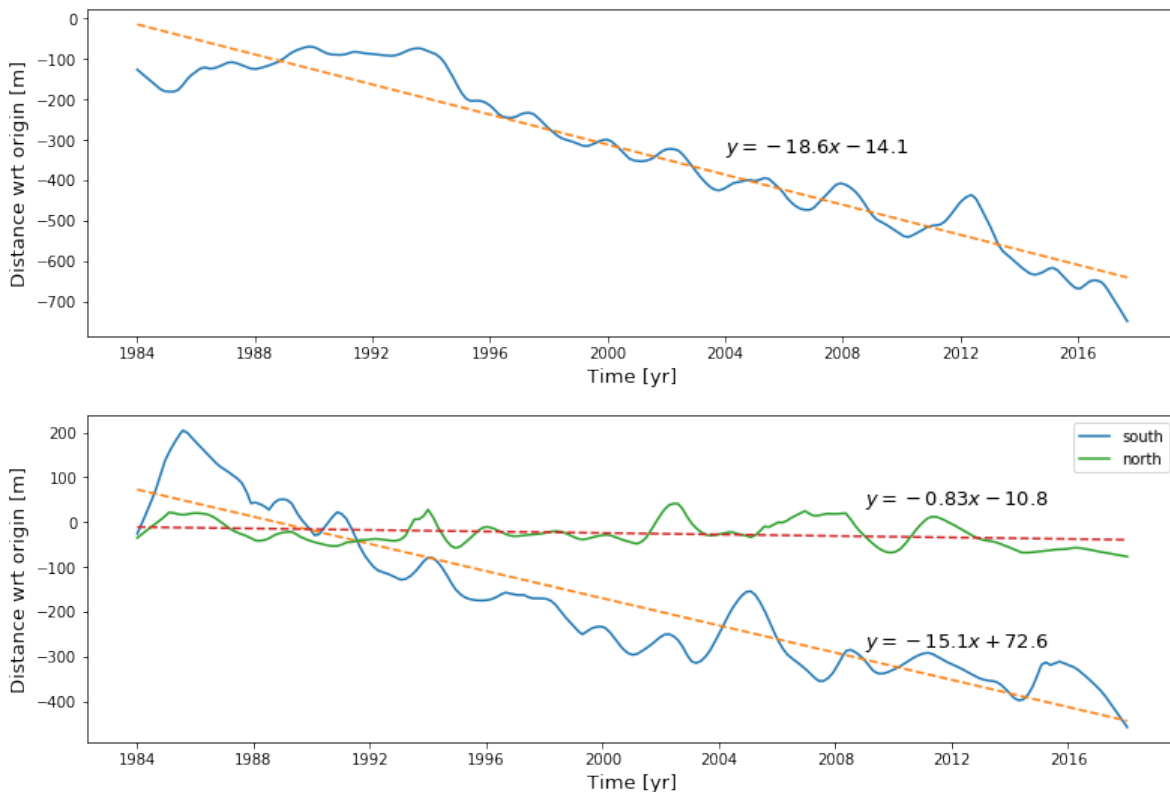


Figure 4.23: Trend components of ensemble averaged shoreline movement at Gatseau sandspit (upper) and Cap Ferret sandspit (lower). Dashed lines represent the least-squares best fits. The shoreline variation in the south part of the Cap Ferret sandspit (near the tip) were spatially averaged at transect 13, 14 and 15; the variation in the north part were averaged at transect 7-12, and 16.

Sea level rise has long been assumed as the primary driver for the observed long-term shoreline erosion (Vellinga & Leatherman 1989). The coastline retreat induced by SLR can be estimated through the Bruun rule (Retreat = RSLR (L/d)), which assumes that the nearshore profile translates upward and landward to adjust to sea level rise (Bruun 1962). Although Bruun rule showed the poor agreement with observations in many locations worldwide, it may provide a fair indication of the isolated impact of SLR. According to Zhang et al. (2004), L/d is of the order 50 to 150. The RSLR rate is about 2.60 mm/yr at SW France, which was obtained from PSMML (2018) (1247, Port Tudy, Figure A.14). Thus, Bruun effect gives a sea-level-rise-driven erosion an order of magnitude smaller than the value derived from the SDS over the last three decades. Other potential drivers inducing the large shoreline retreat at the two sandspits are specified below.

Except for the Bruun effect, the sea-level-rise driven basin infilling also influences the shoreline changes adjacent to tidal inlets (Ranasinghe et al. 2013). Thus, increased erosion can be expected on the shorelines adjacent to the Maumusson and Arcachon inlets (i.e. Gatseau sandspit and Cap Ferret sandspit, Figure A.13), although unlikely up to an order of magnitude (Castelle et al. 2018). According to Rosati (2005), the long-term shoreline changes are mostly governed by large-scale coastal sediment budget, such as variation in river sediment supply and SLR. Therefore, other than the influence of sea-level-rise driven basin infilling, the shortage of sediment input from the inner shelf might be another plausible reason.

#### 4.5.2. Other sites

It highly possible that SLR also influences the shoreline variation at other sites of interests. However, we do not focus on the shoreline responses to SLR on the open coasts, since the shoreline changes induced by SLR are relatively trivial over three decades, especially for the coasts with the steep slope.

#### 4.5.3. Discussion and conclusion

The shoreline variation induced by SLR was analyzed with the SDS in this section. We focused on the coastlines at Gatseau sandspit and Cap Ferret sandspit in SW France. It is good to know that the erosion rates derived from the SDS are mostly in line with the analysis of Castelle et al. (2018). Since Bruun effect gives a sea-level-rise-driven erosion an order of magnitude smaller than the value derived from the SDS, other drives are considered as the main factors for shoreline retreat at the two sandspits, including the sea-level-rise driven basin infilling and the deficit of sediment input.

To sum up, the coverage of satellite mission on temporal scale limits the capabilities of using the SDS for studying shoreline variation caused by SLR. However, longer-recorded SDS can be expected as the time goes by. Therefore, it is highly possible that the SDS will become a more powerful tool to be employed for studying the long-term shoreline variation governed by SLR in the future.

## 4.6. Anthropogenic processes

In this section, the shoreline changes governed by anthropogenic processes are studied with the SDS. We focused on the shoreline dynamics influenced by beach nourishment projects at Wrightsville. The capabilities of using the SDS to unravel the spatial variation along the shorelines governed by human influences are tested here.

### 4.6.1. Wrightsville Beach

**Background:** Wrightsville Beach is an 8-km barrier island system located on the southern North Carolina coast (Figure A.17). It lies south of Figure Eight Island, separated by Mason Inlet, and north of Masonboro Island, separated by Masonboro Inlet. Gares et al. (2006) used the LIDAR data to identify the responses of beach and dune to a beach nourishment project at Wrightsville Beach in 1998. They found that about two thirds of the initial fill sediment were removed from the subaerial part of the beach in the first year. They also stated that the three hurricanes happened in 1998 and 1999 caused a severe erosion in the region, which may help to remove the nourished sediment to the adjacent shoreline.

Based on the latest available satellite image (2018-04-28), 59 transects were generated perpendicular to the SDS with the spatial resolution of 125 m along the Wrightsville Beach (Figure 4.24). The SDS were obtained from Sentinel 2 dataset with the composite averaging window set as 180 days. The intersections between the SDS and transects were generated over 34 years to create time series of shoreline variation.



Figure 4.24: Transect positions at Wrightsville Beach.

#### Spatially differentiated shoreline variation

In 1998, a beach-fill project was carried out at Wrightsville Beach, North Carolina. We focused on shoreline responses in the following years after the beach nourishment project through the SDS. The coastline is divided into several intervals representing the locations of nourished, transition and non-nourished zones (Figure 4.25), the divisions of which were adjusted according to Gares et al. (2006).

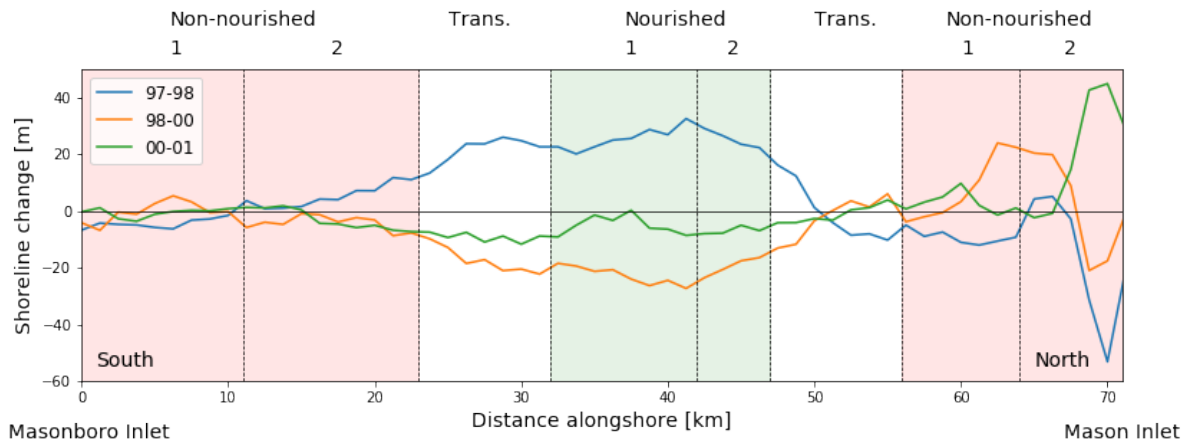


Figure 4.25: Shoreline changes at Wrightsville Beach from 1997 to 2001.

It can be observed that the shoreline moved seaward in the nourished zone in 1997-1998. Less beach accretion happened within the south transition zone and part of the north transition zone near the main nourishment area. At the northern end of the island, there was as much as 53 m of erosion south of the Mason Inlet (within the north non-nourished 2 zone), and the erosion was less intensive further south of the inlet (within the north non-nourished 1 zone) with the retreat about 10 m. At the south end of the island, the coastline change was less spatially differentiated: the shoreline retreated about 5 m within the south non-nourished 1 zone, whereas accreted up 15 m in the south non-nourished 2 zone.

Almost all of the materials placed on the beach were removed in 1998-2000. In the central part of the island (the nourished zone), the shoreline retreated about 15-25 m during the two years. The shoreline within the south transition zone showed less significantly erosion, retreating about 9-20 m, and the shoreline of the south non-nourished zone changed between -5 to 5 m. In the area north of the nourished zone, the shoreline changes were more spatially variable. Large accretion occurred in most part of the north non-nourished area, while severe erosion can be observed at the shoreline adjacent to the Mason Inlet. For the north transition zone, the shoreline closed to the main nourished area retreated up to 15 m during the two years, while meanwhile the shoreline accreted in the north part of that region.

Most part of the coastline showed few changes in 1999-2000. Shoreline remained stable in the south non-nourished 1 zone during this time period, but eroded up to 8 m in the south non-nourished 2 zone. For the nourished and the south transition zone, shoreline retreated up to 10 m. Considerable accretion can be observed at the northern end, reaching up to 40 m south of the Mason Inlet.

#### 4.6.2. Discussion and conclusion

The spatially differentiated shoreline variation was unravelled with the SDS in this section. We focused on the shoreline dynamics governed by nourishment projects at Wright Beach. It is good to know that most of analysis results derived based on the SDS are in line with the analysis of Gares et al. (2006). Therefore, the SDS could be used as an indicator to study the spatial variability of shoreline changes governed by the beach nourishment projects.

# 5

## Discussion

### 5.1. Sensitivity analysis

In this section, we performed a sensitivity analysis to demonstrate the influence of changing the image composite window on unravelling shoreline dynamics with the SDS. The principle of the image composite technique is to use a sequence of satellite images to create a single composite image (Section 2.1.2). Longer averaging windows have the tendency towards generating a higher accuracy of the SDS (lower average offset values), but the information on shoreline variability within the time sequence is lost in the process (Hagenaars et al. 2018). In order to identify the influence of moving average time windows on unravelling shoreline dynamics, the shoreline changes at the beaches of Perth (Figure 5.1) are analyzed as an example using a moving average time sequence window of 30, 90, 180 and 360 days for generating the SDS. The time series of shoreline positions and analysis results of shoreline movement through PCA, STL decomposition and FFT methods were compared with different lengths of moving average time windows.



Figure 5.1: Transects position at the Perth beach (red) and the position of two groins (orange).

The original time series of shoreline positions at transect 3 created with different composite windows are shown in Figure B.1. It can be observed that the range of shoreline movement decreases with increasing length of the composite window ( $d_t$ ). Seasonal variation could be distinguished from the original time series when  $d_t$  equals 30, 90 and 180 days. However, no seasonal pattern is shown in the SDS generated with  $d_t = 360$ , because the shoreline changes on the seasonal scale are averaged

out with the long averaging window.

The results of the PCA of shoreline variation generated with the four averaging windows are shown in Figure B.2. When  $d_t$  equals 30, 90 and 180 days, the changes of the length of averaging windows do not lead to large variation of the characteristics of modes and the percentage of shoreline movement correspondingly explained by them. When the length of the averaging window increases to 360 days, however, the SDS cannot show the pattern that shoreline variation at transect 12 is out of phase with respect to that at transect 7 and 3.

The smoothing parameters used for the STL decomposition are listed in Table 4.4, and the result plots are shown in Figure B.3. The range of extracted trend components increases when the length of the averaging window goes up, while the range of seasonal components decreases in the meanwhile. The index  $R_{st}$  equals  $50/35 = 1.43$ ,  $40/40 = 1$ ,  $29/46 = 0.63$  and  $7/60 = 0.117$  when  $d_t$  equals 30, 90, 180 and 360, respectively. The result plots of FFT are shown in Figure B.4. The index  $\beta$  equals 1 when  $d_t$  equals 30, 90 and 180, while  $\beta$  equals 0.073 when  $d_t$  equals 360. Thus, the beaches at Perth can be classified as seasonal beaches with  $d_t = 30, 90$  or 180, while they are sorted as non-seasonal ones when  $d_t$  equals 360.

The seasonal components of shoreline changes at transect 3 and 12 extracted by STL decomposition are shown in Figure B.5. The reversed phases of seasonal variation at the two transects can be observed when  $d_t$  equals 30, 90 and 180. The factors induce the reversed shoreline dynamics at the two transects on the seasonal scale was discussed in Section 4.2.2.

To sum up, for the coastline movement at Perth, the shoreline variation on the seasonal scale can be clearly extracted through the SDS composited with the short length of averaging window ( $d_t = 30, 90$  or 180), and meanwhile the spatial pattern of shoreline changes can also be detected. However, when the satellite images are composited annually ( $d_t = 360$ ), the SDS fail to detect seasonal and spatial variation in the region. Therefore, the longer averaging window reduces the capabilities of using the SDS to detect the shoreline variation on short-term scales, which is less suitable to be used for unravelling the intra-annual coastline dynamics governed by seasonal forcing or storms.

## 5.2. Summary of analysis results

Figure 3.1 provides an overview of the beach classification of the eleven coasts, which also summarizes the capabilities of using the SDS on unravelling shoreline variation governed by different forcing types. The result plots of the PCA, STL decomposition and FFT of shoreline variation used for calculating the index  $\beta$ ,  $R_{st}$  and  $\alpha$  are shown in Appendix C.

The limitations of using the SDS on studying coastline dynamics are mainly caused by the inadequate or even unavailable satellite images when events happen. On the short-term scale, the low frequency of satellite image acquisition and the image composite technique reduce the accuracy of the SDS to be used for studying shoreline variation governed by storms. On the long-term scale, as the SDS are only obtainable after March 1984, the shoreline changes governed by SLR may need to be investigated with the combination of other types of dataset, such as historical maps or topographic surveys. The SDS show a better performance to be used for unravelling shoreline variation on the medium-term scales governed by seasonal forcing, climate variability (e.g. ENSO and PDO) or land subsidence. In these cases, the missing images do not greatly impair the ability of the SDS to unravel the characteristics of shoreline variation, and the detected shoreline positions over three decades are relatively sufficient to be used for studying shoreline responses to these forcing types.

Case	Beach classification		Capabilities of using the SDS to unravel shoreline variation						Remarks
	Seasonal	Rotational	Storm	Seasonal forcing	Climate variability	Subsidence	SLR	Human modification	
Fire Island	No	No	Weak	-	-	-	-	High	Focus: Halloween Storm, Nor'Ida, Hurricane Irene, Hurricane Sandy and the large-scale replenishment project in 2009. The SDS failed to unravel shoreline changes caused by storms due to low frequency of satellite images and image composite technique.
Perranporth	No	No	Weak	-	-	-	-	-	Focus: Extreme storm events in 1989/90, 1993/94, 1994/95, 2006/07 and 2013/14. As no images were taken during 1991-1997, only storms in 2006/07 and 2013/14 were analyzed.
Valencia	No	No	Moderate	-	-	-	-	-	Focus: the six storms between 2001-11 and 2002-05.
Perth	Yes	No	-	High	-	-	-	High	Focus: the reversed phase of shoreline changes on the seasonal scale caused by the seasonal wave climate and the influence of groins.
Ocean shore	Yes	No	-	High	Moderate	-	-	-	Focus: El Niño events during 2015/16 and 1997/98. The SDS are able to capture the variation pattern that shoreline erosion rate was higher at south than that at north during the El Niño of 2015/16. However, they failed to extract this feature during the El Niño of 1997/98 due to the small number of obtainable satellite images.
Narrabeen	No	Yes	-	-	High	-	-	-	Focus: El Niño event in 1997/98 and beach rotational feature.
Ocean Beach	Yes	Yes	-	-	High	-	-	-	Focus: El Niño events in 1997/98, 2009/10 and 2015/16.
Nile	No	No	-	-	-	High	-	-	Focus: the high rate of shoreline retreat at the coast of Rosetta mouth due to land subsidence caused by groundwater extraction and deficit of sediment input caused by river damming.
SW France	No	No	-	-	-	-	Moderate	-	Focus: SLR and SLR driven basin infilling effects on coastline change. The influence of SLR on open coasts can only be captured on long (greater than 50 years) timescales, while the SDS are only available over 30 years for now.
Wrightsville	Yes	Yes	-	-	-	-	-	High	Focus: Beach nourishment project in 1998.
Moruya, Pedro	No	Yes	-	-	-	-	-	-	Focus: synchronous oscillation and rotation of the three beaches located in Southeast Australia.

Figure 5.2: Summary of analysis results.



# 6

## Conclusions and recommendations

### 6.1. Conclusions

Coastal zones all over the world have become heavily populated and developed due to the aesthetic value and diverse ecosystem services that they provide (Luijendijk et al. 2018). In recent years, however, climate change and anthropogenic pressures have exacerbated unprecedented coastal recession, threatening billions of dollars' worth of coastal developments and infrastructure (Ranasinghe et al. 2012). In order to counteract the erosion trend and protect shoreline positions, it is necessary to carry out reliable assessments of shoreline dynamics to monitor the erosion process. Therefore, the present study aims to explain different spatial and temporal patterns of sandy shoreline evolution.

The satellite derived shorelines (SDS) can be analyzed to get a first understanding of the coastline evolution in the period of 1984 – present (Hagenaars et al. 2017). However, the application range of using the SDS to extract behavioural patterns of sandy shoreline variation is still unknown. In the present study, we generated the SDS as derived by Hagenaars et al. (2017), involving the automated sub-pixel extraction of shoreline with an accuracy of 10-30 m (depending on the satellite mission). We focused on the shoreline changes governed by different forcing types, including storms, seasonal forcing, climate variability, land subsidence, SLR and anthropogenic processes. We decomposed the time series of shoreline positions with a range of data analysis methods, which extract spatiotemporal patterns of shoreline variation and correlate the variation patterns to forcing types. We assessed the application range of using the SDS for coastline studies by comparing the spatiotemporal patterns of shoreline variation derived from the SDS with the conclusions listed in the related literature.

The shoreline changes at the eleven knowledge-intensive sites were focused on, each of which was selected based on the available documentation to verify if the influence of a specific forcing type could be unravelled through the SDS. The selected sites include Narrabeen, Moruya and Pedro, Perranporth, Ocean Shores (CRLC), the Nile Delta, Perth, Ocean Beach, Fire Island, Gatseau sandspit and Cap Ferret sandspit (SW France), the Gulf of Valencia and Wrightsville Beach. It should be noted that the shoreline dynamics at one site is probably governed by different forcing types, but we only focused on the influence of one or two representative forces for each site of interest.

The process framework shown in Figure 6.1 can be applied to almost any sandy beach worldwide for extracting shoreline change patterns. A seasonal-trend decomposition procedure based on Loess (STL decomposition) was employed to decompose shoreline variation into trend, seasonal, and remainder components on the basis of locally weighted regression (Loess). Fast Fourier transform (FFT) and wavelet analysis were used to convert a signal from the time domain to frequency space. Principal component analysis (PCA) was applied to extract the dominant modes of variability contained in a data set. Correlation analysis was used to measure the strength of association between coastline changes and forcing types. Three indices ( $\beta$ ,  $R_{st}$  and  $\alpha$ ) were then calculated to classify rotational/non-rotational and seasonal/non-seasonal beaches based on the analysis results of the SDS.

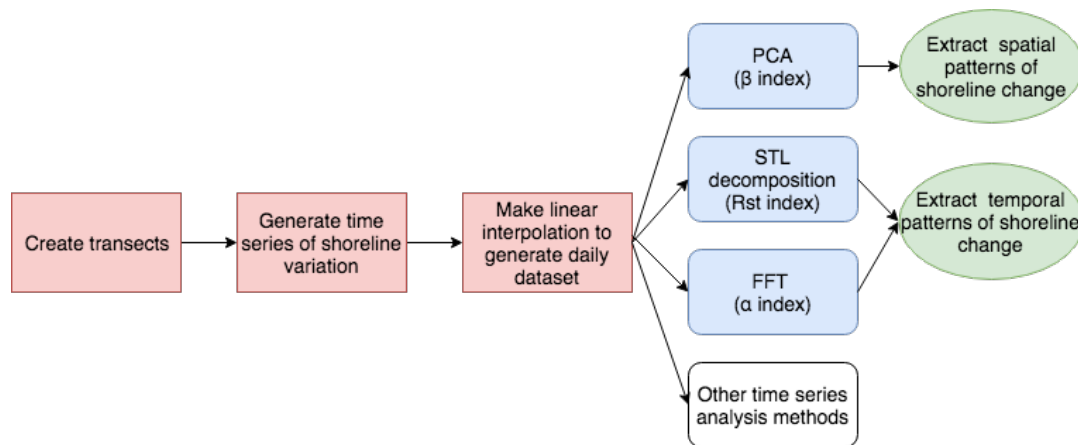


Figure 6.1: The framework for time series analysis of shoreline variation derived from SDS.

After analyzing the shoreline variation at the eleven sites of interests, we successfully distinguished different signals based on the SDS that were likely driven by different forcing types. The main research question is addressed after answering the first two sub-questions.

### I. Does the time series of the SDS contain signatures of expected shoreline behaviour?

1. The SDS partly unravel the shoreline variation governed by storms at Fire Island, the Gulf of Valencia and Perranporth. The low frequency of satellite image acquisition and the image composite technique reduce the capabilities of using the SDS for studying shoreline changes on the short-term scale governed by storms.

2. The SDS indicate that coastlines change greatly on the seasonal scale at Ocean Shores and Perth, which are caused by the seasonal variation of wave climate and littoral drift direction, respectively, in line with the analysis of [Ruggiero et al. \(2005\)](#) and [Masselink & Pattiaratchi \(2001\)](#). The results of STL decomposition of shoreline movement suggest that the seasonal component accounts for a large part of the overall shoreline variation ( $R_{st} > 0.3$ ) at both sites. The FFT analysis supports this conclusion by showing that noticeable spikes exist on the annual scale at the two beaches ( $\alpha > 0.5$ ).

3. The SDS show that coastlines mainly change on the inter-annual scale at Narrabeen and Ocean Beach, and the inter-annual variation is probably induced by climate variability (e.g. El Niño/Southern Oscillation (ENSO)). This hypothesis was tested with the correlation analysis of the climate indices (i.e. MEI and SOI) and shoreline movement. The results indicate that the shoreline changes at the two beaches correlate well with the ENSO events, corroborated by the analysis of [Short & Trembanis \(2004\)](#) and [Barnard et al. \(2011\)](#).

4. The SDS indicate that the shorelines mainly vary on the decadal scale at the Nile Delta and the SW of France, which could be correlated to the land subsidence and sea-level-rise driven basin infilling (and sediment deficiency), respectively. The trend component analysis shows that the shoreline erosion rate was fast at both sites during the last three decades, which is in line with the analysis of [Ali & El-Magd \(2016\)](#) and [Castelle et al. \(2018\)](#).

5. The SDS show that the coastlines change in synchronized rotational mode at Narrabeen, Moruya and Pedro, supported by the analysis of [Short et al. \(2014\)](#). The shoreline variation on the spatial scale was unravelled with PCA, and the results show that the percentage of variation explained by the rotational mode is large at the three sites ( $\beta > 15\%$ ). Cross-correlation analysis was then carried out and it corroborates the PCA results. It is interesting to know that only the three beaches in southeast Australia exhibit clearly rotational features, while all the other sites of interests do not show obvious rotational patterns. The specific phenomena could be explained by the fact that Narrabeen, Moruya and Pedro are all embayed beaches, and the changes of wave direction induced by ENSO can result in

rotational patterns of these coasts.

6. The SDS indicate that the anthropogenic processes govern the shoreline variation at Wrightsville Beach. The beach nourishment projects largely influence shoreline changes on the spatial scale, in line with the analysis of [Gares et al. \(2006\)](#).

## **II. To what extent is the limitation of the SDS important for unravelling shoreline dynamics?**

The main limitations in using the SDS to study coastline changes are related to: 1) the limited coverage of satellite mission on the temporal scale; 2) low frequency of satellite image acquisition.

Regarding the first issue, although satellite images can be used to detect shoreline positions over 30 years, it is still not sufficiently long for studying influence of SLR on open coasts. According to [Le Cozannet et al. \(2016\)](#), the influence of SLR on open coasts can only be captured on long timescales (greater than 50 years). Thus, only using the SDS to assess the impact of SLR on open coasts may not provide promising results, and thus other types of data (e.g. historical maps or topographical survey) are required to combine. Additionally, the limited length of the record requires the signals in the extreme low frequency range shown in FFT results to be interpreted cautiously as they are frequently spurious.

Regarding the second issue, the SDS may not be considered as the best solution when the purpose is to evaluate the real impact of a particular storm on shoreline changes. [Masselink et al. \(2006\)](#) stated that beach responses to storms are difficult to be observed when the survey occurs a long time after the event, particularly if the beach recovery is rapid. However, sometimes the first image after a storm is taken so long afterwards that the shoreline variation due to storms is not recorded (e.g. Hurricane Sandy on Fire Island), and sometimes several events may happen between two consecutive available images. Furthermore, the large foam induced by the breaking waves and thick clouds could reduce the accuracy of the SDS for unravelling shoreline dynamics. The composite averaging window (e.g. 180 days) used for extracting the SDS can also impair the capabilities of the SDS to unravel shoreline responses to extreme storms, as the large shoreline variation caused by storms might be averaged out over time.

After answering the above sub-questions, the main research question is addressed:

### **What is the application range of using the SDS for unravelling shoreline dynamics?**

In the present study, the capabilities of using the SDS for unravelling shoreline dynamics were tested on eleven sandy beaches. It is promising to see that most of the extracted spatiotemporal patterns of shoreline variation on the seasonal scale (due to seasonal forcing), inter-annual scale (due to climate variability) and decadal scale (due to land subsidence) are in line with the analysis of the relevant literature, in which the dataset such as field measurements or video monitoring were used. Moreover, the influence of groins and beach nourishment projects on shoreline changes can also be clearly unravelled using the SDS. However, the SDS cannot be considered as the best solution to study shoreline variation governed by storms, considering the low frequency of satellite image acquisition and the influence of the image composite technique. Moreover, only using the SDS to assess the shoreline responses to SLR may not provide promising results, since the limited length of the record (over 30 years) make it hard to capture the influence of SLR on open coasts on long-term scales.

To sum up, the SDS could be used as an ideal tool for unravelling coastline dynamics on seasonal, inter-annual and decadal scales governed by the seasonal forcing, climate variability and land subsidence, respectively. The shoreline changes caused by beach nourishment projects can also be clearly unravelled with the SDS. The introduction of new satellite missions can be expected in the near future, which helps to obtain an increasing temporal, spatial and spectral resolution of satellite images ([Hagenaars et al. 2018](#)). Therefore, it is highly possible that the SDS will become a more powerful tool for studying shoreline changes governed by extreme storms as time goes by. Furthermore, when the longer-recorded SDS are achieved in the future, it can be expected that the capabilities of using the

SDS for studying the long-term shoreline variation governed by SLR will be improved.

## 6.2. Recommendations

Based on the findings of this report, we make several recommendations for future research and practical applications.

1. If one would like to unravel shoreline changes through the SDS at a 'new site' where no background information can be achieved from literature, it is recommended to start with processing the SDS using the framework shown in Figure 6.1. The PCA can extract the dominant modes of shoreline variation on the spatial scale, and FFT and STL decomposition can be used to get a first understanding of coastline changes on the temporal scale.
2. It should be noted that the original time series of shoreline positions derived from the SDS are always worthwhile to be observed before any data processing methods being applied. Normally, approx. 1-2 satellite images are available each month, depending on the temporal granularity, temporal coverage of the satellite mission and the quality of the images. However, sometimes the SDS may show a blank period due to the influence of thick cloud covers or wave-inducing foams. The relatively long blank period can result in misleading results if the overall time series of shoreline positions are analyzed without preprocessing. For instance, the result plot of FFT of interpolated shoreline positions may show an unrealistic spike on the long-term scale when a long blank period exists. The blank period could be left out when the shoreline changes during that period of time are not the key point of the research; otherwise, the analysis results should be cautiously examined to avoid the misleading ones.
3. The threshold values for classifying rotational/non-rotational and seasonal/non-seasonal beaches can be researched further. The threshold values used in the present study were determined based on the background information of shoreline changes at eleven sites obtained from literature. The values could be adjusted and refined further when more knowledge-intensive beaches are analyzed with the SDS.
4. The criteria of beach classification could be employed for any beach worldwide through the SDS. It is interesting to know what percentage of the world's sandy beaches largely change on the seasonal scale. Moreover, it is good to study if the distinct rotational pattern of shoreline variation mostly exhibits at embayed beaches and caused by the change of wave direction due to ENSO.
5. An increasing temporal, spatial and spectral resolution of satellite images can be expected in the future, so the capabilities of using the SDS to study shoreline changes governed by storms can be investigated further. In addition, when longer-recorded shoreline positions are obtainable as time goes by, we can test the feasibility of using the SDS for unravelling the influence of SLR on open coasts.

# Bibliography

- Aarninkhof, S. G. J., Caljouw, M. & Stive, M. J. F. (2001), Video-Based, Quantitative Assessment of Intertidal Beach Variability, in 'Coastal Engineering 2000', American Society of Civil Engineers, Reston, VA, pp. 3291–3304.
- Ali, E. M. & El-Magd, I. A. (2016), 'Impact of human interventions and coastal processes along the Nile delta coast, Egypt during the past twenty-five years', *The Egyptian Journal of Aquatic Research* **42**(1), 1–10.
- Baart, F., Van Gelder, P. H., De Ronde, J., Van Koningsveld, M. & Wouters, B. (2011), 'The effect of the 18.6-year lunar nodal cycle on regional sea-level rise estimates', *Journal of Coastal Research* **28**(2), 511–516.
- Barnard, P. L., Allan, J., Hansen, J. E., Kaminsky, G. M., Ruggiero, P. & Doria, A. (2011), 'The impact of the 2009–10 El Niño Modoki on US West Coast beaches', *Geophysical Research Letters* **38**(13).
- Barnard, P. L., Eshleman, J., Erikson, L. H. & Hanes, D. M. (2007), Coastal processes study at ocean beach, San Francisco, CA: summary of data collection 2004–2006, Technical report, US Geological Survey.
- Barnard, P. L., Short, A. D., Harley, M. D., Splinter, K. D., Vitousek, S., Turner, I. L., Allan, J., Banno, M., Bryan, K. R., Doria, A., Hansen, J. E., Kato, S., Kuriyama, Y., Randall-Goodwin, E., Ruggiero, P., Walker, I. J. & Heathfield, D. K. (2015), 'Coastal vulnerability across the Pacific dominated by El Niño/Southern Oscillation', *Nature Geoscience* **8**(10), 801–807.
- Baumann, J., Chaumillon, E., Bertin, X., Schneider, J.-L., Guillot, B. & Schmutz, M. (2017), 'Importance of infragravity waves for the generation of washover deposits', *Marine Geology* **391**, 20–35.
- Bender, C. J. & Dean, R. G. (2003), 'Wave field modification by bathymetric anomalies and resulting shoreline changes: a review with recent results', *Coastal Engineering* **49**(1–2), 125–153.
- Blatter, C. (2003), *Wavelets: a primer*, Universities Press.
- Boak, E. H. & Turner, I. L. (2005), 'Shoreline Definition and Detection: A Review', *Journal of Coastal Research* **214**, 688–703.  
**URL:** <http://www.bioone.org/doi/abs/10.2112/03-0071.1>
- Bouvier, C., Balouin, Y. & Castelle, B. (2017), 'Video monitoring of sandbar-shoreline response to an offshore submerged structure at a microtidal beach', *Geomorphology* **295**, 297–305.
- Brenner, O. T., Lentz, E. E., Hapke, C. J., Henderson, R. E., Wilson, K. E. & Nelson, T. R. (2018), 'Characterizing storm response and recovery using the beach change envelope: Fire Island, New York', *Geomorphology* **300**, 189–202.
- Bria, O. N. (1999), 'John G. Proakis and Dimitris G. Manolakis, digital signal processing. principles, algorithms, and applications', *Journal of Computer Science & Technology* **1**.
- Bruun, P. (1962), 'Sea-level rise as a cause of shore erosion', *Journal of the Waterways and Harbors Division* **88**(1), 117–132.
- Bryant, E. (1983), 'Regional sea level, southern oscillation and beach change, New South Wales, Australia', *Nature* **305**(5931), 213.
- Bureau of, M. (2018), 'Southern Oscillation Index'.  
**URL:** <http://www.bom.gov.au/climate/glossary/soi.shtml>

- Butel, R., Dupuis, H. & Bonneton, P. (2002), 'Spatial variability of wave conditions on the french atlantic coast using in-situ data', *Journal of Coastal Research* **36**(96), 108.
- Castelle, B., Dodet, G., Masselink, G. & Scott, T. (2017), 'A new climate index controlling winter wave activity along the atlantic coast of europe: The west europe pressure anomaly', *Geophysical Research Letters* **44**(3), 1384–1392.
- Castelle, B., Guillot, B., Marieu, V., Chaumillon, E., Hanquiez, V., Bujan, S. & Poppeschi, C. (2018), 'Spatial and temporal patterns of shoreline change of a 280-km high-energy disrupted sandy coast from 1950 to 2014: Sw france', *Estuarine, Coastal and Shelf Science* **200**, 212–223.
- Castelle, B., Marieu, V., Bujan, S., Splinter, K. D., Robinet, A., Sénéchal, N. & Ferreira, S. (2015), 'Impact of the winter 2013–2014 series of severe western europe storms on a double-barred sandy coast: Beach and dune erosion and megacusp embayments', *Geomorphology* **238**, 135–148.
- Chac, P. & Wriggers, W. (2002), 'Fast Fourier Transform'.  
**URL:** [https://en.wikipedia.org/wiki/Fast\\_Fourier\\_transform](https://en.wikipedia.org/wiki/Fast_Fourier_transform)
- Cleveland, R. B., Cleveland, W. S. & Terpenning, I. (1990), 'Stl: A seasonal-trend decomposition procedure based on loess', *Journal of Official Statistics* **6**(1), 3.
- Dagum, E. B. & Bianconcini, S. (2016), *Seasonal Adjustment Methods and Real Time Trend-Cycle Estimation*, Springer.
- Dallas, K. L. & Barnard, P. L. (2011), 'Anthropogenic influences on shoreline and nearshore evolution in the san francisco bay coastal system', *Estuarine, Coastal and Shelf Science* **92**(1), 195–204.
- Davidson-Arnott, R. (2010), *Introduction to coastal processes and geomorphology*, Cambridge University Press.
- Davidson, M., Splinter, K. & Turner, I. (2013), 'A simple equilibrium model for predicting shoreline change', *Coastal Engineering* **73**, 191–202.
- de Rooij, T. (2017), Wavelet analysis in the field of coastal engineering, PhD thesis, Delft University of Technology.
- Del Río, L., Plomaritis, T. A., Benavente, J., Valladares, M. & Ribera, P. (2012), 'Establishing storm thresholds for the spanish gulf of cádiz coast', *Geomorphology* **143**, 13–23.
- Dodet, G., Bertin, X. & Taborda, R. (2010), 'Wave climate variability in the north-east atlantic ocean over the last six decades', *Ocean modelling* **31**(3-4), 120–131.
- Dolan, R., Hayden, B. P., May, P. & May, S. (1980), 'The reliability of shoreline change measurements from aerial photographs', *Shore and Beach (ISSN: 0037-4237)* **48**(4), 22–29.
- Donchyts, G., Baart, F., Winsemius, H., Gorelick, N., Kwadijk, J. & van de Giesen, N. (2016), 'Earth's surface water change over the past 30 years', *Nature Climate Change* **6**(9), 810.
- Elias, E. P. & Hansen, J. E. (2013), 'Understanding processes controlling sediment transports at the mouth of a highly energetic inlet system (san francisco bay, ca)', *Marine Geology* **345**, 207–220.
- Else, T. M. (2017), 'The NAO explained'.  
**URL:** <https://weatherworksinc.com/nao-definition>
- Erban, L. E., Gorelick, S. M. & Zebker, H. A. (2014), 'Groundwater extraction, land subsidence, and sea-level rise in the mekong delta, vietnam', *Environmental Research Letters* **9**(8), 084010.
- Eshleman, J. L., Barnard, P. L., Erikson, L. H. & Hanes, D. M. (2007), Coupling alongshore variations in wave energy to beach morphologic change using the swan wave model at ocean beach, san francisco, ca, in '10th International Workshop on Wave Hindcasting and Forecasting (Oahu, Hawaii), Paper F', Vol. 4, p. 20p.

- Finkl, C. W. (2004), 'Coastal classification: systematic approaches to consider in the development of a comprehensive scheme', *Journal of Coastal research* pp. 166–213.
- Fragkopoulos, T. (2016), Deriving a global identification tool of sandy beaches using satellite images, Msc thesis, Delft University of Technology.
- French, P. W. (2002), *Coastal defences: processes, problems and solutions*, Routledge.
- Gares, P. A., Wang, Y. & White, S. A. (2006), 'Using lidar to monitor a beach nourishment project at wrightsville beach, north carolina, usa', *Journal of Coastal Research* pp. 1206–1219.
- Gelfenbaum, G. & Kaminsky, G. M. (2010), 'Large-scale coastal change in the columbia river littoral cell: An overview', *Marine Geology* **273**(1-4), 1–10.
- Gorelick, N., Hancher, M., Dixon, M., Ilyushchenko, S., Thau, D. & Moore, R. (2017), 'Google Earth Engine: Planetary-scale geospatial analysis for everyone', *Remote Sensing of Environment* **202**, 18–27.  
**URL:** <http://dx.doi.org/10.1016/j.rse.2017.06.031>
- Graps, A. (1995), 'An introduction to wavelets', *IEEE computational science and engineering* **2**(2), 50–61.
- Gratiot, N., Anthony, E. J., Gardel, A., Gaucherel, C., Proisy, C. & Wells, J. (2008), 'Significant contribution of the 18.6 year tidal cycle to regional coastal changes', *Nature Geoscience* **1**(3), 169.
- Grenci, L. (2018), 'Other Teleconnections: It's More than El Niño'.
- Hagenaars, G., de Vries, S., Luijendijk, A. P., de Boer, W. P. & Reniers, A. J. (2018), 'On the accuracy of automated shoreline detection derived from satellite imagery: A case study of the sand motor mega-scale nourishment', *Coastal Engineering* **133**(June 2017), 113–125.  
**URL:** <http://linkinghub.elsevier.com/retrieve/pii/S0378383917302399>
- Hagenaars, G., Luijendijk, A., de Vries, S., de Boer, W., Hagenaars, G., Luijendijk, A., de Vries, S. & de Boer, W. (2017), 'Long term coastline monitoring derived from satellite imagery', *Coastal Dynamics 2017*.
- Hanley, D. E., Bourassa, M. A., O'Brien, J. J., Smith, S. R. & Spade, E. R. (2003), 'A quantitative evaluation of enso indices', *Journal of Climate* **16**(8), 1249–1258.
- Hansen, J. E. & Barnard, P. L. (2010), 'Sub-weekly to interannual variability of a high-energy shoreline', *Coastal Engineering* **57**(11-12), 959–972.
- Hapke, C. J., Brenner, O., Henderson, R. E. & Reynolds, B. (2013), Coastal change from hurricane sandy and the 2012-13 winter storm season: Fire island, new york, Technical report, US Geological Survey.
- Hoegh-Guldberg O (2017), 'Understanding Climate Variability and Change'.  
**URL:** <https://www.pacificclimatefutures.net/en/help/climate-projections/understanding-climate-variability-and-change/>
- Hurrell, J. W. (1995), 'Decadal trends in the north atlantic oscillation: regional temperatures and precipitation', *Science* **269**(5224), 676–679.
- Hyndman, R. J. & Athanasopoulos, G. (2014), *Forecasting: principles and practice*, OTexts.
- Idier, D., Castelle, B., Charles, E. & Mallet, C. (2013), 'Longshore sediment flux hindcast: spatio-temporal variability along the sw atlantic coast of france', *Journal of Coastal Research* **65**(sp2), 1785–1790.
- JAMSTEC-APL (2009), 'Modoki ENSO A New Phenomenon is Found in the Tropical Pacific'.  
**URL:** [http://www.jamstec.go.jp/frcgc/research/d1/iod/enmodoki\\_home\\_s.html.en](http://www.jamstec.go.jp/frcgc/research/d1/iod/enmodoki_home_s.html.en)
- Jensen, J. R. (2009), *Remote sensing of the environment: An earth resource perspective 2/e*, Pearson Education India.

- Jiménez, J. A., Sancho-García, A., Bosom, E., Valdemoro, H. I. & Guillén, J. (2012), 'Storm-induced damages along the catalan coast (nw mediterranean) during the period 1958–2008', *Geomorphology* **143**, 24–33.
- Jones, P. D., Jonsson, T. & Wheeler, D. A. (1997), 'Monthly values of the North Atlantic Oscillation Index from 1821 to 2000'. Supplement to: Jones, PD et al. (1997): Extension to the North Atlantic Oscillation using early instrumental pressure observations from Gibraltar and South-West Iceland. *International Journal of Climatology*, 17(13), 1433–1450, [https://doi.org/10.1002/\(SICI\)1097-0088\(19971115\)17:13%3C1433::AID-JOC203%3E3.0.CO;2-P](https://doi.org/10.1002/(SICI)1097-0088(19971115)17:13%3C1433::AID-JOC203%3E3.0.CO;2-P).  
**URL:** <https://doi.org/10.1594/PANGAEA.56559>
- Kamdi, S. & Krishna, R. (2012), 'Image segmentation and region growing algorithm', *International Journal of Computer Technology and Electronics Engineering (IJCTEE) Volume 2*.
- Komar, P. D. (1998), 'Beach processes and sedimentation'.
- Le Cozannet, G., Oliveros, C., Castelle, B., Garcin, M., Idier, D., Pedreros, R. & Rohmer, J. (2016), 'Uncertainties in sandy shorelines evolution under the bruun rule assumption', *Frontiers in Marine Science* **3**, 49.
- Lentz, E. E. & Hapke, C. J. (2011), 'Geologic framework influences on the geomorphology of an anthropogenically modified barrier island: assessment of dune/beach changes at fire island, new york', *Geomorphology* **126**(1-2), 82–96.
- Lentz, E. E., Hapke, C. J., Stockdon, H. F. & Hehre, R. E. (2013), 'Improving understanding of near-term barrier island evolution through multi-decadal assessment of morphologic change', *Marine Geology* **337**, 125–139.
- Library, P. U. (2007), 'Interpreting Regression Output'.  
**URL:** [https://dss.princeton.edu/online\\_help/analysis/interpreting\\_regression.htm](https://dss.princeton.edu/online_help/analysis/interpreting_regression.htm)
- Liew, S. C. (2001), 'Principles of Remote Sensing'.  
**URL:** <http://www.crisp.nus.edu.sg/research/tutorial/rsmain.htm>
- Lindsey, R. (2014), 'Winter of 2013-14 already tops 2012-13 for number of hurricane-force storms in North Atlantic'.  
**URL:** <https://www.climate.gov/news-features/featured-images/winter-2013-14-already-tops-2012-13-number-hurricane-force-storms>
- Linham, M. M. & Nicholls, R. J. (2010), 'Technologies for climate change adaptation'.
- Liu, Q., Trinder, J. C. & Turner, I. L. (2017), 'Automatic super-resolution shoreline change monitoring using landsat archival data: a case study at narrabeen–collaroy beach, australia', *Journal of Applied Remote Sensing* **11**(1), 016036.
- Lu, D., Mausel, P., Brondizio, E. & Moran, E. (2004), 'Change detection techniques', *International journal of remote sensing* **25**(12), 2365–2401.
- Luijendijk, A., Hagenaars, G., Ranasinghe, R., Baart, F., Donchyts, G. & Aarninkhof, S. (2018), 'The state of the world's beaches', *Scientific reports* **8**.
- Masselink, G., Austin, M., Scott, T., Poate, T. & Russell, P. (2014), 'Role of wave forcing, storms and nao in outer bar dynamics on a high-energy, macro-tidal beach', *Geomorphology* **226**, 76–93.
- Masselink, G., Castelle, B., Scott, T., Dodet, G., Suanes, S., Jackson, D. & Floc'h, F. (2016), 'Extreme wave activity during 2013/2014 winter and morphological impacts along the atlantic coast of europe', *Geophysical Research Letters* **43**(5), 2135–2143.
- Masselink, G., Kroon, A. & Davidson-Arnott, R. (2006), 'Morphodynamics of intertidal bars in wave-dominated coastal settings—a review', *Geomorphology* **73**(1-2), 33–49.
- Masselink, G. & Pattiaratchi, C. (2001), 'Seasonal changes in beach morphology along the sheltered coastline of perth, western australia', *Marine Geology* **172**(3-4), 243–263.

- MASSELINK, G., SCOTT, T., CONLEY, D., DAVIDSON, M. & RUSSELL, P. (2015), Regional variability in atlantic storm response along the southwest coast of england, in 'The Proceedings of the Coastal Sediments 2015', World Scientific.
- Masselink, G. & Short, A. D. (1993), 'The effect of tide range on beach morphodynamics and morphology: a conceptual beach model', *Journal of Coastal Research* pp. 785–800.
- Mazzarella, A., Giuliacci, A. & Scafetta, N. (2013), 'Quantifying the multivariate enso index (mei) coupling to co<sub>2</sub> concentration and to the length of day variations', *Theoretical and applied climatology* **111**(3-4), 601–607.
- Miller, J. K. & Dean, R. G. (2007), 'Shoreline variability via empirical orthogonal function analysis: Part i temporal and spatial characteristics', *Coastal Engineering* **54**(2), 111–131.
- Ming, F., Yang, Y., Zeng, A. & Jing, Y. (2016), 'Analysis of seasonal signals and long-term trends in the height time series of igs sites in china', *Science China Earth Sciences* **59**(6), 1283–1291.
- Mortlock, T. R. & Goodwin, I. D. (2016), 'Impacts of enhanced central pacific enso on wave climate and headland-bay beach morphology', *Continental Shelf Research* **120**, 14–25.
- Morton, R. A. (2002), 'Factors controlling storm impacts on coastal barriers and beaches: a preliminary basis for near real-time forecasting', *Journal of Coastal Research* pp. 486–501.
- Nicholls, R. J. & Cazenave, A. (2010), 'Sea-level rise and its impact on coastal zones', *science* **328**(5985), 1517–1520.
- NIWA (2016), 'Storms and cyclones'.  
**URL:** <https://www.niwa.co.nz/education-and-training/schools/students/storms>
- NOAA (2017), 'What is subsidence?'.  
**URL:** <https://oceanservice.noaa.gov/facts/subsidence.html>
- Null, J. (2011), 'El nino and la nina years and intensities based on oceanic nino index (oni).  
of Mathematics, E. (2012), 'Regression analysis'.  
of the Interior, U. D. (2017), 'Land Subsidence: Cause & Effect'.  
**URL:** [https://ca.water.usgs.gov/land\\_subsidence/california-subsidence-cause-effect.html](https://ca.water.usgs.gov/land_subsidence/california-subsidence-cause-effect.html)
- Osborn, T. J. (2004), 'Simulating the winter north atlantic oscillation: the roles of internal variability and greenhouse gas forcing', *Climate Dynamics* **22**(6-7), 605–623.
- Osborn, T. J. (2011), 'Winter 2009/2010 temperatures and a record-breaking north atlantic oscillation index', *Weather* **66**(1), 19–21.
- Pardo-Pascual, J. E., Almonacid-Caballer, J., Ruiz, L. A., Palomar-Vázquez, J. & Rodrigo-Alemany, R. (2014), 'Evaluation of storm impact on sandy beaches of the gulf of valencia using landsat imagery series', *Geomorphology* **214**, 388–401.
- Pascual, J. E. P. & i Verger, V. M. R. (1991), *La erosión antrópica en el litoral valenciano*, Generalitat Valenciana. Conselleria d'Obres Públiques, Urbanisme i Transports.
- Phinn, S. R. & Hastings, P. A. (1992), 'Southern oscillation influences on the wave climate of south-eastern australia', *Journal of Coastal Research* pp. 579–592.
- Polikar, R. (1996), 'The engineer's ultimate guide to wavelet analysis-the wavelet tutorial', available at <http://www.public.iastate.edu/~rpolikar/WAVELETS/WTtutorial.html>.
- PSMSL (2018), 'Permanent service for mean sea level'.  
**URL:** <http://www.psmsl.org/products/trends/>
- Psutty, N., Grace, M. & Pace, J. (2005), 'The coastal geomorphology of fire island, a portrait of continuity and change', *Fire Island Seashore Science Synthesis Paper. Boston, MA. National Park Service*.

- Ranasinghe, R., Callaghan, D. & Stive, M. J. F. (2012), 'Estimating coastal recession due to sea level rise: Beyond the Bruun rule', *Climatic Change* **110**(3-4), 561–574.
- Ranasinghe, R., Duong, T. M., Uhlenbrook, S., Roelvink, D. & Stive, M. (2013), 'Climate-change impact assessment for inlet-interrupted coastlines', *Nature Climate Change* **3**(1), 83.
- Ranasinghe, R., McLoughlin, R., Short, A. & Symonds, G. (2004a), 'The southern oscillation index, wave climate, and beach rotation', *Marine Geology* **204**(3-4), 273–287.
- Ranasinghe, R., McLoughlin, R., Short, A. & Symonds, G. (2004b), 'The Southern Oscillation Index, wave climate, and beach rotation', *Marine Geology* **204**(3-4), 273–287.
- Rao, C. R., Rao, C. R., Statistiker, M., Rao, C. R. & Rao, C. R. (1973), *Linear statistical inference and its applications*, Vol. 2, Wiley New York.
- Regnauld, H., Jennings, S., Delaney, C. & Lemasson, L. (1996), 'Holocene sea-level variations and geomorphological response: an example from northern brittany (france)', *Quaternary Science Reviews* **15**(8-9), 781–787.
- Release, N. P. S. N. (2011), 'Fire Island National Seashore, Fire Island National Seashore reopens after Hurricane Irene: most facilities open by Labor Day weekend.'  
**URL:** <https://www.nps.gov/fiis/learn/news/fire-island-national-seashore-reopens-after-hurricane-irene.htm>
- Release, N. P. S. N. (2015), 'Status of Old Inlet Breach on Fire Island'.  
**URL:** <https://www.nps.gov/fiis/learn/news/status-of-old-inlet-breach-on-fire-island.htm>
- Rob, S. (2017), 'Climate Variability vs. Climate Change – What's the Difference?'
- Rosati, J. D. (2005), 'Concepts in sediment budgets', *Journal of Coastal Research* pp. 307–322.
- Rosati, J. D. & Ebersole, B. A. (1997), Littoral impact of ocean city inlet, maryland, usa, in 'Coastal Engineering 1996', pp. 2779–2792.
- Ruggiero, P., Kaminsky, G. M., Gelfenbaum, G. & Voigt, B. (2005), 'Seasonal to interannual morphodynamics along a high-energy dissipative littoral cell', *Journal of Coastal Research* pp. 553–578.
- Sanjaume, E. & Pardo-Pascual, J. (2005), 'Erosion by human impact on the valencian coastline (e of spain)', *Journal of Coastal Research* pp. 76–82.
- Scott, T., MASSELINK, G., O'HARE, T., DAVIDSON, M. & RUSSELL, P. (2015), Multi-annual sand and gravel beach response to storms in the southwest of england, in 'The Proceedings of the Coastal Sediments 2015', World Scientific.
- Shepard, F. P. (1963), *Submarine geology*, USA.
- Short, A., Cowell, P., Cadee, M., Hall, W. & Van Dijk, B. (1995), Beach rotation and possible relation to the southern oscillation, in 'Proceedings of the ocean and atmospheric pacific international conference', National Tidal Facility, The Flinders University of South Australia, pp. 329–334.
- Short, A. D., Bracs, M. A. & Turner, I. L. (2014), 'Beach oscillation and rotation: local and regional response at three beaches in southeast australia', *Journal of Coastal Research* **70**(sp1), 712–717.
- Short, A. D. & Trembanis, A. C. (2004), 'Decadal scale patterns in beach oscillation and rotation narrabeen beach, australia—time series, pca and wavelet analysis', *Journal of Coastal Research* pp. 523–532.
- Short, A. D., Trembanis, A. C. & Turner, I. L. (2001), Beach oscillation, rotation and the southern oscillation, narrabeen beach, australia, in 'Coastal Engineering 2000', pp. 2439–2452.
- Short, A. D. & Trenaman, N. (1992), 'Wave climate of the sydney region, an energetic and highly variable ocean wave regime', *Marine and Freshwater Research* **43**(4), 765–791.

- Staff, N. C. f. A. R. (2015), 'The Climate Data Guide: Overview: Climate Indices.'  
**URL:** <https://climatedataguide.ucar.edu/climate-data/overview-climate-indices>
- Stanley, D. J. & Warne, A. G. (1998), 'Nile delta in its destruction phase', *Journal of Coastal Research* pp. 795–825.
- Stanley, J.-D. & Clemente, P. L. (2017), 'Increased land subsidence and sea-level rise are submerging egypt's nile delta coastal margin', *GSA Today* **27**(5), 4–11.
- Steve, D. (2018), 'The three phases of the El Niño–Southern Oscillation (ENSO)'.  
**URL:** <http://www.bom.gov.au/climate/enso/history/In-2010-12/three-phases-of-ENSO.shtml>
- Stive, M. J., Aarninkhof, S. G., Hamm, L., Hanson, H., Larson, M., Wijnberg, K. M., Nicholls, R. J. & Capobianco, M. (2002), 'Variability of shore and shoreline evolution', *Coastal Engineering* **47**(2), 211–235.
- Stockdon, H. F., Sallenger Jr, A. H., List, J. H. & Holman, R. A. (2002), 'Estimation of Shoreline Position and Change Using Airborne Topographic Lidar Data', *Journal of Coastal Research* **18**(3), 502–513.  
**URL:** <http://www.jstor.org/stable/4299097>
- Stockhause, M. & Höck, H. (2010), Integrated climate data center (icdc) at the cluster of excellence at the university of hamburg, in 'Proceedings of the Data Management Workshop', Vol. 29, p. 2009.
- Team, C. P. C. I. (2012), 'North Atlantic oscillation (NAO)'.  
**URL:** <http://www.cpc.ncep.noaa.gov/data/teledoc/nao.shtml>
- Thieler, E. R., Gayes, P. T., Schwab, W. C. & Harris, M. S. (1999), Tracing sediment dispersal on nourished beaches: two case studies, *Coastal Sediments*.
- Torrence, C. & Compo, G. P. (1998), 'A practical guide to wavelet analysis', *Bulletin of the American Meteorological society* **79**(1), 61–78.
- Turner, I. L., Harley, M. D., Short, A. D., Simmons, J. A., Bracs, M. A., Phillips, M. S. & Splinter, K. D. (2016), 'A multi-decade dataset of monthly beach profile surveys and inshore wave forcing at narrabeen, australia', *Scientific data* **3**, 160024.
- Vellinga, P. & Leatherman, S. P. (1989), 'Sea level rise, consequences and policies', *Climatic Change* **15**(1-2), 175–189.
- Vincent, L., Dolan, R., Hayden, B. & Resio, D. (1976), 'Systematic variations in barrier-island topography', *The Journal of Geology* **84**(5), 583–594.
- Weggel, J. R. (1979), A method for estimating long-term erosion rates from a long-term rise in water level., Technical report, COASTAL ENGINEERING RESEARCH CENTER FORT BELVOIR VA.
- Wikipedia, F. (2012), 'Local regression'.  
**URL:** [https://en.wikipedia.org/wiki/Local\\_regression](https://en.wikipedia.org/wiki/Local_regression)
- Wilhelm, J. (2015), 'In Regression analysis what does the Rsquare represent?'.  
**URL:** [https://www.researchgate.net/post/In\\_Regression\\_analysis\\_what\\_does\\_the\\_Rsquare\\_represent](https://www.researchgate.net/post/In_Regression_analysis_what_does_the_Rsquare_represent)
- Wilson, K. E., Adams, P. N., Hapke, C. J., Lentz, E. E. & Brenner, O. (2015), 'Application of bayesian networks to hindcast barrier island morphodynamics', *Coastal Engineering* **102**, 30–43.
- Winant, C. D., Inman, D. L. & Nordstrom, C. E. (1975), 'Description of seasonal beach changes using empirical eigenfunctions', *Journal of Geophysical Research* **80**(15), 1979–1986.
- Wolter, K. (2000), 'Multivariate enso index (mei)', *Climate Diagnostics Center Report at www. cdc. noaa. gov* .
- Yates, M., Guza, R. & O'Reilly, W. (2009), 'Equilibrium shoreline response: Observations and modeling', *Journal of Geophysical Research: Oceans* **114**(C9).
- Zhang, K., Douglas, B. C. & Leatherman, S. P. (2004), 'Global warming and coastal erosion', *Climatic Change* **64**(1-2), 41.



# List of Figures

1.1	Temporal and spatial scales in coastal morphodynamics. . . . .	2
1.2	An example of a range of visibly discernible shoreline indicator features, Duranbah Beach, New South Wales, Australia (E: Seaward dune vegetation line, G: Storm/debris line, H: An old high tide water level, I: Previous high tide high water level, K: Wet/dry line or runup maxima, L: Groundwater exit point, M: Instantaneous water line, N: shorebreak maximum intensity.). Figure from Boak & Turner (2005). . . . .	3
1.3	Tidal datums used along the New South Wales coastline, Australia. Figure from Boak & Turner (2005). . . . .	3
1.4	Global hot spots of beach erosion and accretion; the red (green) circles indicate erosion (accretion) for the four relevant shoreline dynamic classifications (see legend). The bar plots to the right and at the bottom present the relative occurrence of eroding (accreting) sandy shorelines per degree latitude and longitude, respectively. The numbers presented in the main plot represent the average change rate for all sandy shorelines per continent. Figure from Luijendijk et al. (2018). . . . .	4
1.5	Methodology to test the application range of using the SDS for unravelling sandy shoreline dynamics. . . . .	4
2.1	The workflow of the methodology for deriving the SDS as a coastal state indicator. Summarized based on Hagenaaers et al. (2018) and Luijendijk et al. (2018). . . . .	9
2.2	NDWI resulting binary image (left) and NDWI histogram (right) for Sentinel 2 image acquire on 1984-05-03 10:38:32. An optimal threshold value of -0.01 classifies the NDWI values into water (blue) and land (green) pixels. Figure from Hagenaaers et al. (2018). . . . .	10
2.3	The principle of the image composite technique based on the distribution of all TOA reflectance values within the image composite time window per pixel. Figure from Hagenaaers et al. (2018). . . . .	10
2.4	Time series of the SDS positions and the MSL contour lines obtained from the survey projected along transect 54 on Sand Engine. An OLS fit is made based on the information between 01 and 04-2013 and 01-07-2016. Figure from Hagenaaers et al. (2017). . . . .	11
2.5	Global distribution of sandy shorelines; the coloured dots along the world's shoreline represent the local percentage of sandy shorelines (yellow is sand, dark brown is non-sand). Figure from Luijendijk et al. (2018). . . . .	12
2.6	A guide to the timescale applicable to weather, climate variability and climate change. Figure from Hoegh-Guldberg O (2017). . . . .	14
2.7	Three-dimensional depiction of three important phases of the El Niño/Southern Oscillation (ENSO): Normal (left), La Niña (centre) and El Niño (right). Figure from Hoegh-Guldberg O (2017). . . . .	15
2.8	Anomalous SST during El Niño Modoki (left) and conventional El Niño (right). Figure from JAMSTEC-APL (2009). . . . .	16
2.9	Positive and negative phase of NAO. Figure from Greci (2018). . . . .	16
2.10	Global mean sea level evolution over the 20th and 21st centuries. Figure from Nicholls & Cazenave (2010). . . . .	17
2.11	Predicted shifting of the MHWL under the 18.6-year nodal tidal cycle for the next decade. Figure from (Gratiot et al. 2008). . . . .	18
3.1	The global map of all the considered sites. . . . .	22
3.2	View of a signal in the time and frequency domain. Figure from Chac & Wriggers (2002). . . . .	32
3.3	Time series and it's Fourier transform. Figure from Polikar (1996). . . . .	33

3.4	Schematic representation of the four different analyses of a signal. Figure from de Rooij (2017).	34
3.5	Time series and wavelet transform of the time series. Figure from Polikar (1996).	35
3.6	Classification model of beach state of Masselink & Short (1993).	37
3.7	PCA result of shoreline variation at Moruya.	38
3.8	The STL decomposition result of shoreline variation at Perth. The filtering parameters are listed in Section 4.2.2	39
3.9	The result plot of FFT of shoreline variation at Ocean Shores (CRLC) (Section 4.2.1).	39
3.10	The framework for time series analysis of shoreline variation derived from the SDS.	40
3.11	Transect locations at Narrabeen Beach.	41
3.12	The result plot of PCA of shoreline movement at Narrabeen Beach.	42
3.13	Result plot of STL decomposition of shoreline change at transect 29 on Narrabeen Beach. The annually averaged seasonal component and the long-term trend component are shown in the second and third panel, respectively. The original shoreline change and remainder component are shown at the top and bottom panels, respectively.	43
3.14	The result plot of FFT of the shoreline variation at Narrabeen Beach from 1987 to 2017.	44
3.15	The result plot of wavelet analysis of shoreline variation at Narrabeen Beach.	45
3.16	The time series of monthly averaged Troup Southern Oscillation index (SOI) from 1997-1998 (3-month filtered time series). Data from Australia Government Bureau of Meteorology.	45
3.17	Lagged cross-correlations between the SOI and shoreline variation at (a) Tr9 (northern part), and (b) Tr29 (southern part) on Narrabeen Beach.	46
3.18	The fit result for shoreline variation at transect 9 with the ordinary least squares model. The explanation of parameters listed in the figure can be achieved in Section 3.3.2.	46
3.19	Transect locations at Moruya and Pedro.	48
3.20	The result plots of PCA of shoreline variation at Moruya (M1-M3) and Pedro (P4-P6) (Figure 3.19). The meaning of axes can be found in Section 3.2.3.	49
3.21	The result plot of the STL decomposition of shoreline movement at M1, Moruya.	50
3.22	The result plot of the STL decomposition of shoreline movement at P1, Pedro.	50
3.23	Result plots of FFT of shoreline changes at Moruya and Pedro from 1984 to 2017.	51
4.1	Transect locations at west (left) and east (right) Fire Island.	54
4.2	Time series of ensemble averaged shoreline positions at the west Fire Island in 2005-2013. The black dots represent the time when the satellite images were taken.	55
4.3	Shoreline variation at transect 1 on the east Fire Island. Red dots represent the time when satellite images were taken.	55
4.4	Transect positions at Saler Beach (left) and Cullera Beach (right).	56
4.5	Shoreline responses to the storms on Saler Beach (upper pannel) and Cullera Beach (lower pannel). The start date of each storm is shown with dotted lines (11/10/01, 11/14/01, 12/14/01, 3/28/02, 4/2/02, 5/6/02) and detailed information is shown in Table 4.2. The red dots represent the time when the satellite images were taken.	57
4.6	Transect locations at Ocean Shores.	59
4.7	The result plot of the STL decomposition of shoreline variation at transect 6, Ocean Shores.	60
4.8	The seasonal component of shoreline variation at transect 0 and 6 from 2000 to 2004.	60
4.9	The result plot of FFT of shoreline change at transect 6 on Ocean Shores.	61
4.10	Transect locations at the Perth (red) and the positions of groins (orange).	62
4.11	The result plot of the STL decomposition at transect 3 on the coast of Perth.	62
4.12	The result plot of FFT analysis of shoreline positions at transect 3 on the Floreat beach and the north City beach.	63
4.13	The seasonal components of shoreline changes at transect 3 and 12. The orange panels show the time period of January to March (summer in Australia).	63
4.14	Transect locations at Ocean Beach.	65
4.15	Shoreline variation derived from SDS at Ocean Beach (1997-2016, residual component removed). Orange panels represent winter months (December to February).	66

4.16 (a) Winter shoreline retreat normalized by the mean value versus winter $H_s$ normalized by the mean (the trend line $y = 2.04x - 1.03$ ). (b) Winter shoreline retreat normalized by the winter mean versus MEI (the trend line $y = 0.297x + 0.986$ ). . . . .	67
4.17 Time series of winter $H_s$ normalized by winter mean (upper panel) and the MEI index (lower panel). . . . .	67
4.18 Time series of shoreline positions at transect 0 (north) and transect 6 (south) at Ocean Shores from 2015 to 2016 (17 months) and from 1997 to 1998 (17 months). The red dots illustrate the time when the satellite images were taken. . . . .	68
4.19 Transect locations at the Rossetta mouth. . . . .	70
4.20 The trend component of shoreline change at Rosetta mouth (the red dot line) with the lines of linear fit (blue segments). . . . .	71
4.21 Transect locations at Gatseau sandspit (left) and Cap Ferret sandspit (right). . . . .	72
4.22 The average coastline erosion rates at two sandspits over the last 3 decades. . . . .	73
4.23 Trend components of ensemble averaged shoreline movement at Gatseau sandspit (upper) and Cap Ferret sandspit (lower). Dashed lines represent the least-squares best fits. The shoreline variation in the south part of the Cap Ferret sandspit (near the tip) were spatially averaged at transect 13, 14 and 15; the variation in the north part were averaged at transect 7-12, and 16. . . . .	73
4.24 Transect positions at Wrightsville Beach. . . . .	75
4.25 Shoreline changes at Wrightsville Beach from 1997 to 2001. . . . .	76
5.1 Transects position at the Perth beach (red) and the position of two groins (orange). . .	77
5.2 Summary of analysis results. . . . .	79
6.1 The framework for time series analysis of shoreline variation derived from SDS. . . . .	82
A.1 Aerial photo (source: NSW Department of Lands) of the Narrabeen embayment—showing the locations of the five monthly survey transects (PF1, PF2, PF4, PF6, and PF8) (b) the beach with respect to the Sydney coastline (c) map of Australia. Figure from Turner et al. (2016). . . . .	99
A.2 a) The three primary 'modes' of wave climate in the Tasman Sea, and b) the shoreline response of embayed beaches. El Niño events are associated with more Mode 3, causing a clockwise rotation of the shoreline. La Niña periods promote more Mode 1 and 2 wave conditions, leading to an overall anti-clockwise rotation of the beach. Figure from Mortlock & Goodwin (2016). . . . .	100
A.3 Map of southeast Australia showing the location and details of Narrabeen, Moruya and Pedro beaches. Figure from Short et al. (2014). . . . .	100
A.4 Description and location of the study area. The bottom-left panel shows location map and bathymetry of the region near Perranporth. The two photos of Perranporth at the top of the figure, taken from the ARGUS position, illustrate the typical winter beach state (left) with a linear bar and the typical summer beach state (right) with pronounced transverse bar/rip morphology. Figure from Masselink et al. (2014). . . . .	101
A.5 Difference from average wind speed across the Northern Hemisphere for January-February 2014. Figure from Lindsey (2014). . . . .	101
A.6 Map of the 165-km long CRLC with erosion hot spots identified (black dots). Figure from Gelfenbaum & Kaminsky (2010). . . . .	102
A.7 Map of geographic features and network of major canals, drains, and pumping stations in the Nile delta. Figure from Stanley & Clemente (2017). . . . .	102
A.8 Map of Perth beaches. Figure from Masselink & Pattiaratchi (2001). . . . .	103
A.9 Aerial photos of Floreat beach and north City beach. Figure from Masselink & Pattiaratchi (2001). . . . .	103
A.10 Left: location plot of SF Bay. Right: Location plot of Ocean Beach. Figure from Elias & Hansen (2013). . . . .	104
A.11 (a) Location of Fire Island in relation to Long Island, N.Y. and northeastern U.S. coastline. (b) Map of Fire Island showing the various management regimes present, 3 distinct geologic regions. Figure from Brenner et al. (2018). . . . .	104

A.12	Fire Island replenishment history showing approximate volumes and spatial locations of emplacement along shore. Figure from Lentz et al. (2013).	105
A.13	Location of Gatseau and Cap Ferret sand spits and Maumusson and Arcachon tidal inlets. Figure from Castelle et al. (2018).	106
A.14	Trend in relative sea level at European tide gauge stations. Figure from: <a href="https://www.eea.europa.eu/data-and-maps/figures/trend-in-relative-sea-level-4">https://www.eea.europa.eu/data-and-maps/figures/trend-in-relative-sea-level-4</a>	107
A.15	Location of the Gulf of Valencia. Figure from <a href="https://en.wikipedia.org/wiki/Gulf_of_Valencia">https://en.wikipedia.org/wiki/Gulf_of_Valencia</a> .	107
A.16	Location of Saler Beach and Cullera Beach.	108
A.17	Location of Wrightsville Beach. Figure from Gares et al. (2006)	109
A.18	Beach nourishment history of Wrightsville Beach. Figure from Thieler et al. (1999)	109
B.1	Time series of shoreline positions generated with different lengths of averaging windows.	112
B.2	The PCA results of shoreline variation at Perth.	113
B.3	The result plots of STL decomposition of shoreline variation at Perth.	114
B.4	The result plots of FFT of shoreline variation at transect 3.	115
B.5	The seasonal components of shoreline variation at transect 3 and 12. The orange panels show the time period of January to March (summer in Australia).	116
C.1	The PCA results of shoreline variation at different sites of interests.	119
C.2	The STL decomposition results of shoreline variation at different sites of interests.	122
C.3	The seasonal-diagnostic plots of choosing seasonal smoothing parameters for STL decomposition at different sites of interests.	125
C.4	The FFT results of shoreline variation at different sites of interests.	128
C.5	The reconstructed shoreline changes using only the components with a frequency of larger than 2 years.	129
C.6	Time series of shoreline movement at transect 9 and transect 29 on Narrabeen Beach	130
C.7	The trend components of shoreline change at the three main transects at Moruya and Pedro.	130
C.8	Time series of shoreline change at transect 0 and 6 (Ocean Shores).	131
C.9	Time series of shoreline position at transect 2 on mouth of Rosetta branch.	131
C.10	Trend components of shoreline change at Gatseau sandspit and Cap Ferret sandspit.	132
D.1	The trend components for the five main transects.	133
D.2	The trend components for shoreline change at transect 2, transect 9 and transect 29.	134
D.3	Transects position at Perranporth.	136
D.4	The result plot of PCA of shoreline movement at Perranporth.	137
D.5	Time series of shoreline position for transect 9.	137
D.6	The result plot of linear interpolation of time series of shoreline position for transect 9.	137
D.7	The result plot of the STL decomposition at transect 9 on Perranporth.	138
D.8	The result plot of FFT of shoreline position at Perranporth from 2006 to 2017.	139
D.9	The trend (upper panel) and residual (lower panel) components of shoreline change at transect 9 from 2006 to 2017.	139
D.10	Time series of offshore significant wave height ( $H_s$ ) at Perranporth from October 2013 to March 2014.	140
D.11	The time series of winter NAO index (bars) with the one-year filtered time series (red line).	141
D.12	The relationship between winter NAO and $H_s$ . The red line represents the least-squares best fit ( $y = 0.31x + 3.15$ ).	141
D.13	Lagged cross-correlations between $H_s$ and shoreline position at Perranporth with the peak value at (40, -0.53).	141
D.14	The result plot of PCA of shoreline movement at Floreat beach and the north City beach in Perth.	143

# List of Tables

2.1	Frequently used datasets in the earth engine data catalog . . . . .	8
3.1	Parameters for STL decomposition of coastline movement at Narrabeen Beach. . . . .	43
3.2	Parameters for STL decomposition of shoreline variation at Moruya and Pedro. . . . .	49
3.3	Variability and trends of shoreline positions at the three beaches over 1998-2017. . . . .	52
4.1	Name, date and general impacts of storms within the recent historic storm record at Fire Island, NY used in the present study (adjusted according to Brenner et al. (2018)). . . . .	54
4.2	Information related to the storms from 2001-11 to 2002-05. Adjusted based on Pardo-Pascual et al. (2014) . . . . .	57
4.3	Parameters for STL decomposition of shoreline movement at Ocean Shores. . . . .	60
4.4	Parameters for STL decomposition of shoreline variation at Perth. . . . .	62
4.5	Shoreline positions before and after winters (1997- 2016). . . . .	66
D.1	The standard deviation values for the shoreline variation at five main transects over 30 years. . . . .	134
D.2	Cross-correlation coefficient (at zero lag) matrix for trend components of shoreline position at Narrabeen Beach. . . . .	134
D.3	Correlation within sites. . . . .	135
D.4	Correlation between sites. . . . .	135
D.5	Parameters for STL decomposition of coastline change at Perranporth. . . . .	138





## Maps of the sites of interests

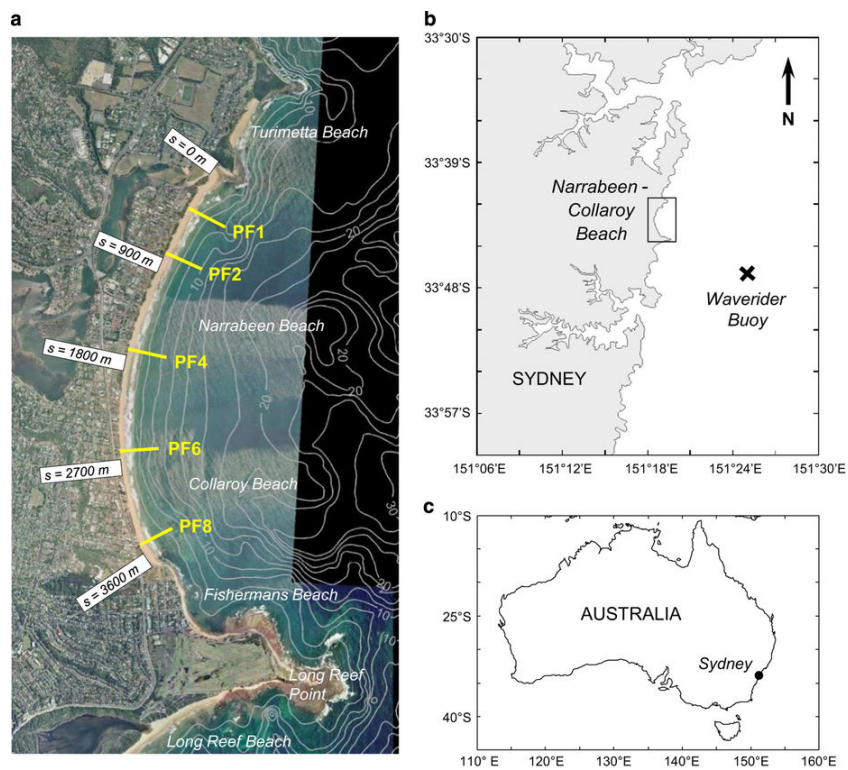


Figure A.1: Aerial photo (source: NSW Department of Lands) of the Narrabeen embayment—showing the locations of the five monthly survey transects (PF1, PF2, PF4, PF6, and PF8) (b) the beach with respect to the Sydney coastline (c) map of Australia. Figure from [Turner et al. \(2016\)](#).

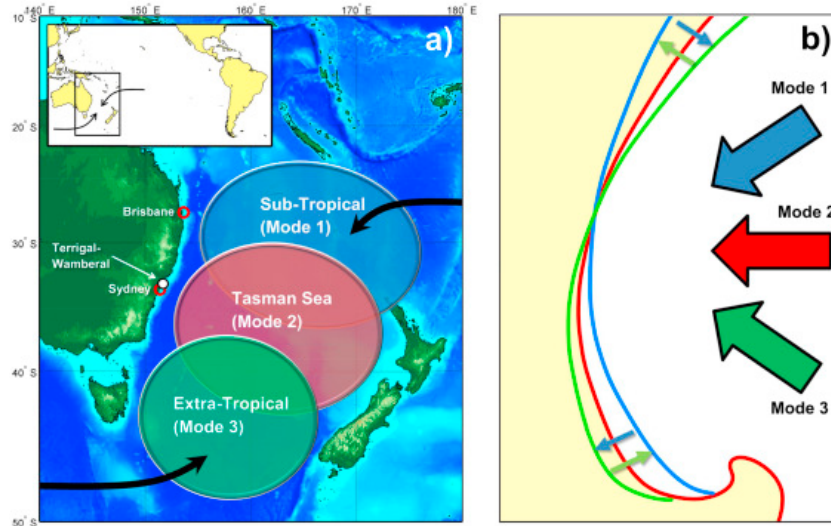


Figure A.2: a) The three primary 'modes' of wave climate in the Tasman Sea, and b) the shoreline response of embayed beaches. El Niño events are associated with more Mode 3, causing a clockwise rotation of the shoreline. La Niña periods promote more Mode 1 and 2 wave conditions, leading to an overall anti-clockwise rotation of the beach. Figure from [Mortlock & Goodwin \(2016\)](#).

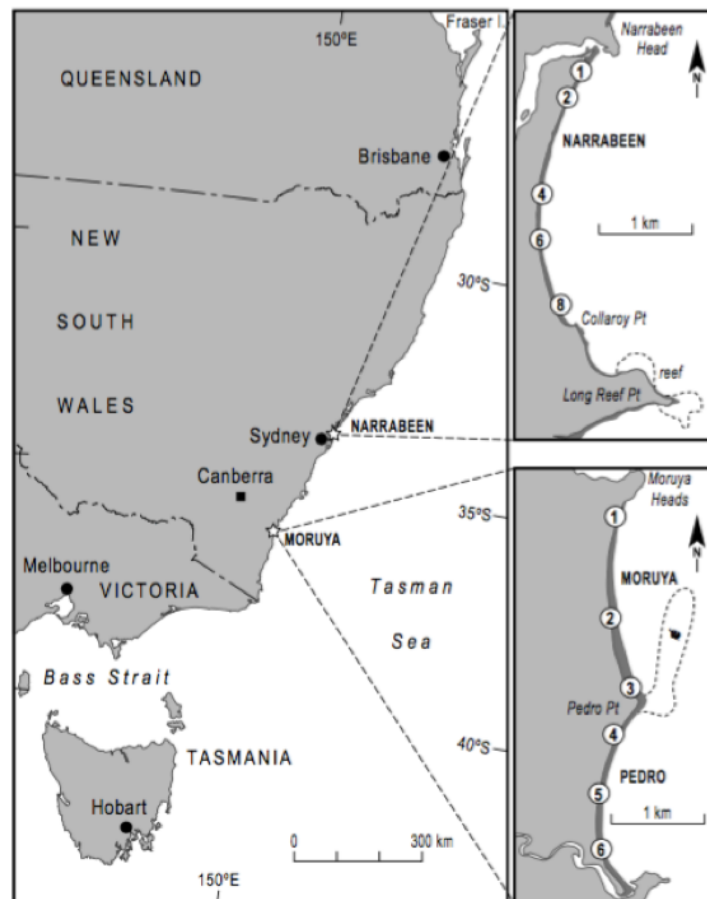


Figure A.3: Map of southeast Australia showing the location and details of Narrabeen, Moruya and Pedro beaches. Figure from [Short et al. \(2014\)](#).

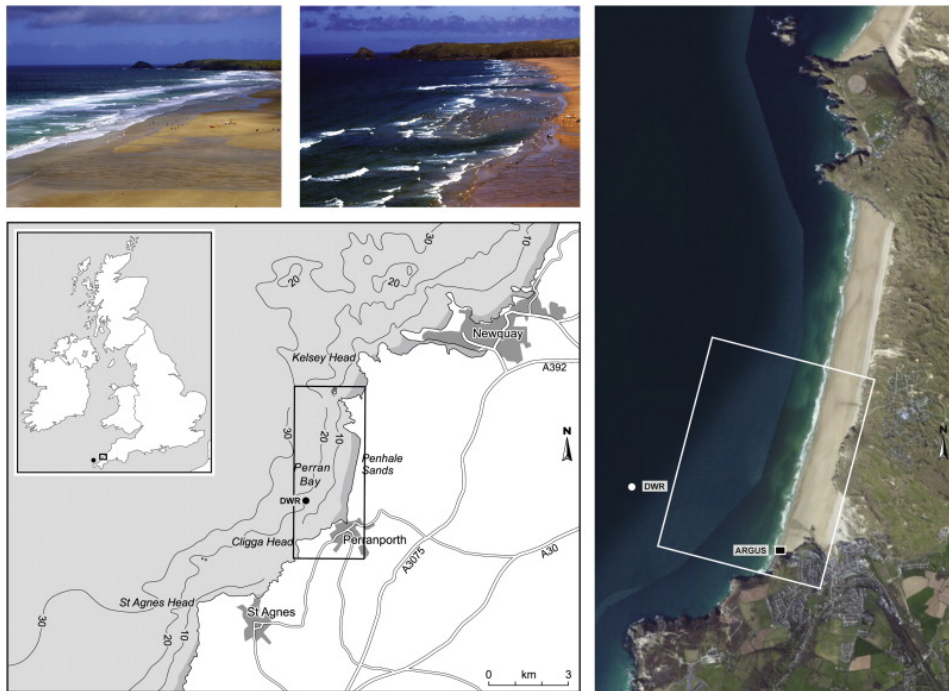


Figure A.4: Description and location of the study area. The bottom-left panel shows location map and bathymetry of the region near Perranporth. The two photos of Perranporth at the top of the figure, taken from the ARGUS position, illustrate the typical winter beach state (left) with a linear bar and the typical summer beach state (right) with pronounced transverse bar/rip morphology. Figure from [Masselink et al. \(2014\)](#).

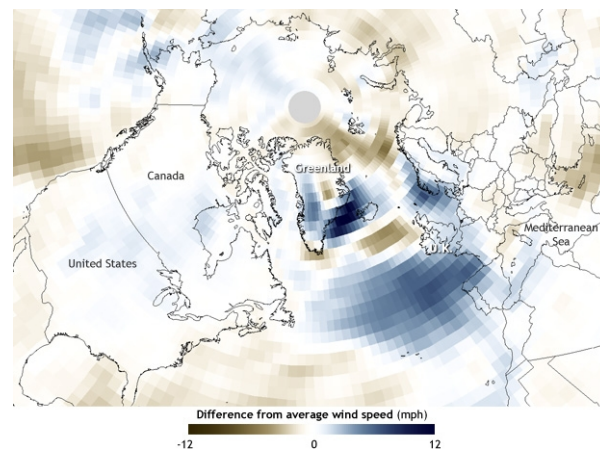


Figure A.5: Difference from average wind speed across the Northern Hemisphere for January-February 2014. Figure from [Lindsey \(2014\)](#).

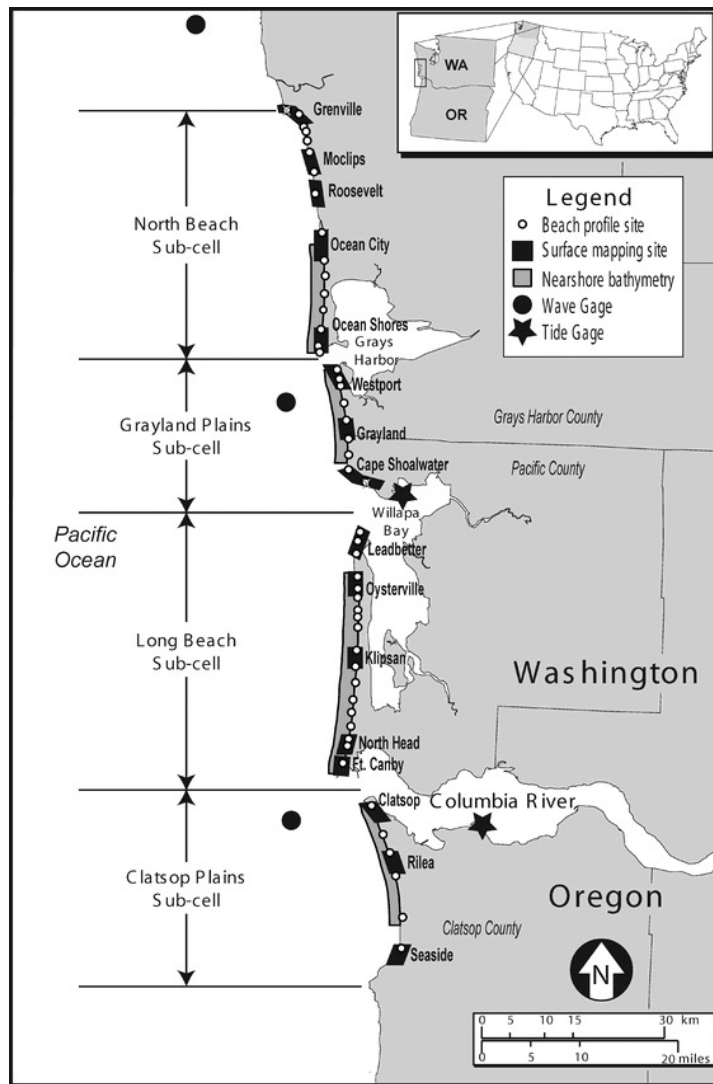


Figure A.6: Map of the 165-km long CRLC with erosion hot spots identified (black dots). Figure from Gelfenbaum & Kaminsky (2010).

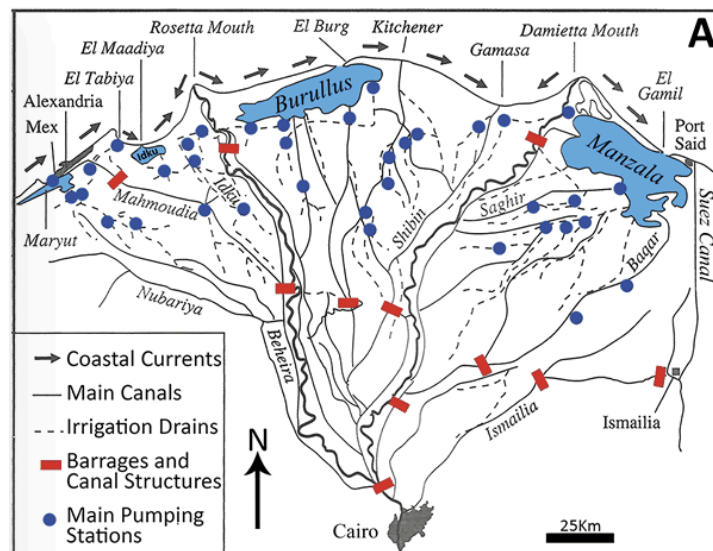


Figure A.7: Map of geographic features and network of major canals, drains, and pumping stations in the Nile delta. Figure from Stanley & Clemente (2017).

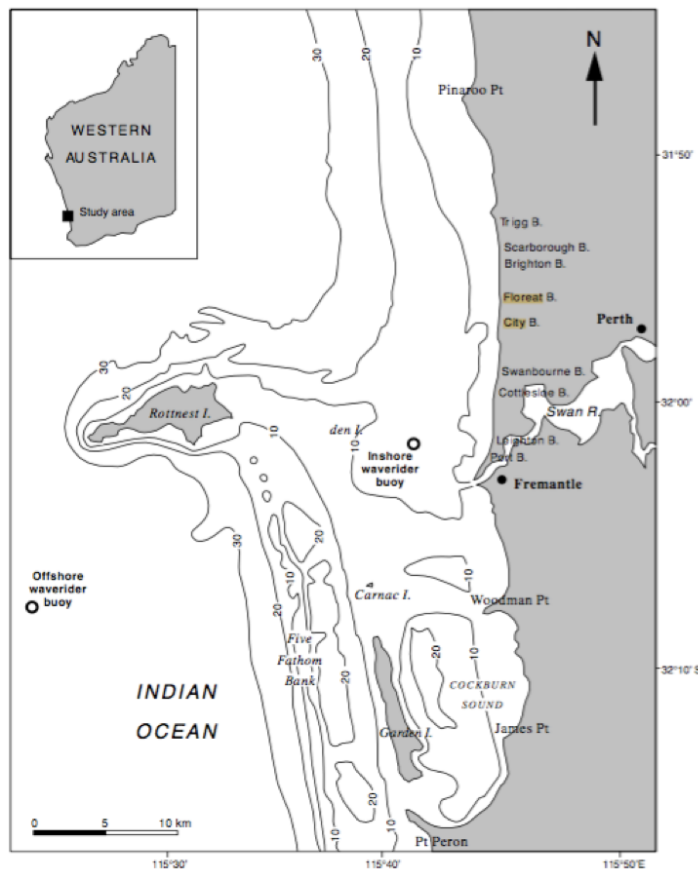


Figure A.8: Map of Perth beaches. Figure from [Masselink & Pattiaratchi \(2001\)](#).

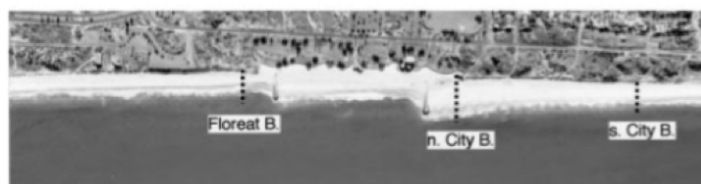


Figure A.9: Aerial photos of Floreat beach and north City beach. Figure from [Masselink & Pattiaratchi \(2001\)](#).

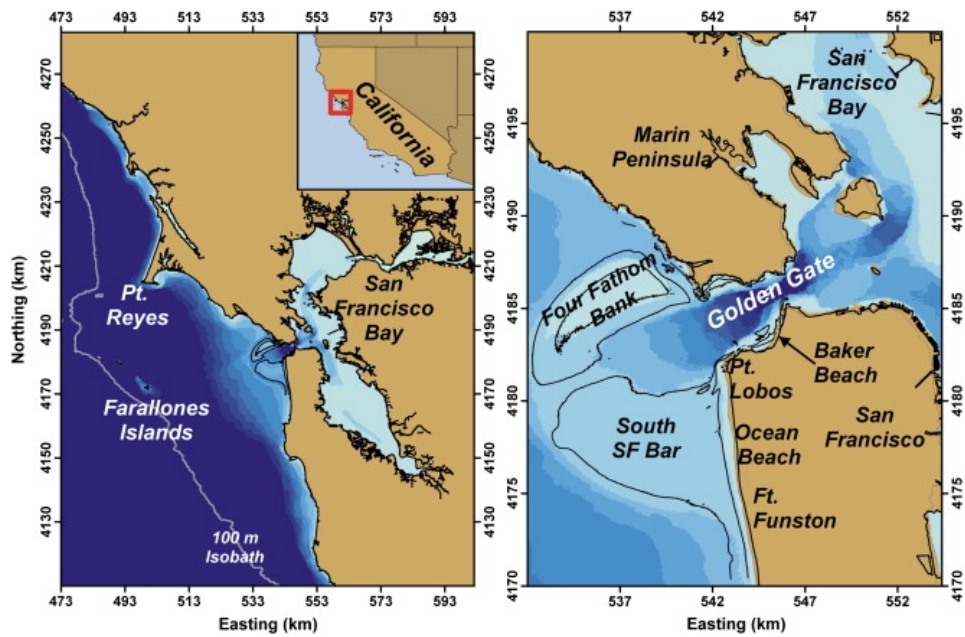


Figure A.10: Left: location plot of SF Bay. Right: Location plot of Ocean Beach. Figure from [Elias & Hansen \(2013\)](#).



Figure A.11: (a) Location of Fire Island in relation to Long Island, N.Y. and northeastern U.S. coastline. (b) Map of Fire Island showing the various management regimes present, 3 distinct geologic regions. Figure from [Brenner et al. \(2018\)](#).

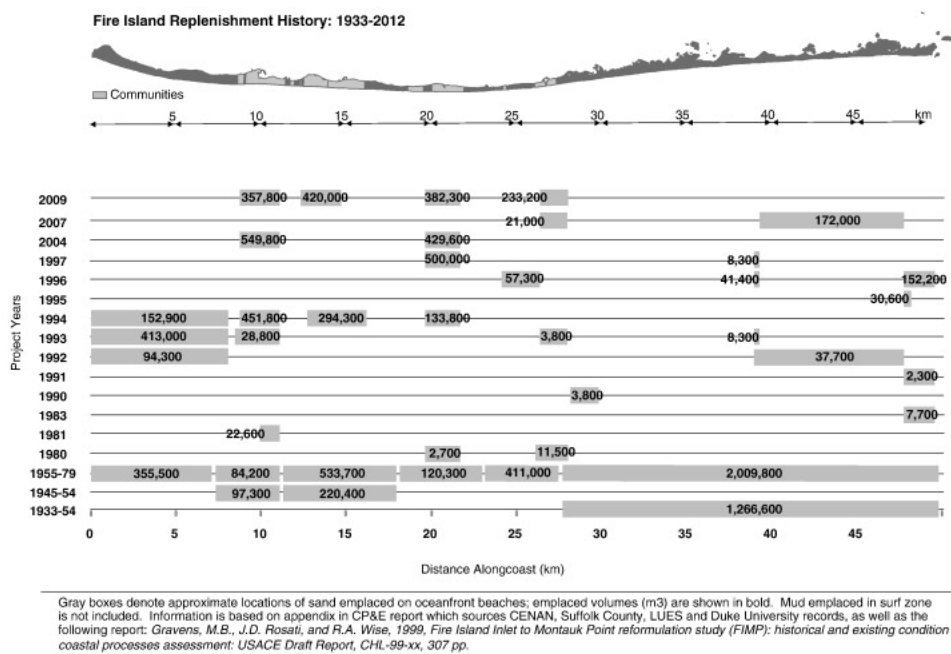


Figure A.12: Fire Island replenishment history showing approximate volumes and spatial locations of emplacement along shore. Figure from [Lentz et al. \(2013\)](#).



Figure A.13: Location of Gatseau and Cap Ferret sand spits and Maumusson and Arcachon tidal inlets. Figure from [Castelle et al. \(2018\)](#).

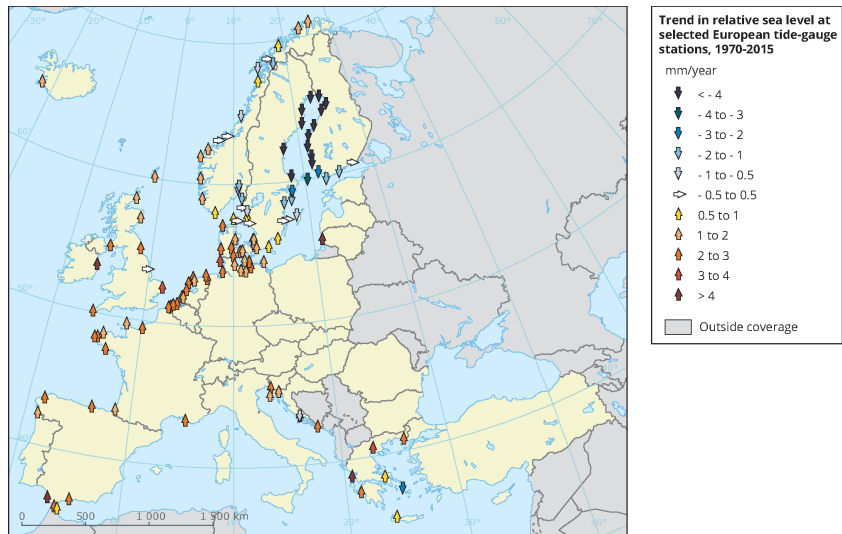


Figure A.14: Trend in relative sea level at European tide gauge stations. Figure from: <https://www.eea.europa.eu/data-and-maps/figures/trend-in-relative-sea-level-4>



Figure A.15: Location of the Gulf of Valencia. Figure from [https://en.wikipedia.org/wiki/Gulf\\_of\\_Valencia](https://en.wikipedia.org/wiki/Gulf_of_Valencia).



Figure A.16: Location of Saler Beach and Cullera Beach.

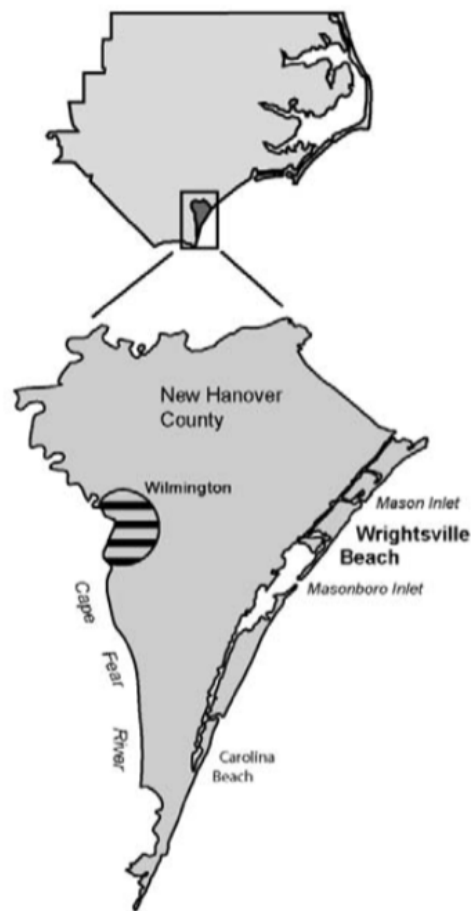


Figure A.17: Location of Wrightsville Beach. Figure from [Gares et al. \(2006\)](#)

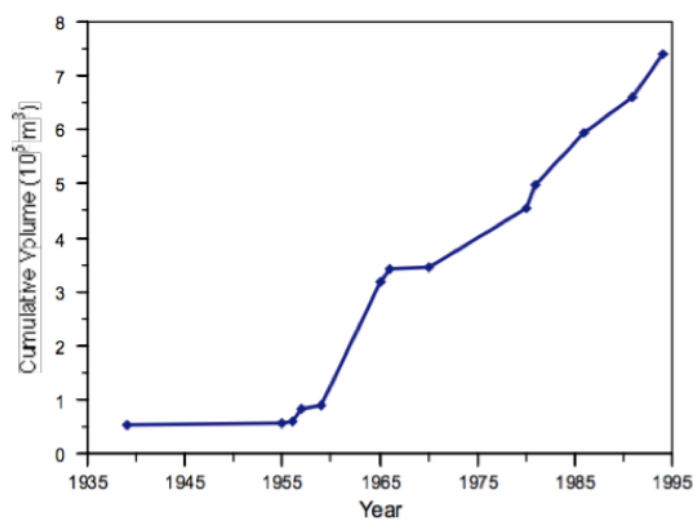


Figure A.18: Beach nourishment history of Wrightsville Beach. Figure from [Thieler et al. \(1999\)](#)



# B

## Figures of sensitivity analysis

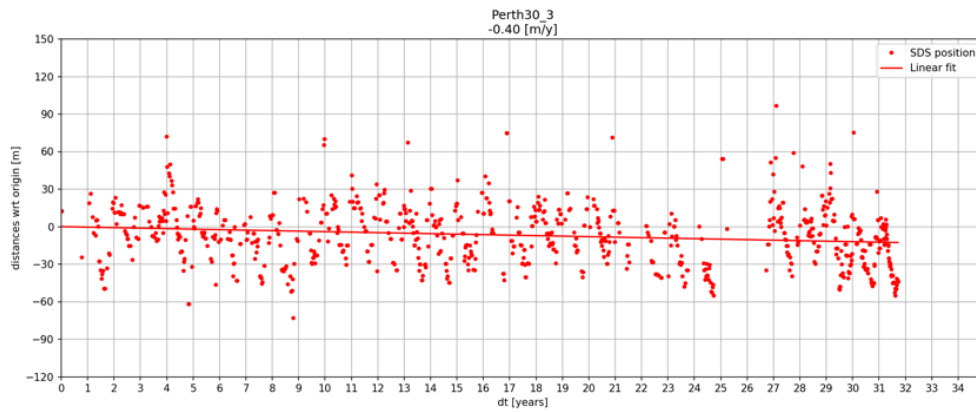
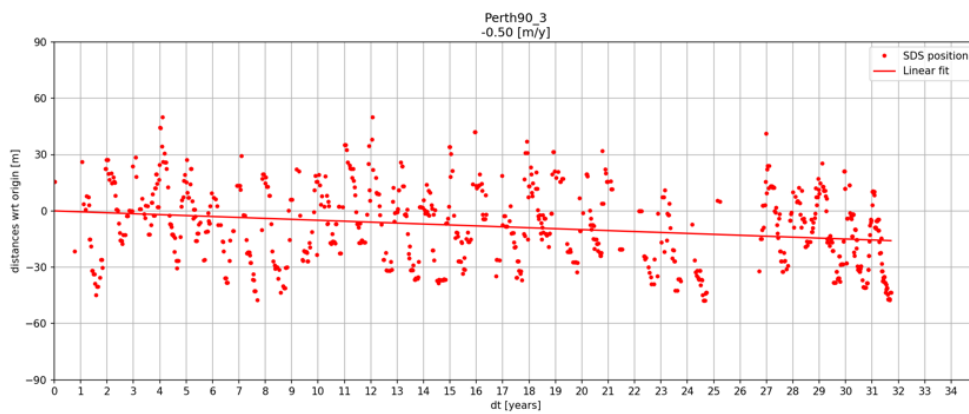
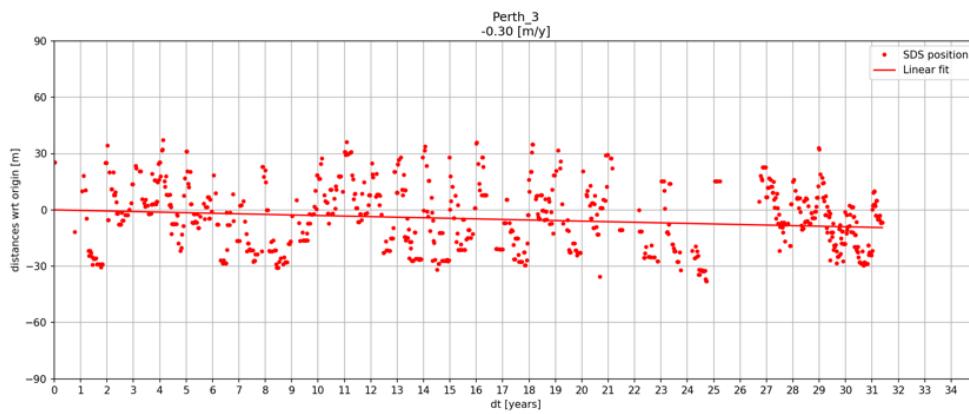
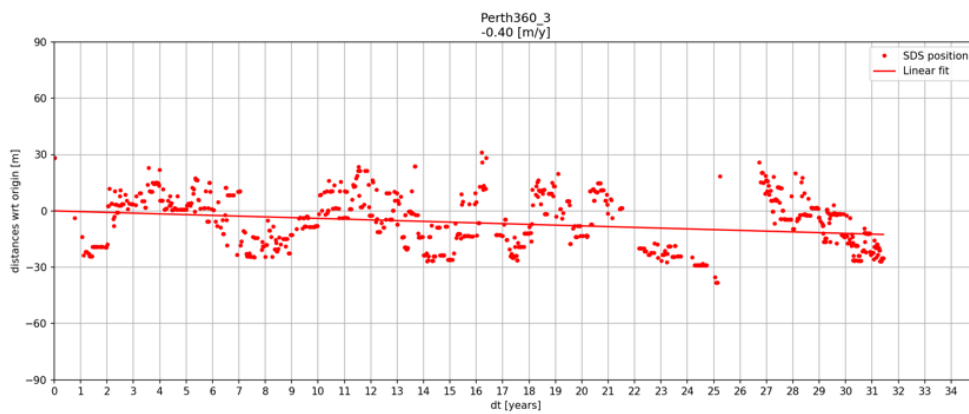
(a)  $dt = 30$ (b)  $dt = 90$ (c)  $dt = 180$ (d)  $dt = 360$ 

Figure B.1: Time series of shoreline positions generated with different lengths of averaging windows.

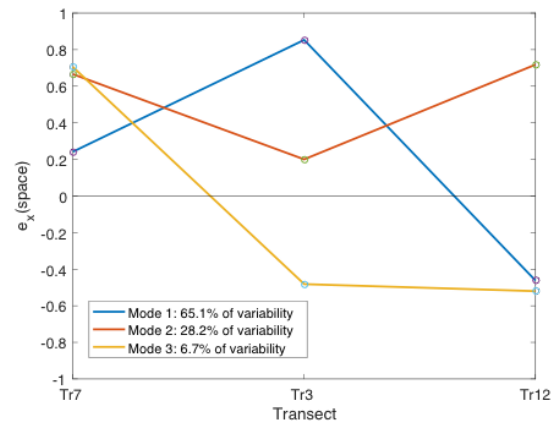
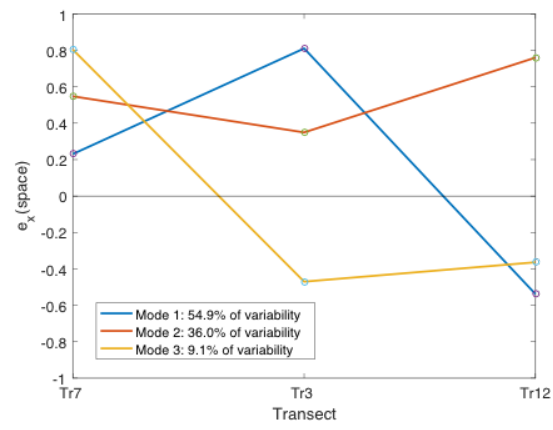
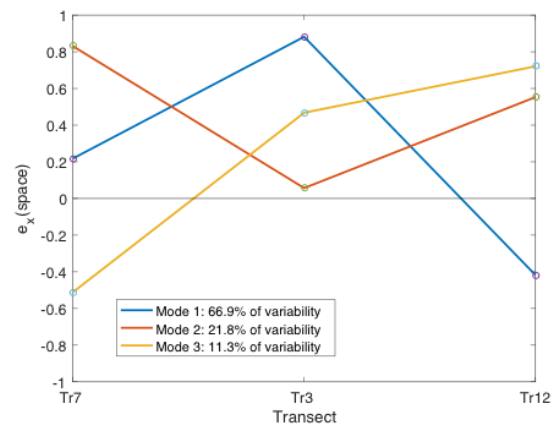
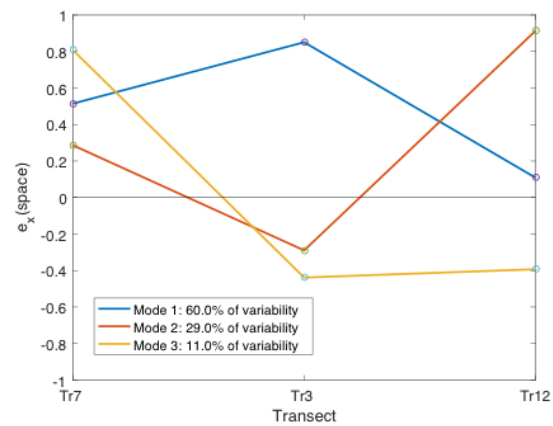
(a)  $dt = 30$ (b)  $dt = 90$ (c)  $dt = 180$ (d)  $dt = 360$ 

Figure B.2: The PCA results of shoreline variation at Perth.

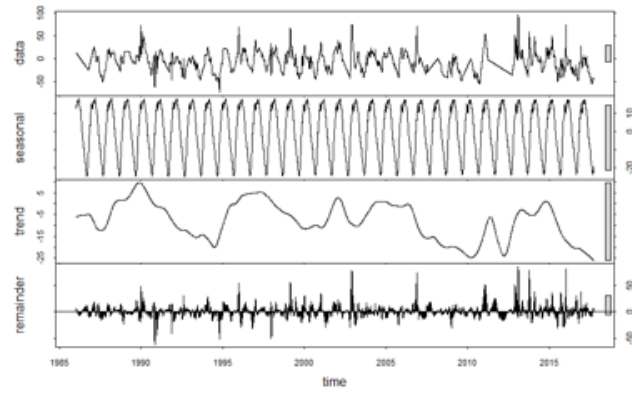
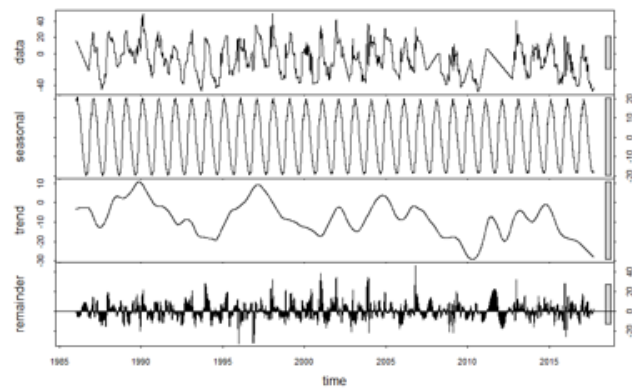
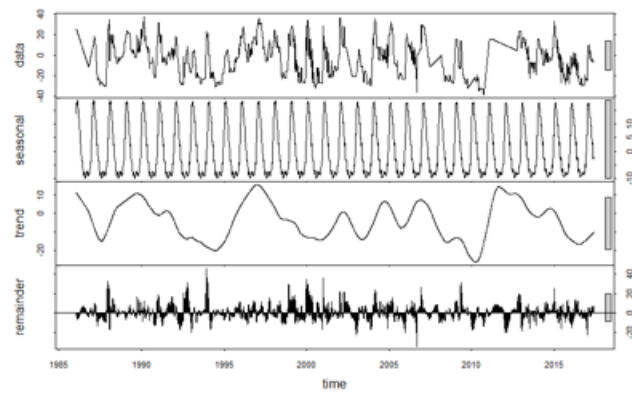
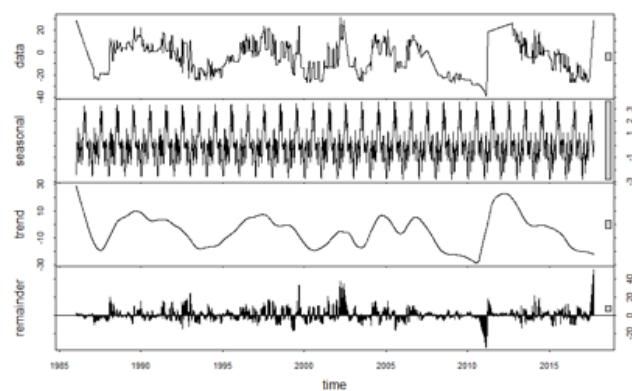
(a)  $dt = 30$ (b)  $dt = 90$ (c)  $dt = 180$ (d)  $dt = 360$ 

Figure B.3: The result plots of STL decomposition of shoreline variation at Perth.

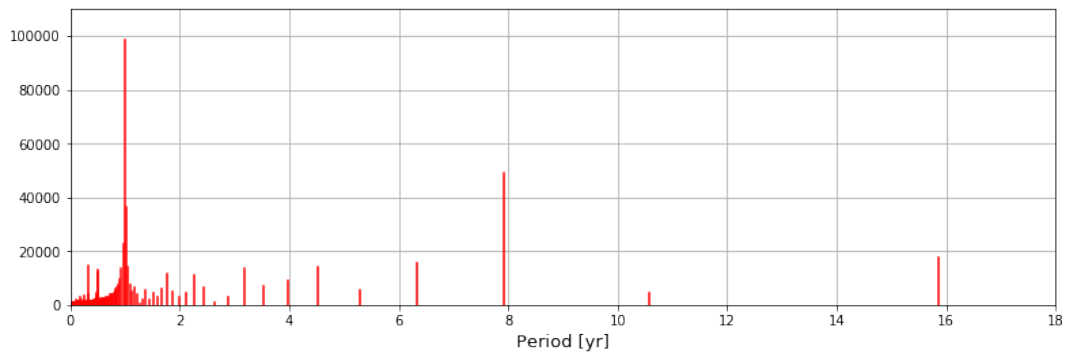
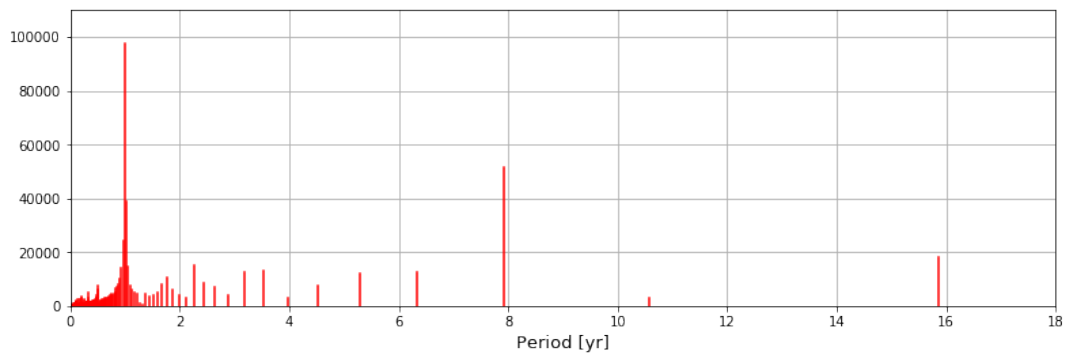
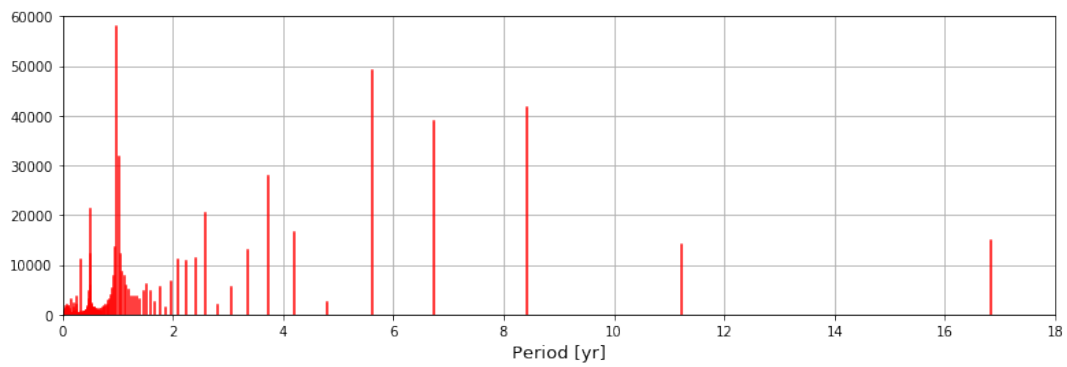
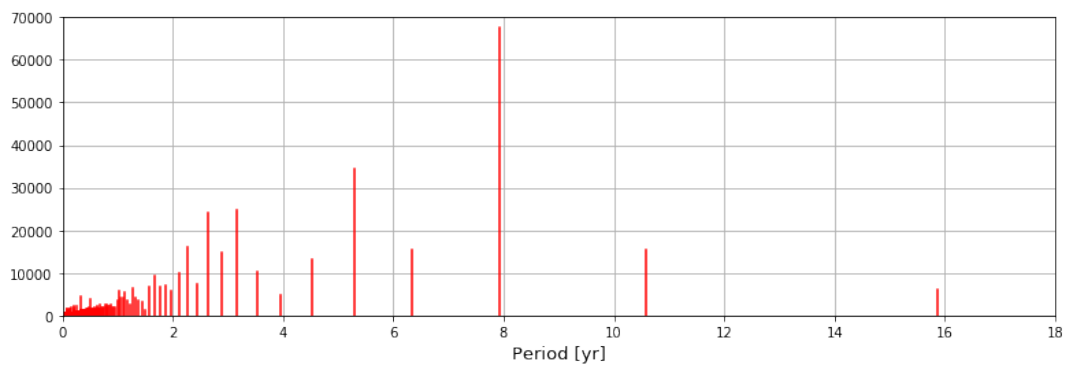
(a)  $dt = 30$ (b)  $dt = 90$ (c)  $dt = 180$ (d)  $dt = 360$ 

Figure B.4: The result plots of FFT of shoreline variation at transect 3.

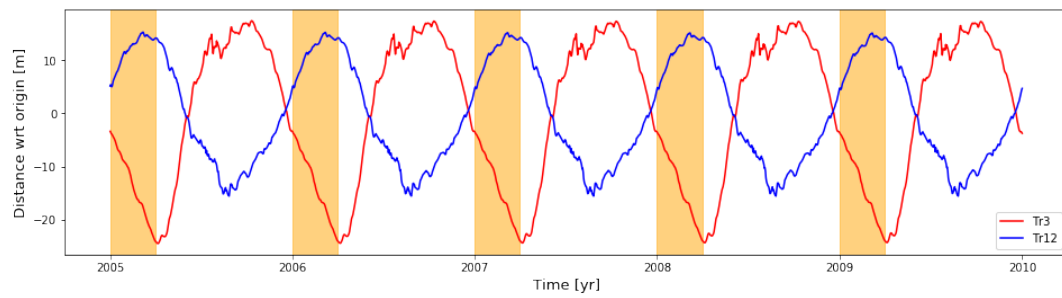
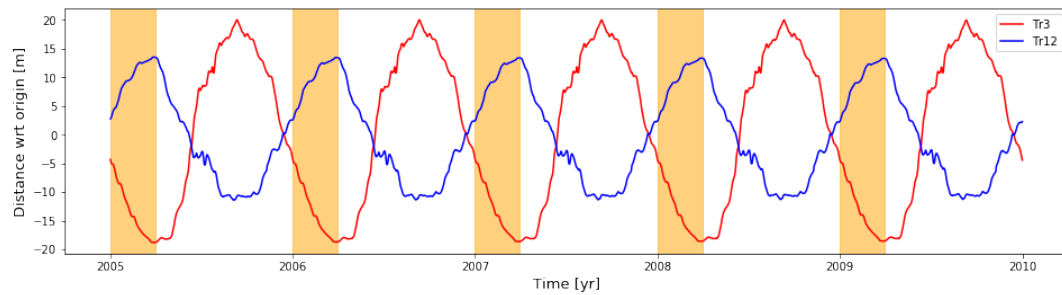
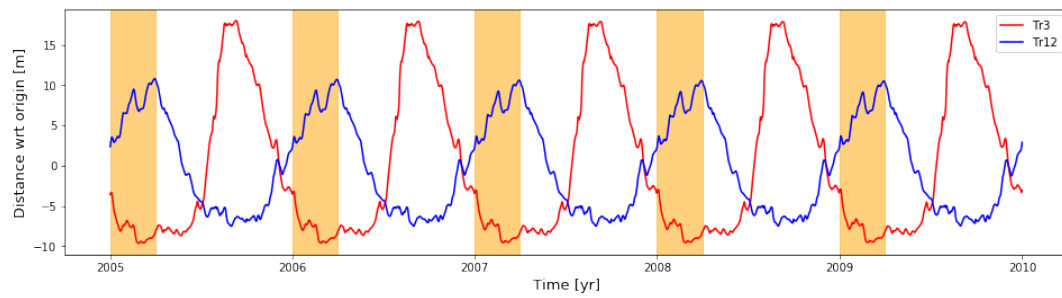
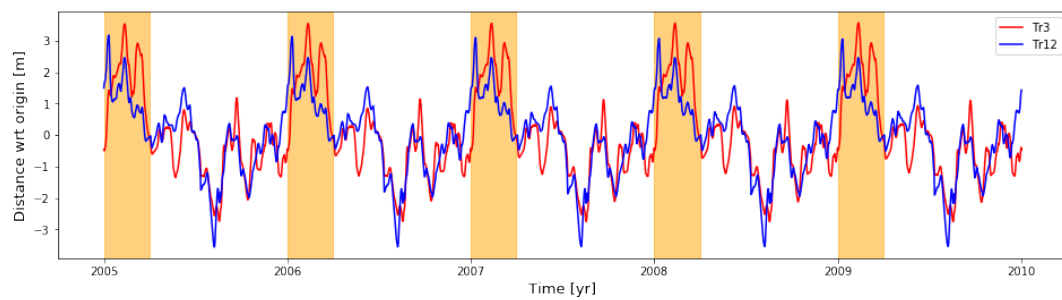
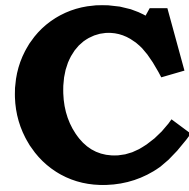
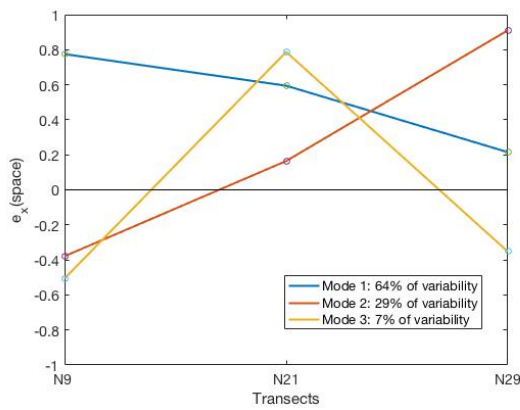
(a)  $dt = 30$ (b)  $dt = 90$ (c)  $dt = 180$ (d)  $dt = 360$ 

Figure B.5: The seasonal components of shoreline variation at transect 3 and 12. The orange panels show the time period of January to March (summer in Australia).

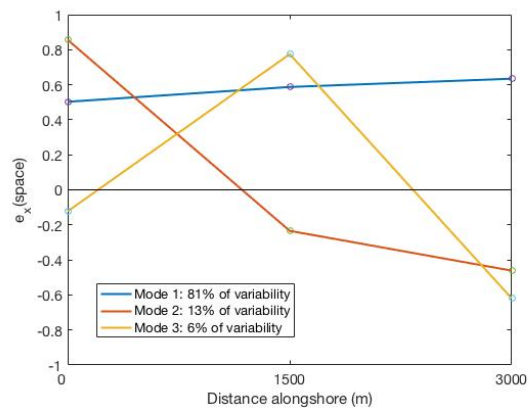


# Result plots of data analysis

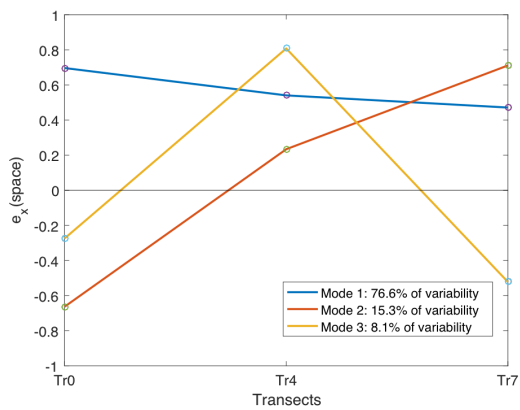
## The result plots of PCA



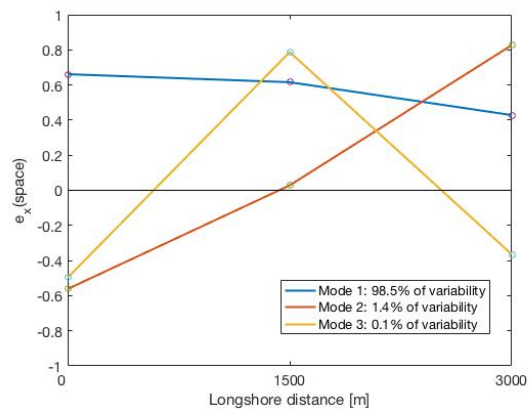
(a) Narrabeen Beach



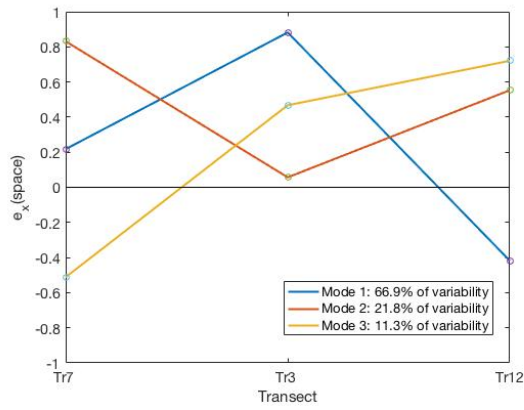
(b) Perranporth



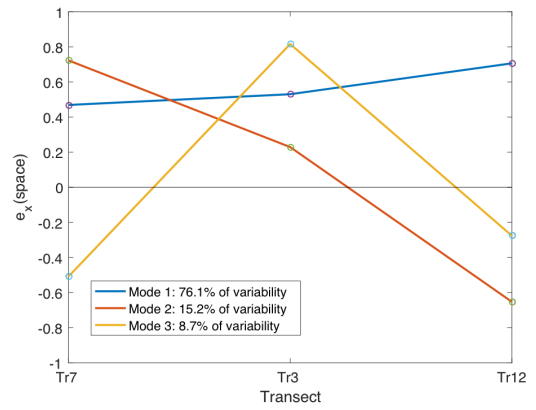
(c) Ocean Shores



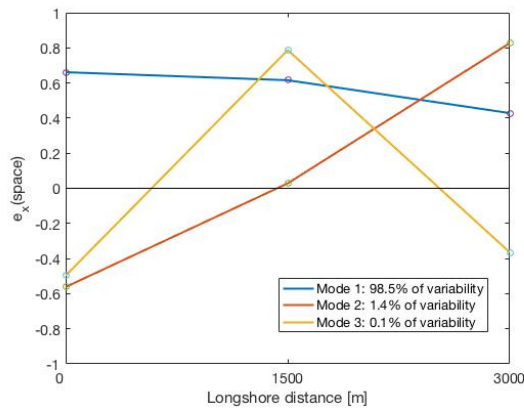
(d) The Nile Delta



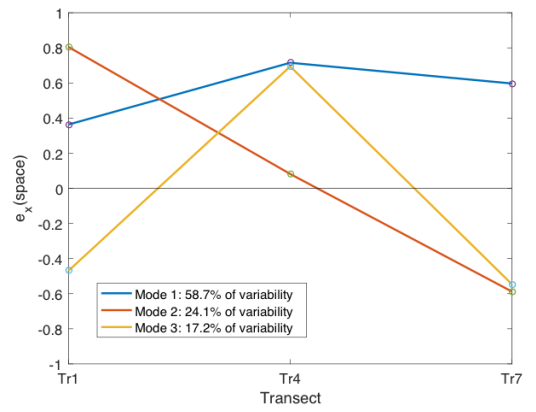
(e) Perth



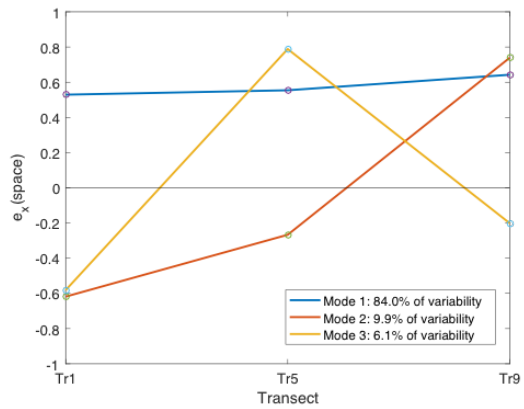
(f) Ocean Beach



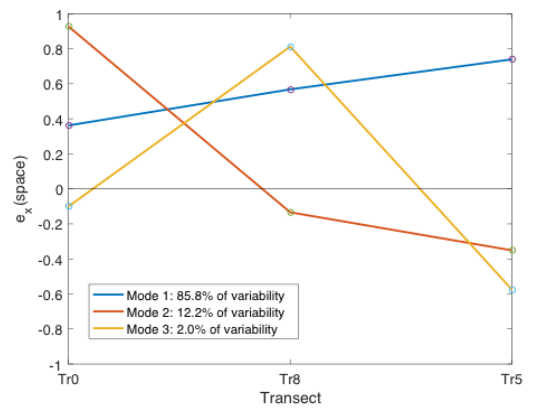
(g) The Nile Delta



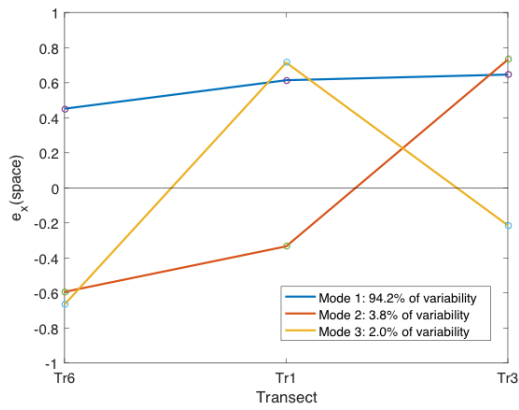
(h) West Fire Island



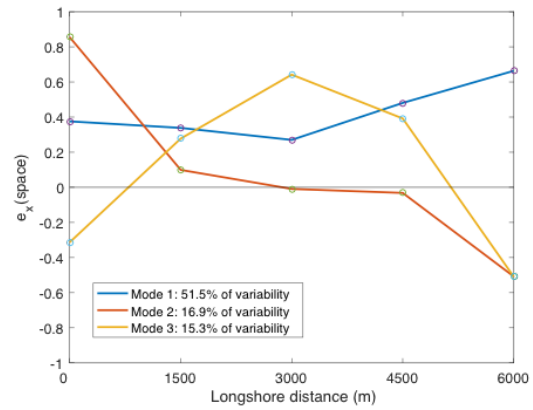
(i) Saler Beach



(j) Cullera Beach



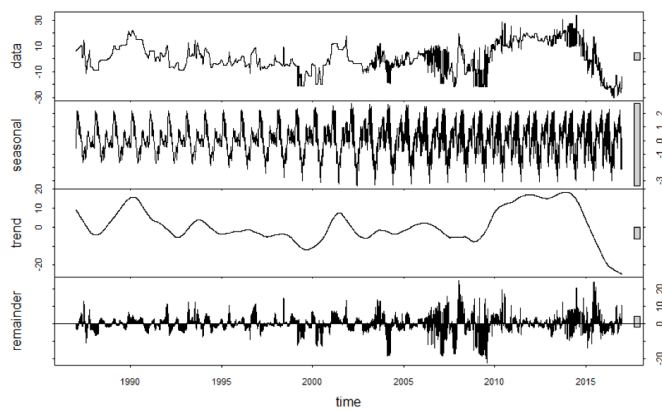
(k) Gatseau sandspit



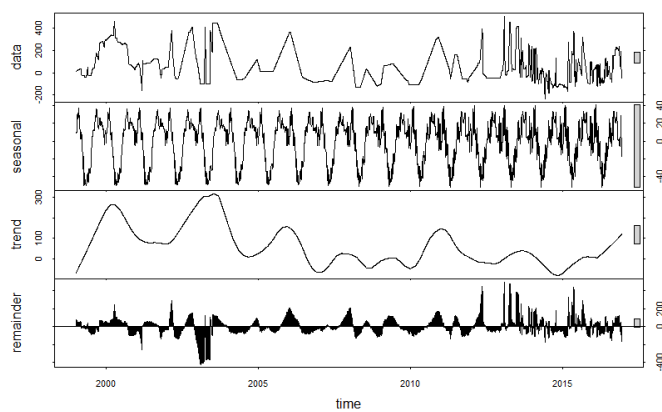
(l) Wrightsville Beach

Figure C.1: The PCA results of shoreline variation at different sites of interests.

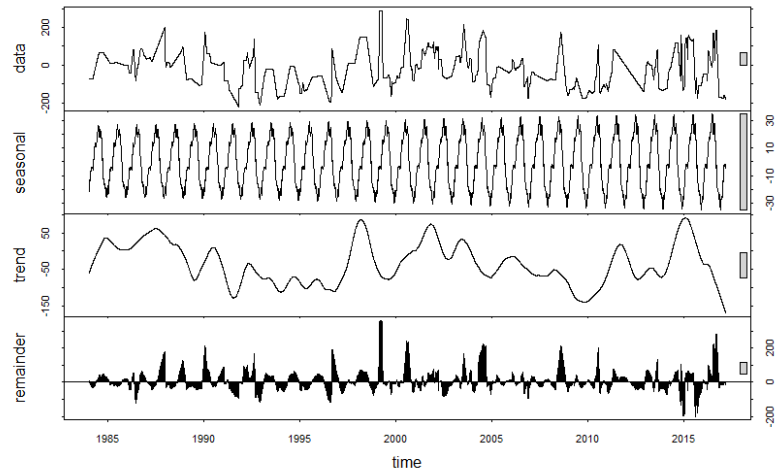
## The result plots of STL decomposition



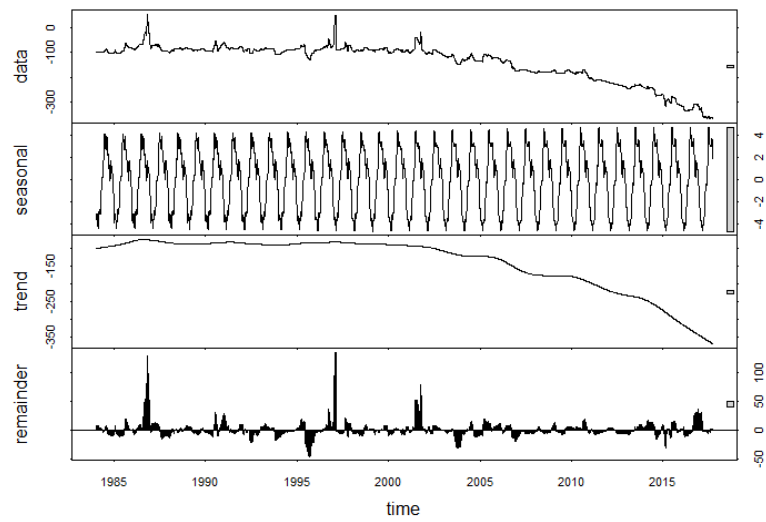
(a) Narrabeen Beach



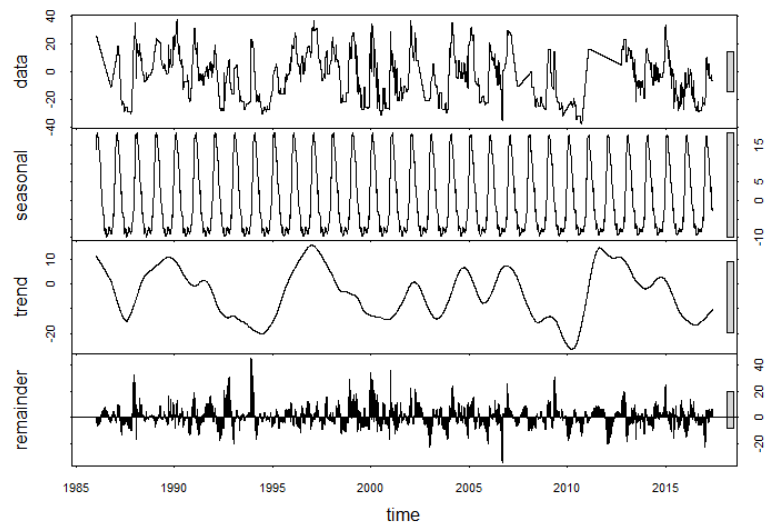
(b) Perranporth



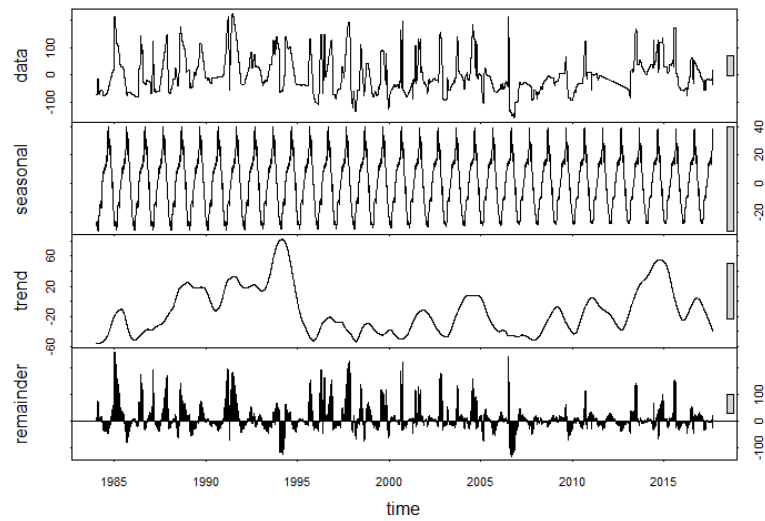
(c) Ocean Shores



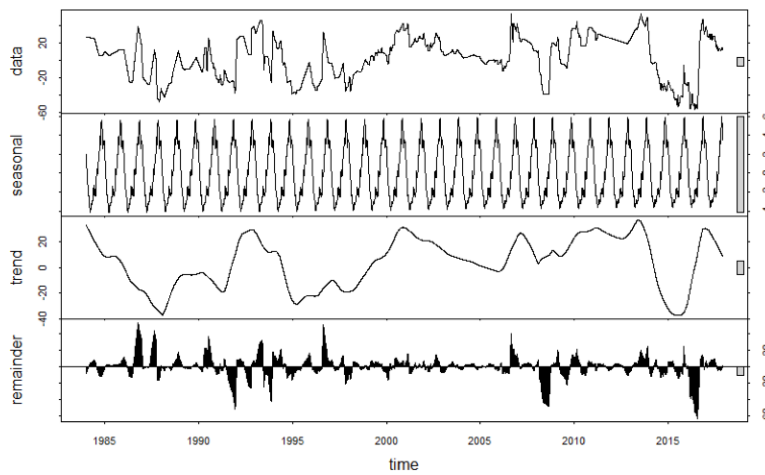
(d) The Nile Delta



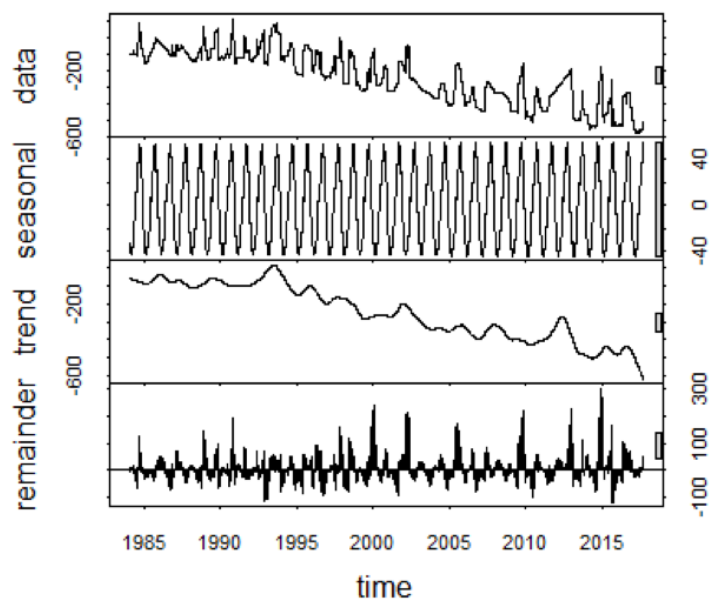
(e) Perth



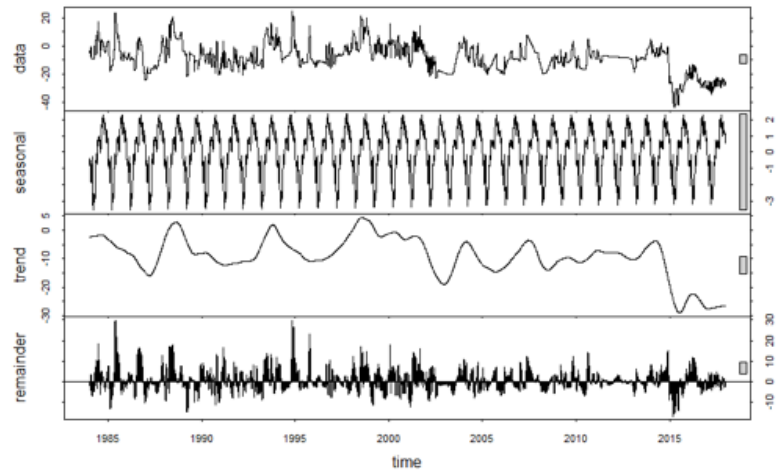
(f) Ocean Beach



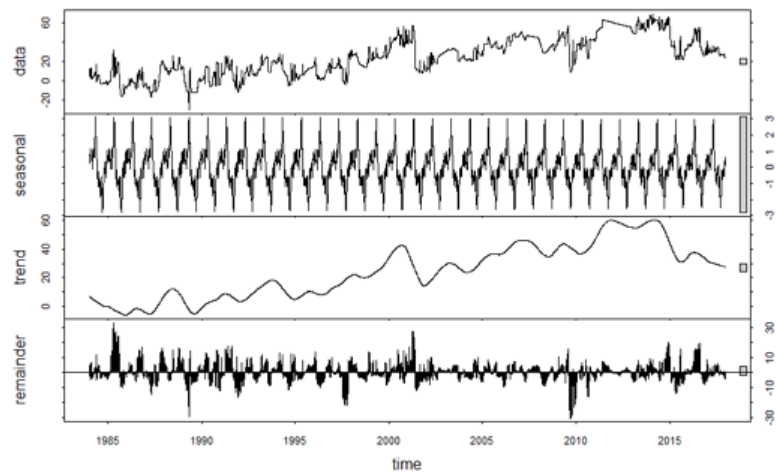
(g) Fire Island



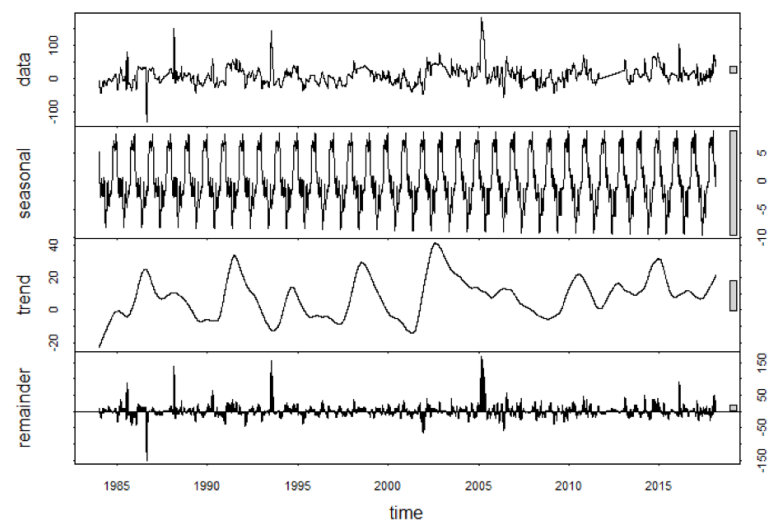
(h) Gatseau sandspit



(i) Saler Beach



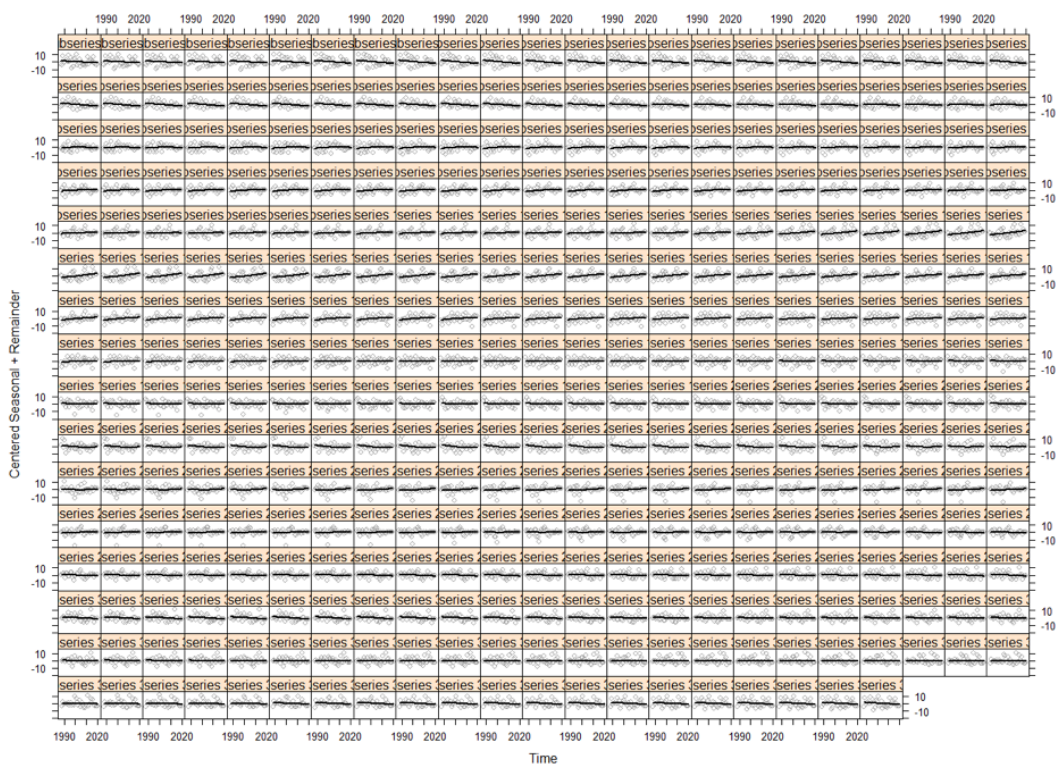
(j) Cullera Beach



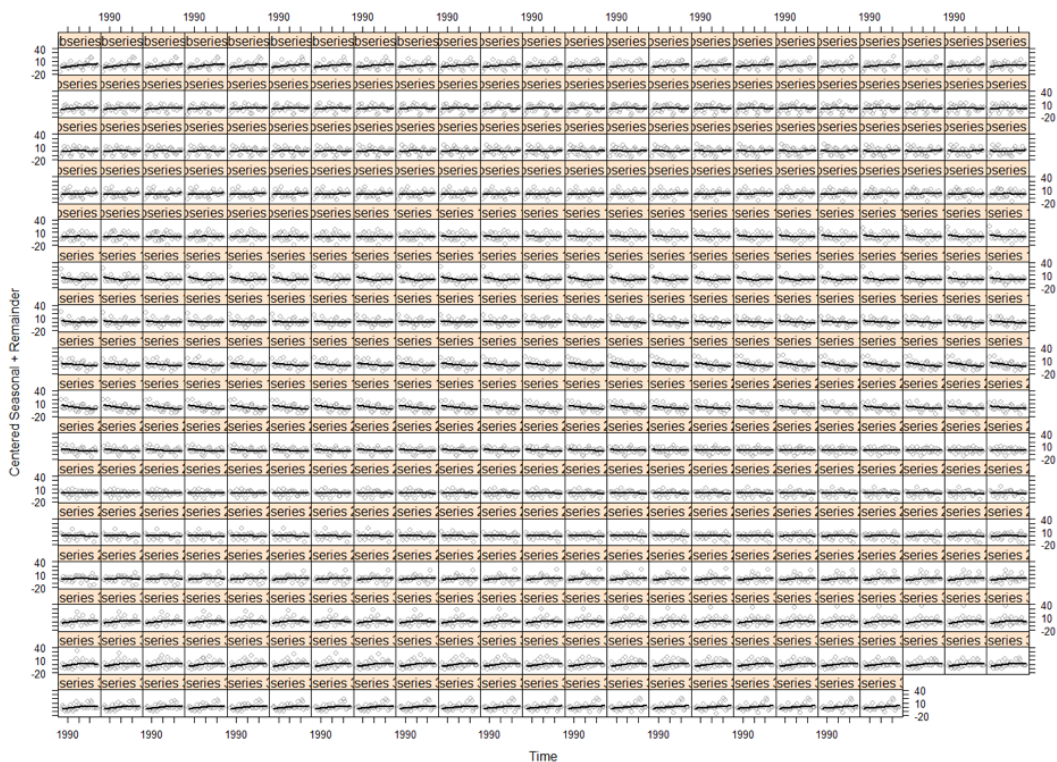
(k) Wrightsville

Figure C.2: The STL decomposition results of shoreline variation at different sites of interests.

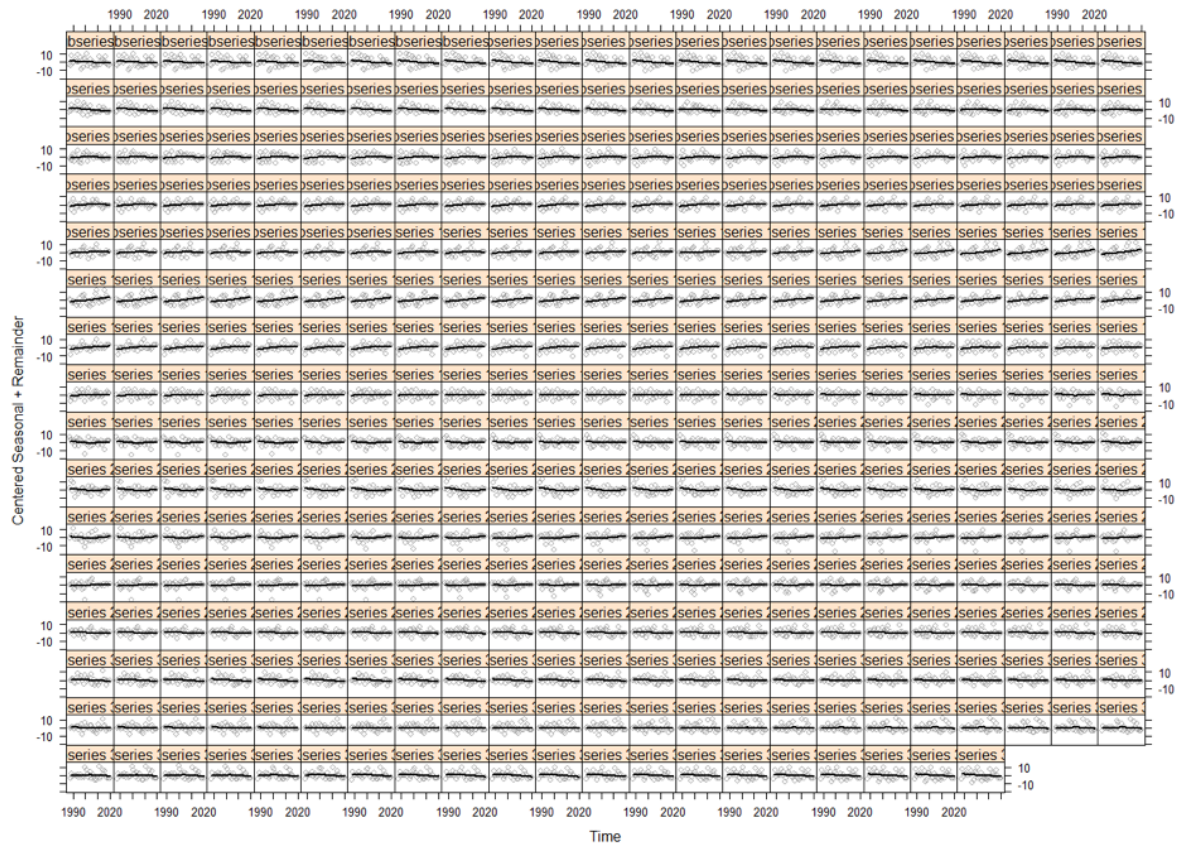
## Seasonal-diagnostic plots



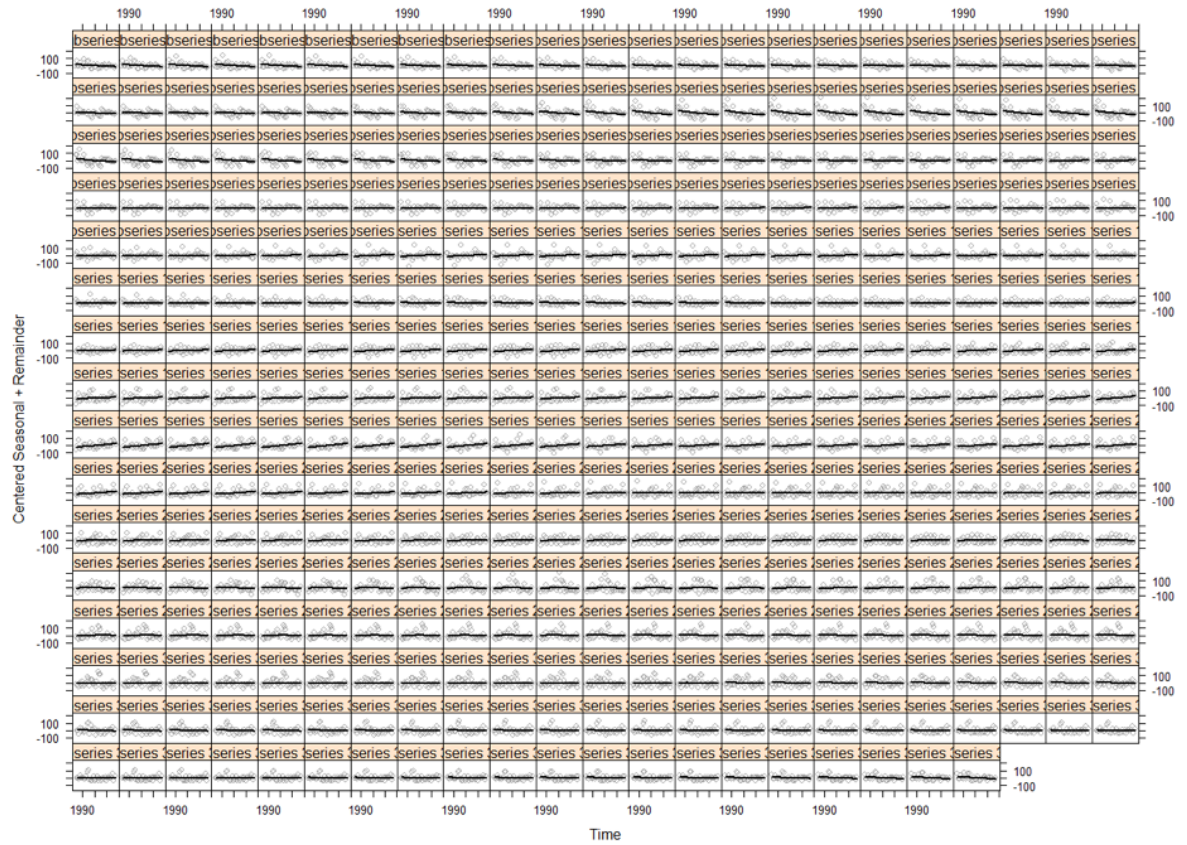
(a) Narrabeen Beach



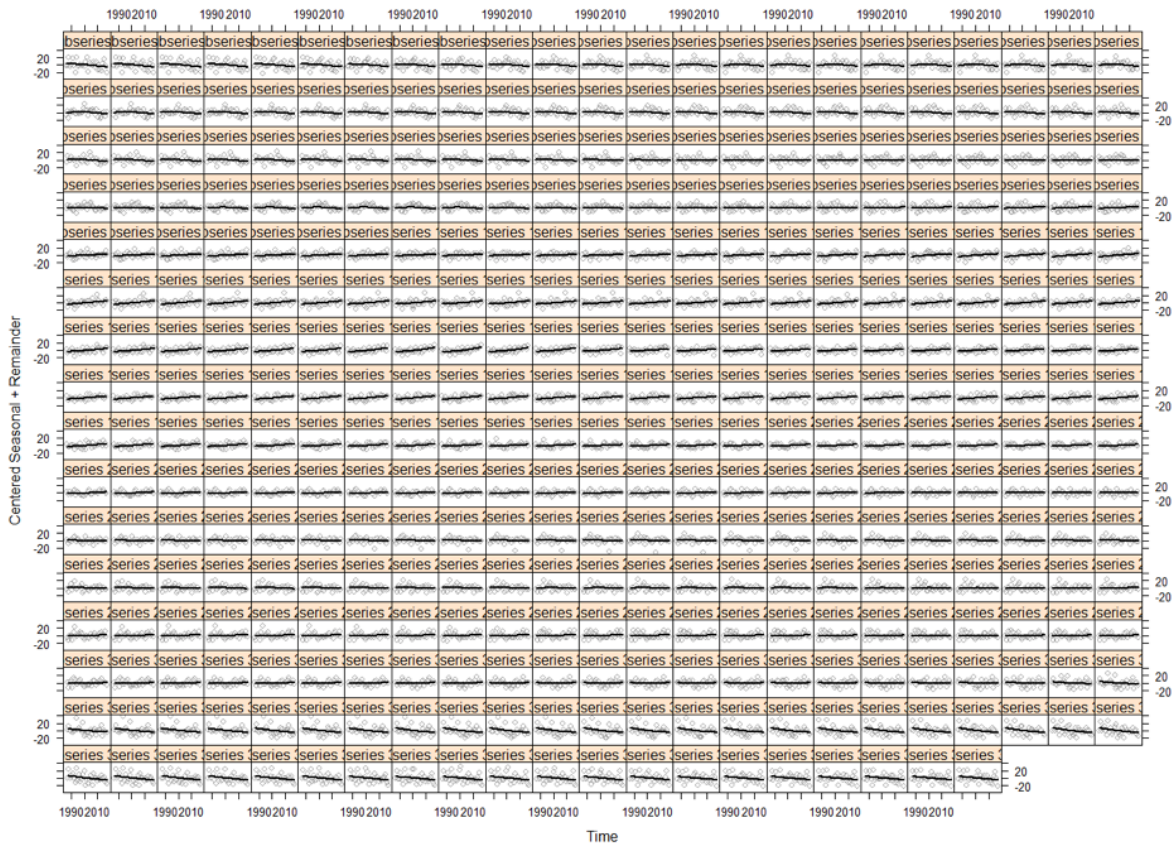
(b) Moruya



(c) Pedro



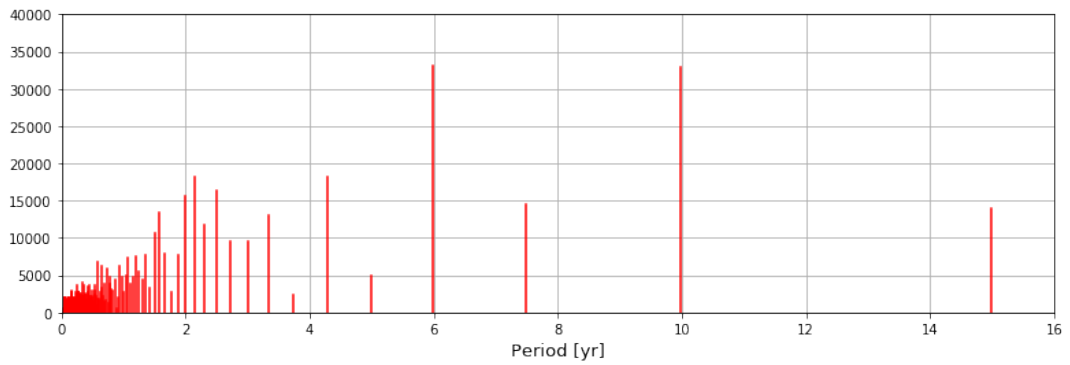
(d) Ocean Shores



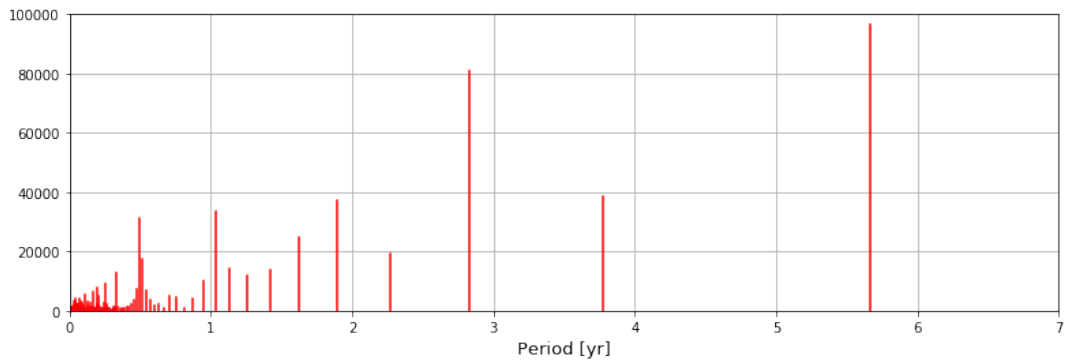
(e) Perth

Figure C.3: The seasonal-diagnostic plots of choosing seasonal smoothing parameters for STL decomposition at different sites of interests.

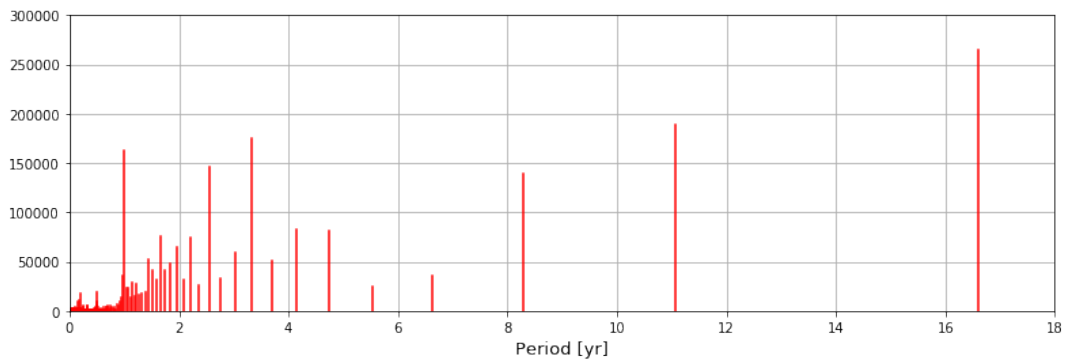
## The result plots of FFT



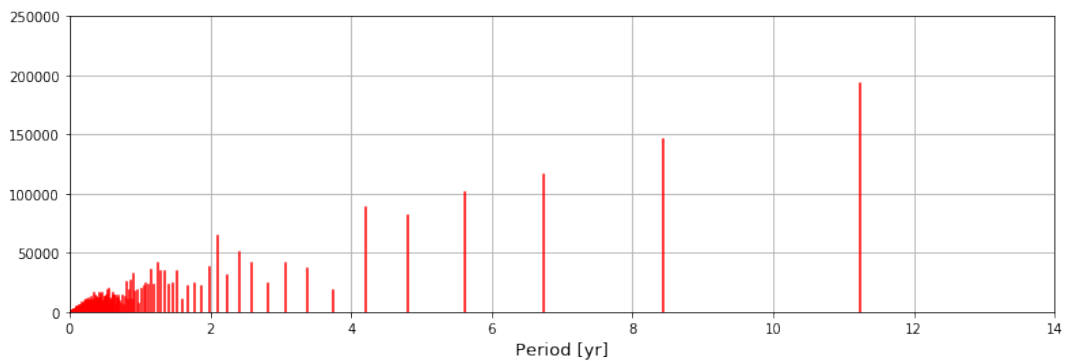
(a) Narrabeen Beach



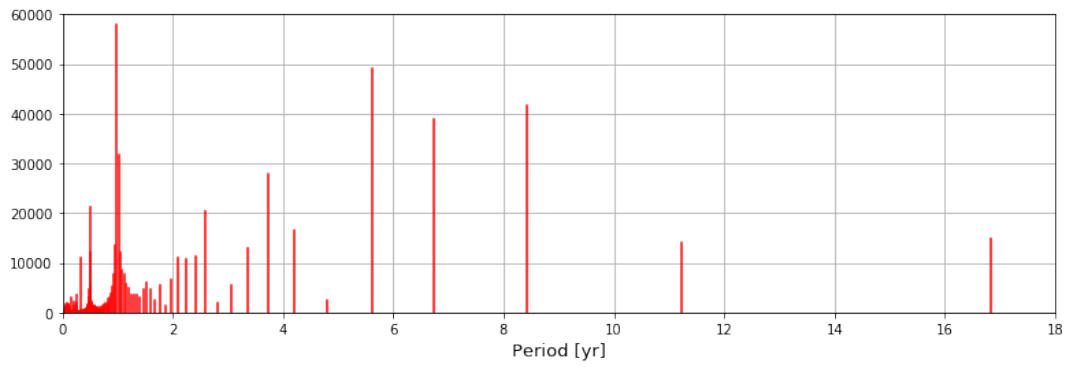
(b) Perranporth



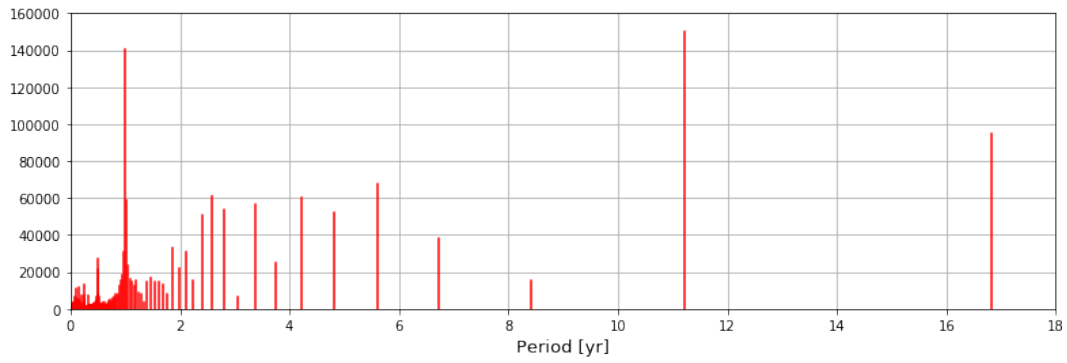
(c) Ocean Shores



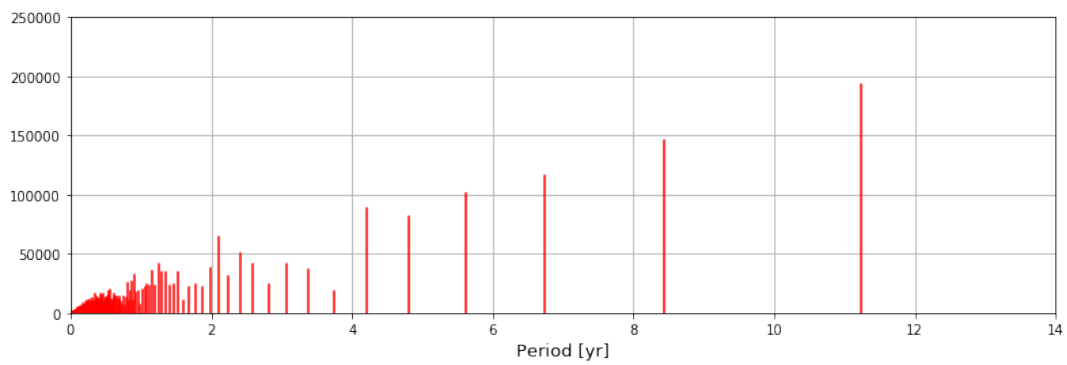
(d) The Nile Delta



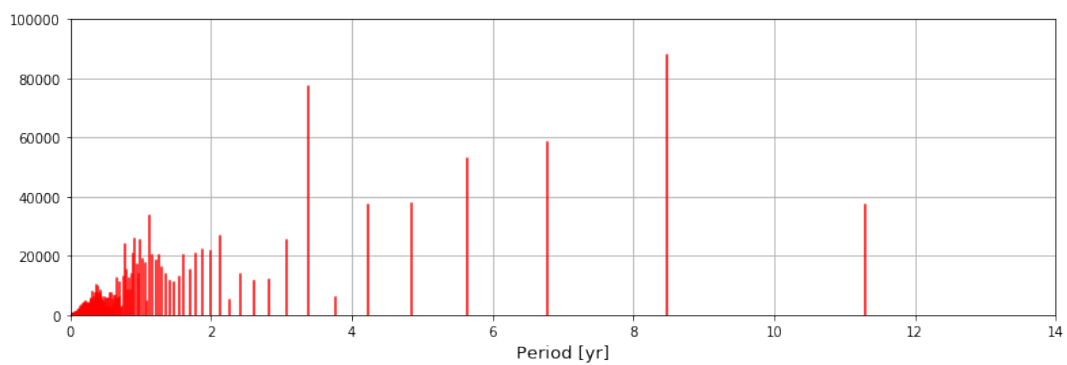
(e) Perth



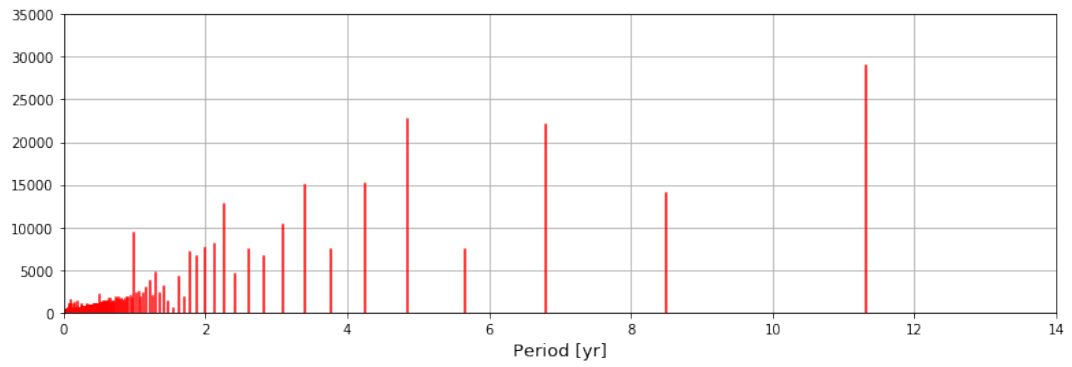
(f) Ocean Beach



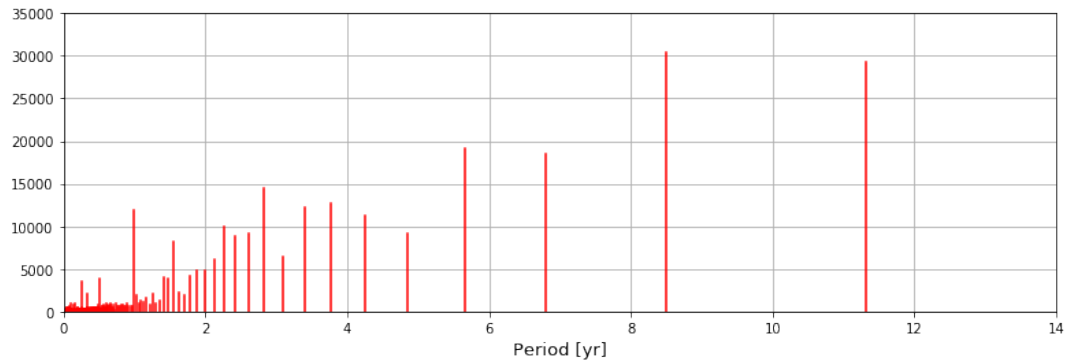
(g) The Nile Delta



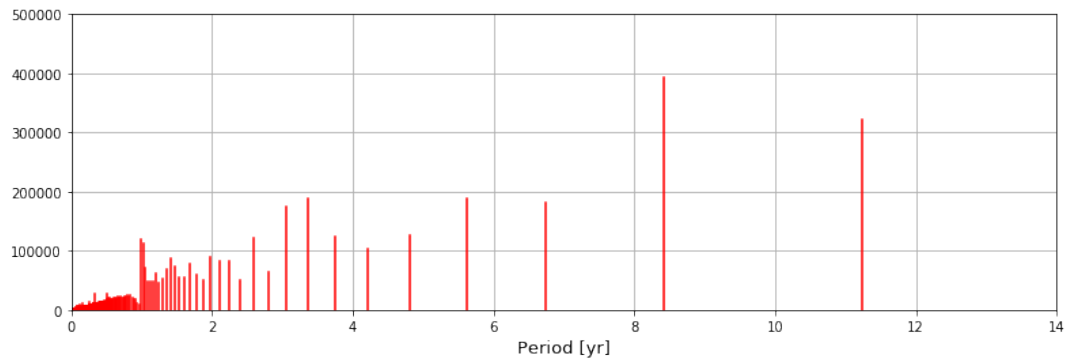
(h) West Fire Island



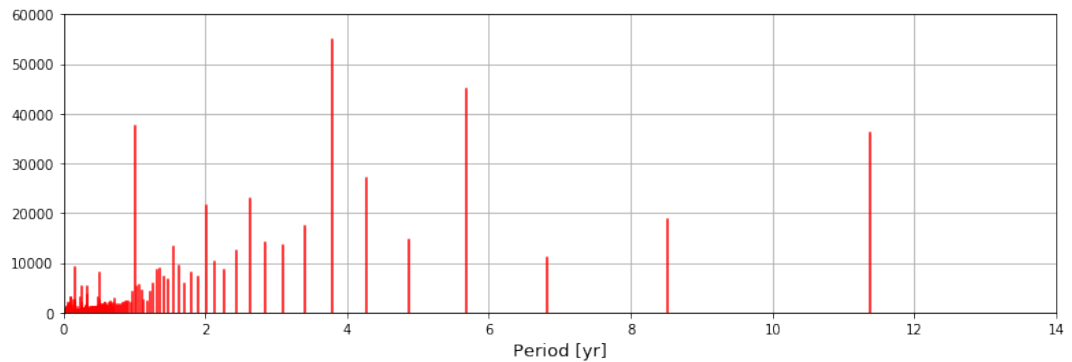
(i) Saler Beach



(j) Cullera Beach



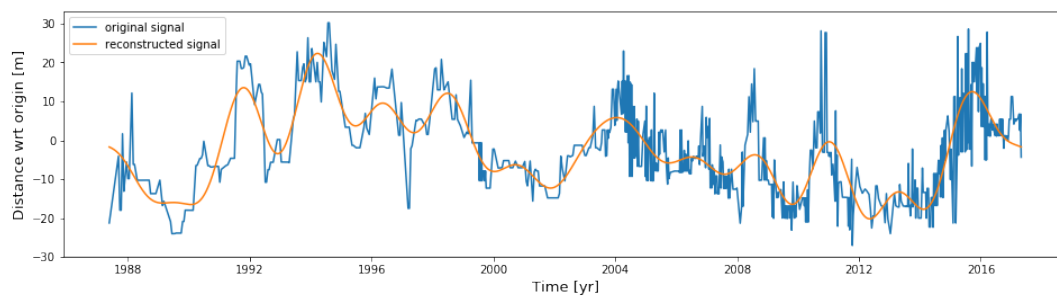
(k) Gatseau sandspit



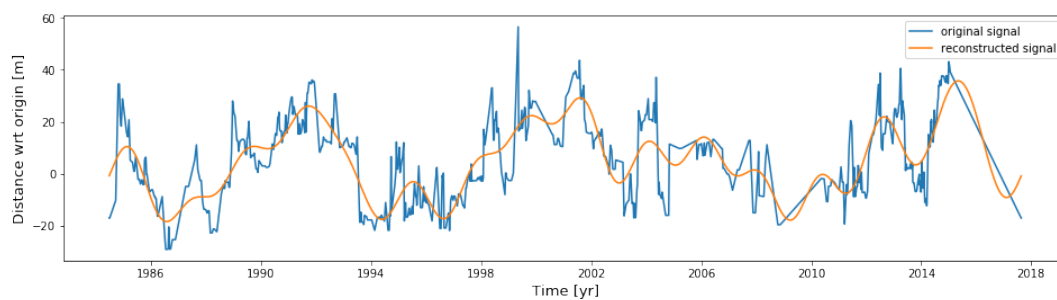
(l) Wrightsville Beach

Figure C.4: The FFT results of shoreline variation at different sites of interests.

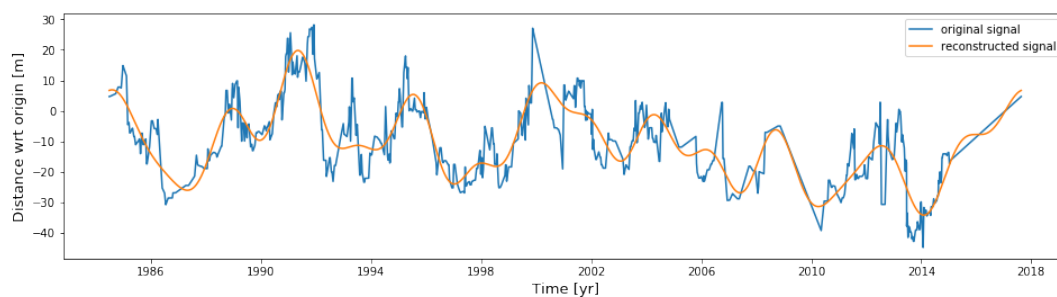
## Inverse fast Fourier transform



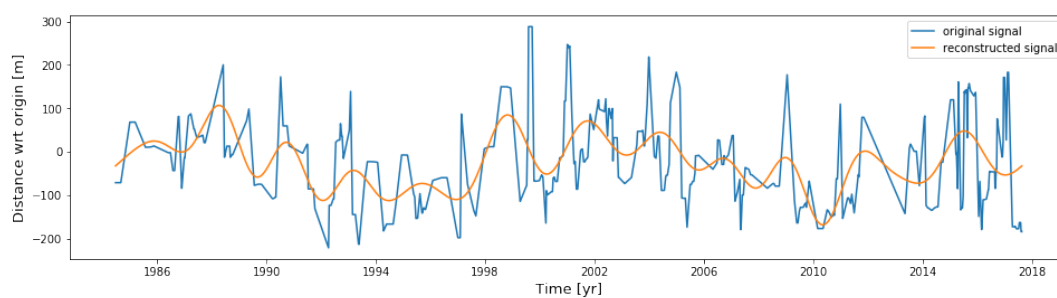
(a) Narrabeen Beach



(b) Moruya



(c) Pedro



(d) Ocean Shores

Figure C.5: The reconstructed shoreline changes using only the components with a frequency of larger than 2 years.

## Others

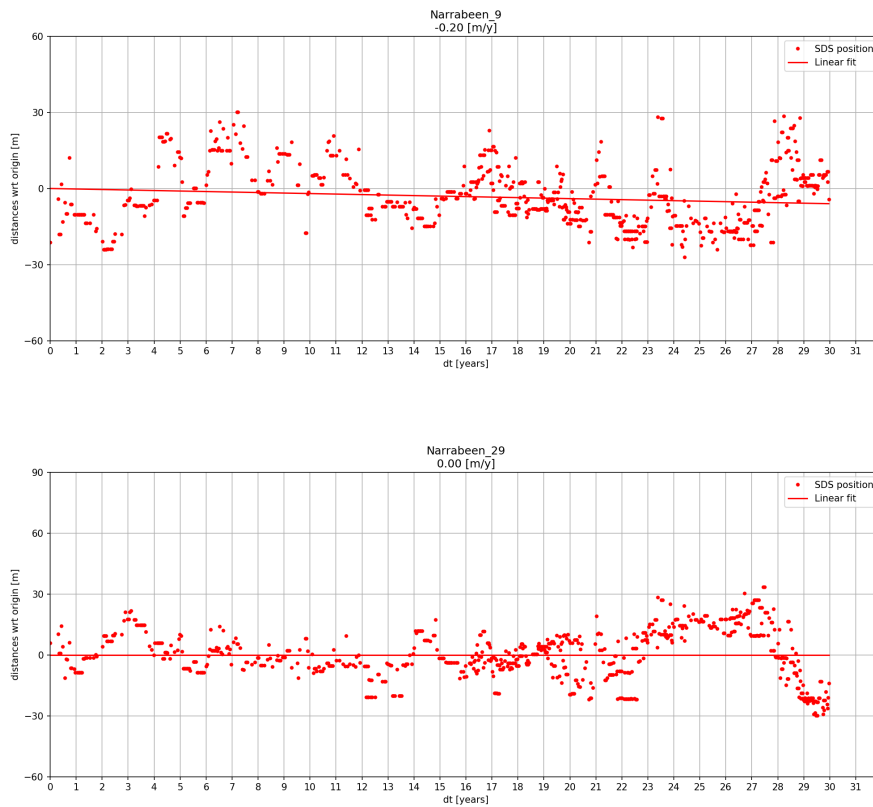


Figure C.6: Time series of shoreline movement at transect 9 and transect 29 on Narrabeen Beach

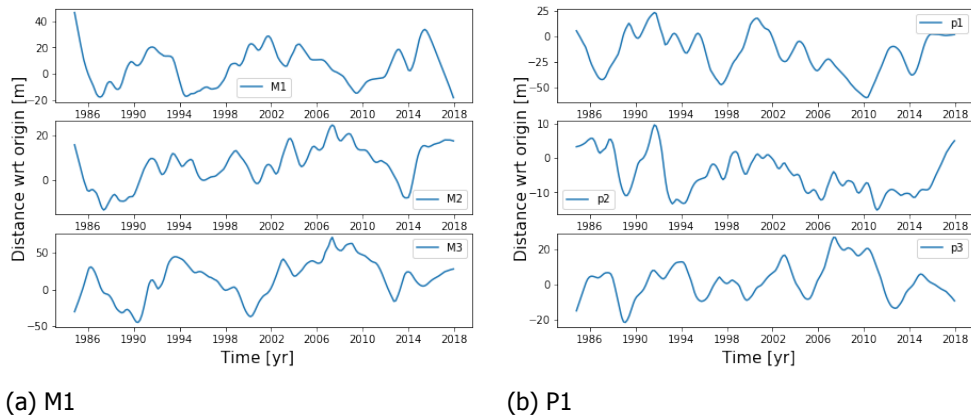
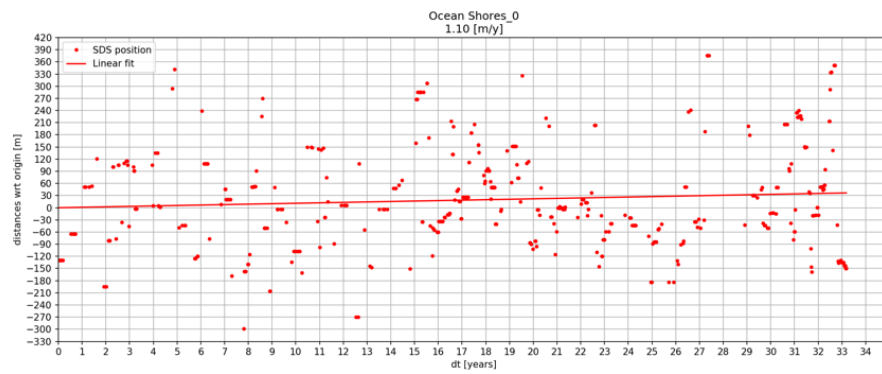
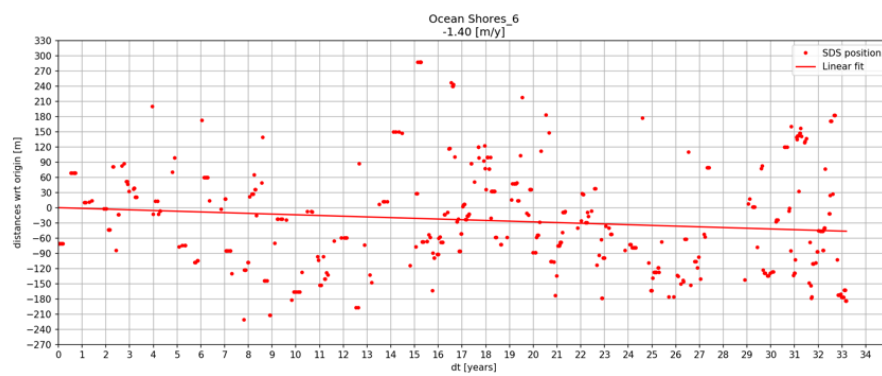


Figure C.7: The trend components of shoreline change at the three main transects at Moruya and Pedro.



(a) Tr0 (northern part)



(b) Tr6 (southern part)

Figure C.8: Time series of shoreline change at transect 0 and 6 (Ocean Shores).

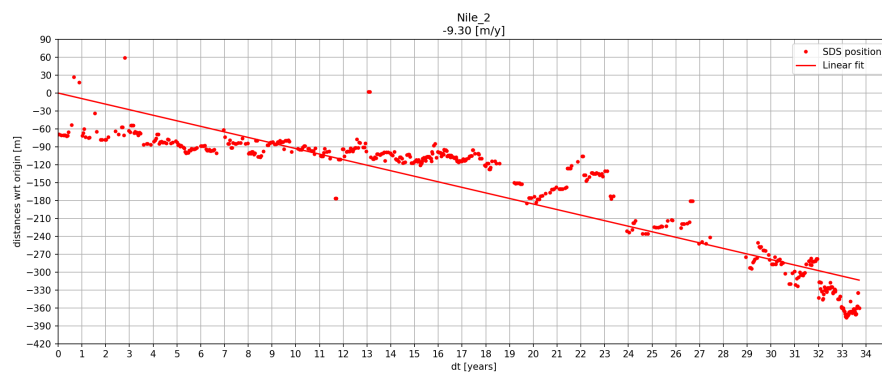
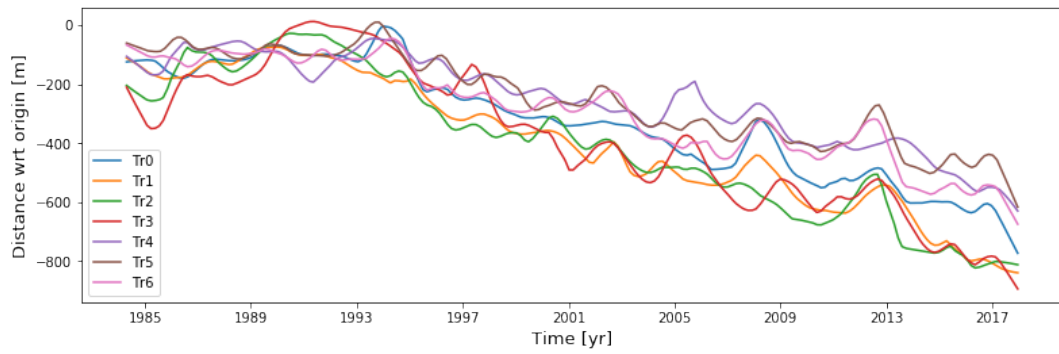
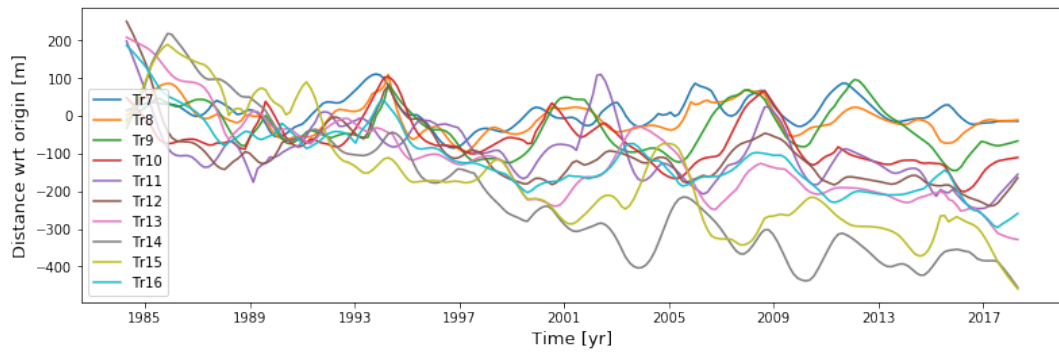


Figure C.9: Time series of shoreline position at transect 2 on mouth of Rosetta branch.



(a) Gatseau sandspit



(b) Cap Ferret sandspit

Figure C.10: Trend components of shoreline change at Gatseau sandspit and Cap Ferret sandspit.

# D

## Other data process techniques

### D.1. Narrabeen Beach

#### Trend analysis

In this section, the trend components for the shoreline variation at the five main transects (Figure 3.11) are extracted to reveal both beach oscillation (erosion-accretion) and rotation between the boundary headlands at Narrabeen Beach (Figure D.1).

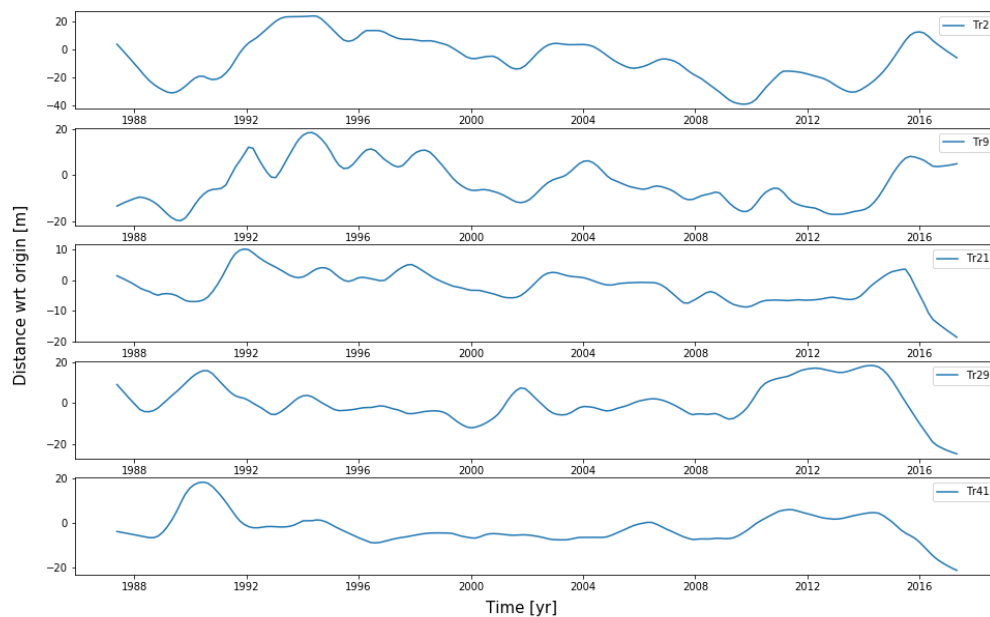


Figure D.1: The trend components for the five main transects.

The standard deviation values (STD) for shoreline movement over the 30 years at the five transects are shown in Table D.1. The large value of transect 2 indicates large shoreline variation at the north end transect over the three decades. On the other hand, transect 21 has a relatively small value, which shows that the middle transect behaves like a 'hinge'. However, transect 41 also has a relatively small STD value, which is not that reasonable considering the rotational pattern of the beach. One of the probable reasons is that the spatial resolution of the SDS is around 30 m (Hagenaars et al. 2018),

and thus the errors of the shoreline detection become higher when shoreline movement is not that 'obvious', which is the case at the Narrabeen Beach.

Table D.1: The standard deviation values for the shoreline variation at five main transects over 30 years.

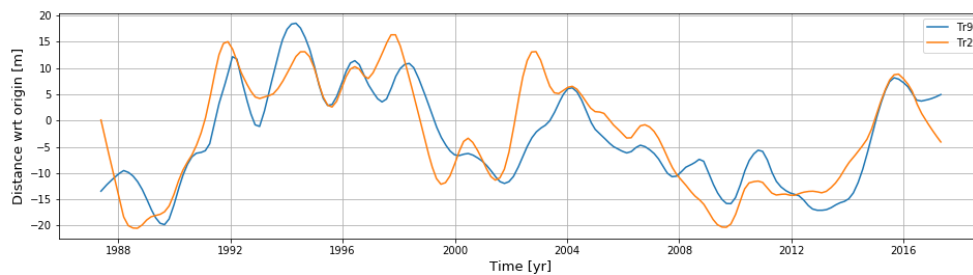
Transects	Tr2	Tr9	Tr21	Tr29	Tr41
<b>Standard deviation value (m)</b>	15.9	9.24	4.87	8.88	6.5

The cross-correlation coefficients (at zero lag) were estimated for the main transects as shown in Table D.2. The P-values are 0.00 for all these correlations, indicating the statistical significance associated with the correlation is very high.

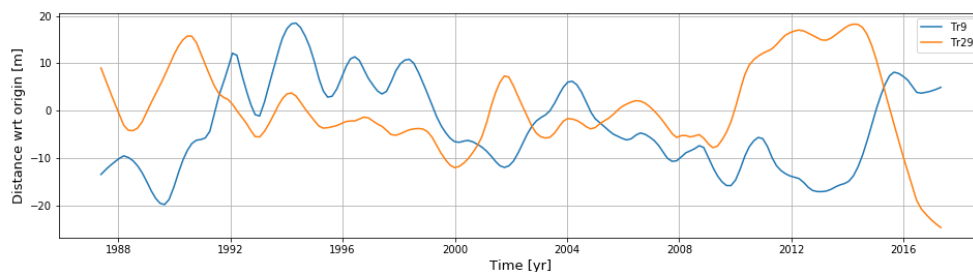
Table D.2: Cross-correlation coefficient (at zero lag) matrix for trend components of shoreline position at Narrabeen Beach.

Transects	Tr2	Tr9	Tr21	Tr29	Tr41
Tr2		0.879	0.568	-0.415	-0.344
Tr9			0.555	-0.442	-0.332
Tr21				0.056	0.09
Tr29					0.824

The high positive correlation between transect 2 and 9 (0.879) indicates that any variations in shoreline position at transect 2 also occur at transect 9, as shown in Figure D.2a. The correlation coefficient for shoreline movement at transect 9 and 29 is -0.44, and for signals at transect 2 and 41 the coefficient is -0.344, showing shoreline change out of phase at the two ends (i.e. beach rotation) as shown in Figure D.2b.



(a) Trend components for Tr2 and Tr9



(b) Trend components for Tr9 and Tr29

Figure D.2: The trend components for shoreline change at transect 2, transect 9 and transect 29.

The result of trend analysis supports the conclusion made in Section 3.6.1 that the Narrabeen Beach has a rotational feature.

## D.2. Moruya and Pedro

### Correlation analysis of trend components

In this section, the trend components for the three main transects of each beach (Figure 3.19) are analyzed (Figure C.7) to reveal both beach oscillation (erosion-accretion) and rotation from 1998-01 to 2017-01. The correlation analysis (Table D.3 and D.4) shows some significant features of the three beaches. At Moruya and Pedro the southern end of each beach is significantly negatively correlated with the northern, indicating that both beaches have the same rotational pattern as Narrabeen Beach. Additionally, the southern and northern profiles are significantly positively correlated between the two sites, together with the significant negative correlation between M1 and P3 (M3 and P1) showing that the response of beaches is synchronous. The P-values are 0.00 for all these correlations, showing the statistical significance associated with the correlation is very high.

Table D.3: Correlation within sites.

<b>Narrabeen</b>	N9	N21	N29
N9	-	0.476	-0.5
N21	-	-	0.094
N29	-	-	-
<b>Moruya</b>	M1	M2	M3
M1	-	-0.282	-0.621
M2	-	-	0.618
M3	-	-	-
<b>Pedro</b>	P1	P2	P3
P1	-	0.522	-0.593
P2	-	-	0.003
P3	-	-	-

Table D.4: Correlation between sites.

	<b>P1</b>	<b>P2</b>	<b>P3</b>
<b>M1</b>	0.824	0.312	-0.51
<b>M2</b>	-0.294	0.010	0.623
<b>M3</b>	-0.744	-0.407	0.764
	<b>N9</b>	<b>N21</b>	<b>N29</b>
<b>M1</b>	0.594	0.375	-0.211
<b>M2</b>	0.176	-0.021	-0.447
<b>M3</b>	-0.354	-0.141	-0.021
	<b>N9</b>	<b>N21</b>	<b>N29</b>
<b>P1</b>	0.622	0.064	-0.378
<b>P2</b>	0.512	0.127	-0.644
<b>P3</b>	-0.238	-0.058	-0.147

## D.3. Perranporth

**Background:** Perranporth is a double-barred beach of low-tide bar/rip type, dominated by cross-shore surf zone driven sediment transport and shore-normal waves (Masselink et al. 2014). According to Scott et al. (2015), since 1990 the 5 periods for highest 4-month mean  $H_s$  were during the winter of 1989/90, 1993/94, 1994/95, 2006/07 and 2013/14, and intertidal beach sediment volume was used to study the erosion and recovery events at Perranporth. They made a conclusion that the erosion events in 2006/7 and 2007/8 winters caused a severely depleted beach, which was followed by several years

of beach recovery (2008-2013), and then terminated by another erosional event in 2014.

**Hypothesis:** The time series of shoreline change derived from the SDS can be used for unravelling the storm effects at Perranporth.

Based on the newest available satellite image (2017-04-20), 11 transects were created perpendicular to the SDS at Perranporth with spatial resolution of 500 m (Figure D.3). SDS was obtained from Landset 5, Landset 7 and Landset 8 dataset. The intersections between SDS and transects were created to represent shoreline variation at Perranporth over 30 years .



Figure D.3: Transects position at Perranporth.

### Principal component analysis

PCA was performed on shoreline change at both ends and center profiles at Perranporth (Figure D.4). Mode 1 (81%) indicates shoreline oscillation, showing that the primary mode consists a uniform shoreline advancement or recession with the ends experiencing similar changes. Mode 2 represents the rotational feature ( $\beta$  equals 13% < 15%), so the beach at Perranporth is classified as a **non-rotational** beach.

The time series of shoreline movement at all the transects were compared, and they all exhibit similar patterns. Thus, shoreline movement at transect 9 was selected as a representative (Figure D.5). The following time series analysis will mainly focus on shoreline change at transect 9.

The availability of SDS is not optimistic at the beginning of 15 years, especially from 1991 to 1997, during which time almost no satellite images could be used for shoreline detection at Perranporth (Figure D.5, dt =7-13). To reduce the influence of missing points for time series analysis, linear interpolation method was applied to preprocess the original signals and the result is shown in Figure D.6. However, due to the time span of missing point is quite long (1991-1997), which takes up almost 1/5 of the whole time series, the overall linear interpolated signals may result in misleading results when the STL decomposition, FFT analysis or wavelet analysis are applied. For example, a non-real spike may appear in frequency space at relatively high time scale based on the result of FFT. As Perranporth was targeted to mainly study the effects of extreme storms on shoreline change, the second half of signals might be enough for analyzing, because there was a series of extreme storms striking along the Atlantic coast of Europe during 2006/07 and 2013/14 winters (Section 3.1). Thus, the first half of data is omitted for the following analysis.

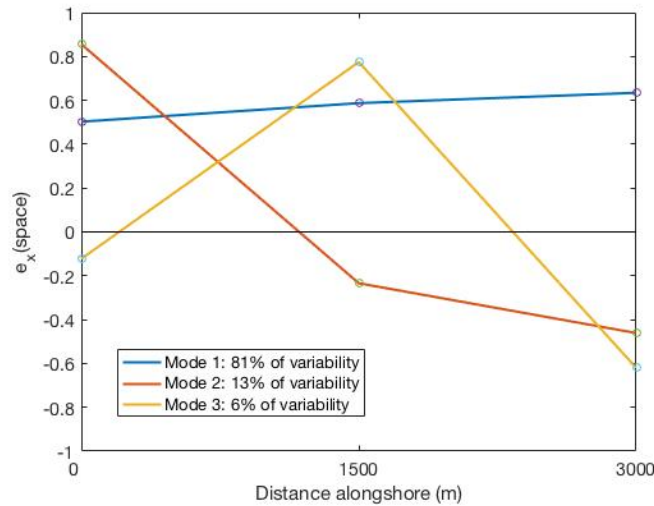


Figure D.4: The result plot of PCA of shoreline movement at Perranporth.

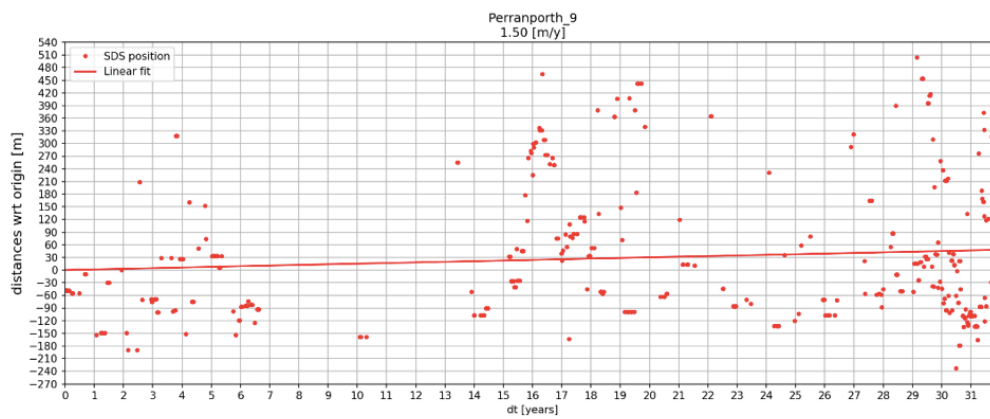


Figure D.5: Time series of shoreline position for transect 9.

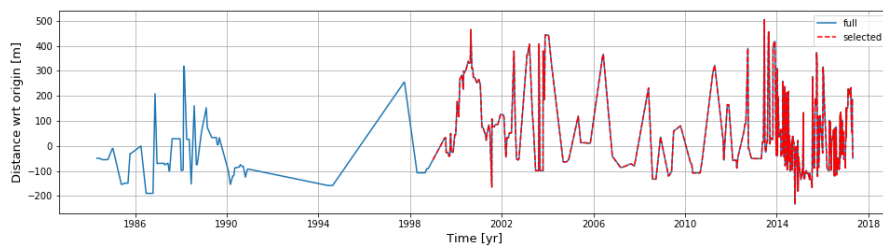


Figure D.6: The result plot of linear interpolation of time series of shoreline position for transect 9.

### The STL decomposition and FFT analysis

The smoothing parameters used for the STL decomposition at Perranporth are listed in Table D.5. The seasonal smoothing parameter  $n_s$  and trend smoothing parameter  $n_t$  are chosen in order to visually elucidate trends. Thus, for the inner loop portion, the annual seasonal component was firstly smoothed by locally weighted regression (loess) with  $p = n_s = 21$  on the original time series, and then smoothed by several moving averages of length  $n_p = n_t = 365$ . The trend component was then created by applying a moving average with the length  $n_t = 573$  (around 1.5 years) on the deseasonalized series. All the other parameters are set as the same as those for Narrabeen Beach (Section 3.6.2).

Table D.5: Parameters for STL decomposition of coastline change at Perranporth.

Parameter	$n_p$	$n_s$	$n_t$	$n_l$	$n_o$	$n_i$
Values	365	21	573	365	5	1

Figure D.7 shows the result plot of the STL decomposition of shoreline change at transect 9. Compared with the STL result plot at Narrabeen Beach (Figure 3.13), the seasonal component takes more part in the overall shoreline variation at Perranporth, but still the trend component weights more in the overall variation ( $R_{st} = 96/384 = 0.25 < 0.3$ ). The seasonal components for the first decade and the rest of signal are different to some extent, which can be explained by the larger number of available satellite images for the second half of the time series.

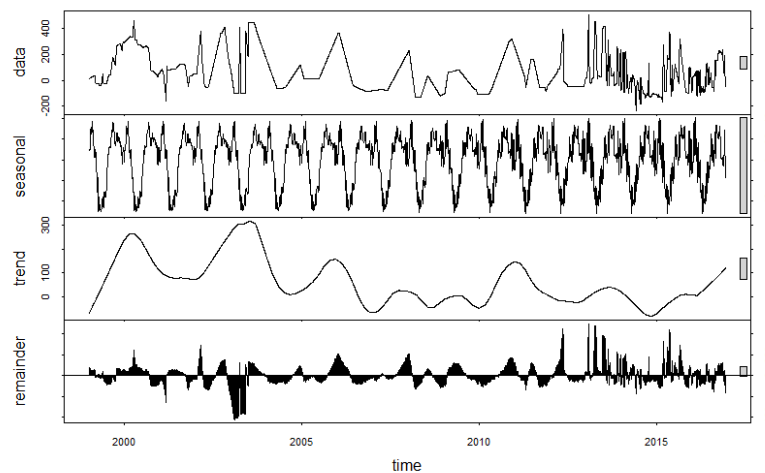


Figure D.7: The result plot of the STL decomposition at transect 9 on Perranporth.

The result plot of FFT of shoreline change at transect 9 from 2006 to 2017 is shown in Figure D.8, from which several peaks can be distinguished (the residual component was removed from the time series to eliminate the influence of storms on frequency analysis). High shoreline variation can be observed in the time scale of 3 to 6 years, which might be caused by North Atlantic Oscillation (NAO) and will be testified in Section D.3. NAO is one of the major modes of atmospheric variability in the Northern Hemisphere, and it has an unpredictable 3-5 year cyclical behaviour (Section 2.2.3). Additionally, according to the analysis in Section D.3 the recovery sequence was multi-annual, which may also interpret the high variation in 3-5 year scale. The seasonal variation is more obvious compared to that at Narrabeen Beach, and the index  $\alpha$  equals 0.32 ( $< 0.5$ ) at Perranporth. However, Perranporth is still classified as a **non-seasonal** beach, since both indices are below the thresholds.

### Trend and residual components analysis

In this section, the capability of SDS on unravelling shoreline response to storms at Perranporth is tested. As the availability of SDS is relatively optimal during the extreme storm events from 2006 to 2017, the trend and residual components were mainly analyzed during this period of time (Figure D.9).

It can be observed that the shoreline was severely eroded due to the storms in 2006/7 and 2007/8 winters, after which the beach recovered gradually during the next 4-5 years until 2012 and reached 2006 pre-storm state (trend component, Figure D.9). This multi-annual beach recovery process was also analyzed by Scott et al. (2015), and they explained the recovery by the influence of significantly low-energy winters and moderately high-energy summer during 2009-2011. Figure D.9 also shows

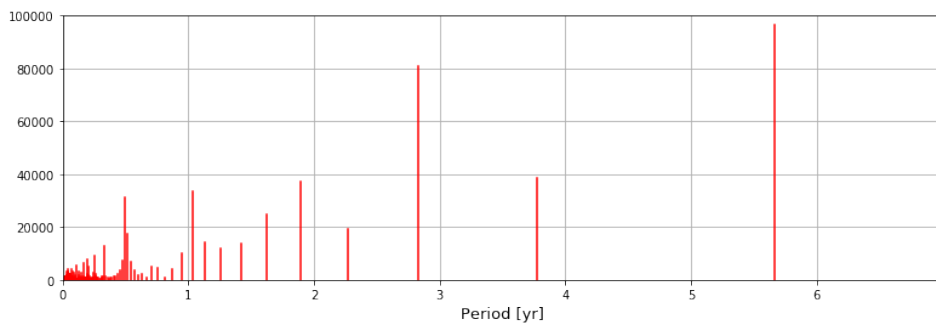


Figure D.8: The result plot of FFT of shoreline position at Perranporth from 2006 to 2017.

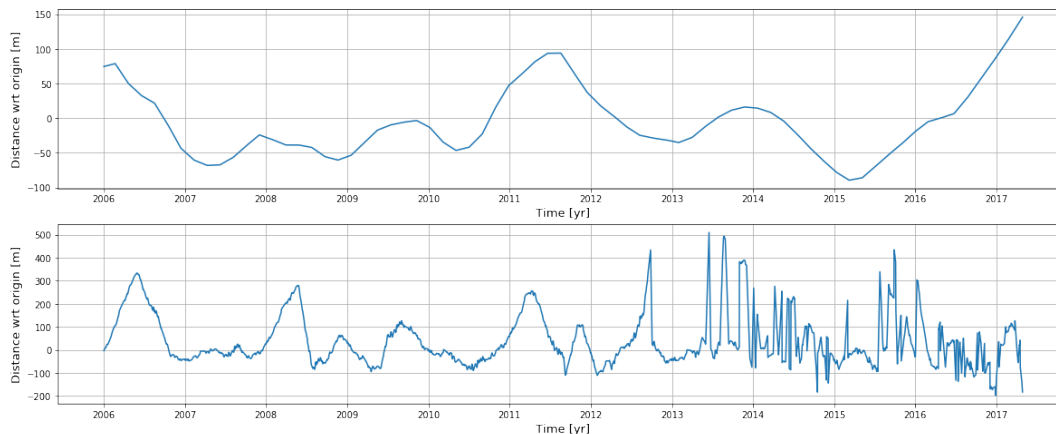


Figure D.9: The trend (upper panel) and residual (lower panel) components of shoreline change at transect 9 from 2006 to 2017.

that the recovery phase was terminated by another erosional trend in winters of 2012 and 2014, and the recovery rate after storms in the winter of 2014 was faster than that after 2006 and 2007. The above analysis results derived from SDS largely accord with the conclusions from [Scott et al. \(2015\)](#), which was based on the analysis of the intertidal beach sediment volume at Perranporth, indicating that SDS might be used as a type of indicator for studying coast states at Perranporth.

The recovery process with varying rate can be explained as follows. According to [MASSELINK et al. \(2015\)](#), the source for the initial post-storm recovery was from available sediment directly below the low water region, entrained onshore during low-moderate energy post-storm shoaling and surf zone conditions, and this process is normally fast. Moreover, a decoupled multi-annual beach recovery process also existed after the extremely energetic winters, the source of which came from the offshore (storm) bar deposits. Since the frequency of mobility potential is different, these eroded sediment respond on a different time scale ([Scott et al. 2015](#)).

For the residual component, the width for each spike should be small, which is not the case during the years from 2006 to 2012 (lower panel, Figure D.9). This might be caused by the fact that the number of satellite images for SDS is relatively small during this period of time, which can be checked with Figure D.5 ( $dt = 21-27$ ), resulting in the residual component varying more like a 'trend component' from 2006 to 2012 (not a reasonable result). Thus, the residual component is only analyzed from 2012-2017.

The magnitude of the residual component shows the extent of the abnormal case deviate from the general trend. Although the intertidal beach sediment volume always decreased during storms, the SDS may retreat or accrete depending on the specific time when the satellite images were taken. If the images are captured during storms when the water level is high and waves are striking the beach profile, the shoreline position retreats. However, if the images are taken just after storms, the deposited sediment from the dunes and upper beach can induce shoreline accretion. Therefore, the absolute

magnitude of the residual component shows the extent of the abnormal case. The striking spikes from 2013 to 2015 indicates that the shoreline was not in a 'normal condition' due to the extreme storms. Additionally, the spikes are less significant several months after the start of recovery (after the start of 2006), which can possibly be explained by the fact that the rate of shoreline accretion is more rapid at the beginning of the recovery process.

### Shoreline movement, $H_s$ and the NAO

Masselink et al. (2014) showed that winter averaged  $H_s$  and associated morphodynamic indices are strongly correlated with the NAO and displayed an unpredictable 3-5 year cyclical behaviour at Perranporth. In order to assess the ability of the SDS to unravel the relation among shoreline movement, significant wave height and the NAO at Perranporth, the cross-correlation values were calculated in this section.

According to Masselink et al. (2014), there is a strong ( $r^2 = 0.81$ ) linear relationship between predicted and measured wave height at Perranporth, and the hindcast offshore WWIII can be used as the representative for describing forcing at Perranporth. The 3-hourly modelled wave data at the 1000-m isoline was obtained from Masselink et al. (2016) at the model node of 67 (Wave Watch III model). Figure D.10 shows that from December 2013 to March 2014, there were 19 individual storms with offshore significant wave heights ( $H_s$ ) > 6.1 m (1% exceedance wave height), resulting in a mean  $H_s > 4m$  for the period.

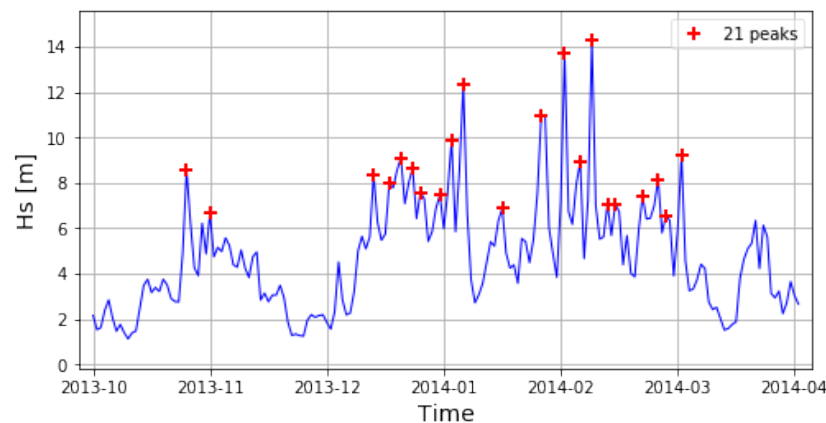


Figure D.10: Time series of offshore significant wave height ( $H_s$ ) at Perranporth from October 2013 to March 2014.

Figure D.11 shows the extended winter NAO data during the period 1984 to 2017 obtained from the Climatic Research Unit, University of East Anglia web site ([www.cru.uea.ac.uk](http://www.cru.uea.ac.uk)). The NAO index represents the difference between the normalized pressures at Gibraltar and Reykjavik following Jones et al. (1997), and a positive NAO index means the pressure differential is larger than normal (Masselink et al. 2014). According to Masselink et al. (2014), NAO may affect inter-annual beach behaviour through its control on the wind and wave conditions. Thus, the correlation coefficient between the NAO and  $H_s$  was calculated during the period of October 2013 to March 2014 (Figure D.12), and a positive correlation ( $r = 0.31$ , P-value = 0.00) between winter NAO regional atmospheric forcing and winter-averaged  $H_s$  was identified. The negative correlation between  $H_s$  and the shoreline change at transect 9 is shown in Figure D.13, indicating that increasing wave height was accompanied by erosion at the beach. The lag associated with the peak value shows that shoreline change at transect 9 lag  $H_s$  by around 40 days at Perranporth. Furthermore, based on Masselink et al. (2014), autocorrelation analysis of both wave  $H_s$  (winter) and the NAO identified weak but significant correlations ( $r = 0.2$ ) at lags of 4–5 years. Thus, it is important to consider these long-term inter-annual cycles when interpreting the representativeness of the SDS to unravel the beach change.

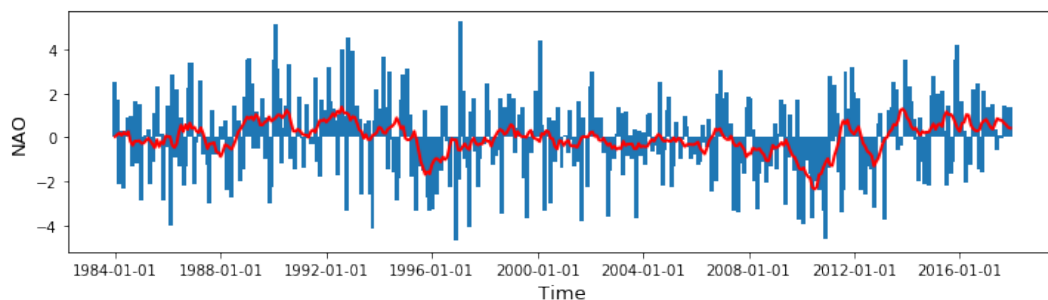


Figure D.11: The time series of winter NAO index (bars) with the one-year filtered time series (red line).

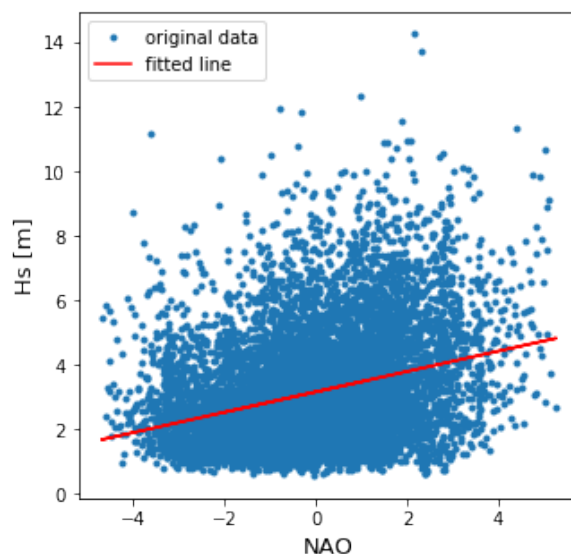


Figure D.12: The relationship between winter NAO and  $H_s$ . The red line represents the least-squares best fit ( $y = 0.31x + 3.15$ ).

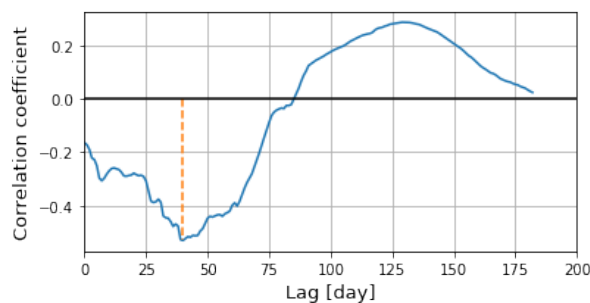


Figure D.13: Lagged cross-correlations between  $H_s$  and shoreline position at Perranporth with the peak value at (40, -0.53).

### Discussion and conclusion

The result of PCA shows that Mode 1 (81%) represents shoreline oscillation and Mode 2 (13%) indicates the rotational feature (Figure D.4). The low percentage ( $\beta = 13\%$ ) of the rotational feature suggests that Perranporth is a **non-rotational** beach. Due to the large number of missing points from 1984 to 2005 (Figure D.5), only the second half of time series were utilized for analysis at Perranporth.

The trend, seasonal and residual components of shoreline variation were generated by the STL decomposition method. The seasonal component takes more part in the overall shoreline variation compared with that of Narrabeen Beach, corroborated with the result of FFT (Figure D.8). However, since both indices are below the threshold ( $R_{st} = 0.25$  and  $\alpha = 0.32$ ), Perranporth is classified as a **non-seasonal**

## beach.

The analysis of trend component of shoreline change shows that the erosion and recovery events can be distinguished based on SDS (Figure D.9), and the results largely accord with the analysis of Scott et al. (2015). The absolute value of the residual component indicates the extent of the abnormal case, and the spikes from 2013 to 2015 suggest that the shoreline was not in a 'normal condition' due to the extreme storms. The spikes are less significant after several months of the start of 2006, showing that rate of shoreline recovery became lower after several months of the start of recovery process.

Positive correlation ( $r = 0.31$ , P-value = 0.00) between the winter NAO regional atmospheric forcing and winter-averaged  $H_s$  was identified (Figure D.12). The cross-correlation between  $H_s$  and shoreline position shows that increasing wave height was accompanied by erosion at the beach, and the variation of shoreline position at transect 9 lag the  $H_s$  by around 40 days (Figure D.13). Finally, it should be noted that the shortage of satellite images greatly impact the capability of SDS to be used as the coastal state indicator, especially when a large number of missing points exist within a specific period of time (e.g. 1991 to 1997 at Perranporth, Figure D.5 and D.6).

## Perth

The background information of shoreline changes at Floreat beach and north City beach in Perth is specified in Section 4.2.2. In this section, the spatial variation along the shoreline governed by the construction of groins is unravelled with the SDS.

### Principal component analysis

The PCA was carried out on the shoreline variation at transect 7, 3 and 12 (Figure 4.10) of Floreat beach and the north City beach (Figure D.14). The primary mode (mode 1) accounts for 66.9% of the shoreline variation: the coastline at transect 3 exhibits the largest variability, followed by that at transect 7 and then transect 12. The signs of loading at transect 7 and 3 are the same, indicating that the shoreline changes at the two transects exhibit synchronized movement (Section 3.2.3). In contrast, the coastline variation at transect 12 is out of phase with respect to transect 7 and transect 3.

The above patterns of shoreline variation can be explained by the influence of the groins located between transect 3 and 12 (Figure 4.10). The beaches located on the updrift side of the groin widen due to the accumulation of sediment against the obstruction, while the beaches downdrift undergo erosion as a result of the sediment shortage. As transect 7 and 3 are both at the north side of groins while transect 12 is located on the south side, it is reasonable to observe the similar pattern of shoreline variation at transect 7 and 3 and the disparate pattern at transect 12. Additionally, the larger variability at transect 3 compared with that at transect 7 can be explained by the shorter distance of transect 3 to the groins.

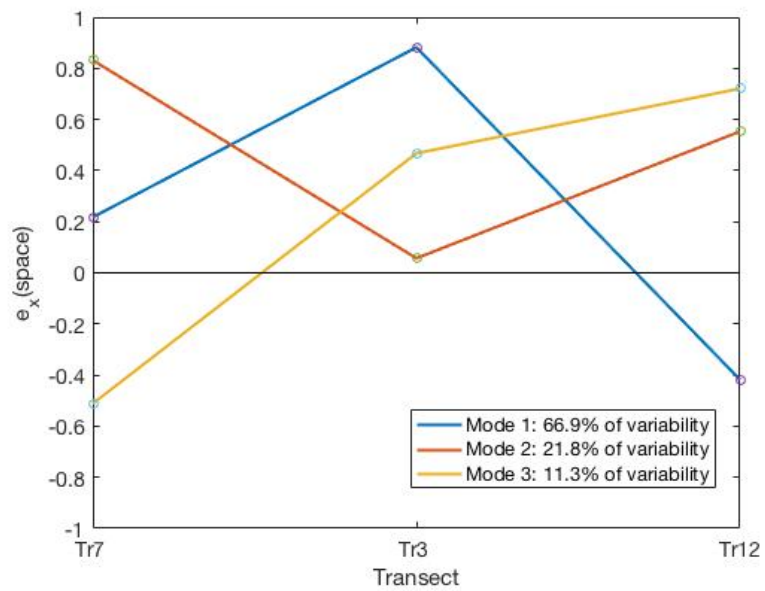


Figure D.14: The result plot of PCA of shoreline movement at Floreat beach and the north City beach in Perth.